Atomistic simulation of the structure and dynamics of grain boundaries in mantle forming minerals

Harris, D. J.

Award date:
1997

Awarding institution:
University of Bath

Atomistic Simulation of the Structure and Dynamics of Grain Boundaries in Mantle Forming Minerals

Submitted by D.J. Harris

for the degree of PhD

of the University of Bath

1997

Copyright

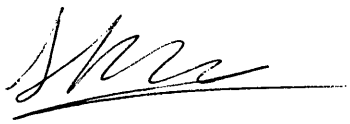

ProQuest LLC
789 East Eisenhower Parkway
P.O. Box 1346
Ann Arbor, MI 48106-1346

Summary

The aim of this thesis is to use atomistic simulation to study the effect of pressure and temperature upon the structure, energies and dynamical properties of a series of grain boundaries in mantle forming minerals using a combination of atomistic simulation techniques such as Static and Lattice Dynamical energy minimisation, Molecular Dynamics and Monte Carlo.

Chapter 1 introduces the composition of the Earth as a function of depth and indicates the high pressures and temperatures found at the depth of the mantle. The chapter also discusses the experimental methods which are available for studying mineral properties and details the current state of atomistic simulation of grain boundaries. Chapters 2 and 3 discuss the methodology used in this work including the form of the potential model that is the basis for all the calculations.

The remaining chapters present the results of the work. Chapter 4 details the method used to generate simple grain boundaries in MgO and the results of static energy minimisation of these boundaries to calculate the energies required to form the grain boundaries and their stability with respect to dissociation into two free surfaces.

The work presented in chapter 5 extends the calculations presented in chapter 4 by including pressure and temperature to see what effect this has on the structure and energies of the grain boundaries. Molecular dynamics is used to calculate the melting of MgO containing a grain boundary compared to bulk.

Chapter 6 describes the extension of static and lattice dynamics calculations used in the previous two chapters to grain boundaries in other mantle forming minerals, namely stishovite and perovskite.

Chapter 7 presents the results of Molecular Dynamics calculations to model diffusion at grain boundaries of MgO and stishovite. The importance of defect concentrations at grain boundaries for this process is shown and the results are compared to available experimental data. The effect of pressure upon diffusion is also calculated.

Chapter 8 illustrates the relationship that is found between grain boundary misorientation angle and grain boundary energy. It describes the use of a Monte Carlo method to simulate grain growth using this relationship.

Acknowledgements

I would like to thank Dr Steve Parker for his help and advice throughout the course of this PhD. Without him this would not be possible. I would also like to thank Dr Graeme Watson for his valuable input when things got tricky. Thanks go also to the N.E.R.C. for funding this work and to M.S.I. for the provision of their INSIGHTII graphics package which has been used for many of the illustrations.

I would like to thank the various members of Dr Parker's research group, Peter Oliver, John Purton, Toby Kelsey, Nora de Leeuw, Manon Higgins and Sue Redfern for their help and support. Finally I would like to thank my parents for helping me out at all stages of my education and Mr G. Gillson for his excellent juggling tips which helped to calm me when things got hectic.

Contents

1 Introduction

Atomistic simulation has been demonstrated to be a useful tool for studying structures and energies in inorganic solids at the atomistic scale. Much work has focused upon materials with industrial applications such as ceramics (Sayle et al. 1996, Catlow et al. 1997) and microporous materials (Titiloye et al. 1991, Catlow et al. 1995). However, this method can also be applied to problems concerning mineral properties. Examples of applications include bulk structure (Catlow et al 1982, Parker 1983a, 1983b, Swainson and Dove 1995), surfaces (Davies et al. 1994), defects (Wright and Catlow 1994), dislocations (Watson et al. 1996), grain boundaries (Davies 1992), the effect of temperature and pressure (Kubicki and Lasaga 1992, Harris et al. 1996), phase transitions (Matsui and Price 1992, Belonoshko and Dubrovinski 1995), thermodynamic properties (Kapusta and Guillope 1993, Patel et al. 1996) and diffusion (Harris et al. 1997).

The aim of the work described in this thesis is to use atomistic simulation to investigate the properties of grain boundaries in mantle forming minerals. These properties include the structure and energy of the boundaries as a function of pressure and temperature, processes for diffusion at the grain boundary and grain growth. The minerals considered are periclase (MgO), stishovite (SiO_2) and perovskite ($MgSiO_3$).

This chapter will describe first the Earth's interior identifying where the minerals are chiefly located. Secondly, a short explanation of the experimental methods used to study the bulk and interfaces of minerals will be given and finally a discussion of previous work to model grain boundaries using atomistic simulation will be presented.

1.1 Composition of the Earth

The Earth was formed from a solar nebula of gas and dust particles. As the solar nebula cooled via radiation the gas cloud condensed into solid particles which collected together, eventually forming the planet. The solid particles consisted of the less volatile elements and thus the Earth consists primarily of iron, nickel, magnesium, silicon and oxygen (Anderson 1989). The forming planet was heated from a number of sources, firstly, solar radiation, secondly, the gravitational energy released as particles fell to the surface and finally from the decay of radioisotopes within the planet. This heating caused fractionation of the chemical elements with the denser crystals sinking and the more volatile ones rising, leading to a zonal structure. The extremely volatile elements eventually formed the planetary atmosphere whilst the very dense elements formed an iron/nickel core (Mason 1966).

The inaccessibility of the Earth makes studying its composition very difficult. Direct observation of rock structures from deep in the Earth is impossible, the deepest hole, in the Kola Peninsula in the former Soviet Union, is only 12 km deep (Fifield 1988). However indirect methods are available, namely the study of meteorites and the use of seismic waves.

1.1.1 Meteorites

Meteorites provide a method for studying rocks which are very old. They can be divided into three main categories; siderites, which consist primarily of metals; aerolites, which are mainly silicates with little metal; siderolites which are a mixture of silicates and metals. Many of these meteorites, specifically the Carbonaceous Chondrites, have a composition of heavier elements which is thought to be very

similar to the Earth (Brown and Mussett 1981). Although able to provide data concerning the elements found within the Earth, meteorites are unable to provide information concerning the variation in structure as a function in depth. Additionally, meteorites are generally difficult to find due to their similarity to Earth rocks; most meteorites are found in the Antarctic. A more direct approach for studying the Earth's interior structure is the use of Seismology.

1.1.2 Seismology

Seismology is the study of the interior of the Earth by means of seismic waves. Seismic waves can be generated by several means but the only sources which are detectable on the opposite side of the planet are earthquakes and nuclear explosions. The waves generated can be divided into two main types, longitudinal or primary (P-) waves and transverse or secondary (S-) waves. The interior structure of the Earth is investigated by measuring the way in which these waves are reflected and refracted by changes in the density, composition etc. which is possible due to the velocity of the waves being proportional to the elastic modulus and inversely proportional to the density, i.e.

$$V_p = \sqrt{\frac{K + \frac{3}{4}\mu}{\rho}} \qquad 1.1$$

$$V_s = \sqrt{\frac{\mu}{\rho}} \qquad 1.2$$

where K is the bulk modulus, μ is the shear modulus and ρ is the density.

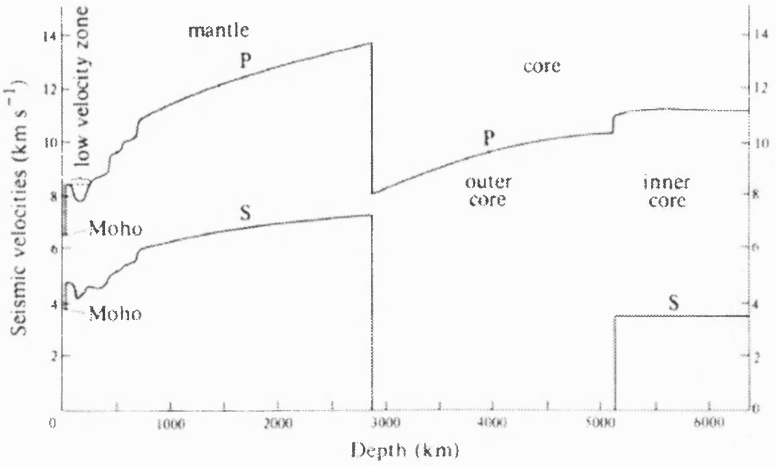

Figure 1.1. Profile of seismic velocity against depth (taken from Hart et al. 1977).

1.2 Structure of the Earth

The evidence from seismic wave and meteorite studies has led to the conclusion that the Earth consists of a series of distinct layers at which the velocities of the seismic waves are altered (figure 1.1 and 1.2).

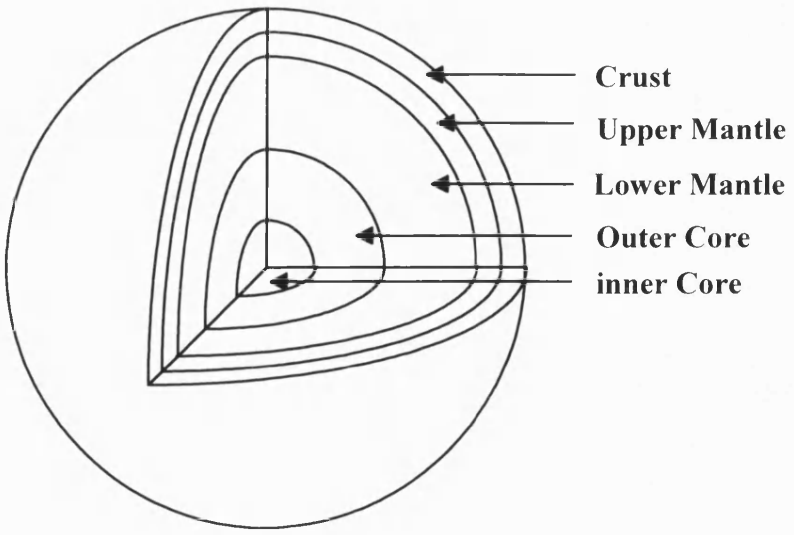

Figure 1.2. Layered structure of the Earth.

1.2.1 The Crust

Of the major divisions of the Earth's interior the crust is the most easily studied. It represents 0.4 percent of the Earth's mass and ranges from between 5 to 15 km in thickness for the oceanic crust, to 30 to 50 km thick for continental crust (Anderson 1989). It primarily consists of silicates with small quanties of calcium, potassium, sodium, aluminium and magnesium most commonly in the form of feldspars and quartz.

1.2.2 The Mantle

The mantle primarily contains magnesium, silicon, iron and oxygen in the form of silicates and oxides. Small amounts of calcium and aluminium are also found. It consists of three major partitions which include the upper mantle (to a depth of about 400 km), the transition zone (between 400 and 670 km) and the lower mantle (below 670 km).

Seismic studies have shown that there is a reduction in sound velocity in the top of the upper mantle which is thought to be caused by partial melting. This region mostly contains olivine, orthopyroxene, clinopyroxene and garnet. The transition zone contains a number of discontinuities which are thought to be caused by phase transformations of minerals due to increasing pressure and temperature. For example, olivine (Mg_2SiO_4) with isolated SiO_4 tetrahedra is thought to transform to β-spinel (which contains corner sharing tetrahedra) at the 400 km discontinuity. Similarly at lower depths β-spinel converts to γ-spinel. This data is derived from high pressure experimental data and estimations of the conditions within the Earth.

In the lower mantle γ-spinel transforms to $MgSiO_3$-perovskite and periclase (MgO). SiO_2 transforms from α-quartz to coesite and then to the denser phase stishovite as the pressure increases. The major components of the lower mantle are therefore MgO, perovskite and high pressure forms of SiO_2 such as stishovite.

1.2.3 The Core

The core consists of the inner and outer core and represents approximately 32 percent of the Earth's mass. Seismic studies have shown that shear waves are unable to propagate through the outer core (figure 1.1) which means that it is a liquid. Based on cosmic abundances (for example Greenwood and Earnshaw (1984)) it is thought that the core consists primarily of iron with some lighter elements such as nickel, sulfur, oxygen and silicon which account for the differences between seismic P-wave velocities in the core and in pure iron.

The inner core is thought to be solid and one theory suggests that it was frozen out of the liquid outer core. The effect of a solid iron core spinning within a liquid outer core leads to the dynamo effect which is thought to generate the Earth's magnetic field.

1.3 Plate Tectonics and Mantle Creep

The theory of plate tectonics was developed in the 1960s to explain the surface of the Earth, volcanic and earthquake activity. It assumes that the Earth can be divided into a small number of large plates (the Lithosphere) which are formed at spreading ridges and move relative to each other before being pushed back down into the mantle at points where two plates meet. The Lithosphere comprises of the crust and the top

layer of the mantle. The driving force for the movement of the plates is convection of the mantle which is thought to occur by either two layer convection, where the upper and lower mantle convect separately, or whole mantle convection, where the upper and lower mantle mix (Mckenzie 1983).

Convection of the mantle occurs by a process known as creep. There are three main types of creep;

(i) Dislocation creep which is also known as power law creep since the rate of creep is proportional to the stress to a power n. This form of creep occurs when there is motion of a dislocation due to the continuous breaking and making of bonds. Two varieties of dislocation creep can occur. The first is known as glide controlled creep and occurs when the movement of the dislocation is blocked due to the large activation energies caused by obstacles which have dimensions on the order of a few interatomic distances. This can be overcome by thermal agitation. The second type is recovery controlled creep which occurs when the obstacles are too large to be overcome thermally (e.g. the obstacles are caused by other dislocations). The obstacles can dissolve away by mutual destruction of dislocations which is thermally controlled.

(ii) Nabarro-Herring creep, also known as diffusion creep, occurs when vacancies self diffuse through the grains which make up the polycrystalline substance. Since this process requires a high concentration of vacancies with large mobility Nabbaro-Herring creep would be expected at very high temperatures. In addition, if the grain size is large then this form of creep is affected by the presence of dislocations. The creep is Newtonian in nature with the rate of creep proportional to the applied stress (Poirier 1985).

(iii) Coble creep occurs where matter is transported along grain boundaries rather than through a material. This form of creep is thought to occur at lower temperatures than required for Nabarro-Herring creep due to lower the activation energy (Poirier 1985). One of the central aims of this thesis will be to examine the effect of grain boundaries on the activation energy of ionic transport.

Experiments have suggested that diffusion is most facile at grain boundaries (Atkinson and Taylor 1981, Wuensch and Tuller 1994). In the following section we will discuss the nature of grain boundaries.

1.4 Grain Boundaries

Grain Boundaries are formed when two crystals of differing orientation intersect and can be divided into two classes, tilt and twist grain boundaries. Tilt grain boundaries are formed when the two misorientated grains are related by a mirror plane at the grain boundary followed by a shift of one grain relative to the other. A special case occurs when there is no shift in which case the grain boundary is termed a mirror boundary. Twist grain boundaries are formed by the rotation of one grain relative to the other about an axis perpendicular to the grain boundary plane. Grain boundaries can be formed as a combination of both tilt and twist but for this work we have restricted ourselves to modelling only pure tilts or twists.

Several models have been proposed to describe grain boundaries and a short description of each of these will follow. The first method is the dislocation model (Burgers 1939, Bragg 1940) which states that grain boundaries with small orientation differences can be described by a series of dislocations lying on the prescribed plane of the grain boundary (see figure 1.3).

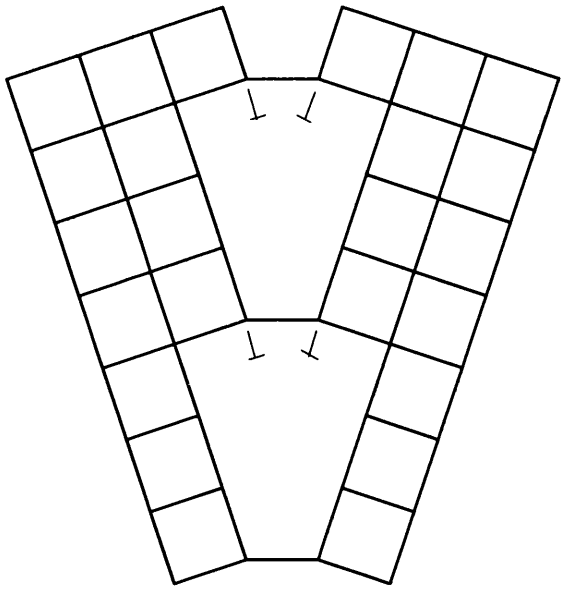

Figure 1.3. Dislocation model of a simple tilt grain boundary

The energy of the boundary with respect to misorientation has been derived by Read and Shockley (1950) and is given by

$$\gamma_b = \gamma_0 \theta(A - \ln \theta) \qquad 1.3$$

where γ_0 is related to the rigidity modulus, G, and the Poisson ratio, σ, as follows

$$\gamma_0 = \frac{Ga(\cos \varphi + \sin \varphi)}{4\pi(1 - \sigma)} \qquad 1.4$$

where a is the lattice spacing and φ is the angle of orientation of the boundary. The quantity A in equation 1.3 depends upon the energy of atoms at the dislocation itself, due to an incomplete nearest neighbour shell and the resulting strain. Neither γ_0 or A is dependent on θ, the angle of misfit.

This method has problems; in high angle boundaries the dislocation cores can overlap and cannot be resolved. Even in low angle boundaries there can be some ambiguity in resolving the dislocation content.

The second model, the structural unit model, describes a grain boundary in terms of small structural units (Pond et al. 1978, Ashby et al. 1978). The boundary is formed from two or more groups of closely packed structural units. Sutton and Vitek (1982) calculated a series of configurations for BCC and FCC metals and found that the favoured boundaries containing only one type of structural unit corresponded to those 'special' boundaries which experimentally were found to have local minima in grain boundary energy. However, again this method has problems since the identification of the structural units is not unique (Sutton and Vitek 1983a, b, Balluffi and Bristowe 1984).

The third model is the coincident site lattice or CSL model (Bollmann 1970) which describes the grain boundary in terms of two interpenetrating crystal of differing orientation. A coincident site occurs when a point in one lattice matches with a point in the second lattice. Since the two lattices are periodic the coincident sites form a periodic arrangement. The inverse of the ratio of coincident sites to lattice sites is termed Σ. Tilt grain boundaries are formed by removing the ions from one lattice on one side of the grain boundary and removing ions from the second lattice on the other side of the grain boundary. An explanation of the application of the CSL model to twist boundaries will be given in chapter 4. The CSL model is however unable to predict structure or energy of grain boundaries since no constant relationship has been found between Σ and these properties (Goodhew 1980).

1.5 Experimental methods

A variety of experimental methods are available for studying the structure and properties of bulk material, surfaces and grain boundaries in minerals. In this section these methods will be discussed.

1.5.1 Experimental Determination of Mantle Mineral Properties

One problem with the study of mantle properties is the high pressures which are required. For pressures up to 100 GPa the Diamond Anvil Cell (DAC) is commonly used in experiment. This apparatus consists of two opposed diamond anvils between which the sample is placed (figure 1.4) in the centre of a metal foil gasket. The sample is subjected to a pressure when a force pushes the anvils together and the very small surface area of the diamond anvils (typically about 0.5 mm^2 (Jayaraman 1983)) multiplies the applied load by a large factor.

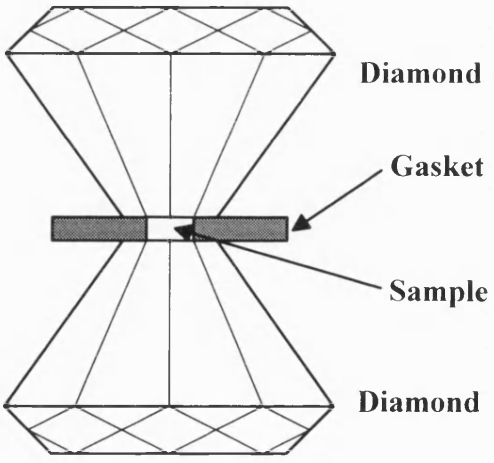

Figure 1.4. Schematic diagram of the DAC.

The pressure is measured by introducing a small piece of ruby into the pressure chamber with the sample. Its fluorescence is excited with a He-Cd laser and the resulting spectra measured. Pressure causes the ruby lines to shift to a higher wavelength and work by Xu et al. (1986) showed that the relationship between pressure and wavelength was almost linear.

High temperatures can be generated by two methods. The first of these, the use of an external heater, has problems since it also heats up the anvils and can cause damage to the apparatus above 500 °C. The second method involves directing a laser through one of the anvils onto the sample. One reason why diamonds are used is that they have a high degree of transparency to a broad range of the electromagnetic spectrum. Temperatures of up to 5000 K at pressures of up to 100 GPa have been achieved (Jeanloz and Heinz 1984). The temperature can be measured using either optical pyrometry or, more recently, a spectroradiometer to record the thermal radiation from the sample (Godwal et al. 1990).

There are limitations to this method. The sample is only about 10-500 μg and can experience a large temperature gradient of up to 1000 K over a few micrometers (Kerr 1991) and pressure gradients of several GPa (Bell et al. 1984). In addition, the temperature can be controlled to only $\pm$100 K at high temperatures and this can effect the accuracy of phase transition experiments (Navrotsky 1987).

For pressures above 100 GPa the Shockwave method can be used. Shockwaves are generated within the sample by placing it either under a plate with an explosive device above or by driving a plate at high velocity onto the sample (figure 1.5). This method is able to generate pressures in the sample of up to 400 GPa using conventional explosives or up to 2000 GPa using a nuclear device (Ahrens 1987). A

big drawback with this method however is that the whole sample does not necessarily experience the same pressure. Also, the assumption must be made that the sample remains 'frozen' in its high pressure state after the release of pressure.

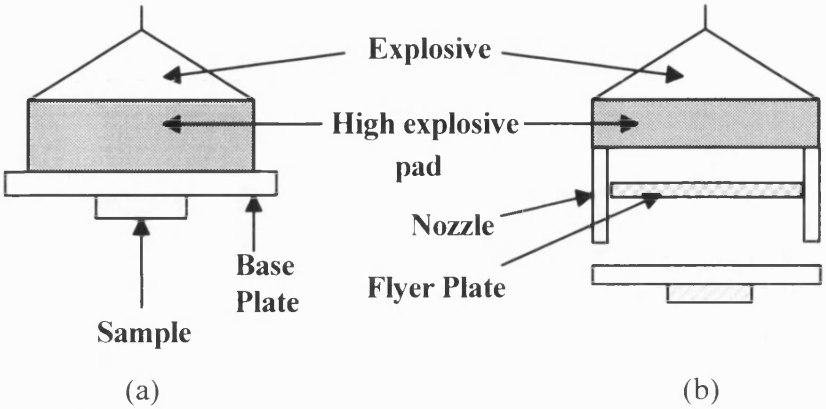

Figure 1.5. Schematic representation of shockwave apparatus using a) an explosive device and b) a high velocity projectile.

These methods can be used in conjunction with several experimental methods to determine various mineral properties. DAC can be used with X-ray diffraction and shocked samples can be used with both x-ray and neutron diffraction to determine properties including lattice parameters (Balmer et al. 1997), compressibility (Catti et al. 1994), thermal expansivity (Pavese et al. 1995) and phase transitions (Vogt and Schmahl 1993). An alternative method of determining phase diagrams is the use of calorimetric studies (Akaogi et al. 1995) which measures heat changes in materials and thus allows the calculation of thermodynamic properties.

Infra-red and Raman experiments can determine the bonding properties of minerals and the presence of water within minerals which may have a major effect on mantle properties (Pawley et al. 1993). Ultrasonic waves (Webb and Jackson 1993) or

Brillouin spectroscopy (Zha et al. 1996) can be employed to determine elastic constants.

1.5.2 Grain Boundary Methods

Although some of the techniques used for surface observations are applicable to the study of grain boundary composition (e.g. XPS and AES (Theunissen et al. 1992)), most experiments are conducted using either x-ray diffraction or direct imaging techniques. X-ray diffraction reflects the symmetry of the structure under investigation and grain boundaries produce extra spots in the diffraction pattern (Hagege et al. 1982). This method has been used to study for example, the location of amorphous phases between ZnO grains (Katkov et al. 1996) where it was found that the amorphous phase preffered to be at multiple grain junctions.

Direct imaging techniques are often used in conjunction with x-ray diffraction to characterise grain boundaries (e.g. Chen et al. 1993). Electron microscopy techniques (SEM, TEM and HRTEM) have been used to study a variety of grain boundaries in materials such as NiO (Merkle and Smith 1987a,b, Merkle 1994) which are discussed further in chapters 4 and 5, TiO_2 (Lee et al. 1993) structurally analogous to stishovite (see chapter 6) and alumina (Höche et al. 1994).

Determination of relative grain boundary energies is possible by measuring the grain boundary tension. Two methods are available to do this; measuring the dihedral angle at the triple points where grain boundaries meet or by thermal grooving experiments. The latter method has been used to study the variation in the ratio of grain boundary energy to surface energy with misorientation angle for a series of [001]

(Dhalenne et al. 1979) and [011] tilt grain boundaries in NiO (Dhalenne et al. 1982). This method is explained in more detail in chapter 8.

1.5.3 Surface Methods

Surface techniques are divided into destructive, where the surface is destroyed as it is probed, and non-destructive. The primary destructive technique is secondary ion mass spectroscopy (SIMS) where the surface is bombarded with an energetic (500-3000 eV) beam of primary ions which remove the uppermost layer of the surface as secondary ions which are then detected. This can be applied to examining, for example, hydroxylation of surfaces (Bourgeois et al. 1992).

There are many types of non-destructive techniques. Low energy electron diffraction (LEED) uses low energy electrons (0-1000 eV) to probe the surface. Since the electrons are of such low energy they only penetrate the top few layers and have a very small effect on surface processes. The intensities of the back-scattered electrons can be measured allowing the generation of a surface diffraction pattern. This method has been applied to studying the geometry of water adsorped onto an MgO surface (Xu and Goodman 1997).

Auger electron spectroscopy (AES) uses higher energy (1000-3000 eV) to bombard the surface and eject core electrons. As the high energy state relaxes by a higher energy electron dropping to the core orbital it releases energy, specific to the parent ion, in the form an electromagnetic wave or a secondary electron allowing identification of the parent species. Resolutions down to a few nm are possible. The technique can be used to characterise the composition thin surface layers, for example Xu et al. (1996) studied thin binary-oxide films such as MgO-NiO.

Another method for studying surface composition is X-ray or ultra-violet photoelectron spectroscopy. This technique also uses high energy radiation to cause electrons to be emitted from either the valence orbitals (UPS) or the core orbitals (XPS). By measuring the difference in energy between the incidence beam and the emitted electron's kinetic energy the binding energy of the electron can be calculated to a precision of 0.1 eV. This method has proved useful in studying the adsorption of water on surfaces of TiO_2 (Wang et al. 1995).

There are several forms of microscopy which are also useful for imaging a surface. Scanning Electron Microscopy (SEM) scans a beam of electrons across the surface and measures the secondary and backscattered electrons. Resolution can be in the order of nm although the technique requires a conducting surface to prevent charge accumulation, and thus a metal coating such as gold is often used. Similarly Transmission Electron Microscopy (TEM) can be used. More recently, Atomic Force Microscopy (AFM) and Scanning Tunnelling Microscopy (STM) have allowed resolution almost to the atomic scale. These methods have been used to study the surface topology of hematite and showed the presence of pits and steps (Johnsson et al. 1991).

Determination of surface energies is difficult but several methods have been used including cleavage (Gilman 1960, Westwood and Hitch 1963, Melcholsky et al. 1976, Rice et al. 1981), fibre elongation (Parikh 1958), multiphase equilibrium (Kingery 1954) and contact angle (Nikolopoulos 1985) however these have given a variety of results. For example, the surface energy of MgO has been calculated to be in the range of 0.15 Jm^{-2} to 10 Jm^{-2} (Gilman 1960, Melcholsky et al. 1976, Rice et al. 1981).

1.6 Simulation of Bulk Properties in Minerals

Early atomistic simulation was concerned with the calculation of lattice energy (e.g. forsterite calculations by Catti 1981). The first major study by Parker (Catlow et al. 1982, Parker 1983a, 1983b) predicted crystal structures in a series of silicates and was able to successfully model the orthorhombic lattice distortion in $CaTiO_3$-perovskite. Simulation of SiO_2 was advanced by Sanders et al. (1984) who introduced a potential for α-quartz which modelled the directional nature of the bonding using a three body bending term between O-Si-O.

These early calculations considered only the static case, i.e. they were effectively at zero Kelvin and without the zero point energy. However, the introduction of the computer code PARAPOCS (Parker and Price 1989) allowed the minimisation of crystal structure with respect to temperature and an applied pressure. They modelled polymorphs of Mg_2SiO_4 and obtained good agreement with experiment for thermodynamic data and phase diagrams.

Work by Dove (1989), Patel (1991), Winkler et al. (1991) and Jackson and Price (1992) demonstrated the transferability of potential models by modelling a series of systems with good agreement with experiment. For example, Dove (1989) used the potentials of THB1 (tested on forsterite) (Parker and Price 1987a, b) to model enstatite. Patel (1991) used a potential based on the Sanders potential (Sanders et al. 1984) to model oxygen isotope equilibrium in albite, diopside, fosterite, pyrope, α-quartz and wollastanite. Jackson and Price (1992) derived a potential for calcite which was then transferred to aragonite.

More recently work by Wall et al. (1993) extended the study of high pressure phases by testing the empirical equations of state used to extrapolate the elastic

properties of minerals at mantle pressures and temperatures (Weidner 1986, Duffy and Anderson 1989).

Molecular Dynamics has also been used either alone or in conjunction with lattice dynamics to study mineral properties at pressure. Swainson and Dove (1995) used Molecular Dynamics to model the ordering in alpha- and beta-cristobalite. They found that the beta-phase to be much more disordered than the alpha-phase, in agreement with experiment. (Mg,Fe)SiO3-perovskite and analogous materials have been modelled for a variety of reasons including the study of proposed fast ion conduction in the mantle (Kapusta and Guillope 1988, Wall and Price 1989, Watson et al. 1992, Watson et al. 1995), thermodynamic properties in the mantle (Winkler and Dove 1992, Kapusta and Guillope 1993, Patel et al. 1996) and phase transitions (Matsui and Price 1992, Belonoshko and Dubrovinski 1996). Molecular Dynamics has also been applied to study the melting of other mantle minerals including stishovite (Belonoshko and Dubrovinski 1995), periclase (MgO) (Ferneyhough et al. 1994, Vocadlo and Price 1996) and perovskite (Kubicki and Lasaga 1992).

Thus atomistic simulation has been applied to studying a range of bulk properties in minerals generally with good agreement with experiment. However, rocks are polycrystalline with grain boundaries forming between individual grains. The next section briefly reviews the use of atomistic simulation to model grain boundaries.

1.7 Simulation of Grain Boundaries

Atomistic simulation of grain boundaries is used as a useful tool for the interpretation of HRTEM data. This technique has been used successfully for electron

microscopy readings on TiO_2-rutile (Lee et al. 1993, Dahman et al. 1994) and Al_2O_3 (Höche et al. 1994, Chen et al. 1995).

The grain boundary structure of simple symmetric tilt grain boundaries of NiO were first simulated by Duffy and Tasker (1983a, 1983b) as part of a study into nickel corrosion. They found that the ceramic boundaries contained open channel structures unlike the equivalent metallic boundaries. However, there were differences between the calculated structure and those observed in HRTEM studies (Merkle and Smith 1987a).

Harding et al. (1989) showed that there were alternative stable structures at zero Kelvin. However, these were less stable than the Duffy and Tasker structure and emphasised that grain boundaries are not thermal defects. In addition, they included temperature into the calculation via harmonic lattice dynamics to see if this affected the relative stability of the boundaries. They found no significant alteration to the structures beyond thermal expansion. Counterman et al. (1988) used Molecular Dynamics to study twist boundaries in NaCl with temperature. They also found that the boundary was completely stable up to the melting point.

Other grain boundaries in single ceramic materials have been studied using atomistic simulation including hematite, Fe_2O_3, (Davis 1992) and Al_2O_3 (Kenway 1994, Mackrodt 1986). Tasker and Stoneham (1987) extended grain boundary calculations by modelling interfaces between NiO and BaO. This work was further extended by Sayle et al (1993, 1994) who considered more complicated heteroepitaxial boundaries including CeO_2 on Al_2O_3 and $YBa_2Cu_3O_{6.5}$ on MgO.

More recently, work has considered metal-metal oxide interfaces (Tasker 1990) including Ag/MgO (Duffy et al. 1992, Purton et al. 1997), Au/MgO (Duffy et

al. 1993) and Ag/NiO (Duffy et al. 1995). Development of these techniques may be of importance when considering simulations of the mantle/core interface.

Grain boundaries are good sources of defects and atomistic calculations have been carried out on a series of grain boundaries to examine their effect upon structure and properties. Duffy and Tasker (1984) calculated the space charge effect of cation vacancies in NiO to measure the enhancement of the defects upon diffusion. More recently, Sayle et al. (1995) included defects into twist boundary calculations and found them to be essential for boundary stability. The diffusion of defects in cubic materials has been studied using Molecular Dynamics (Meyer et al. 1996).

Computer simulation can also be applied to modelling grain growth. Extensive work has been carried out on grain growth in both two dimensions (e.g. Anderson et al. 1983, 1984) and three dimensions (Mulheran and Harding 1991).

1.8 Aims of the Thesis

The aims of this thesis can be divided into four key areas. Firstly, to model, without the inclusion of temperature, a series of grain boundaries in mantle forming minerals, namely MgO, SiO_2 stishovite and $MgSiO_3$ perovskite. This will examine ways of generating the boundaries and obtaining their energy minima. A selection of MgO and stishovite free surfaces will also be modelled in order to calculate the stability of the grain boundaries with respect to dissociation into two free surfaces. Secondly, we will model the grain boundaries at high pressure and temperature. This will allow us to calculate the effect of mantle conditions in order to determine if this causes any structural transitions or changes in the relative stability of the boundaries. Diffusion is an important process within the Earth because creep (Poirier 1985) is

believed to be the mechanism by which convection within the mantle can occur (Anderson 1989) and as experiments have suggested that grain boundaries are regions of high diffusivity (Atkinson and Taylor 1981) clearly boundary diffusion will contribute to the creep process. Thus the third area of study will be to model vacancy migration in the bulk and at the grain boundaries of MgO and stishovite to calculate the relative diffusivities and to calculate the effect of pressure on diffusion. Finally, we will consider simple the models of grain growth. Previous simulations have considered growth using a model that does not use realistic boundary energies. We will attempt to build upon this work by considering real surface and grain boundary energies in order to generate a 'realistic' model of grain growth.

However, before considering the results the following two chapters will describe the potential models and theoretical techniques that are an important part of this work.

2 Potential Models

2.1 Introduction

Simulation of ionic solids requires the calculation of the interaction energies and the forces acting between the ions. Ideally *ab initio* methods would be used to model these energies and forces. However, for simulation cells which contain greater than 50 or so atoms/ions this becomes too computationally expensive and so a classical atomistic approach is adopted. Central to the accuracy of atomistic calculations is the reliability of the potential models which describe the forces acting between ions within the crystal in terms of long and short range interactions.

Several different potential forms have been used in this work; descriptions of the potential parameters will be given in the relevant chapters. In this chapter a general description of atomistic simulation methods will be given including the derivation and transferability of the potentials which becomes important when modelling properties of materials for which potentials are not available; for example, phases not fitted to or extreme conditions where the bond lengths have changed.

2.2 The Born Model of Ionic Solids

Our atomistic calculations are based on the Born model of ionic solids, in which a potential model is used to represent the ions. Although the use of the Born model is a trade off between accuracy and time compared to *ab initio* techniques, previous studies of minerals using the Born model of solids (Catlow et al. 1982, Parker 1983a, Price and Parker 1984, Sanders et al. 1984, Price and Parker 1987a, Parker and Price 1989, Wall et al. 1993) have proven very successful at predicting

both structure and energy and therefore this model will be used in this work. The lattice energy, defined as the energy released when ions at infinite separation are brought to their respective lattice sites, arises from the electrostatic and short range interactions between the charged ions and is given by

$$U = \sum_{ij} \frac{q_i q_j}{4\pi\varepsilon_0 r_{ij}} + \sum_{ij} \phi_{ij}(r_{ij}) + \sum_{ijk} \phi_{ijk}(\theta - \theta_0) + ... \qquad 2.1$$

where $k \neq j \neq i$, q_i and q_j are the charges of ions i and j respectively, ε_0 is the permittivity of a vacuum, ϕ_{ij} is a potential function and r_{ij} is the ion separation.

The first term in equation 2.1 represents the long range Coulombic interactions, the second term represents the short range interactions and the third term the three-body interactions. Further terms can be added to model four or other many body interactions.

2.3 The Coulomb Interaction

The most important term of equation 2.1 is the Coulomb term which contributes the majority of the lattice energy. The Coulomb energy is calculated by summing the interactions of pairs of neighbouring charged ions within a given radius, i.e.

$$U_c = \sum_{ij} \frac{q_i q_j}{4\pi\varepsilon_0 r_{ij}} \qquad 2.2$$

where q_i and q_j are the charges of ions i and j respectively, ε_0 is the permittivity of a vacuum and r_{ij} is the inter ion separation.

One difficulty with the Coulomb term (which is proportional to 1/r) is that the convergence of the energy with r is poor. Various mathematical techniques have been adopted to overcome the poor convergence, amongst these for simulations where the unit cell is repeated in three dimensions the method of Ewald (1921) is often used whilst for the two dimensional case which allows the modelling of planar defects such as surfaces, an adaptation of Ewald's method by Parry (1975, 1976) is used. The two methods will be discussed in more detail in the following sections.

2.3.1 The Ewald Method

There are two ways of describing this method. The first is that of Kittel (1963) which describes the manipulation of the point charges by addition and subtraction of Gaussian functions. The second method, which is described below, involves using a mathematical expression for 1/r and more closely follows the coding of the methods used within this work.

The first stage is to use the identity

$$\frac{1}{r} = \frac{2}{\pi^{\frac{1}{2}}} \int_0^\infty \exp(-r^2t^2)dt \qquad 2.3$$

This integral can be split at an arbitrary point η. The choice of this point does not affect the final result but will affect the rate at which the two terms will converge .

The split integral is

$$\frac{1}{r} = \frac{2}{\pi^{\frac{1}{2}}}\left[\int_0^\eta \exp(-r^2t^2)dt + \int_\eta^\infty \exp(-r^2t^2)dt\right] \qquad 2.4$$

Treating the two terms separately as T_1 and T_2, Fourier transformation of the first term into reciprocal space gives

$$T_1 = \frac{2}{\pi^{\frac{1}{2}}} \int_0^{\eta} \frac{1}{8t^3\pi^{\frac{3}{2}}} \left[\int_{-\infty}^{\infty} \exp\left(\frac{-G^2}{4t^2}\right) \cdot \exp(-i\underline{G}\underline{r}) d\underline{G} \right] dt \qquad 2.5$$

where $\underline{G}$ is a reciprocal vector.

By making the substitution

$$s = \frac{-G^2}{4t^2}$$

$$\text{then } ds = \frac{G^2}{2t^3} dt \qquad 2.6$$

Let

$$\frac{dt}{8t^3\pi^{\frac{3}{2}}} = \frac{dt}{4\pi^{\frac{3}{2}}G^2} \cdot \frac{G^2}{2t^3} = \frac{1}{4\pi^{\frac{3}{2}}G^2} ds \qquad 2.7$$

and the limits of the integral of ds can be obtained from

$$\text{as} \quad t \to 0 \quad s \to -\infty$$

$$\text{and as } t \to \eta \quad s = \frac{-G^2}{4\eta^2}$$

Substituting this into equation 2.5 gives

$$T_1 = \frac{2}{\pi^{\frac{1}{2}}} \int_{-\infty}^{\frac{-G^2}{4\eta^2}} \left[\int_{-\infty}^{\infty} \left(\frac{1}{4\pi^{\frac{3}{2}}G^2} \right) \cdot \exp(s) \cdot \exp(-i\underline{G}\underline{r}) d\underline{G} \right] ds \qquad 2.8$$

$$T_1 = \frac{2}{\pi^{\frac{1}{2}}}\left[\int_{-\infty}^{\infty}\left(\frac{1}{4\pi^{\frac{3}{2}}G^2}\right)\cdot\exp(s)\cdot\exp(-i\underline{G}\underline{r})d\underline{G}\right]_{-\infty}^{\frac{-G^2}{4\eta^2}} \qquad 2.9$$

$$T_1 = \frac{1}{2\pi^2}\int_{-\infty}^{\infty}\left(\frac{1}{G^2}\right)\cdot\exp\left(\frac{-G^2}{4\eta^2}\right)\cdot\exp(-i\underline{G}\underline{r})d\underline{G} \qquad 2.10$$

With the addition of the volume per reciprocal vector $(2\pi)^3/V$, where V is the volume of the periodic cell, this integral becomes equivalent to a summation over reciprocal vectors and the first term becomes

$$T_1 = \frac{4\pi}{V}\sum_{G}\left(\frac{1}{G^2}\right)\cdot\exp\left(\frac{-G^2}{4\eta^2}\right)\cdot\exp(-i\underline{G}\underline{r}) \qquad 2.11$$

If this term is summed over all the sites within the periodic cell we can define the reciprocal lattice vector $\underline{G}$ in terms of unit cell reciprocal lattice vectors, k, as shown in equation 2.12

$$\underline{G} = 2\pi(n_1k_1 + n_2k_2 + n_3k_3) \qquad 2.12$$

where n_1, n_2 and n_3 are integers and k_1, k_2 and k_3 satisfy the condition

$$k_i \cdot a_j = \delta_{ij} \qquad 2.13$$

where a_j is the real space vectors and δ_{ij}=1 if i=j and 0 otherwise, i.e. k_1, k_2 and k_3 are the unit cell's reciprocal lattice vectors.

Thus we can define a reciprocal lattice vector $\underline{K}$ composed of the unit cell reciprocal lattice vectors, i.e.

$$\underline{K} = \underline{n}(k_1 + k_2 + k_3) \qquad 2.14$$

where $\underline{n}$ is the number of periodic repeat units in the three directions. Thus

$$\underline{G} = 2\pi\underline{K}\underline{n} \qquad 2.15$$

and the first term becomes

$$T_1 = \frac{4\pi}{V}\sum_{\underline{n}}\left(\frac{1}{4\pi^2K^2n^2}\right)\cdot\exp\left(\frac{-\pi^2K^2n^2}{\eta^2}\right)\cdot\exp(-2i\pi\underline{n}\underline{K}\underline{r}) \qquad 2.16$$

$$T_1 = \frac{1}{\pi V}\sum_{\underline{n}}\left(\frac{1}{K^2n^2}\right)\cdot\exp\left(\frac{-\pi^2K^2n^2}{\eta^2}\right)\cdot\exp(-2i\pi\underline{n}\underline{K}\underline{r}) \qquad 2.17$$

In the case of a charge neutral cell the $\underline{n}$=0 term is zero and thus can be ignored. This is not true for charged cells (Allan et al. 1987, Watson et al. 1997) where a charge correction must be applied.

The second term from equation 2.4, T_2, can be solved in real space using the error function

$$\mathrm{erf}(x) = \frac{2}{\pi^{\frac{1}{2}}}\int_x^\infty \exp(-s^2)ds \qquad 2.18$$

to give

$$T_2 = \frac{1}{r}\cdot\mathrm{erfc}(\eta r) \qquad 2.19$$

If we include the charges the whole summation in real and reciprocal space becomes

$$\frac{1}{2\pi V}\sum_{\underline{n}}\left[\left(\frac{1}{K^2n^2}\right)\cdot\exp\left(\frac{-\pi^2K^2n^2}{\eta^2}\right)\cdot\sum_{ij}{}' q_iq_j\cdot\exp(-2i\pi\underline{n}\underline{K}\underline{r})\right]$$

$$+\frac{1}{2}\sum_{ij}{}'\frac{q_iq_j}{r_{ij}}\mathrm{erfc}(\eta r) \qquad 2.20$$

There is no self interaction term included in the real space contribution but this does occur in the reciprocal space part of the sum. It is easily calculated and can be removed using

$$\sum_i \frac{-q_i^2\eta}{\pi^{\frac{1}{2}}} \qquad 2.21$$

Further simplification is possible if required. The vector $\underline{r}_{ij}$ is the distance between lattice site pairs. By dividing by the reciprocal lattice vector matrix this can be transformed into crystallographic co-ordinate space

$$\underline{R}_{ij} = \frac{\underline{r}_{ij}}{\underline{\underline{K}}} \qquad 2.22$$

Thus the second part of T_1 becomes

$$\sum_{ij} q_iq_j\cdot\exp\left(-2i\pi\underline{n}\underline{R}_{ij}\right) \qquad 2.23$$

which is effectively the difference between two crystallographic positions and thus the term can be split

$$\Sigma_i\, q_i \cdot \exp\left(2i\pi \underline{n}\underline{X}_i\right)\ \Sigma_j\, q_j \cdot \exp\left(-2i\pi \underline{n}\underline{X}_j\right) \qquad 2.24$$

The sum is performed from n to -n and thus the two terms become equivalent giving

$$\left[\Sigma_i\, q_i \cdot \exp\left(-2i\pi \underline{n}\underline{X}_i\right)\right]^2 \qquad 2.25$$

Including this and the real space self interaction gives the full charge summation component of the lattice energy, U_l

$$U_l = \frac{q_1 q_2}{2\pi V} \Sigma_{\underline{n}} \left\{ \left(\frac{1}{K^2 n^2}\right) \cdot \exp\left(\frac{-\pi^2 K^2 n^2}{\eta^2}\right) \cdot \left[\Sigma_i\, q_i \cdot \exp\left(-2i\pi \underline{n}\underline{X}_i\right)\right]^2 \right\}$$

$$+\frac{1}{2} \Sigma'_{ij} \frac{q_i q_j}{r_{ij}} \mathrm{erfc}(\eta r) + \Sigma_i \frac{-q_i^2 \eta}{\pi^{\frac{1}{2}}} \qquad 2.26$$

The 3N force vector and the 3Nx3N co-ordinate matrix are obtained by differentiation of equation 2.26 to give the first and second derivatives respectively.

2.3.2 The Parry Summation

The Parry method (1975, 1976) is used for summing the Coulomb term when two dimensional periodicity is used, for example, in the simulation of planar defects such as grain boundaries and surfaces. The method treats the system as a series of

charged planes of ions which are assumed to repeat in two dimensions rather than in three dimensions. The Coulomb contribution to the lattice energy is therefore given by

$$U = \frac{1}{2}\sum_{ij} q_i q_j \left[\sum_{\underline{L}} \frac{1}{\left|\underline{r}_{ij} + \underline{L}\right|} \right] \qquad 2.27$$

where $\underline{L}$ is the two dimensional lattice vectors and $\underline{r}_{ij}$ is the inter ion separation.

Using the identity for 1/r given in equation 2.3 for the Ewald summation we generate two terms which are then summed in real and reciprocal space. In the Ewald method the reciprocal space term is summed for all cases where $\underline{n}$ is not equal to zero. In a two dimensional system rumpling of the charged planes at the surface or grain boundary leads to charge separation and so the $\underline{n}$ equals zero term is required. In addition, the distance $\underline{r}_{ij}$ is split into two components for convenience, $\underline{u}_{ij}$ perpendicular to the plane of lattice vectors and $\underline{p}_{ij}$ in the plane of lattice vectors. This gives for T_1, the reciprocal space term

$$T_1 = \frac{\pi}{A}\left[-2\underline{u}_{ij} \cdot \operatorname{erf}\left(\eta^2 \underline{u}_{ij}\right) - \frac{2\exp\left(-\eta^2 \underline{u}_{ij}^2\right)}{\pi^{\frac{1}{2}}\eta} \right]$$

$$+\frac{\pi}{A}\sum_{\underline{K}\neq 0}\left[\frac{\exp\left(\underline{K}\underline{i}\underline{p}_{ij}\right)}{\underline{K}} \left\{ \begin{array}{l} \exp\left(\underline{K}\underline{u}_{ij}\right) \cdot \operatorname{erfc}\left(\frac{\underline{K}}{2\eta} + \eta \underline{u}_{ij}\right) \\ +\operatorname{erf}\left(-\underline{K}\underline{u}_{ij}\right) \cdot \operatorname{erfc}\left(\frac{\underline{K}}{2\eta} + \eta \underline{u}_{ij}\right) \end{array} \right\} \right] \qquad 2.30$$

where $\underline{K}$ is the two dimensional reciprocal lattice vector and A is the area.

The real space component, T_2, is calculated in a similar manner giving

$$T_2 = \sum_{\underline{L}} \left[\frac{\operatorname{erfc}\left(\eta \left| \underline{r}_{ij} + \underline{L} \right| \right)}{\left| \underline{r}_{ij} + \underline{L} \right|} \right] \qquad 2.31$$

The first and second derivatives of energy with respect to co-ordinates which are needed for energy minimisation are found by differentiation and are given by Harding (1988).

2.4 Short Range Interactions

The second term of the Born model of ionic solids considers the contributions to the lattice energy from the short range interactions. These interactions include both attractive terms which can be attributed to Van der Waals forces and repulsive terms which can be attributed to electron cloud overlap. Several mathematical formulae or potentials types can be used to model these interactions as a function of distance and the choice of these may depend upon the system being modelled. The simplest of these is the harmonic function for covalent molecules which has the form;

$$\phi(r) = \frac{1}{2} K (r - r_o)^2 \qquad 2.32$$

where r_o is the equilibrium bond distance and K is the bond force constant. This potential is used for systems with bonding interactions where the atoms share electrons and is suitable as long as the separation, r, is close to the equilibrium bond distance.

The most common potential used for modelling ionic (or semi ionic) solids and indeed for this work is the Buckingham potential function for non-bonded

interactions. Generally ions do not share electrons in non-bonded interactions and thus the potential represents the interaction of the electron charge clouds. To fully model the interaction the ion charges are also required. The Buckingham potential has the form

$$V(r) = A\exp\left(\frac{-r}{\rho}\right) - \frac{C}{r^6} \qquad 2.33$$

where A, ρ, and C are parameters. The attractive part of the potential is proportional to r^{-6} whilst the repulsive part is defined by an exponential term. The potential model parameters are obtained by fitting to either experimental data or to *ab initio* energy surfaces (see section 2.7) and thus the individual parameters may have no real meaning.

2.5 Three Body interactions

The third term in the Born model of solids represents three body interactions. Studies have shown (Sanders et al. 1984, Price and Parker 1987a, b) that in some cases simple two body potentials are unable to accurately model crystal structures and properties. The use of three body terms allows the inclusion of some directionality to the bonding and they have been used with success in modelling systems such as quartz (Sanders et al. 1984) where they have been applied to the O-Si-O bond to model the tetrahedral angle.

The most common form of the three body term is

$$V(\theta) = \frac{1}{2}K_{ijk}(\theta - \theta_o)^2 \qquad 2.34$$

where K_{ijk} is the bond bending force constant, θ_o is the equilibrium bond angle and θ is the angle centred around ion i as shown in figure 2.1.

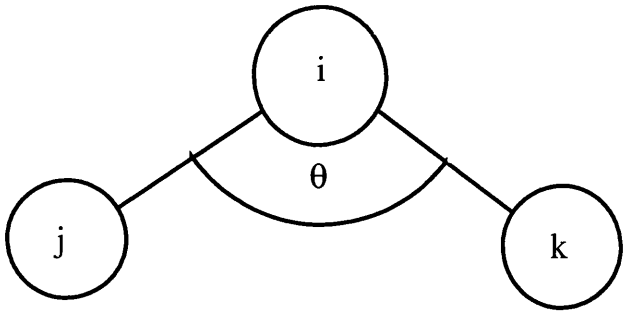

Figure 2.1 Schematic representation of a three body interaction

The Born model can be extended by adding further terms in order to represent interactions between greater numbers of ions. For example, four body terms model torsional interactions between two planes of atoms (for example in benzene).

2.6 Electronic Polarisability

Polarisation is defined as the distortion of the electron cloud surrounding an ion when it is placed into an asymmetrical electric field and so the polarisability of an ion is a measure of its susceptibility to this effect. The simplest model is the rigid ion model which treats the ions as point charges and thus it ignores electronic polarisability completely. As a result it poorly models low frequency optic vibrational modes since these are strongly coupled to polarisability. The high frequency dielectric constant has a value of unity in the rigid ion model because the vibrations concerned

do not affect the rigid cores. In addition, if a charged defect is introduced into a crystal the surrounding ions will polarise in order to stabilise the charge. The rigid ion model is unable to correctly model this effect (Catlow and Mackrodt 1982).

There are several methods to model polarisability. The simplest of these is the *point polarisable ion model* (PPI) which is described below.

2.6.1 Point Polarisable Ion Model

By setting the polarisability of an ion, α, the dipole moment, μ, dependent upon the electric field, E, can be calculated using the relationship

$$\mu = \alpha E \qquad 2.35$$

where α is the polarisability. From this the energy of interacting dipoles can be calculated.

Although this model is generally accepted for simulating simple molecular systems it does fail when describing ionic solids. The reason for this is due to the omission of coupling between short range repulsions and polarisation which is strong in ionic crystal systems. Omitting these interactions results in a poor description of dielectric and defect properties and thus underestimation of defect energies.

To overcome these problems methods can be used which treat the electron charge cloud as a separate species. The most commonly used of these methods is the *shell model* which is described in the next section.

2.6.2 The Shell Model

The shell model of Dick and Overhauser (1958) is a simple mechanical description of the ion. As shown in figure 2.2 the ion is split into a massless shell of charge Y and a core of charge X which contains all of the mass of the ion. The total charge on the ion is the sum of X and Y.

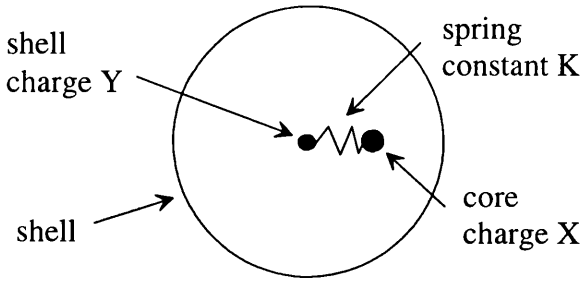

Figure 2.2 Schematic representation of the shell model

The core and shell are coupled by a harmonic spring with a spring constant, k, and this gives rise to an interaction energy between the core and shell of an ion, i, of

$$\phi_i(r_i) = \frac{1}{2}k_i r_i^2 \qquad 2.36$$

where the polarisability, α, of a free ion is given by

$$\alpha_i = \frac{Y^2}{4\pi\varepsilon_0 k_i} \qquad 2.37$$

The associated short range potentials are made to act between the shells which effectively couples the polarisability to the short range potential and thus overcomes the problems of the PPI model.

There are problems associated with the shell model, the first being the increased number of species generated which leads to longer computing times for simulations. This is especially true for molecular dynamics simulations where the periodic cells need to be large enough to reduce the effect of boundary conditions on the ion motion. If the cell is too small an ion would interact with its image in a neighbouring cell and this would impose unwanted symmetry constraints upon the cell. Thus a large number of species is required which is increased further by the application of the shell model. In these situations the rigid ion model is used by necessity. A second problem is in the potential derivation which is discussed in the following sections. Despite its shortcomings the shell model is effective at modelling properties including defect energies, dielectric properties and phonon dispersion curves (Cochran 1973).

2.7 Derivation of Potential Parameters

There are several methods by which the potential parameters can be derived and these can be grouped into two main categories, empirical methods and non-empirical methods. The following sections will describe these methods.

2.7.1 Empirical Methods

Empirical derivation of potentials involves using experimental data to fit the parameters, the most common method uses a least squares fitting routine. An initial trial set of parameters is given and from these the properties are calculated. The model is compared to experimental data including dielectric properties, elastic constants, cohesive energy and phonon frequencies and then the parameters are iteratively

adjusted until the best agreement with experimental data is obtained. A second method of fitting is relaxed fitting where the structure is relaxed to its energy minimum for the trial potential and the parameters are adjusted by comparing the difference between the calculated and experimental structures.

Included in the empirical derivation is the determination of the charges for the Coulomb term given in equation 2.2. The charges derived are termed 'effective charges' since the charge is not intended to reflect the real charge density. Two methods are available, the first of these involves empirically fitting the charges with the rest of the potential to best represent the forces acting between the ions. The second involves assigning valence charges to the ions. The rest of the potential is then fitted empirically to give the correct force between ions with these charges. The choice of method is dependent upon the properties being considered. For example, problems may arise in the case of defects where charge neutrality may not be retained unless valence charges are used, i.e. if non-valent charges are used in an MgO potential or a CaO potential problems may occur in the case of Ca substitution in MgO or vice versa. Empirical fitting is often needed to derive the shell model parameters since non-empirical derivation of these parameters is very difficult.

There are problems with empirical derivation. Firstly the method relies entirely upon the experimental data which in some situations will not be available. Secondly, in the case of high symmetry structures empirical derivation can be very difficult since the number of observable parameters is too small to derive unambiguously all of the short range and shell model terms. Thirdly, the method is only able to fit the parameters for equilibrium spacing of ions in the model compound. One partial solution is to fit the potential to a series of structures at different pressures and

temperatures or to multiple phases. However, problems may still arise when modelling defects where the ions are not close to their equilibrium positions.

To reduce the number of variables the cation-cation interactions are often neglected for oxide systems. This is reasonable since non-empirical methods have shown that in most cases the cation-cation interactions are small.

2.7.2 Non-empirical Derivation

The second class of interatomic potential derivation is non-empirical which involves calculation of the potential parameters from first principles. This allows the calculation of the charge density required for the Coulomb term using *ab initio* methods in an attempt to model the real charge distribution in the crystal. Calculation of the interaction energy between two ions as a function of separation can be achieved by techniques including the Hartree-Fock molecular orbital method used by Catlow and Heyes (1972) and the electron gas method of Gordon and Kim (1972). The most commonly used is the electron gas method which treats the electron density of the ions as a degenerate Fermi gas in which the total energy of the interacting ions is given by

$$E_{total} = E_{elec} + E_{exch} + E_{ke} + E_{corr} \qquad 2.38$$

where E_{elec} is the electrostatic coulomb energy, E_{exch} is the exchange energy, E_{ke} is the zero point kinetic energy and E_{corr} is the energy due to correlations between the electronic motions. These components are expressed in terms of electron densities which are usually calculated by using Hartree-Fock wave functions.

Another class of non-empirical methods are *ab initio* Hartree-Fock or DFT calculations. These can be performed on small clusters or periodic cells (Gale et al.

1992). The clusters are chosen such that they are representative of the bulk system. Thus for example, van Beest et al. (1990) derived a force field for silicas by performing cluster calculations on H_4SiO_4, the smallest cluster containing the SiO_4 building unit of silicas. The geometry of the cluster was distorted for two modes, the first a Si-O symmetrical stretch and the second where the oxygen atoms bent towards each other pairwise. These modes were chosen so as to allow the fitting of the Si-O and the O-O interactions. At regular intevals for these distortions self-consistent field calculations were performed and a potential energy surface was built up to which the potentials were then fitted.

2.7.3 Comparison of empirical and non-empirical techniques

Non-empirical techniques have advantages over empirical techniques. They are able to describe very accurately the nearest neighbour interactions across a range of inter ion separations which allows simulations of structures where the ions have moved away from their equilibrium positions, for example systems with defects. The second advantage is that non-empirical techniques can derive potentials in systems for which there is no experimental data. This is especially useful for simulations of mineral systems at high pressures and temperatures which are difficult to achieve in experiment. However empirical techniques also have some advantages also. Firstly, some parameters such as those used for the shell model or many body terms are very difficult or computationally expensive to derive non-empirically and empirically fitting offers an easier alternative. In addition, often non-empirical techniques do not quite model bulk properties correctly since although they are good at modelling nearest neighbour interactions they are often unable to correctly predict long range

Van der Waals dispersion. This was the case with the van Beest potential mentioned previously. It is therefore common to complement the non-empirical calculations with additional empirical fitting to experimental data in order to modify and improve the potential. Potentials derived in this manner are termed semi-empirical.

2.8 Potential Transferability

The potentials used in this work have been derived empirically from bulk properties. Their application to surfaces and grain boundaries assumes that the charge and polarisability of the surface ions is essentially that of bulk. However the ionic environment in the vicinity of surfaces and grain boundaries may be quite different and thus the use of these potentials must be justified.

In the case of surfaces, advances in quantum calculations have allowed this assumption to be tested. Recent work (Mackrodt 1992, Manassidis and Gillan 1994) has compared quantum calculations from first principles with classical potential model calculations on the properties of surfaces of alumina and found good agreement between the two methods. They showed that for the unrelaxed surface, the charge state and potential field was quite different from bulk but relaxation returned the charges to bulk-like values.

Work on the surfaces of MgO (Colburn 1992) has shown that the use of bulk potentials gives good agreement of surface structure with experiment. Quantum calculations (Causa et al. 1986a, b) have shown that the ionicity at the surface is very similar to the bulk affirming the validity of using bulk potentials to model surfaces.

Calculations to compare anion polarisability at surfaces and in the bulk has been performed in LiF and MgO by Fowler and Tole (1988). They used *ab initio*

self-consistent field calculations to determine the charge distribution for O^{2-} and F^{-} for a series of co-ordination numbers and found that there was little difference in effective anion size and shape for various surface sites and from those in the bulk.

Since it has been shown that the potentials are readily transferable to the calculation of surfaces it is reasonable to suggest that they are also transferable to the calculation of grain boundaries as the co-ordination and potential energy fields are closer to the bulk structure. Potentials derived from bulk have been used to successfully model grain boundaries in both metals (Dahmen et al. 1990) and ceramics (Duffy 1986, Lee et al. 1993).

3 Theoretical Methods

3.1 Introduction

In the previous chapter the form and derivation of the potential models used to calculate interatomic forces was discussed. In this chapter we will discuss the theoretical methods which use these potentials in order to calculate the structure and properties of ionic and partially ionic solids.

The first method to be considered will be that of lattice energy minimisation via constant volume and constant pressure techniques. Next, three methods by which temperature can be included in the simulation will be discussed. The first of these, free energy minimisation, is an extension of the lattice energy minimisation technique which considers the entropy due to thermal vibrations. The second technique, Molecular Dynamics, solves Newton's laws of motion directly in order to calculate ion motion. The last technique to be considered is Monte Carlo simulation in which structural properties are determined using a probability method.

Finally methods for the generation and calculation of two-dimensional planar defects such as surfaces and grain boundaries and their properties will be described.

3.2 Lattice Energy Minimisation

In order to calculate the equilibrium properties for a solid we must first ensure that the ions are at their equilibrium, or minimum energy positions. Lattice energy minimisation accomplishes this by neglecting thermal effects and the zero point energy. The minimisation can be performed efficiently using either matrix methods or a conjugate gradients technique. The matrix methods consist of constant volume and

constant pressure methods. The following sections will describe each of these three methods in turn.

3.2.1 Constant Volume Minimisation

During constant volume energy minimisation the lattice energy, U_L, of the cell is minimised with respect to the ionic co-ordinates only. Several methods are available, in this work the Newton-Raphson method described by Norgett and Fletcher (1970) was used. No account is taken of bulk lattice strains and thus the volume remains constant. The technique is not generally used alone to model pure crystals but is included as a stage in constant pressure minimisation and is used extensively to study systems with point defects (Catlow 1989), surfaces (Tasker et al. 1985) and grain boundaries (Duffy and Tasker 1983a,b, Davies 1992).

The lattice energy is minimised as follows. Initially the lattice energy, U, is expanded about the co-ordinates, $\underline{r}$, to second order using a Taylor expansion (Born and Huang 1954)

$$U(\underline{r}') = U(\underline{r}) + \underline{g}^T \cdot \underline{\delta} + \frac{1}{2}\left(\underline{\delta}^T \cdot \underline{\underline{W}} \cdot \underline{\delta}\right) \qquad 3.1$$

where $\underline{\delta}$ is the displacement of an ion (i.e. the basis strain) which is given by

$$\underline{\delta r} = \underline{r}' - \underline{r} \qquad 3.2$$

$\underline{g}$, the force acting upon a given ion, is the first derivative of the energy with respect to co-ordinates

$$\underline{g} = \frac{\partial U}{\partial \underline{r}} \qquad 3.3$$

and $\underline{\underline{W}}$ is the second derivative matrix

$$\underline{\underline{W}}_{ij} = \frac{\partial^2 U}{\partial r_i \partial r_j} \qquad 3.4$$

If equilibrium conditions are assumed (i.e. there is no change in energy with respect to strain) the derivation of equation 3.1 becomes

$$\frac{\partial U}{\partial \underline{\delta r}} = 0 = \underline{g} + \underline{\underline{W}} \cdot \underline{\delta r} \qquad 3.5$$

which rearranges to

$$\underline{\delta r} = -\underline{\underline{W}}^{-1} \cdot \underline{g} \qquad 3.6$$

This expression would give the displacement leading to the minimum energy at $\underline{r}'$ in a single step if the system were perfectly harmonic with respect to $\underline{r}$. However, the energy of the cell is not perfectly harmonic and thus the displacement merely gives a lower energy configuration. Thus an iterative repetition of this process is used to obtain the minimum energy configuration.

There are two problems with this approach to energy minimisation which both derive from finite computer resources. The first is the cpu memory that is required to store the 3N x 3N second derivative matrix, $\underline{\underline{W}}$. Over the last few years this has become less of a problem with the introduction of super computing facilities which are capable of storing second derivative matrices for cells containing several thousand ions. The second problem, which is also the rate determining step for the calculations,

is the time taken to calculate and invert the second derivative matrix although the introduction over the last four years of relatively cheaper R10000 machines has helped to alleviate this to some degree.

There are two approaches which will help to reduce the computational overheads for the energy minimisation. The first approach is to avoid the problem by using a method which does not require the second derivative matrix. One such method is conjugate gradients minimisation which is useful for very large cells. This method will be described in more detail in section 3.2.3 but suffers from taking many more iterations to complete the minimisation. The second method uses an approach by Fletcher and Powell (1963) which approximates the inverse second derivative matrix without calculating it every step. Given the co-ordinates at iteration k the co-ordinates of the cell at the next iteration, k+1, are given by

$$\underline{r}_{k+1} = \underline{r}_k - \underline{\underline{H}}_k \cdot \underline{g}_k \qquad 3.7$$

where $\underline{\underline{H}}$ is the inverted second derivative matrix, $\underline{\underline{W}}^{-1}$, which is called the Hessian. The Hessian for the next iteration, k+1, is approximated using the method of Davidson (1959), Fletcher and Powell (1963)

$$\underline{\underline{H}}_{k+1} \cong \underline{\underline{H}}_k + \frac{\underline{\delta r} \cdot \underline{\delta r}^T}{\underline{\delta r}^T \cdot \underline{\delta g}} - \frac{\underline{\underline{H}}_k \cdot \underline{\delta g} \cdot \underline{\delta g}^T \cdot \underline{\underline{H}}_k}{\underline{\delta g}^T \cdot \underline{\underline{H}}_k \cdot \underline{\delta g}} \qquad 3.8$$

where $\underline{\delta r} = \underline{r}_{k+1} - \underline{r}_k$ and $\underline{\delta g} = \underline{g}_{k+1} - \underline{g}_k$.

This approximation for $\underline{\underline{H}}_{k+1}$ can then be used to calculate the configuration for iteration k+2 by using equation 3.7. Time is saved using this approach since only the

first derivatives (g) need to be calculated for each iteration however any errors in the estimate are increased each step and thus the second derivative matrix needs to be recalculated every 10-30 iterations.

3.2.2 Constant Pressure Minimisation

In addition to minimising the cell with respect to co-ordinate positions, the constant pressure minimisation method also removes any bulk strains acting on the cell by adjusting the cell dimensions. The bulk strains, $\underline{\underline{\varepsilon}}$, cause all vectors and coordinates in the cell, $\underline{r}$, to be modified

$$\underline{r}' = \left(\underline{\underline{I}} + \underline{\underline{\varepsilon}}\right)\underline{r} \tag{3.9}$$

where $\underline{r}'$ represents the transformed (i.e. final) vectors and co-ordinates, $\underline{\underline{I}}$ is the identity matrix. Using the Voigt notation this expression can be given in vector form as

$$\begin{bmatrix} x' \\ y' \\ z' \end{bmatrix} = \begin{bmatrix} 1+\varepsilon_1 & \frac{1}{2}\varepsilon_6 & \frac{1}{2}\varepsilon_5 \\ \frac{1}{2}\varepsilon_6 & 1+\varepsilon_2 & \frac{1}{2}\varepsilon_4 \\ \frac{1}{2}\varepsilon_5 & \frac{1}{2}\varepsilon_4 & 1+\varepsilon_3 \end{bmatrix} \begin{bmatrix} x \\ y \\ z \end{bmatrix} \tag{3.10}$$

where x, y and z are components of r.

The first derivative of the lattice energy with respect to strain, known as the static pressure, can be found using the chain rule. Here,

$$\frac{\partial U}{\partial \underline{\underline{\varepsilon}}_i} = \frac{\partial U}{\partial \underline{r}} \cdot \frac{\partial \underline{r}}{\partial \underline{r}^2} \cdot \frac{\partial \underline{r}^2}{\partial \underline{\underline{\varepsilon}}_i} \tag{3.11}$$

where the first term is the first derivative vector, $\underline{g}$ (i.e. the force), the second term becomes r/2 and the third term can be found by squaring equation 3.9.

$$\left[\underline{r}' = \left(\underline{\underline{I}} + \underline{\underline{\varepsilon}}\right)\underline{r}\right]^2 \Rightarrow \underline{r}'^2 = \underline{r}^2 + 2\underline{r}^\alpha \cdot \underline{\underline{\varepsilon}} \cdot \underline{r}^\beta + \underline{r}^\alpha \cdot \underline{\underline{\varepsilon}}^2 \cdot \underline{r}^\beta \qquad 3.12$$

Thus

$$\frac{\partial \underline{r}^2}{\partial \underline{\varepsilon}_i} = 2\underline{r}^\alpha \cdot \underline{r}^\beta + 2\underline{\underline{\varepsilon}} \cdot \underline{r}^\alpha \cdot \underline{r}^\beta \qquad 3.13$$

On assuming the equilibrium condition of no strain, i.e. $\underline{\varepsilon}$=0, equation 3.13 becomes

$$\frac{\partial \underline{r}^2}{\partial \underline{\varepsilon}_i} = 2\underline{r}^\alpha \cdot \underline{r}^\beta \qquad 3.14$$

where

i	1	2	3	4	5	6
r^α	x	y	z	y	x	x
r^β	x	y	z	z	z	y

As the Coulomb interaction is calculated using the Ewald method (see section 2.3.1) a transformation from $\underline{r}$ to $\underline{r}'$ will also result in a transformation of the reciprocal lattice vectors from $\underline{G}$ to $\underline{G}'$ and the cell volume from V to V'. These are modified in a similar manner to the real space vectors and coordinates, thus

$$\underline{\underline{G}}' = \left(\underline{\underline{I}} + \underline{\underline{\varepsilon}}\right)^{-1} \cdot \underline{\underline{G}} \qquad 3.15$$

and

$$V' = \det\left(\underline{\underline{I}} + \underline{\underline{\varepsilon}}\right) \cdot V \qquad 3.16$$

The derivatives with respect to strain are given by

$$\frac{\partial \underline{G}'^2}{\partial \underline{\varepsilon}_i} = -2\underline{G}^{\alpha} \cdot \underline{G}^{\beta} \qquad 3.17$$

and

$$\frac{\partial V'}{\partial \underline{\varepsilon}_i} = V \qquad 3.18$$

Thus the static pressure when using the Ewald method is given by the sum of the derivatives of the components of U dependant on $\underline{r}$, $\underline{G}$ and V, i.e.

$$\frac{\partial U}{\partial \underline{\varepsilon}_i} = \frac{\partial U(\underline{r})}{\partial \underline{\varepsilon}_i} + \frac{\partial U(\underline{G})}{\partial \underline{\varepsilon}_i} + \frac{\partial U(V)}{\partial \underline{\varepsilon}_i} \qquad 3.19$$

Once the mechanical strain has been calculated we also need to calculate the constant of proportionality between the stress and strain. This is the elastic compliance matrix which is the inverse of the elastic constant matrix. The elastic constants are defined as the second derivatives of the lattice energy with respect to strain. In order to find this the lattice energy is expanded to second order

$$U(\underline{r}') = U(\underline{r}) + \underline{g} \cdot \underline{\delta} + \frac{1}{2}\underline{\delta}^T \cdot \underline{\underline{W}} \cdot \underline{\delta} \qquad 3.20$$

where in this case $\underline{\delta}$ is the 3N+6 strain matrix which contains components of both the internal, $\underline{\delta r}$, and the six independent bulk strains, $\underline{\varepsilon}$. The transformed co-ordinates, r', are thus defined as

$$\underline{r}' = (\underline{\underline{I}} + \underline{\underline{\varepsilon}}) \cdot (\underline{r} + \underline{\delta r}) \qquad 3.21$$

The second derivative matrix is now larger than for the constant volume case and contains a combination of co-ordinate and strain derivatives.

$$\underline{\underline{W}} = \begin{bmatrix} \frac{\partial^2 U}{\partial r^2} & \frac{\partial^2 U}{\partial r \partial \varepsilon} \\ \frac{\partial^2 U}{\partial \varepsilon \partial r} & \frac{\partial^2 U}{\partial \varepsilon^2} \end{bmatrix} = \begin{bmatrix} \underline{\underline{W}}_{rr} & \underline{\underline{W}}_{\varepsilon r} \\ \underline{\underline{W}}_{r\varepsilon} & \underline{\underline{W}}_{\varepsilon\varepsilon} \end{bmatrix} \qquad 3.22$$

where $\underline{\underline{W}}_{rr}$ is the second derivative co-ordinate matrix (3N by 3N), $\underline{\underline{W}}_{\varepsilon r}$ and $\underline{\underline{W}}_{r\varepsilon}$ are the mixed co-ordinate and strain second derivative matrices (3N by 6 and 6 by 3N), and $\underline{\underline{W}}_{\varepsilon\varepsilon}$ is the strain second derivative matrix (6 by 6).

If the equilibrium condition $\underline{g}$=0 is assumed (i.e. the crystal is at zero strain) and $\underline{\delta}$ is split into its separate components ($\underline{\delta}$ and $\underline{\varepsilon}$) equation 3.20 becomes

$$U(\underline{r}') = U(\underline{r}) + \frac{1}{2}\underline{\delta r} \cdot \underline{\underline{W}}_{rr} \cdot \underline{\delta r} + \underline{\delta r} \cdot \underline{\underline{W}}_{r\varepsilon} \cdot \underline{\varepsilon} + \frac{1}{2}\underline{\varepsilon} \cdot \underline{\underline{W}}_{\varepsilon\varepsilon} \cdot \underline{\varepsilon} \qquad 3.23$$

If this expression is differentiated with respect to $\underline{\delta r}$ and equilibrium conditions are assumed this gives

$$\frac{\partial U}{\partial \underline{\delta r}} = 0 = \underline{\delta r} \cdot \underline{\underline{W}}_{rr} + \underline{\underline{W}}_{r\varepsilon} \cdot \underline{\varepsilon} \qquad 3.24$$

Thus

$$\underline{\delta r} = -\underline{\underline{W}}_{rr}^{-1} \cdot \underline{\underline{W}}_{r\varepsilon} \cdot \underline{\varepsilon} \qquad 3.25$$

If this is substituted into equation 3.23 the expression becomes

$$U(\underline{r}') = U(\underline{r}) + \frac{1}{2}\underline{\varepsilon} \cdot \left[\underline{\underline{W}}_{\varepsilon\varepsilon} - \left(\underline{\underline{W}}_{\varepsilon r} \cdot \underline{\underline{W}}_{rr}^{-1} \cdot \underline{\underline{W}}_{r\varepsilon} \right) \right] \cdot \underline{\varepsilon} \qquad 3.26$$

As mentioned previously, the elastic constants are defined as the second derivative of energy with respect to strain, normalised to the cell volume. Thus if equation 3.26 is differentiated twice with respect to strain the elastic constants are given by

$$\underline{\underline{C}} = \frac{1}{V}\left[\underline{\underline{W}}_{\varepsilon\varepsilon} - \left(\underline{\underline{W}}_{\varepsilon r} \cdot \underline{\underline{W}}_{rr}^{-1} \cdot \underline{\underline{W}}_{r\varepsilon} \right) \right] \qquad 3.27$$

Assuming Hooke's law, the strains are given by the stress (static pressure) divided by the elastic constant matrix

$$\underline{\varepsilon} = \left(\underline{P}_{Static} + \underline{P}_{Applied} \right) \underline{\underline{C}}^{-1} \qquad 3.28$$

The calculated strain can then be used to determine the transformed co-ordinates and lattice vectors via an iterative process until all of the strains are removed. Since the method assumes that there are no basis strains for the current volume (i.e. the co-ordinates are at their minimum energy positions) a constant

volume minimisation is carried out during or after each adjustment of the lattice vectors by the bulk strains in order to remove the basis strains.

3.2.3 Conjugate gradients minimisation

Matrix methods can become impractical when the simulation cell becomes very large due to the time required to calculate and then invert the second derivative matrix. The conjugate gradients method (Fletcher and Reeves 1964) is a useful alternative.

The methodology is based upon the steepest descent technique where the minimisation is guided solely by the direction of the forces at the previous configuration. i.e.

$$r_{n+1} = r_n - \alpha_n \cdot \underline{g}_n \qquad 3.29$$

where α is a scalar which is chosen each turn in order to optimise the minimisation. However, this method is very inefficient since the search direction determined from the current force may not be the quickest route to the lowest point on the energy well.

The conjugate gradients method uses information from the previous iteration in order to determine the current search direction. Thus

$$r_{n+1} = r_n - \alpha_n \cdot \underline{S}_n \qquad 3.30$$

where $\underline{S}_n$ is the current search direction given by

$$\underline{S}_n = \underline{g}_n - \frac{\underline{g}_n^T \cdot \underline{g}_n}{\underline{g}_{n-1}^T \cdot \underline{g}_{n-1}} \cdot \underline{S}_{n-1} \qquad 3.31$$

Initially the search vector is set to the direction of steepest descent (i.e. $\underline{g}_1$). To ensure that the function minimises, subsequent search directions must be mutually conjugate with their predecessor thus satisfying the condition

$$\underline{S}_n \cdot \underline{\underline{W}}_{rr} \cdot \underline{S}_{n-1} = 0 \qquad 3.32$$

where $\underline{\underline{W}}_{rr}$ is the second derivative matrix.

The conjugate gradients method has some advantages over matrix methods. The first of these, that it requires less storage space than the matrix methods since the second derivative matrix is not required, has become less important with the introduction of computers with large storage capacity and memory. The primary advantage is the speed of the calculation since the minimisation only requires the first derivatives to be calculated each step. By comparison the matrix method is slower since it requires inversion or updating of the second derivative matrix. However, the matrix methods are more efficient than conjugate gradients at finding the minimum energy position, i.e. requiring less iterations to accomplish this. Thus for small cells with less than 500 ions the matrix method is used. For cells which are larger, a long way from the minimum energy point, or for which the energy well is not very harmonic, conjugate gradients is used to quickly reach the approximate minimum energy position. For cells that are not excessively large matrix methods can then be used to quickly complete the minimisation. This is especially useful since conjugate gradients does not find the minimum as accurately as matrix methods and it has been

found that such methods are not suitable when calculating the numerical difference in free energy (Watson 1996).

Generally matrix methods are far more efficient than conjugate gradients and thus most of the work presented in this thesis was calculated using matrix methods. A notable exception was the calculations on [011] tilt grain boundaries of MgO (section 8.3.3) which required cells in the order of 1000+ ions.

3.3 Inclusion of Temperature

The static energy minimisation methods described in the previous section take no account of thermal effects and zero point energy. Three methods of including temperature into the calculations will be described in the following sections, the first of these is Lattice Dynamics (section 3.4) where the normal modes of vibration are calculated allowing minimisation of the Gibbs Free Energy. The second method is Molecular Dynamics (section 3.5) in which Newton's Laws of motion are solved for the ions in the cell. This allows the calculation of implicit anharmonic effects although again the zero point energy is not included. The third method is Monte Carlo which uses statistical techniques to calculate a thermodynamic mix of the possible state that a system at equilibrium can exist in.

3.4 Lattice Dynamics

This method, pioneered by Born and Huang (1954), calculates the vibrational frequencies of a three dimensional periodic solid. The computer code PARAPOCS (Parker and Price 1989) utilises this to allow the calculation and thus minimisation of the Gibbs free energy. The Gibbs free energy is given by

$$G = U_L + PV + U_{vib} - TS_{vib} \qquad 3.33$$

where U_L is the static lattice energy, P is the pressure, V is the volume, and (U_{vib}-TS_{vib}) is the vibrational component to the energy which is comprised of the vibrational energy, U_{vib}, entropy, S_{vib}, and the temperature, T. The static lattice energy can be calculated using the methods presented in previous sections. The vibrational terms can be calculated from the normal modes of vibration of the solid (which has 3N degrees of freedom where N is the number of ions) using the expression

$$U_{vib} - TS_{vib} = \frac{1}{w_t} \sum_{q=1}^{P} w_p \sum_{i=1}^{3N} \left(\frac{h\omega_{iq}}{2} - kT \ln (Q_{iq}) \right) \qquad 3.34$$

where w_p is the weighting for the point q sampled in the Brillouin zone, w_t is the total weighting, P is the total number of points sampled, N is the number of ions in the cell, h is Planck's constant, $\Sigma h\omega_{iq}/2$ is the vibrational zero point energy and Q_{iq} is the vibrational partition function for the vibrational mode i with frequency ω_{iq} at the wavevector q in the Brillouin zone, which is given by

$$Q_{iq} = \frac{1}{1 - \exp\left(\frac{-h\omega_{iq}}{kT}\right)} \qquad 3.35$$

Theoretically the vibrational partition function should be integrated over the whole Brillouin zone. However, this is impractical since it would require an infinite number of points to be sampled. Instead the sampling scheme of Fillipini (1976) was used which compares favourably with other schemes that are available (Patel et al.

1991). In this scheme points are chosen within the Brillouin zone such that the greatest concentration of points is towards the zone centre where the variation in phonon frequency is the greatest. The contribution to the overall energy for each point is weighted according to the volume which gives an even sampling scheme. Commonly 8 or 27 points are sampled however for large cells, such as required for some of the grain boundaries in this work, only one point at ¼, ¼, ¼ was chosen. The method used to calculate the normal modes of vibration, which are required in order to calculate the free energy, is described in the following section.

3.4.1 Calculation of Vibrational Modes

The phonon frequencies are calculated using a method proposed for the shell model by Cochran (1977). This method assumes that for a given volume the ions can be treated as independent quantised harmonic oscillators which are fixed at their equilibrium positions. This, the harmonic approximation, is modified to allow the calculation of extrinsic anharmonicity giving the quasi-harmonic approximation where the vibrational frequencies are assumed to vary with volume and are thus recalculated for each volume. This approximation is only valid at temperatures well below the melting temperature where intrinsic anharmonic effects are insignificant.

An ion which is not at its equilibrium position will experience a force, F, related to its displacement, $\underline{\delta r}$, by

$$F = \frac{\partial U_L}{\partial \underline{\delta r}} \qquad 3.36$$

Thus Newton's laws of motion are solved using

$$m \cdot \frac{\partial^2 \underline{\delta r}}{\partial t^2} = \frac{\partial U_L}{\partial \underline{\delta r}} \qquad 3.37$$

where m is the mass of the ion. Since for the shell model the mass of the shell is zero, it is assumed that the shell can relax to its equilibrium position instantaneously, i.e.

$$0 = \frac{\partial U_L}{\partial \underline{w}} \qquad 3.38$$

where $\underline{w}$ is the shell displacement. For this explanation the displacement of the ion, $\underline{\delta r}$, is split into shell displacements, $\underline{w}$, and core displacements, $\underline{u}$.

The periodic nature of the cell must be taken into account by considering the dependence of atomic displacements on the wave vector, q. Thus for cores

$$\underline{u} = \underline{u} \exp(i[q \cdot r - \omega t]) \qquad 3.39$$

and for shells

$$\underline{w} = \underline{w} \exp(i[q \cdot r - \omega t]) \qquad 3.40$$

where r is the atom position and ω is the vibrational frequency. This affects the second derivative matrices in a similar way

$$\underline{\underline{W}}_{ij} = \underline{\underline{W}}_{ij} \exp(i \cdot q \cdot r_{ij}) \qquad 3.41$$

where r_{ij} is the ion separation. This expression is summed for all ion pairs.

Similarly to the constant volume method the lattice energy is expanded to second order and equilibrium conditions (i.e. g=0) are applied

$$U(r') = U(r) + \frac{1}{2}\left(\underline{\underline{W}}_{uu} \cdot \underline{u} \cdot \underline{u} + \underline{\underline{W}}_{uw} \cdot \underline{u} \cdot \underline{w} + \underline{\underline{W}}_{wu} \cdot \underline{w} \cdot \underline{u} + \underline{\underline{W}}_{ww} \cdot \underline{w} \cdot \underline{w}\right) \quad 3.42$$

where $\underline{\underline{W}}_{uu}$ represents the second derivative matrix between cores, $\underline{\underline{W}}_{uw}$ and $\underline{\underline{W}}_{wu}$ between core and shell, and $\underline{\underline{W}}_{ww}$ between shells.

Differentiation of 3.42 with respect to cores and shells allows us to solve Newton's laws of motion (equations 3.37 and 3.38) given that the second derivative of the core displacements with respect to t is

$$\frac{\partial^2 \underline{u}}{\partial t^2} = \omega^2 \underline{u} \quad 3.43$$

to give

$$\omega^2 \underline{\underline{m}} \cdot \underline{u} = \underline{\underline{W}}_{uu} \cdot \underline{u} + \underline{\underline{W}}_{uw} \cdot \underline{w} \quad 3.44$$

for the cores and

$$0 = \underline{\underline{W}}_{uw} \cdot \underline{u} + \underline{\underline{W}}_{ww} \cdot \underline{w} \quad 3.45$$

for the shells where $\underline{\underline{m}}$ is the diagonal matrix of core masses. Rearrangement of 3.45 and substitution into 3.44 removes the shell displacements giving

$$\omega^2 \underline{\underline{m}} \cdot \underline{u} = \left[\underline{\underline{W}}_{uu} - \left(\underline{\underline{W}}_{uw} \cdot \underline{\underline{W}}_{ww}^{-1} \cdot \underline{\underline{W}}_{uw}\right)\right] \cdot \underline{u} \quad 3.46$$

Defining the dynamical matrix, $\underline{\underline{D}}$, as

$$\underline{\underline{D}} = \underline{\underline{m}}^{-\frac{1}{2}} \cdot \left[\underline{\underline{W}}_{uu} - \left(\underline{\underline{W}}_{uw} \cdot \underline{\underline{W}}_{ww}^{-1} \cdot \underline{\underline{W}}_{uw}\right)\right] \cdot \underline{\underline{m}}^{-\frac{1}{2}} \quad 3.47$$

with

$$\underline{u} = \underline{\underline{m}}^{-\frac{1}{2}} \cdot \underline{n} \quad 3.48$$

gives

$$\omega^2 \underline{n} = D \cdot \underline{n} \qquad 3.49$$

This is an eigen vector problem and so the frequencies can be calculated by diagonalising the dynamical matrix. This process must be repeated for all the wave vectors chosen in the sampling scheme.

3.4.2 Minimisation of the Total Pressure

The energy minimisation can now be performed by adjusting the ion co-ordinates and lattice vectors until the sum of the static, kinetic and applied pressures is equal to zero. The minimisation of the static pressure has been described previously (see section 3.2.2), and the total pressure including the kinetic contribution is minimised in a similar manner.

The kinetic pressure is defined as the rate of change of the thermal contribution to the free energy with respect to strain normalised to the cell volume. This can be calculated by applying small strains to the cell, and recalculating the thermal contribution to the free energy. Hence the kinetic pressure in each of the six strain directions can be calculated giving

$$\underline{P}_{vib} = \frac{1}{V} \frac{\partial (U_{vib} - TS_{vib})}{\partial \underline{\varepsilon}} \qquad 3.50$$

which for a simple cubic material simplifies to

$$P_{vib} = \frac{\partial (U_{vib} - TS_{vib})}{\partial V} \qquad 3.51$$

and P_{vib} is now all three components of the leading diagonal of the pressure matrix.

At each stage of the minimisation a constant volume minimisation is performed to ensure that the atoms remain at their minimum energy positions. This reduces the possibility of an atom moving to a position where the harmonic approximation breaks down leading to an imaginary frequency (i.e. ω^2 is negative) and an undefined free energy.

Once each of the pressures has been calculated they can be used to evaluate the strains required to bring the cell to its minimum energy configuration in the same manner as described in section 3.2.2

$$\underline{\underline{\varepsilon}} = \left(\underline{\underline{P}}_{stat} + \underline{\underline{P}}_{vib} + \underline{\underline{P}}_{app} \right) \underline{\underline{\underline{C}}}^{-1} \qquad 3.52$$

This process is repeated iteratively until the total pressure reaches a given tolerance (usually 0.01 GPa). Since the calculation of the kinetic pressure is the most time consuming it is only recalculated after every 5th calculation of the static pressure minimisation or until the total pressure reaches 0.01 GPa.

The calculation of the phonon frequencies also allows the calculation of other thermodynamic properties in addition to the thermal contribution to the free energy. These properties include the vibrational energy, vibrational entropy and the heat capacity.

The problem with this method is that it does not include the full anharmonicity of the energy surface and hence is inappropriate or at best only qualitatively reliable at high temperatures where intrinsic anharmonicity becomes important. Under these

conditions Molecular Dynamics should be used which does allow for explicit treatment of intrinsic anharmonicity and which is described in the following section.

3.5 Molecular Dynamics

Molecular Dynamics (MD) simulations differ from Lattice Dynamics simulations because Newton's laws of motion are solved numerically and the movement of the ions in the simulation cell is calculated as a function of time. This method includes intrinsic anharmonicity explicitly and thus allows the consideration of high temperatures approaching and exceeding the melting point. Initially the ions are assigned random velocities so that the cell begins at the required temperature but with no net translational momentum. i.e.

$$\sum_{i=1}^{N} m_i v_i(0) = 0 \qquad 3.53$$

and

$$\sum_{i=1}^{N} m_i v_i^2(0) = 3Nk_BT \qquad 3.54$$

where m_i and v_i are the mass and velocity of ion i respectively, N is the number of ions in the cell, k_B is Boltzmann's constant and T is the temperature of the simulation.

The forces acting between the ions at a finite time step, t, are calculated using the potential models described in chapter 2 and are used to update the ions' positions, velocities etc. after a finite timestep of δt. The choice of time step is vital since it must allow for lattice vibrations yet be large enough to ensure that the simulation does not exceed the available computing time before significant movement of the ions has occurred. Thus a compromise is made; for this work a time step of 10^{-15} seconds was

chosen which allowed data collection runs of approximately 10^{-11} seconds (10ps). To overcome the effects of the surfaces of the simulation box periodic boundary conditions are applied. The box is surrounded by images of itself which means that if an ion leaves the box its image enters the box on the opposite side. Even with the use of the Ewald method for calculating long range forces the box must be large enough to ensure that an ion does not interact with its image since this would impose unwanted symmetry constraints upon the cell. All of the simulations in this work were performed within the rigid ion model as the inclusion of polarisability was impractical for two reasons. Firstly, since the shells would have a smaller mass than the cores they would move faster which would necessitate the use of shorter time steps (Mitchell and Fincham 1993). This would mean that longer calculations would be required to give the 10 ps runs required. Secondly, the shell model would increase the number of species required. The availability of computer time restricted the number of species that we could explicitly treat to approximately 1200.

3.5.1 Predictor-Corrector Methods

One of the best methods for interpolation of the ion coordinates between time steps is the predictor-corrector method which works as follows. A prediction is made using the current forces at the position, r, velocity, v, and acceleration, a, of the ions at time step (t+δt) by a Taylor expansion about time t. Thus for example, an expansion to third order would give

$$r_i^p(t+\delta t) = r_i(t) + v_i(t)\cdot\delta t + \frac{1}{2}a_i(t)\cdot\delta t^2 + \frac{1}{6}b_i(t)\cdot\delta t^3 \qquad 3.55$$

$$v_i^p(t+\delta t) = v_i(t) + a_i(t)\cdot\delta t + \frac{1}{2}b_i(t)\cdot\delta t^2 \qquad 3.56$$

$$a_i^p(t+\delta t) = a_i(t) + b_i(t)\cdot\delta t \qquad 3.57$$

The values thus calculated are predicted values. A Taylor expansion of Newton's laws of motion is an approximate integration method and thus a correction must be applied to take into account the change in forces over the length of the time step. This is accomplished by calculating the forces at the predicted position, $a_i^c(t+\delta t)$, and comparing them to the predicted forces, $a_i^p(t+\delta t)$, to give a correction factor

$$\Delta a(t+\delta t) = a_i^c(t+\delta t) - a_i^p(t+\delta t) \qquad 3.58$$

This correction factor is then applied to each of the predicted values to give a better approximation of the true positions, velocities, etc. Thus

$$r_i^c(t+\delta t) = r_i^p(t+\delta t) + c_0\Delta a(t+\delta t) \qquad 3.59$$

$$v_i^c(t+\delta t) = v_i^p(t+\delta t) + c_1\Delta a(t+\delta t) \qquad 3.60$$

$$a_i^c(t+\delta t) = a_i^p(t+\delta t) + c_2\Delta a(t+\delta t) \qquad 3.61$$

The correction factors, c_0, c_1 and c_2, are chosen to give optimum accuracy and stability of the trajectories. As is discussed by Gear (1966) different values are assigned to the factors for different orders of expansion. Larger orders of expansion would give greater accuracy to the prediction and correction stages and several algorithms are available. In this work the fifth order predictor-corrector method of Gear (1971) has

been used since this method is more compatible with constant temperature and constant pressure methods described later (Allen and Tildesley 1989).

3.5.2 Constant Pressure and Temperature Methods

Before any data collection runs are performed the simulation cell must be equilibrated to the simulation conditions. This is accomplished by performing scaling runs of approximately 5-10 ps during which the velocities of the ions are scaled to the simulation temperature periodically.

There are several sets of conditions (known as ensembles) at which the simulation can be performed. These include the micro canonical ensemble where the number of particles, energy and volume of the box is kept constant (i.e. NVE), the canonical which has a constant number of particles, volume and temperature (NVT), and the isothermal-isobaric ensemble with a constant number of particles, pressure, and temperature (NPT).

Constant temperature was modelled in this work by the Nosé-Hoover thermostat (Nosé 1984, 1990, Hoover 1985). This is an extended system method in which the simulation box is connected to an external heat bath with one degree of freedom. A potential and kinetic energy is defined for the heat bath and the total potential and kinetic energy of the simulation box and the heat bath is conserved. Energy is allowed to transfer within this constraint between the heat bath and the simulation cell such that the kinetic energy fluctuates slightly about an average value whilst still allowing localised variations in temperature where potential energy is converted into kinetic energy.

Constant pressure MD was modelled in this work by using the method of Parrinello and Rahman (1981) which allows changes in the unit cell dimensions and angles with time as a result of the difference between internal and applied stresses. This is can be envisaged as having a piston in contact with the simulation cell wall which has potential and kinetic energy. The piston moves so as to regulate the pressure.

3.5.3 Properties from Molecular Dynamics

Several crystal properties can be determined from MD simulations. Perhaps the most important is atomic transport or diffusion which can be evaluated from the mean squared displacements (MSD) of the ions. The MSD is the average displacement of an ion from its starting position and is given by

$$\left\langle r_i^2(t)\right\rangle = \frac{1}{N_i}\sum_{i=1}^{N_i}\left[(x_{i(t)}-x_{i(0)})^2+(y_{i(t)}-y_{i(0)})^2+(z_{i(t)}-z_{i(0)})^2\right] \quad 3.62$$

If there is no increase in the MSD then the ions are merely vibrating about their lattice sites. If one of the MSDs increases then an ion of that type is diffusing, if all of them increase then melting has occurred. The diffusion coefficient, D_i, can be calculated from the gradient of the MSD with time

$$\left\langle r_i^2(t)\right\rangle = 6D_i t + B_i \quad 3.63$$

where B_i is the Debye-Waller factor. The problem with using traditional MD to calculate properties of diffusion such as activation energies is that these energies are

high and hence the diffusion pathway cannot be identified except at temperatures approaching the melting point. To overcome this a modified version of the MD code was used in this work to allow diffusion to occur over a shorter time scale (Harris et al. 1997). This modification is described in more detail in chapter 7.

Other properties which can be determined include the melting point. The crystal is deemed to have melted when the MSD for all ions show an increase with time. The melting temperature can be determined by raising the temperature of the simulation in small steps until the crystal melts. Finally, since the co-ordinates are saved during the simulation it is possible to examine both the average and instantaneous structure and structural properties such as the radial distribution function (RDF) which provides a measure of the long range order in the crystal.

3.6 Monte Carlo Simulation

The Monte Carlo method is a statistical technique which is useful when a system in equilibrium can exist in one of several states or to calculate a thermodynamic mix of possible states. The Metropolis algorithm (Metropolis et al. 1953) has been used in this work and essentially the method proceeds as follows. First make a move from the current state to a trial state. Calculate the energy of this new state and compare it to the original state. If the energy of the trial state is lower the trial move is accepted and the new state becomes the current one. If the trial state is higher in energy there is a probability of the trial being accepted based on the difference in energy of the two steps. This is summarised below

$$P = 1 \quad \Delta E \leq 0 \qquad 3.64$$

$$P = \exp\left(\frac{-\Delta E}{k_B T}\right) \quad \Delta E > 0 \qquad 3.65$$

when P is the probability of acceptance and ΔE is the difference in energy between the two states. The method is described in greater detail in chapter 8.

3.7 Calculation of Planar Defect Energies

One of the key features of this work is the calculation of the structure and stability of planar defects such as grain boundaries and surfaces. The calculation of grain boundaries can be accomplished via two methods. The first uses a two region approach which allows the calculation of an isolated boundary and surface. The second method uses three dimensional periodicity which allows the calculation of vibrational properties via programs such as PARAPOCS. The two methods will be discussed in the following sections.

3.7.1 Two Region Approach

In the two region approach, used in the computer code METADISE (Watson et al. 1996) which follows the method of Tasker and Duffy (1983a), the crystal is assumed to consist of blocks containing a series of charged planes parallel to the surface or interface and to be periodic in two dimensions. Surfaces are generated by using a single block whilst putting two blocks together allows the study of interfaces. Each block is divided into two regions, region I and region II (see fig 3.1). The ions in region I are explicitly relaxed during the minimisation whereas the ions in region II are held fixed at their bulk sites although the region may move as a whole

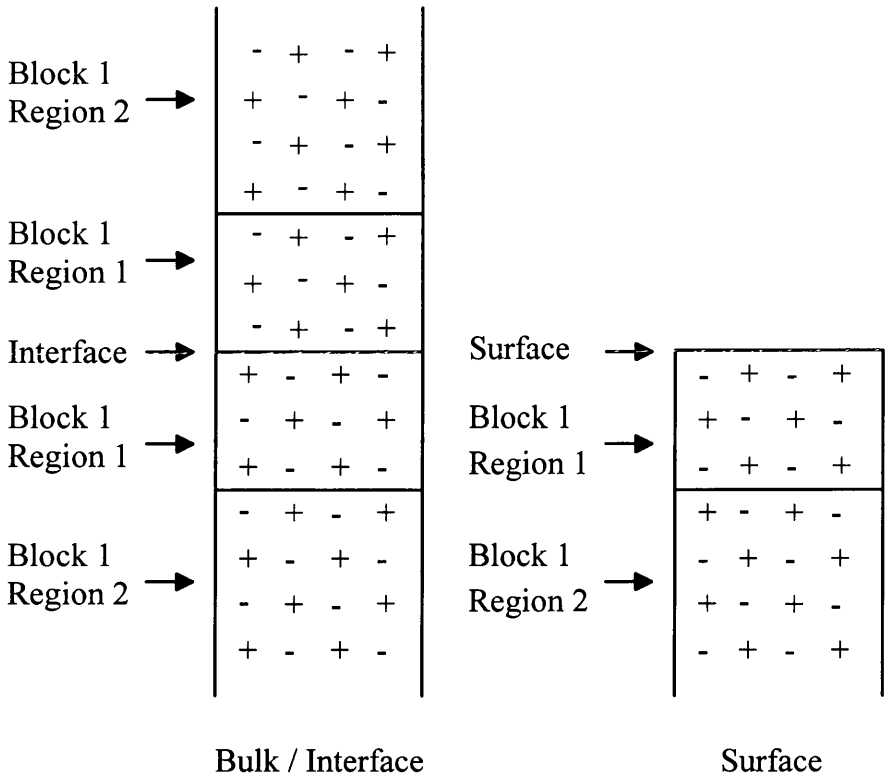

Figure 3.1 Schematic representation of the two region approach used in METADISE for bulk, interface and surface simulations.

The energy of the crystal, U_L, is therefore the sum of the energies due to the two regions

$$U_L = (U_{11} + U_{12}) + (U_{22} + U_{21}) \qquad 3.66$$

where U_{11} is the interaction of region 1 with itself, U_{22} is the interaction of region 2 with itself and U_{12} and U_{21} are the interactions of region 1 and 2 with each other. Since region 2 is held fixed U_{22} will be constant and can therefore be ignored when calculating the energy difference. U_{12} and U_{21} are identical and are referred to as the boundary interaction energy.

The surface energy is defined as the energy per unit area required to form a surface from the bulk. Thus by performing bulk and surface minimisation and calculating the energy of the block in each case the surface energy can be found using

$$\gamma_s = \left(\frac{U_{sf} - \frac{1}{2}U_{bk}}{A} \right) \qquad 3.67$$

where U_{sf} and U_{bk} are the surface and bulk block energies respectively for blocks containing the same number of ions and A is the area.

The energy of a grain boundary can be expressed in two ways. The grain boundary formation energy is defined as the energy required per unit area to form the grain boundary from bulk. The energy is given by

$$\gamma_{gb} = \left(\frac{U_{gb} - U_{bk}}{A} \right) \qquad 3.68$$

where U_{gb} is the block energy of the grain boundary. The grain boundary adhesion energy is defined as the energy per unit area required to split a grain boundary into two surfaces. The energy is given by

$$\gamma_{ad} = \left(\frac{2U_{sf} - U_{gb}}{A} \right) \qquad 3.69$$

where U_{sf} and U_{gb} are the energies for blocks containing the same number of ions.

Since the two region approach uses static energy minimisation to determine the equilibrium structure the energies calculated do not include temperature. In order to

minimise grain boundaries in a lattice dynamics code such as PARAPOCS or a molecular dynamics code a three dimensional approach is required.

3.7.2 Three Dimensional Approach to Grain Boundaries

Grain boundaries are simulated in three dimensions by creating a unit cell from two oriented blocks that form the interface, resulting in two grain boundaries being formed, one at the centre of the cell and one at the cell edge as shown in figure 3.2.

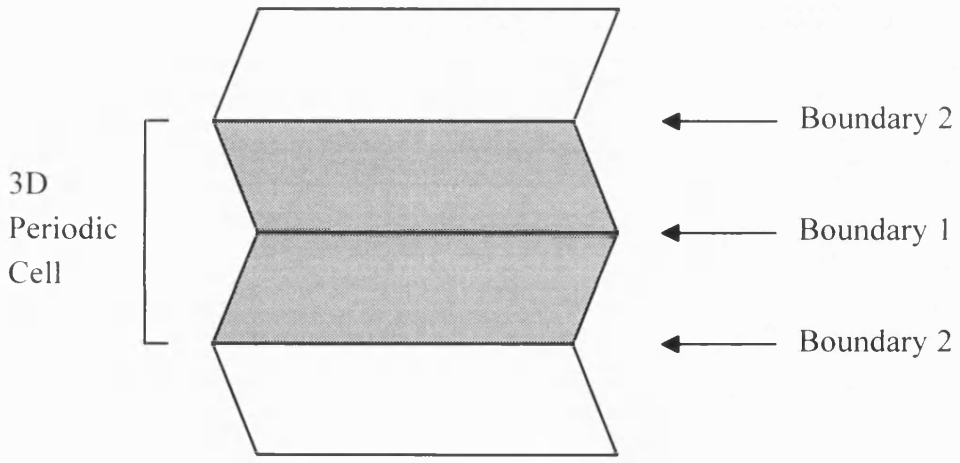

Figure 3.2 Schematic representation of the three dimensional approach to forming grain boundaries

Grain boundary formation energies are defined in the same way, however, care must be taken that the two grain boundaries within the cell are identical to ensure that a distinct energy is calculated rather than the average energy of two different boundaries. Adhesion energies as a function of pressure can not be calculated by this method since it is not possible to calculate the effect of pressure on a surface in a three

dimensional approach. This is because surfaces in three dimensions are simulated using a slab method where the unit cell consists of a slab of material and vacuum. Applying a pressure to this system would cause the unit cell vectors to decrease to the size of the slab thus effectively causing slabs in neighbouring cells to come into contact with each other.

4 Static Lattice Calculations of MgO Grain Boundaries

4.1 Introduction

In this chapter the results of atomistic calculations on the surface energies and structure, crystal morphology, grain boundary energy and structure of periclase (MgO) are presented. In addition to being an important ceramic, MgO is a mineral believed to be an important component of the Earth's lower mantle. It has been chosen due to its importance and because it is a simple cubic face-centered structure, does not have variable oxidation states and thus ideal for investigating the approaches for generating stoichiometric grain boundaries.

4.2 Potentials

Several potential models are available for modelling MgO. In this section we will describe two of these and compare and contrast bulk properties and structural features which have been calculated using them. The potentials will then be used to calculate surface structure and properties and the energies and structures of [001] tilt grain boundaries.

The Sangster-Stoneham (1981) and Lewis-Catlow (1985) potentials have both been developed by empirical fitting to experimental data which includes the structure, cohesive energies, dielectric constants and elastic constants. In addition phonon dispersion curve data were included in the derivation of the Sangster-Stoneham potential. The potential parameters for both potentials are reproduced in tables 4.1 and 4.2.

Interaction	A (eV)	ρ (Å)	C (eV Å^6)
Mg^{2+}-O^{2-}	1275.2	0.3012	-
O^{2-}-O^{2-}	22764.3	0.1490	20.6

Table 4.1a Sangster-Stoneham short range parameters.

Ion	Charge	K (eVÅ^2)	Mass (g mol^{-1})
Mg^{2+} core	+2.00	-	24.0
O^{2-} core	+0.8107	-	16.0
O^{2-} shell	-2.8107	46.128	0.0

Table 4.1b Sangster-Stoneham ion charge, polarisability and mass.

Interaction	A (eV)	ρ (Å)	C (eV Å^6)
Mg^{2+}-O^{2-}	1428.5	0.2945	-
O^{2-}-O^{2-}	22764.3	0.1490	27.88

Table 4.2a Lewis-Catlow short range parameters.

Ion	Charge	K (eVÅ^2)	Mass (g mol^{-1})
Mg^{2+} core	+2.00	-	24.0
O^{2-} core	+1.00	-	16.0
O^{2-} shell	-3.00	54.800	0.0

Table 4.2b Lewis-Catlow ion charge, polarisability and mass.

Property		SS	LC	Expt.	Reference
Elastic Constants (GPa)	C_{11}	360.9	392.5	294	a
	C_{12}	163.1	164.4	155	a
	C_{44}	163.1	164.4	96	a
Lattice Parameter (Å)		4.2276	4.1986	4.21	b
Static dielectric constant ε_{11}		9.90	9.52	9.86	c
High frequency dielectric constant ε_{11}		2.93	2.97	2.96	c

Table 4.3 Comparison of properties calculated using the Sangster-Stoneham (SS) and Lewis-Catlow (LC) potentials with the following experimental data, a) Landolt and Borstien (1979), b) Wyckoff (1963), c) Peckham (1967).

To test the accuracy of the two potentials various data were calculated using the potentials and compared with experimental data. The potential models gave good agreement with experiment and were quite consistent with each other as shown in table 4.3. One exception was the elastic constants. The experimental values of C_{12} and C_{44} are different which is not the case when the potentials were used. The reason for this is that both potentials are central force and hence must satisfy the Cauchy relation for cubic oxides, i.e. $C_{12}=C_{14}$. This relationship applies so long as every lattice particle occupies a centre of symmetry and interact with central forces, thus ensuring no internal strain and is not under any applied pressure. Work by Catlow et al. (1976) showed that when the Cauchy violation was modelled by fitting a breathing shell model to an MgO potential and the results of defect formation were compared to those

of the standard shell model, the defect energy did not change significantly between the two models so long as the dielectric behaviour was correctly reproduced. For this work it was decided not to use this model since the small gain in accuracy did not justify the increased computational expense.

Given the good consistency between the potentials it was decided that the energies and structures of the surfaces and [001] tilt grain boundaries would be calculated using both potentials to allow further comparison.

4.3 Surface Energies, Structure and Equilibrium Crystal Morphologies

Initially the surface structure and energies of MgO were modelled using the two potentials. In addition to determining the morphology of MgO, allowing comparison of the potentials, calculation of the surface energies would allow us to determine the stability of the grain boundaries to be studied with respect to cleavage to form two surfaces (i.e. the adhesion energy). The computer code METADISE (Watson et al. 1996) was employed to calculate the unrelaxed and relaxed structures and energies of a number of surfaces of MgO. Surfaces with the index (h10) were primarily chosen since these indexes would later be chosen for grain boundary simulation, however other indexes up to 2 were also considered. Firstly, to ensure that the lattice energy had converged with region size calculations were performed on the (310) surface and convergence was found to occur for a region 1 thickness of approximately 14 Å. The surface energies were then calculated using the Lewis-Catlow and Sangster-Stoneham potentials.

Miller Index (hkl)	Surface Energies (Jm^{-2})			
	Sangster-Stoneham		Lewis-Catlow	
	Unrelaxed	Relaxed	Unrelaxed	Relaxed
(100)	1.22	1.16	1.31	1.24
(110)	3.40	2.90	3.55	3.01
(210)	2.63	2.00	2.76	2.11
(310)	2.24	1.72	2.37	1.83
(410)	2.02	1.57	2.14	1.68
(510)	1.87	1.49	1.98	1.58
(810)	1.64	1.36	1.74	1.46
(211)	8.44	3.91	8.69	4.08
(221)	11.04	3.38	11.35	3.70

Table 4.4 Relaxed and unrelaxed surface energies of MgO calculated using the Sangster-Stoneham and Lewis-Catlow potential models.

The calculated {100} surface had a much lower surface energy than the other surfaces as shown in table 4.4 which resulted in a cubic morphology dominated by this surface as shown in figure 4.1.

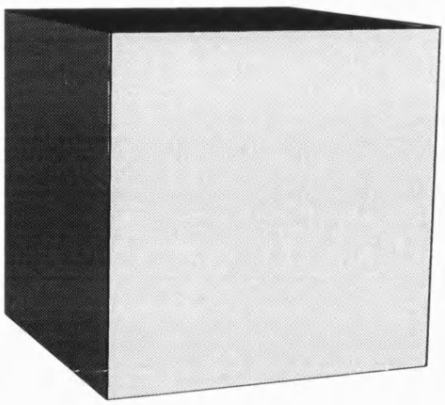

Figure 4.1. Equilibrium morphology of MgO.

The energies calculated for the (100) surfaces by both potentials showed reasonable agreement with experimental observations (Gilman 1960 (1.2 Jm^{-2}), Melcholsky 1976 (3.0 Jm^{-2}), Rice 1981 (10 Jm^{-2})) and previous calculations (Tasker and Duffy 1984). For the (h10) surfaces the relaxed surface energies decreased as the index increased and the number of steps per unit area decreased. A plot of the surface energies against the angle of inclination of the surface for both potentials showed that the energy decreased almost uniformly to that of the {100} surface (figure 4.2).

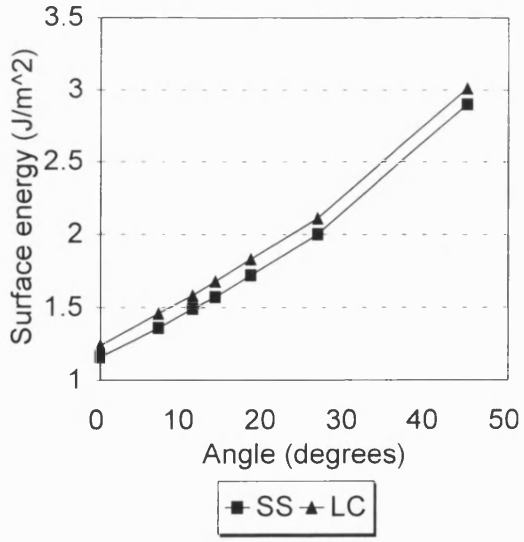

Figure 4.2. The surface energy as a function of angle for the (h10) surfaces of MgO.

Figure 4.3 shows the structure of a selection of surfaces. For all (h10) surfaces the surface ions were 5 co-ordinate with 4 co-ordination at the step edges. There is some relaxation at the step edges with the ions being pulled towards the bulk slightly and this is greater for the magnesium ions. In addition the surface between steps rumples slightly.

The {211} and {221} (figures 43e and f) surfaces consisted of pyramidal structures at the surface with the ions at the tips of these structures 3 co-ordinate whilst the ions on the faces were 5 co-ordinate. The {211} surface showed some relaxation of the ions at the tips of the pyramids which were drawn down slightly towards the bulk with the magnesium ions again moving further than the oxygen ions. The {221} surface relaxed further with the ions at the trench sites moving outwards to effectively remove the step and create a more level surface. The resulting surface energies of 3.91 Jm^{-2} for the {211} and 3.38 Jm^{-2} for the {221} using the Lewis-Catlow potential were high compared to the energies calculated for the (h10) surfaces.

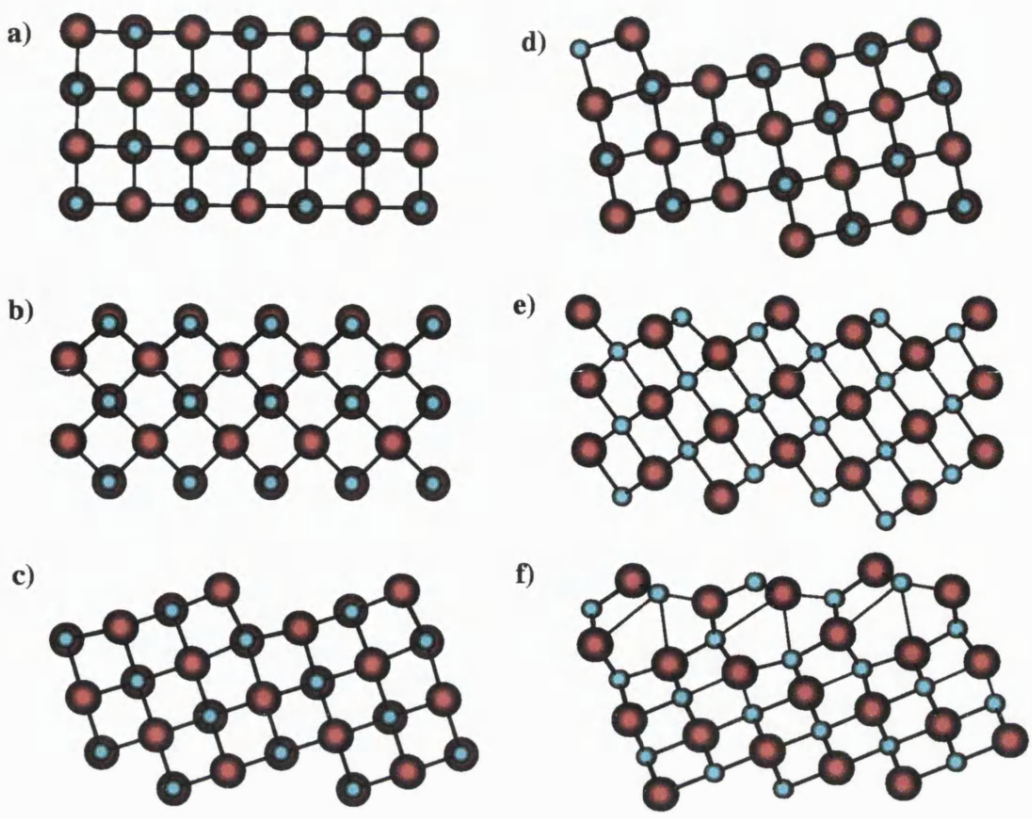

Figure 4.3. The a) (100), b) (110), c) (310), d) (510), e) (211) and f) (221) surfaces of MgO. Surfaces are at the top of each block. Red represents oxygen and cyan represents magnesium

4.4 The [001] tilt grain boundaries of MgO

4.4.1 Introduction

These boundaries, which have been studied experimentally by Merkle (Merkle and Smith 1987a, Merkle 1994), are classified as those which are formed by the rotation of one crystal forming the grain boundary with respect to the other about the [001] axis to create a grain boundary of the form {hk0}. Only boundaries where k=1 were chosen for study because an important aim of this work was to find a simple

method for the generation of tilt grain boundaries and hence a number of examples were investigated. In the following sections our method of grain boundary formation will be outlined and then the results of static lattice calculations upon [001] tilt grain boundaries will be presented.

4.4.2 Generation of Grain Boundaries for Static Lattice Calculations (Σ5)

As an example of a [001] boundary the {310}/[001] Σ5 tilt grain boundary was chosen to develop our methodology. This boundary is formed by placing together the (310) surface of one crystal with the $(3\bar{1}0)$ surface of a second crystal. The unit cell was created by mirroring the (310) surface in the stacking direction to form the two crystals. In order to assign a sensible starting position for the minimisation of the grain boundary structure the code DELTAMOVE, which employed the following approach, was used. One of the two blocks was held fixed whilst the second block was rigidly translated relative to it in the Y and Z directions to form a grid of points. By varying the separation of the blocks the minimum energy for each grid point was obtained with the corresponding height which were displayed using a contour plot. A point on the contour plot with a highly negative interaction energy should be a good starting position for the simulation.

An example is given in figure 4.4 for the {310}/[001] tilt grain boundary which shows two unique sites, indicated by A and B on the plots, with a good interaction energy.

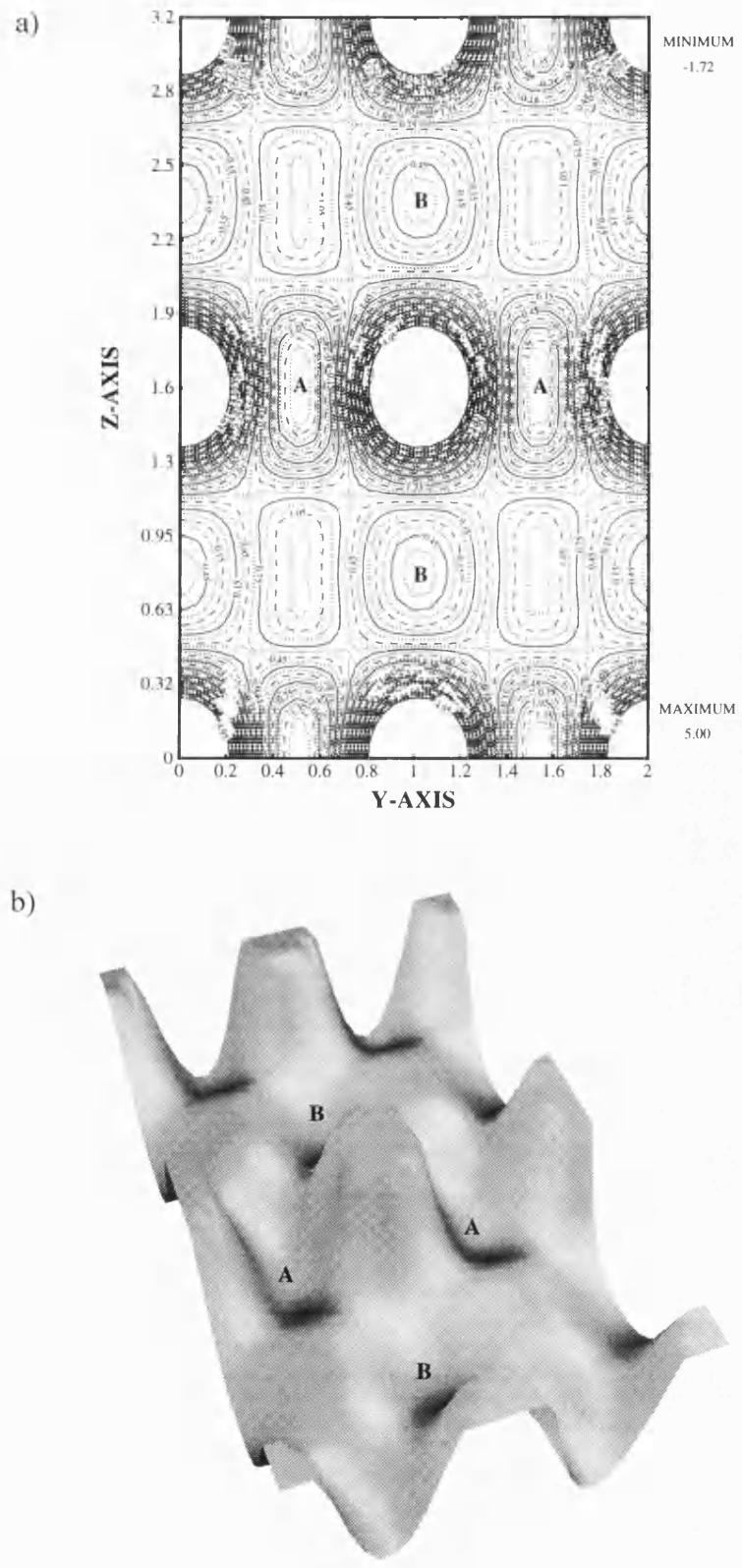

Figure 4.4. Contour plot for the {310}/[001] tilt grain boundary showing a) a grid plot and b) a three dimensional view.

Point A has a more favourable interaction energy at a displacement of 2.54 Å in the Y direction and 0 Å in the Z direction, i.e. one half unit cell shift in the Y direction. Point B has a slightly less favourable interaction energy than point A at a co-ordinate equivalent to a one quarter unit cell shift in the Z direction and 0 Å in the Y direction. Since point A gives a more favourable interaction than point B it could be expected that this configuration would give the lowest energy boundary. However, this method utilises a rigid shift of the two blocks without allowing for relaxation of the boundary which could lead to changes in the order of stability. To test if this was the case both grain boundary structures were modelled.

4.4.3 Lattice Energy Minimisation

The two configurations (figures 4.5a and b) were relaxed to the mechanical equilibrium using the energy minimisation code METADISE giving rise to the structure shown in figure 4.5a and c. Only the relaxed structure of the symmetric tilt boundary is shown since the unrelaxed and relaxed boundaries were almost identical. Point A in the DELTAMOVE plot (figure 4.4) corresponded to the symmetrical tilt grain boundary shown in figure 4.5a which was previously modelled for NiO (Duffy and Tasker 1983a, Harding et al. 1989). The boundary is termed symmetrical since in the unrelaxed structure the lattice sites have a (100) mirror plane of symmetry formed by the grain boundary plane although the ions themselves are of opposite types on either side of the boundary (i.e. magnesium - oxygen). The relaxed structure had a formation lattice energy of 1.77 Jm^{-2} and an adhesion energy of 0.86 Jm^{-2}. It consisted of open channels with magnesium oxygen bonds of length 1.97 Å linking together the two sides of the boundary at the step edges which were shorter than those found in

bulk MgO which were 2.12 Å in length. The channels were probably a result of the large coulombic nature of the potential since for {310}/[001] boundaries of metals these channels are not observed (Hasson et al. 1972). If MgO was placed onto the metal boundary structure the resulting coulombic repulsion due to neighbouring ions of like charge would be too great.

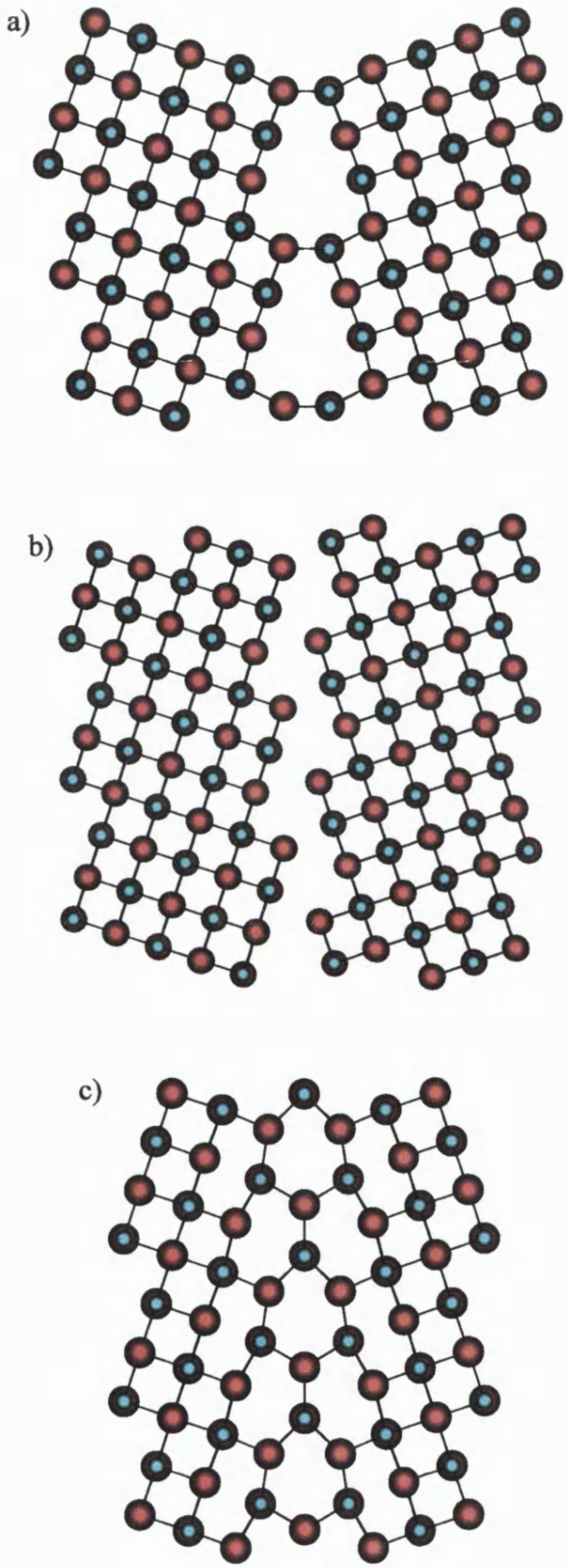

Figure 4.5. The a) relaxed symmetric and b) unrelaxed and c) relaxed asymmetric {310} tilt grain boundaries.

Point B in figure 4.4 corresponded to the asymmetric {310}/[001] tilt grain boundary, so termed because the unrelaxed structure did not have a mirror plane of symmetry for the lattice sites as shown in figure 4.5b. The relaxed structure did have a (100) plane of symmetry with respect to the sites and was more compact than the symmetric grain boundary with no channels, although the bond lengths in the region of the boundary were closer to those of bulk, ranging from 2.05 Å to 2.11 Å as shown in figure 4.5c. However, the calculated energies for this boundary were higher than those of the symmetric structure with a formation lattice energy of 2.20 Jm^{-2} and an adhesion energy of 1.25 Jm^{-2}. This agreed with the data of Harding et al. (1989) who modelled this boundary in NiO and found that this boundary, which had a formation energy of 2.45 Jm^{-2}, was less stable than the symmetrical one with a formation energy of 1.95 Jm^{-2}.

To further compare the energies of the symmetric and asymmetric [001] tilt grain boundaries a boundary with a higher index, the {410}/[001] Σ17 boundary, was chosen. DELTAMOVE calculations showed three areas of good interaction with the favourability decreasing in the order A>C>B (figure 4.6). The A position corresponded to the symmetric tilt grain boundary shown in figure 4.7a. This boundary had a similar structure to the {310}/[001] symmetric tilt gain boundary with a (100) plane of symmetry for the lattice positions, however the magnesium oxygen cross linking bonds in the relaxed structure boundary were 1.95 Å in length, shorter than those in the {310} boundary. The formation energy of the {410} boundary was calculated as 1.82 Jm^{-2}, higher than for the {310}, whilst the adhesion energy was 0.69 Jm^{-2}, lower than for the {310}.

a)

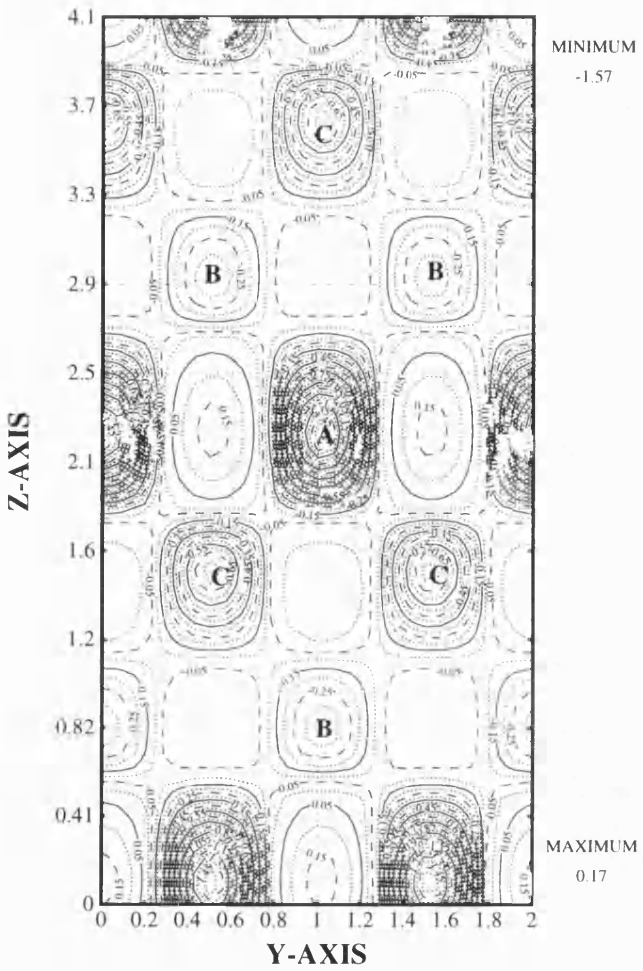

b)

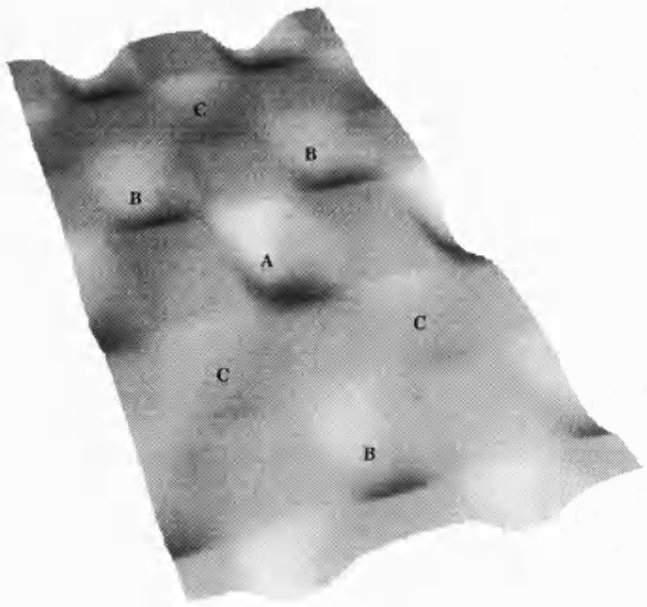

Figure 4.6. Contour plot for the {410}/[001] tilt grain boundary showing

i) a grid plot and ii) a three dimensional view.

a)

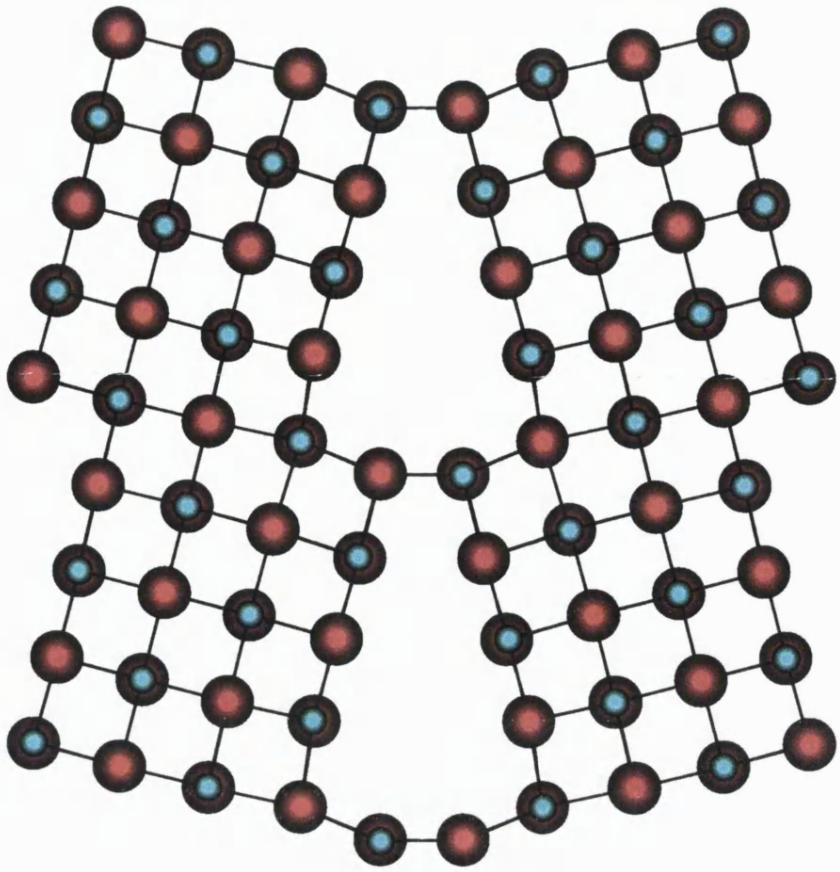

b)

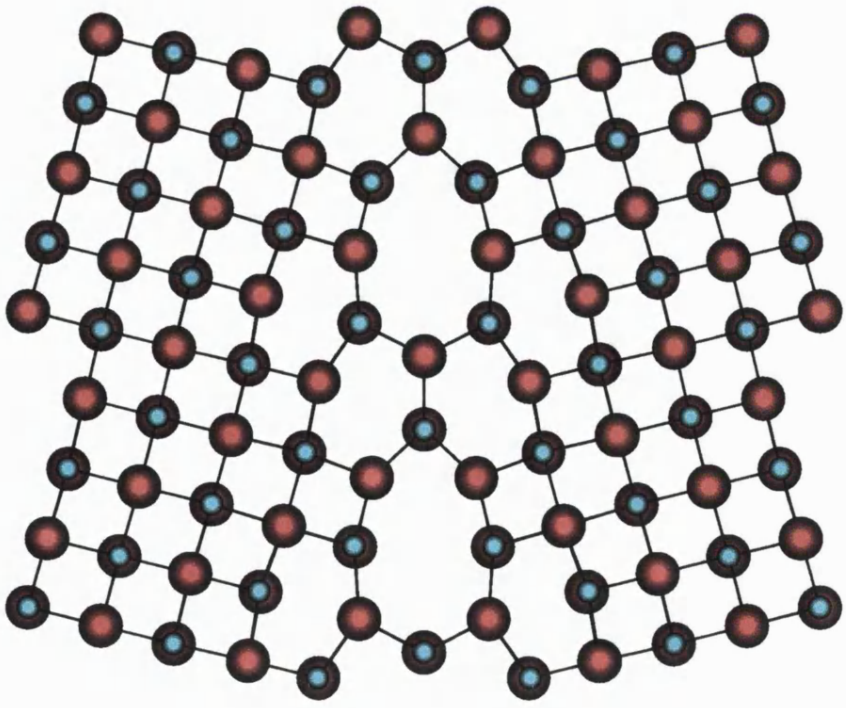

Figure 4.7. The relaxed a) symmetric and b) asymmetric {410} tilt grain boundaries.

Points B and C on the DELTAMOVE plot were found to give identical structures upon minimisation; that of the {410} asymmetric boundary shown in figure 4.7b. This boundary was less stable than the {410} symmetric boundary with a formation lattice energy of 2.31 Jm^{-2}, higher than for the {310}, and an adhesion energy of 0.84 Jm^{-2}.

The calculations upon the grain boundaries of the {310} and {410} tilt grain boundaries demonstrated that the symmetrical grain boundaries were the most stable of the two types at 0 GPa and without the inclusion of temperature.

For the calculation of the relationship between misorientation angle and formation lattice energies only the symmetric boundaries were considered. Static lattice energy calculations were carried out on the remaining {h10} indexes up to h=9. Structures of two of these boundaries, the {110} and {710} are given in figure 4.8. The {110} is both a tilt grain boundary and a stacking fault, thus it was included for completeness so that we could investigate any systematic changes in both structure and stability for this series of grain boundaries. Structurally, the {110} boundary had a greater number of cross linking bonds per unit area than either the {310} or {410} boundaries described earlier. These bonds were also shorter with a length of 1.94 Å compared to 1.97 Å for the {310} and 1.95 Å for the {410) boundary.

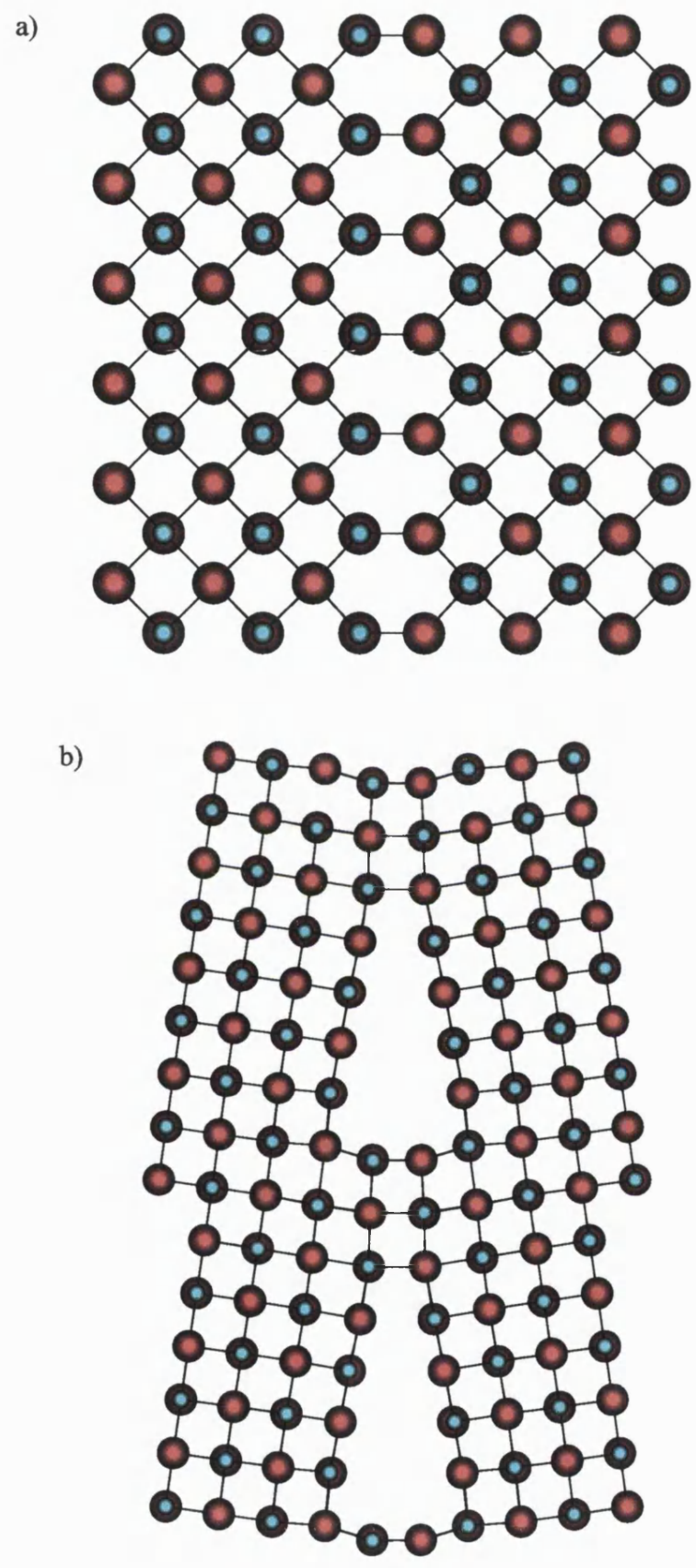

Figure 4.8. The a) {110} and b) {710} symmetric tilt grain boundaries.

The calculated formation lattice energies and adhesion energies for each potential are given in table 4.5 along with the cross-link density which is defined as the number of magnesium oxygen bonds (of less than 2.5 Å in length) linking across the boundary per unit area. The adhesion energies decreased as the index increased which implies that the higher index boundaries would more readily break into two surfaces which is understandable when one considers the surfaces that would be formed. For example, the {210} boundary would break to form the (210) surface which from section 4.3 we have seen had a relatively high surface energy of 2.00 Jm^{-2}. In contrast, as the index increases the surfaces which would be formed approach that of the (100) surface which from table 4.4 we have previously shown to be the most stable. Thus if we consider the adhesion energies alone we would expect the high index surfaces to readily cleave to give two free surfaces.

The formation lattice energies varied smoothly with misorientation angle as shown in fig 4.9 for each potential. For the {110} boundary the formation energy was low at 1.10 Jm^{-2}, but the energy increased as the misorientation angle of the boundary increased until a maxima of 1.82 Jm^{-2} was reached for the {410} symmetric tilt grain boundary. The energies then began to decrease again as the misorientation angle of the boundary decreased further. This is in agreement with the calculations carried out upon NiO [001] tilt grain boundaries by Duffy and Tasker (1983a) and qualitatively with thermal grooving experiments on NiO by Dhalenne et al. (1979).

Miller Index	Boundary Angle (°)	Σ	Formation Energy (Jm^{-2})		Adhesion Energy (Jm^{-2})		Cross-link Density ($Å^{-2}$)
			SS	LC	SS	LC	
{110}	90.0	1	1.10	1.23	4.72	4.79	0.158
{210}	53.1	5	1.60	1.76	2.46	2.46	0.150
{310}	36.9	5	1.77	1.92	1.72	1.74	0.106
{410}	28.1	17	1.82	1.96	1.38	1.41	0.081
{510}	22.6	13	1.80	1.93	1.24	1.24	0.132
{610}	18.9	37	1.75	1.87	1.18	1.18	0.166
{710}	16.3	25	1.73	1.84	1.14	1.14	0.142
{810}	14.3	65	1.70	1.80	1.12	1.13	0.167
{910}	12.7	41	1.69	1.78	1.10	1.10	0.148

Table 4.5. Calculated formation and adhesion energies for the [001] symmetric tilt grain boundaries using the Sangster-Stoneham (SS) and Lewis-Catlow (LC) potentials.

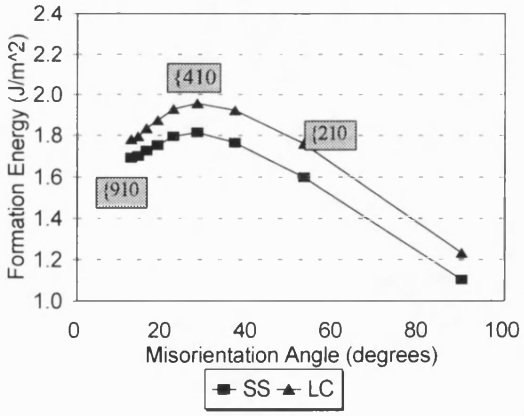

Figure 4.9. Variation of formation lattice energy and misorientation angle for [001] symmetric tilt grain boundaries.

The cross-link density as given in table 4.5 followed a similar pattern to the formation energies. The [110} boundary, which had the lowest formation energy, also had a high cross linking bond density. As the index increased, the spacing between the cross links also increased, causing a decrease in the cross link density until it reached a minima for the {410} which corresponded to the maxima in the formation lattice energy. As the index increased still further the cross linking bond density increased again. Although the distance between the step edges of the boundary increased, extra cross links were formed as a result of the two sides of the boundary drawing closer together due to the decreasing misorientation angle. Ultimately as the index increases still further the resulting structure would tend towards that of bulk MgO. Thus for the formation energy of the {h10} boundaries we would find that as

$$h \rightarrow \infty \ , \ \gamma_{gb} \rightarrow 0$$

and for the adhesion energies

$$h \rightarrow \infty \ , \ \gamma_{ad} \rightarrow 2\gamma_s(100)$$

Thus from the adhesion and formation energies it is clear that the stability of the grain boundaries is a combination of the stability of the free surfaces and the stability of the more bulk-like grain boundary.

Given that the energies calculated using the two potentials agreed with each other it was decided to continue with just one potential. Since one of the aims of this work is to model the effect of temperature on the grain boundaries by calculating the

vibrational entropy the Sangster-Stoneham potential was chosen because it included bulk phonon data in the original fitting (Sangster and Stoneham 1981).

4.5 Twist Grain Boundaries of MgO

The other class of grain boundary is the twist grain boundary which for this work are formed by bring together two surfaces, the (001) and the $(00\bar{1})$ and then rotating one surface with respect to the other around the [001] axis perpendicular to the surface plane. The twist boundaries to be formed share a common face and can therefore be considered as being composed of a pair of two dimensional square lattices. In order to find angles of good coincidence we can use a two dimensional version of CSL theory (Mykura et al. 1980) in the following way. To produce a two dimensional coincident lattice one square lattice is rotated with respect to the second about the [001] axis until two or more lattice sites are coincident in both grains. If the lattice parameters of grain 1 and 2 are a_1 and a_2 the coincidence is given by

$$\left(\frac{a_1}{a_2}\right)^2 = \frac{k^2 + l^2}{m^2 + n^2} \qquad 4.1$$

where k, l, m and n are any integers (Figure 4.10). The rotation angle for this coincidence is given by

$$\theta = \theta_1 \pm \theta_2 = \tan^{-1}\left(\frac{l}{k}\right) \pm \tan^{-1}\left(\frac{n}{m}\right) \qquad 4.2$$

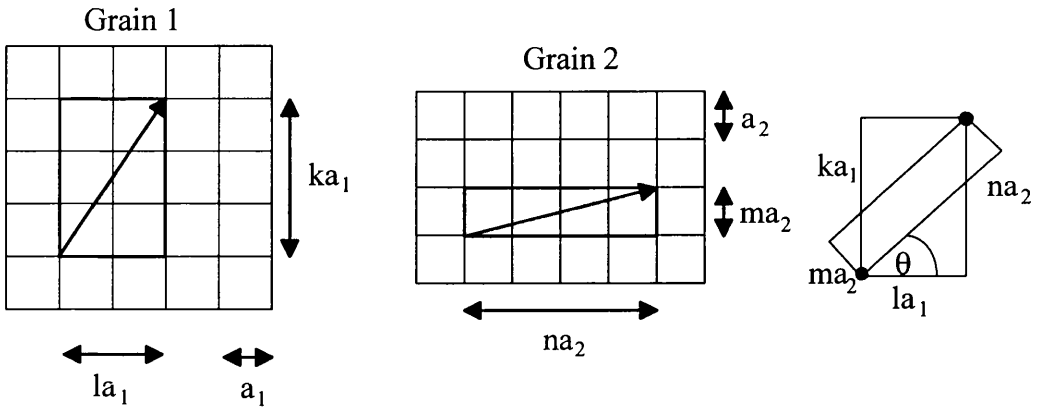

Figure 4.10. Schematic of two grains with lattice parameters a_1 and a_2 forming a coincident site boundary with angle θ.

Generally for two dimensional square CSLs two angles will occur for a given set of l, k, m and n. However, the lattices have fourfold symmetry so positive and negative θ give equivalent interfaces and thus only misorientation up to 45° need to be considered since the lattice will have mirror planes. The inverse coincidence density, Σ^p, for grain 1 and 2 is given by

$$\sum_1^p = m^2 + n \qquad 4.3$$

$$\sum_2^p = k^2 + l^2 \qquad 4.4$$

where Σ^p is used to indicate that this represents a two dimensional planar coincidence rather than a three dimensional one (Gao et al. 1988). The coincidence density ($1/\Sigma^p$) is the fractional number of ions at the grain boundary in grain 1 which are coincident with ions in grain 2. Generally exact coincidence will only occur if equation 4.1 is exactly satisfied, however for MgO this is the case since $a_1=a_2$.

Previous simulations have been carried out on twist grain boundaries of MgO (Sayle et al. 1995) however the aim of their inclusion in this work is to model the effect of pressure and temperature upon their structure and energies. Initially the boundaries were simulated using static lattice energy minimisation in order to generate suitable structures. The boundaries were formed from the (001) and (00$\bar{1}$) surfaces and were rotated around the [001] direction. Four angles of misorientation were considered, 16.25°, 22.62°, 28.07° and 36.87°, since these are the four most commonly observed in experimental studies (Mykura et al. 1980). Energy minimisation of the full density structures determined that they were unstable with respect to cleaving to form the free surfaces. This was due to some of the coincident sites containing identical ions in close proximity. To overcome this a reduced density structure was formed by creating stoichiometric vacancies at the grain boundary to remove the near coincident ions of the same type. The ions to be removed were identified by calculating the Madelung energies of the ions at the boundary region before the relaxation of the cell; those with the most unstable Madelung energies were selected for removal. Minimisation of the reduced density structures was then carried out. The resulting minimised structures are given in fig 4.11-14 and show good comparison to equivalent twist boundaries calculated in NiO (Duffy 1986).

Each of the twist grain boundaries consists of arrays of squares, hexagons and octagons at the interface. In the case of the 16.25° boundary the octagons are separated from each other by a double layer of edge sharing hexagons with MgO squares filling the remaining space. The neighbouring layers above and below this layer show twist distortions from the bulk structure at points adjacent to the octagons in the boundary layer (figure 4.11). The 22.62° boundary has octagons which share an edge with a hexagon and a cross formation of squares. The distortion in the neighbouring layers is

negligible by the second layer (figure 4.12). The 28.07° boundary shows the greatest deviation from the bulk structure. Each of the octagons is surrounded by hexagons and squares however four hexagons surround a square which is at 45° orientation compared to the other squares. Again there is distortion in the neighbouring layers which is negligible by the second layer (figure 4.13). The 36.87° boundary has the simplest structure with each octagon edge sharing with four others and with four squares. There is practically no distortion in the neighbouring layers (figure 4.14).

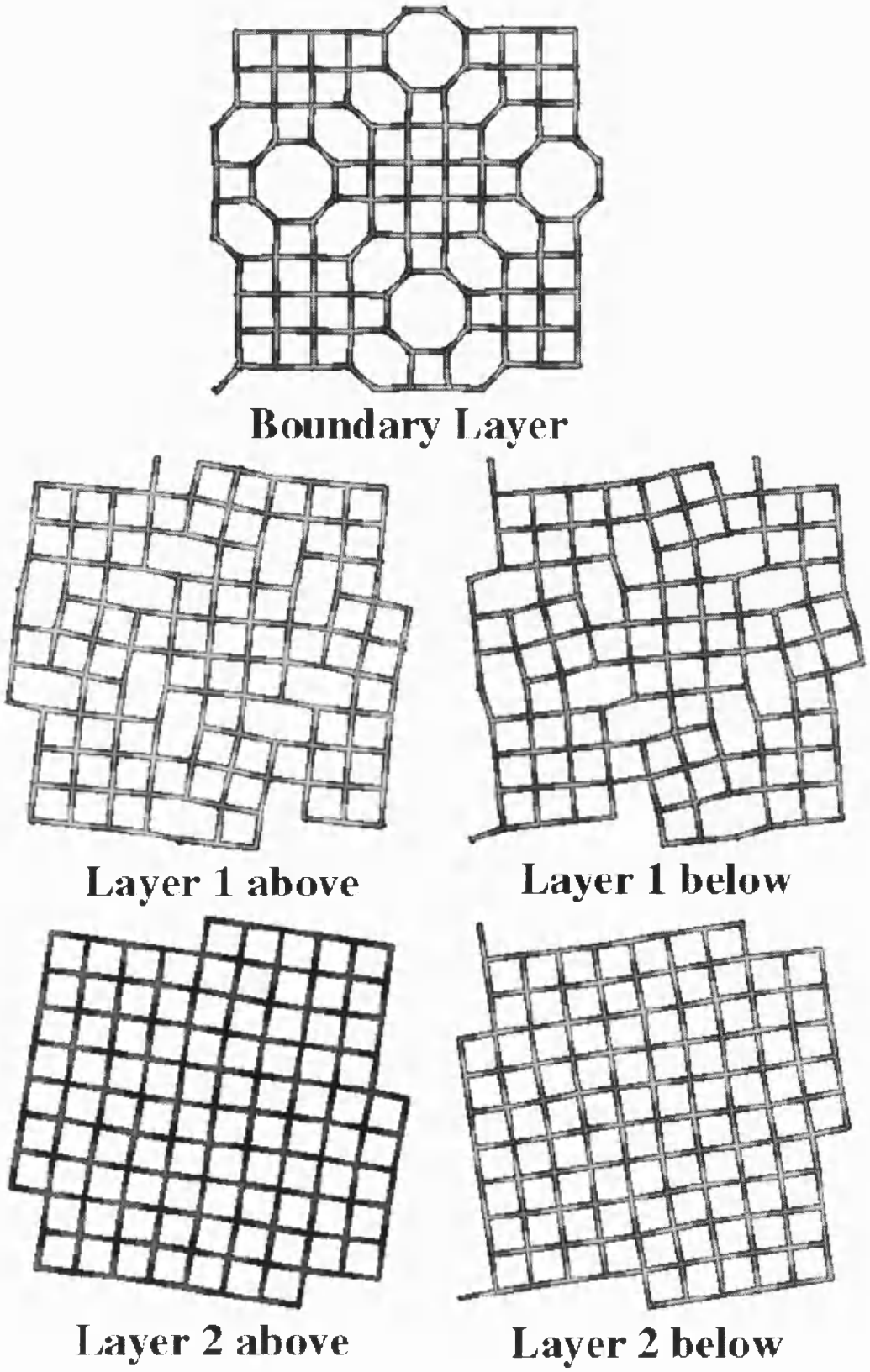

Figure 4.11. The relaxed structure of the 16.25° boundary twist grain boundary.

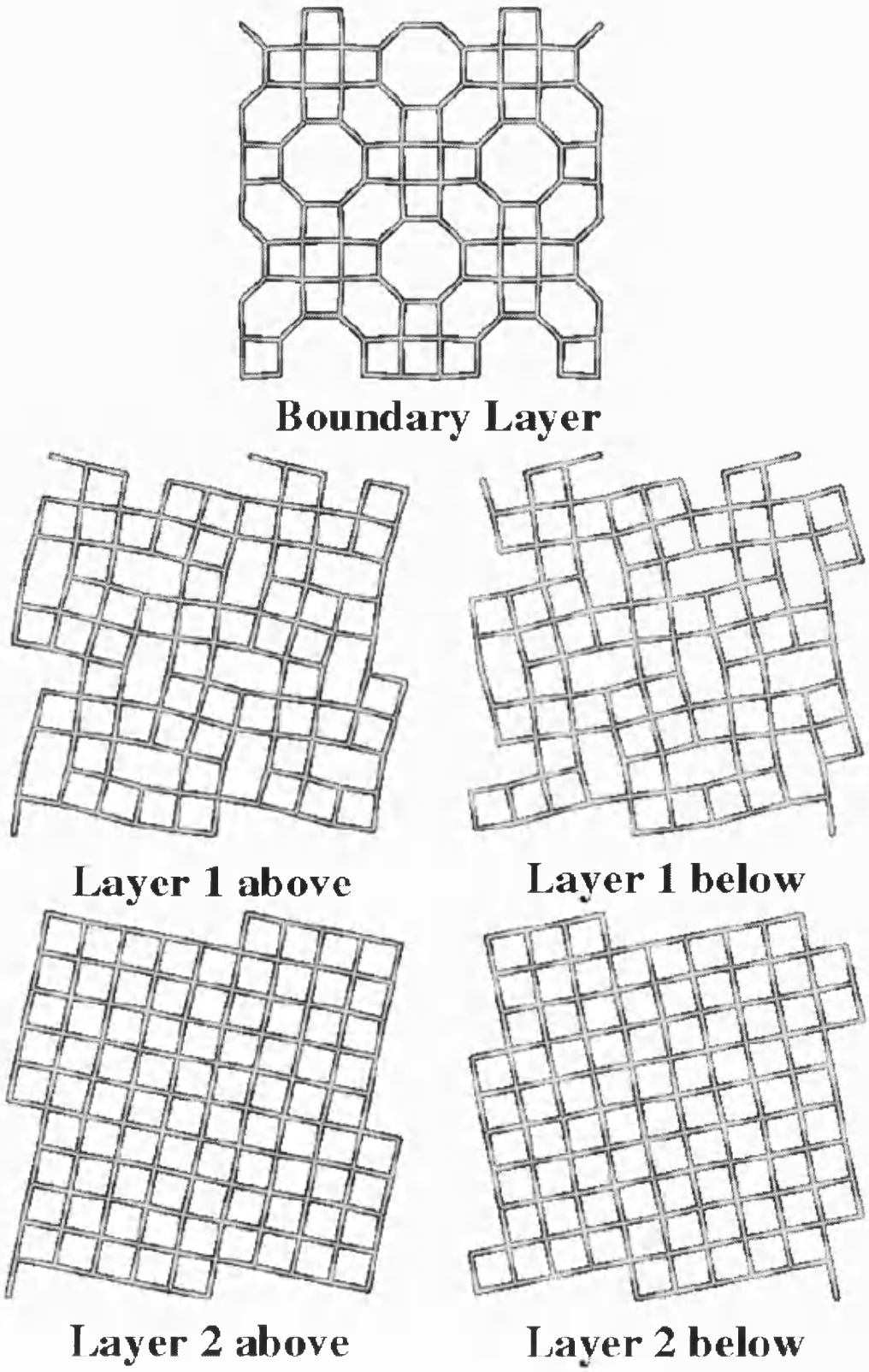

Figure 4.12. The relaxed structure of the 22.62° twist grain boundary.

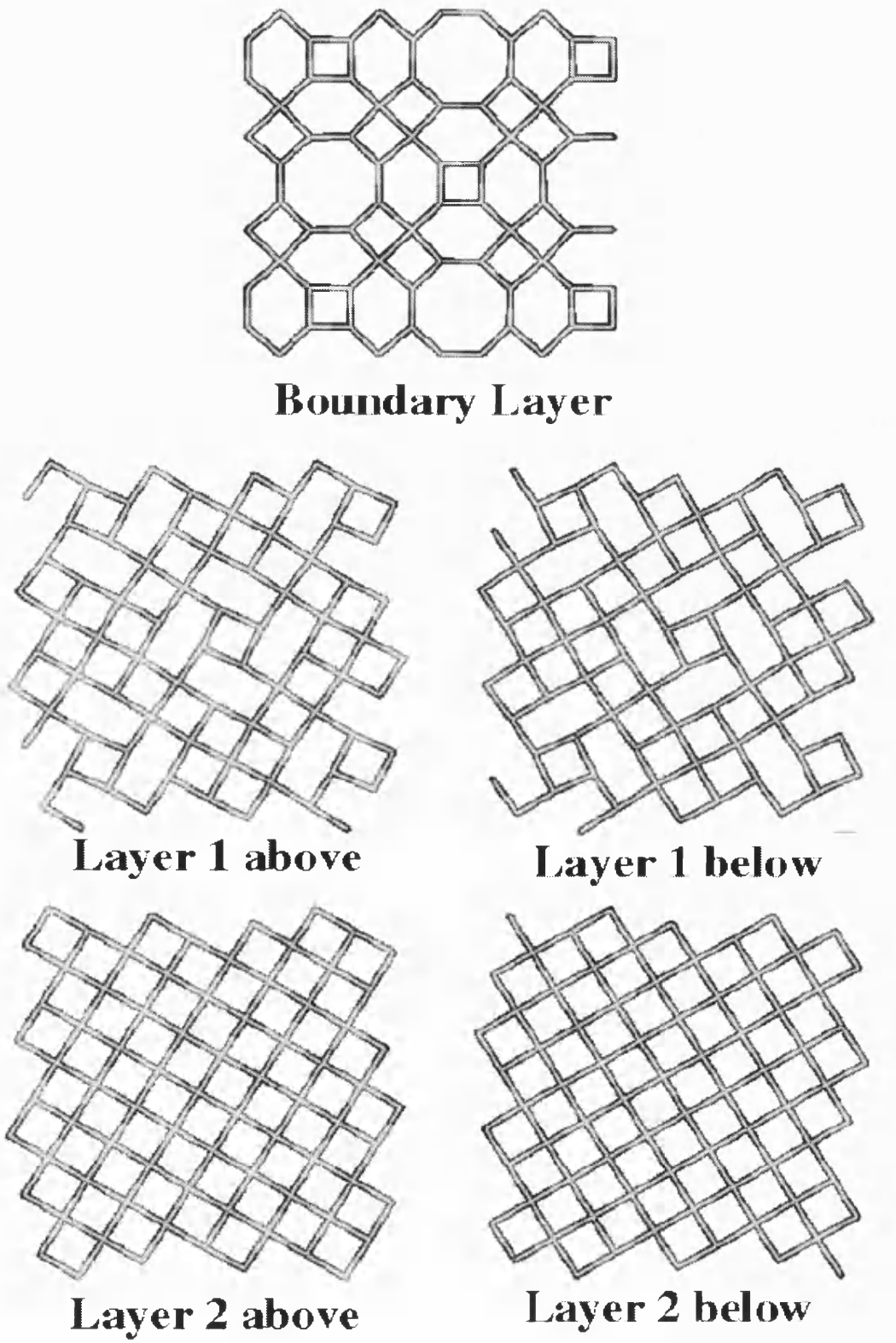

Figure 4.13. The relaxed structure of the 28.07° twist grain boundary.

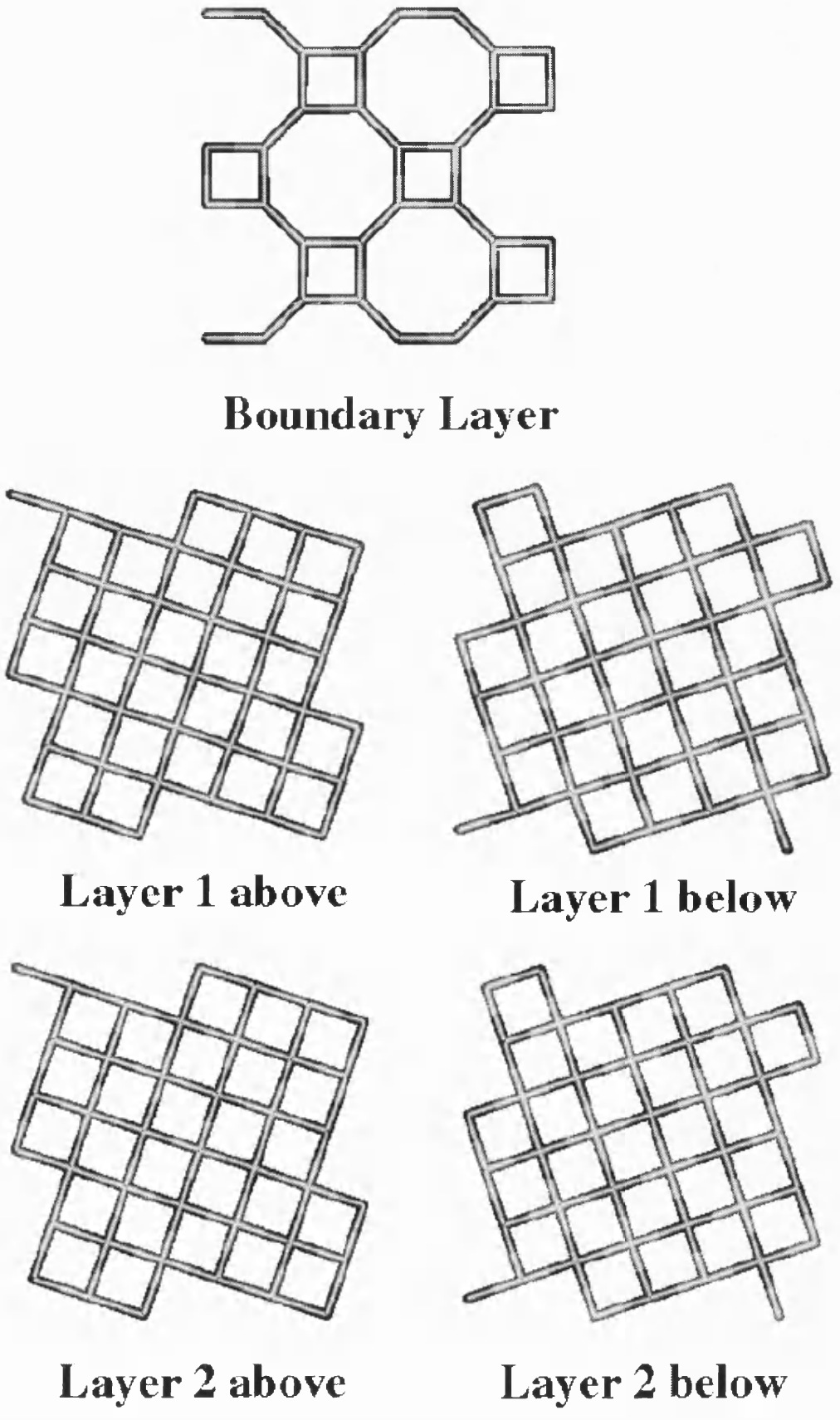

Figure 4.14. The relaxed structure of the 36.87° twist grain boundary.

Since the grain boundaries calculated are reduced density structures the following scheme is used to calculate the formation energy. For simplicity a cell containing 200 ions is shown.

$$Mg_{100}O_{100(s)} \xrightarrow{\gamma_b} Mg_{99}O_{99(gb)} + MgO_{(s)}$$

Thus the grain boundary formation energy (γ_b) is given by

$$\gamma_b = E_{Mg_{99}O_{99}(gb)} + E_{MgO} - E_{Mg_{100}O_{100}} \qquad 4.5$$

Similarly, the reduced density structures mean that two approaches to calculating the adhesion energy can be adopted which are summarised in figure 4.15.

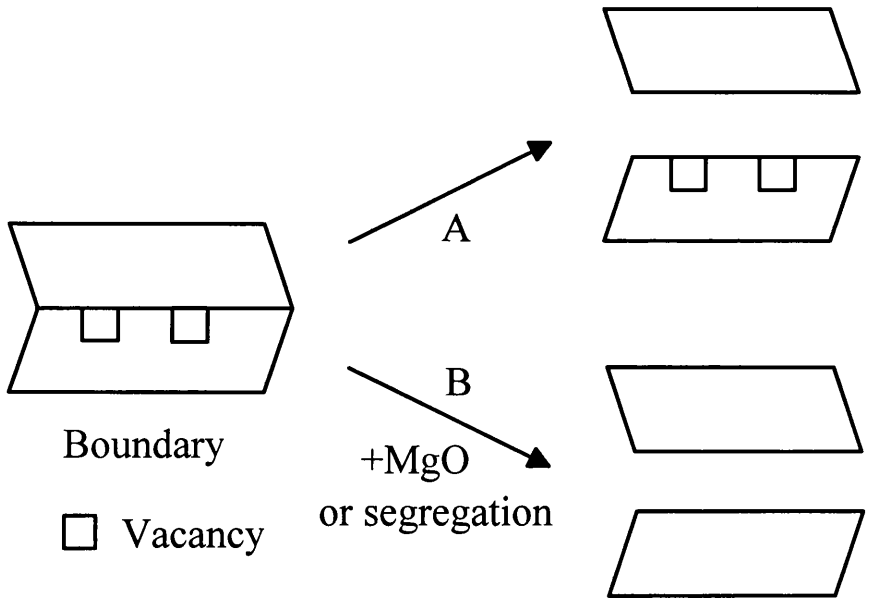

Figure 4.15. Schematic representation of the two surfaces that can formed by breaking a reduced density boundary

In method A the grain boundary breaks to form two surfaces where one is pure and the second contains the stoichiometric vacancies required to form the grain boundary. In this case the adhesion energy is given by

$$\gamma_{ad} = \frac{(E_{psf} + E_{dsf}) - E_{gb}}{A} \qquad 4.6$$

where E_{psf} and E_{dsf} are the energies of the pure and defective surface blocks, E_{gb} is the energy of the grain boundary block and A is the area of the boundary. In method B the vacancies are removed by dissolution into the crystal and the boundary is split to form two pure surfaces. A scheme similar to that for the formation energy can be used to determine the adhesion energy.

$$Mg_{99}O_{99(gb)} + MgO_{(s)} \xrightarrow{\gamma_{ad}} 2\left(Mg_{50}O_{50(surf)}\right)$$

Thus the grain boundary adhesion energy (γ_{ad}) is given by

$$\gamma_{ad} = 2E_{Mg_{50}O_{50}(surf)} - E_{MgO} - E_{Mg_{99}O_{99}(gb)} \qquad 4.7$$

Angle (°)	Σ^p	Formation Energy (Jm^{-2})	Pure Surface Energy (Jm^{-2})	Defective Surface Energy (Jm^{-2})	Adhesion Energy (Jm^{-2})	
					Pure	Defective
16.25	25	1.86	1.16	1.55	0.47	0.86
22.62	13	1.97	1.16	1.75	0.36	0.95
28.07	17	2.30	1.16	1.73	0.02	0.59
36.87	5	1.84	1.16	1.89	0.51	1.24

Table 4.6. Calculated formation and adhesion energies for twist grain boundaries of MgO, where the adhesion energy is either with respect to a perfect bulk crystal or with respect to cleaving a defective boundary (leaving defects at the surface).

Table 4.6 gives the calculated grain boundary formation and adhesion energies for the twist grain boundaries. The formation energies ascend in the order Σ^p 5<25<13<17 whilst conversely the adhesion energies with respect to the formation of pure surfaces decrease. Both adhesion energies, with respect to the pure and defective surfaces, are a direct balance between the formation energy of the boundary and the surface energies for the surfaces which are formed upon breaking the boundary in two, i.e.

$$\gamma_{ad} = \gamma_s^1 + \gamma_s^2 - \gamma_b \qquad 4.8$$

where γ_{ad} is the adhesion energy, γ_s^1 and γ_s^2 are the surface energies of surfaces 1 and 2 respectively and γ_b is the grain boundary formation energy. There does not appear to be any relationship between the formation and pure adhesion energies and the coincidence density.

Experimentally the stability of these grain boundaries has been measured by calculating the distribution of misorientation angle of MgO smoke cubes adsorped onto an MgO substrate (Mykura et al. 1980). Comparison of the calculated adhesion energies for defective surfaces to the frequency of occurrence from experiment showed good agreement with the 36.87° boundary seen to be the most frequent whilst of the four boundaries modelled the 28.07° boundary was observed least frequently in agreement with our calculations.

The differences in the formation energy can partially be rationalised in terms of the structure. The most stable boundary, the 36.87°, has no distortion in the neighbouring layers and a high coincidence. The 16.25° boundary has a lower coincidence but the structure contains large section of square lattice forming a bulk-like structure in the boundary layer. In the less stable 22.62° and 28.07° boundaries this square lattice arrangement becomes smaller. Thus the formation energies seem to be a balance between the coincidence and the degree of distortion from bulk structure at the boundary which follows the coincidence to some degree.

4.6 Conclusions

This chapter has demonstrated the methods developed to generate tilt and twist grain boundaries using MgO as an example. We have shown that the potentials used have been consistent with each other and with bulk experimental data and have successfully applied them to the simulation firstly of the surfaces and then to the grain boundaries of MgO.

The surface calculations showed that as expected the {100} surface was the most stable leading to a cubic morphology. For surfaces of index (h10) the surface

energy increased as the angle of the cut increased. Calculations on the [001] tilt grain boundaries showed that the formation energy increased with increasing index to a maxima for the {410} boundary before decreasing again as the index increased further. This was attributed to the change in density of cross links across the boundary. Minimisation of the twist grain boundaries required the creation of reduced density structures in order to stabilise the boundaries. The trend in the resulting adhesion energies showed reasonable agreement with the experimentally observed occurences of these boundaries.

The work in this chapter has been carried out at 0 GPa and without the inclusion of temperature. In the next chapter we will present calculations on the [001] tilt and the twist grain boundaries as a function of pressure and temperature in order to determine their effect on the structure and energies.

5 The Effect ofTemperature and Pressure on MgO Grain Boundaries.

5.1 Introduction

Pressure and temperature has a large effect upon mineral properties, for example by causing phase transitions (Poirier 1991) and altering diffusion properties and mechanisms (Anderson 1989). However the effect of pressure and temperature on grain boundary structures and stability has not previously been calculated. In chapter four the structure and energies of tilt and twist grain boundaries were calculated via static energy minimisation and therefore did not include temperature. In this chapter we consider the effect of temperature and pressure in order to determine their effect on the structure and properties of the grain boundaries described in chapter 4. Initially, lattice dynamics of tilt boundaries will be considered followed by the use of Molecular Dynamics (MD). The advantage of MD is that the melting of the grain boundary can also be studied. Finally, lattice dynamics is applied to the calculation of twist boundaries.

5.2 [001] Symmetric tilt grain boundaries

Four of the boundaries simulated in chapter 4 were chosen for free energy minimisation (the {110}, {210}, {310} and {410}). Three dimensional unit cells were generated using the method described in section 3.7.2, care was taken to ensure that the two grain boundaries formed were identical so that the energy calculated would be for a single boundary as opposed to an average energy of two different boundaries. In addition, we insured that the distance between each grain boundary was large enough

to ensure that the energy of the cell had converged and there were no boundary-boundary interactions by calculating the boundary formation energy for unit cells with increasing inter boundary distances. A distance of approximately 22Å was required for convergence.

The computer code PARAPOCS (Parker and Price 1989) was used to perform free energy minimisation at a series of pressures and temperatures using the Sangster-Stoneham potential (Sangster and Stoneham 1981) to describe the interactions. Initially pressures of 0, 10, 20, 30 and 40 GPa and temperatures of 300, 600, 1000 and 1200 K were chosen to provide a sufficiently large range to investigate the effect of temperature whilst ensuring that the quasi-harmonic approximation did not break down at any pressure. Various properties of the grain boundaries were calculated including the structure, and formation properties such as static and vibrational lattice energies, PV term, free energy, entropy and zero point energy. Each of these properties are defined in the same manner as the grain boundary formation energy (i.e. difference in energy between the grain boundary and the same number of MgO units in the perfect crystal; see section 3.7.1).

The first issue was to determine the number of points in the Brillouin zone that are required to ensure convergence. Tests were carried out using 1 and 8 points. The results showed that only one point at (0.25, 0.25, 0.25) in the Brillouin zone was needed for convergence. For example, the free energies of the cell for the {310} boundary for 1 and 8 points were -5848.88 and -5848.90 eV, a difference of only 0.02 eV. However for each of the grain boundaries a zone centre (k=0) phonon calculation was performed at each pressure and temperature in order to check for imaginary frequencies which would indicate a dynamical instability and a likely displacive phase

transition. The immediate result of this was that the {110} tilt grain boundary was found to be dynamically unstable at 0 GPa and 0 K, an effect which had not been detectable using static energy minimisation. Animation of this imaginary mode showed that the simulation cell sheared parallel to the grain boundary which resulted in bulk MgO (as this boundary can also be considered a stacking fault). Each of the other grain boundaries was found to be stable under these conditions. This structural transition will be discussed in more detail in section 5.2.6.

One important result of the initial simulations was that temperature had little effect upon the structure or formation energies of the boundaries due to a very small change in vibrational entropy of formation for each boundary. For example, the {210} tilt grain boundary formation free energy at 0 GPa decreased from 1.55 Jm^{-2} at 300 K to 1.50 Jm^{-2} at 1200 K. This corresponded to a change in the formation entropy from $5.5x10^{-5}$ Jm^{-2} to $1.8x10^{-5}$ Jm^{-2}. Thus, for brevity, only the results at a constant temperature of 600 K will be quoted in the following sections.

5.2.1 The {210} symmetric tilt grain boundary

In contrast to the effect of temperature, pressure had a large effect by causing a significant increase of the formation free energy with pressure. The {210} bondary was affected the least of the three boundaries with an increase in formation free energy from 1.53 Jm^{-2} at 0 GPa to 2.50 Jm^{-2} at 10 GPa (see table 5.1) and a slight increase in formation lattice energy (figure 5.1a). The dilation of the grain boundary (i.e. the change in volume per unit area) decreased as the pressure increased from 1.00 Å at 0 GPa to 0.84 Å at 10 GPa, and the formation PV term increased from 0.00 Jm^{-2} (at 0 GPa) to 0.84 Jm^{-2} at 10 GPa. Thus the decrease in volume was outweighed by the

increase in pressure resulting in a large contribution to the free energy. At 20 GPa an imaginary frequency was again observed at the Brillouin zone centre implying a displacive phase transition which will be discussed in more detail in section 5.2.6. The data for this pressure has been included however for completeness.

Pressure (GPa)	{210}	{310}	{410}
0	1.53	1.71	1.78
10	2.50	2.79	2.76
20	3.35	3.52	3.43
30	-	4.20	4.03
40	-	4.81	4.59
60	-	5.84	5.55

Table 5.1. Formation Gibbs free energies as a function of pressure for symmetric tilt grain boundaries of MgO.

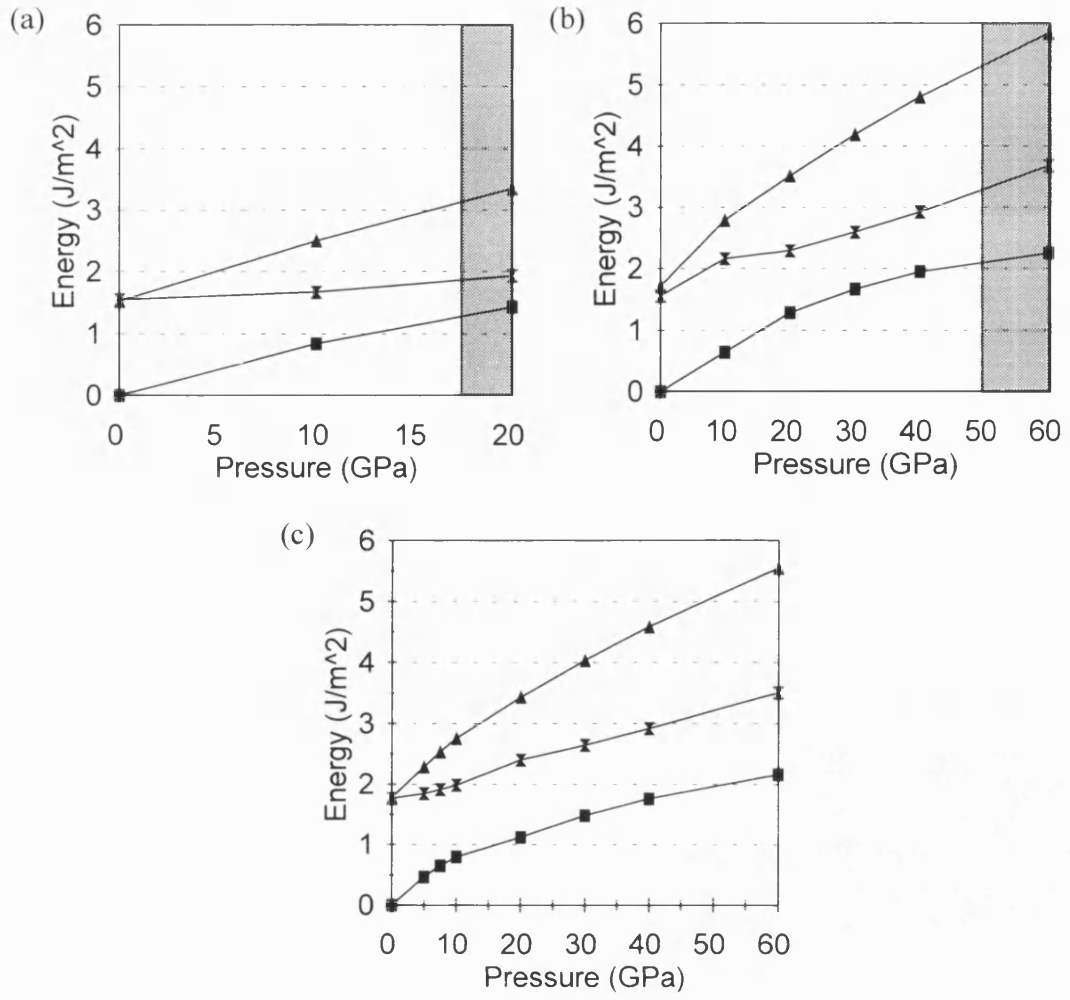

Figure 5.1. The energies of formation for a) the {210}, b) the {310} and c) the {410} symmetric tilt boundaries as a function of pressure at 600 K. Squares represent PV, hourglasses the static lattice energy and triangles the Gibbs Free energy. Shaded regions show where imaginary frequencies were calculated.

5.2.2 The {310} symmetric tilt grain boundary

The {310} boundary also showed an increase in formation free energy with pressure from 1.71 Jm^{-2} at 0 GPa to 4.81 Jm^{-2} at 40 Gpa (table 5.1), however there was

also a change in gradient for the formation lattice energy at 10 GPa as shown in figure 5.1b. No imaginary mode was detected at this pressure in the zero point phonon calculations but a plot of the dilation as a function of pressure revealed a discontinuity as shown in figure 5.2.

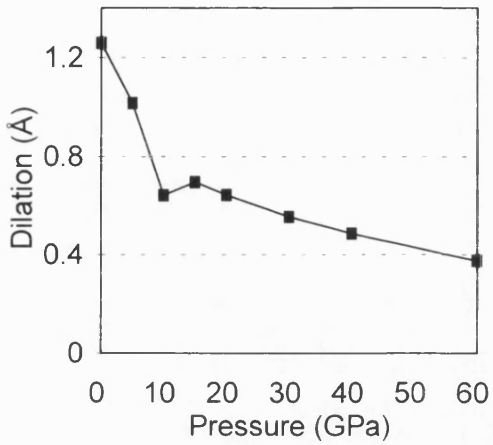

Figure 5.2. Dilation of the {310} symmetric tilt grain boundary as a function of pressure.

To determine the cause of this the distances across the boundary at three points, denoted *a*, *b* and *c* in fig 5.3a were plotted as a function of pressure and are given in figure 5.3b. Examination of these lengths revealed that at approximately 10 GPa the distance *b* decreased as the two sides of the boundary drew together at this point to form the structure shown in figure 5.3c and it is this change in structure that caused the drop in the rate of change in formation lattice energy. As the pressure increased above 10 GPa, the grain boundary retained its general shape but the distance across the boundary slowly decreased.

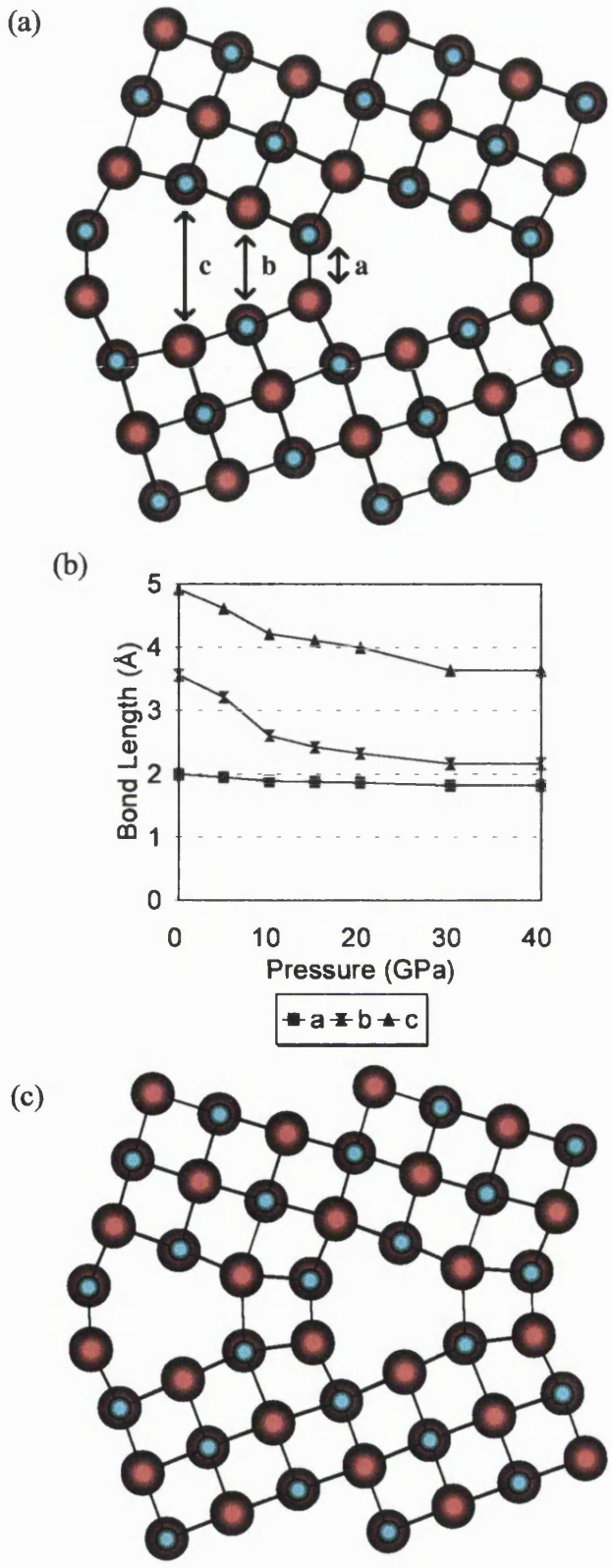

Figure 5.3. a) Structure of the {310} symmetric tilt grain boundary illustrating the cross boundary distances plotted in b) as a function of pressure. c) Structure of the {310} symmetric tilt boundary at 10 GPa and 600 K

5.2.3 The {410} symmetric tilt grain boundary

The {410} showed the same behaviour as the {310} boundary, where the formation lattice energy and formation PV term generally increased (table 5.1, figure 5.1c) and a discontinuity in the distance across the boundary. Four boundary distances (see figure 5.4a) were measured as a function of pressure and these are plotted in figure 5.4b. The grain boundary width reduced continuously up to approximately 10 GPa with the ions at the *b* position drawing much closer together. However, at approximately 20 GPa there was a discontinuity in boundary width and formation lattice energy when the next pair of ions in the boundary at the *c* position also drew closer together over a smaller pressure range. Thus by 30 GPa there were effectively three cross-linking interactions per unit cell as shown in figure 5.5 which resulted in a higher density structure.

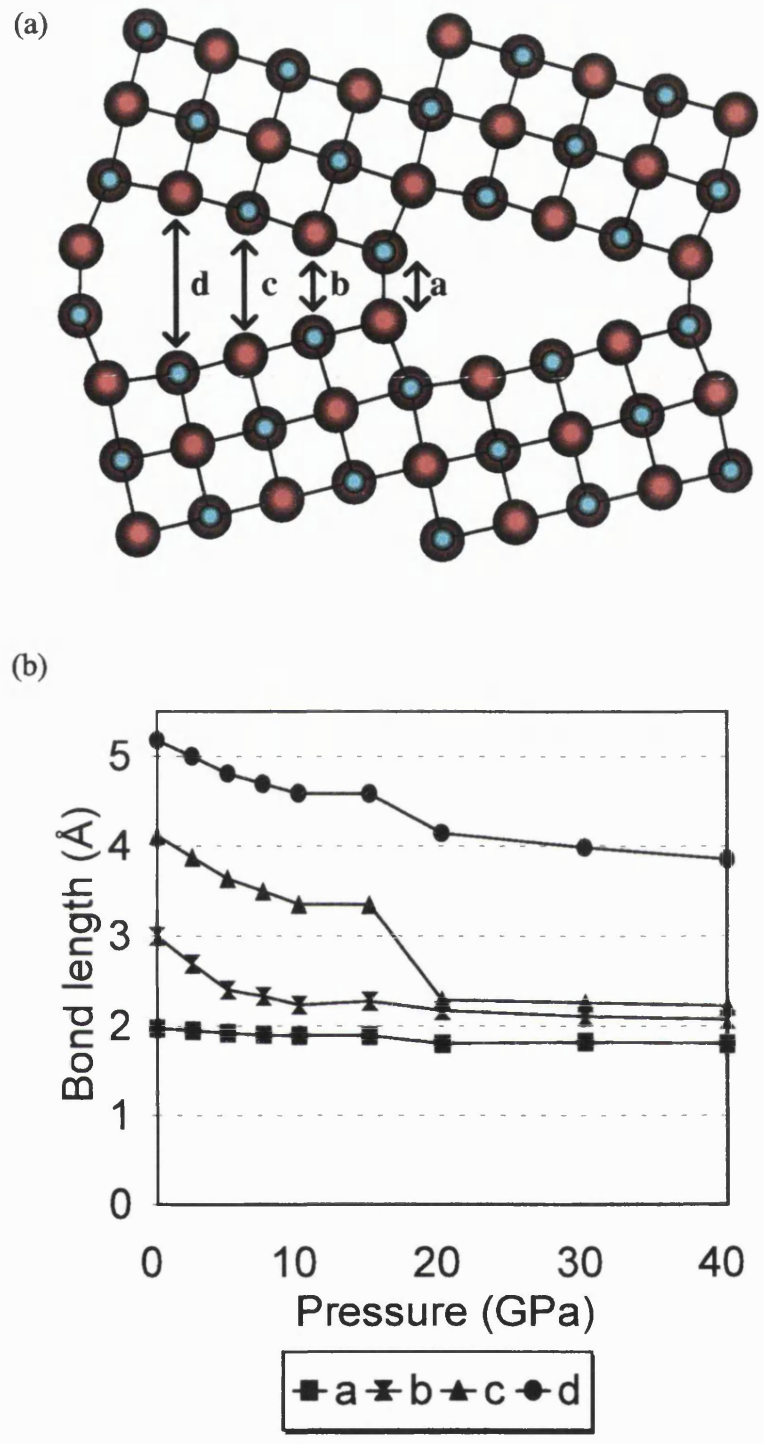

Figure 5.4. a) Structure of the {410} symmetric tilt grain boundary illustrating the cross boundary distances plotted in b) as a function of pressure.

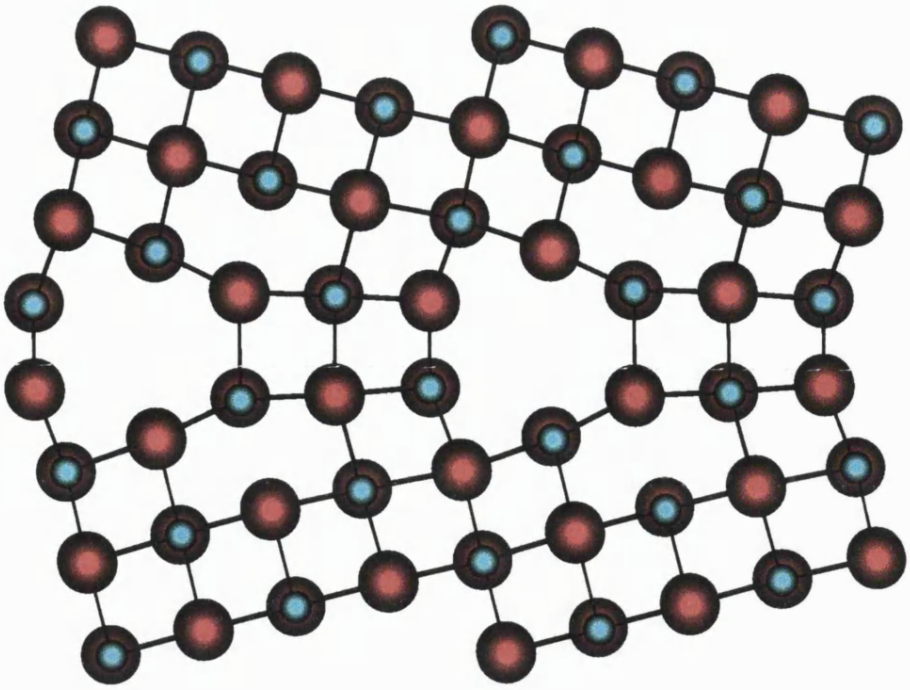

Figure 5.5. The minimised structure of the {410} symmetric tilt grain boundary at 600 K and 30 GPa.

5.2.4 Reversibility of structural transition

In order to examine the reversibility of the high pressure transitions of the {310} and {410} grain boundaries the pressure was reduced from 30 to 0 GPa in steps of 10 GPa. The {310} boundary relaxed back to its original 0 GPa structure, indicating that the high pressure structural transition was reversible.

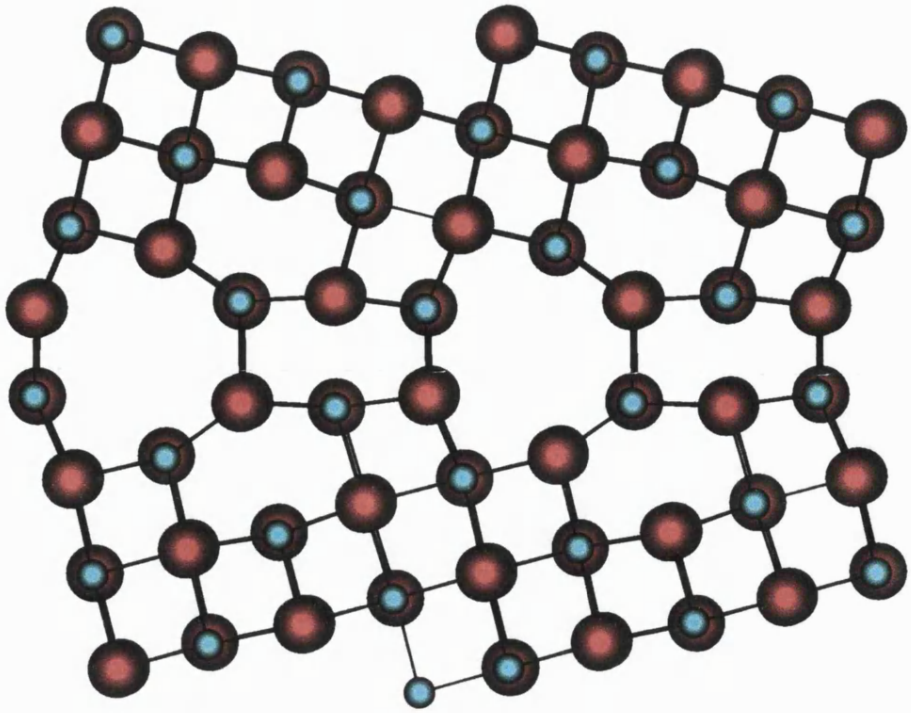

Figure 5.6. The minimised structure of the {410} symmetric tilt grain boundary at 600 K and relaxed back to 0 GPa

In the case of the {410} boundary the structure retained its high pressure form as shown in figure 5.6 but with a slight increase in the cross boundary distance at point *b* from 2.11 Å at 30 GPa to 2.44 Å at 0 GPa. The new 0 GPa structure was more compact with a dilation of 0.82 Å compared to 1.20 Å for the initial low pressure structure; however, the formation free energy increased to 2.00 Jm^{-2} from 1.79 Jm^{-2}, implying that it is only metastable with respect to the original boundary. In order to determine whether this irreversible structural transition was the rule or the exception we considered higher index boundaries. Figure 5.7 shows the distances across the grain boundary for both the {510} and {610} symmetric tilt grain boundaries as a function of pressure. In both cases two discontinuities in the boundary distance were found, at approximately 5 and 20 GPa for the {510} and 7.5 and 30 GPa for the

{610}. This resulted in a total of four crosslinks for the {510} and five for the {610} boundary at 30 GPa (see figure 5.8). The structures were then allowed to relax back to 0 GPa and again almost no change in the structures occured. The new {510} structure was more compact than the original 0 GPa structure with a formation dilation of 0.72 Å compared with 1.18 Å and the formation free energy slightly higher at 2.05 Jm^{-2} compared to 1.78 Jm^{-2}. This again implies that the structure was metastable, although kinetic energy may allow a return to the original structure depending on the size of the energy barriers. The new {610} structure was also more compact with a dilation of 0.72 Å compared with 1.03 Å. However, the new higher density structure formation energy of 1.59 Jm^{-2} compared to 1.72 Jm^{-2} for the initial 0 GPa structure indicated that it will be preferentially formed even at low pressure.

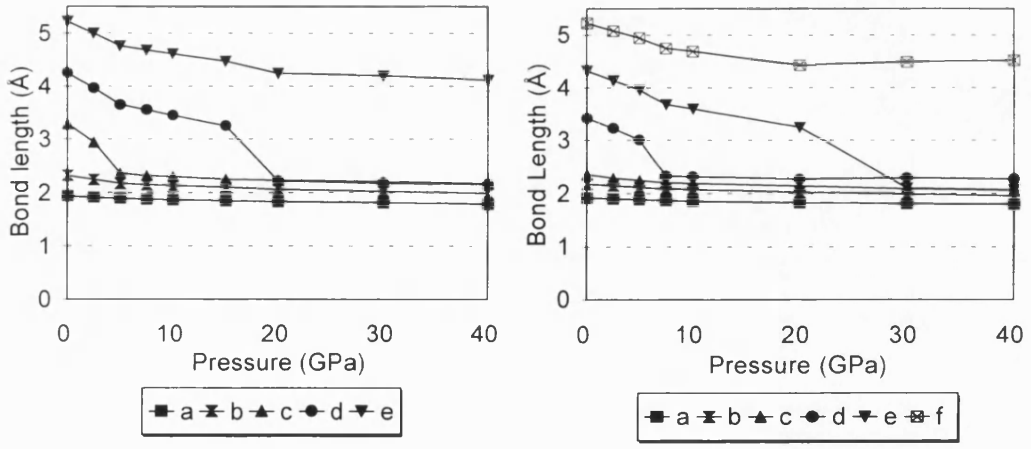

(a) (b)

Figure 5.7. Cross boundary distances as a function of pressure for a) the {510} and b) the {610} symmetric tilt grain boundaries.

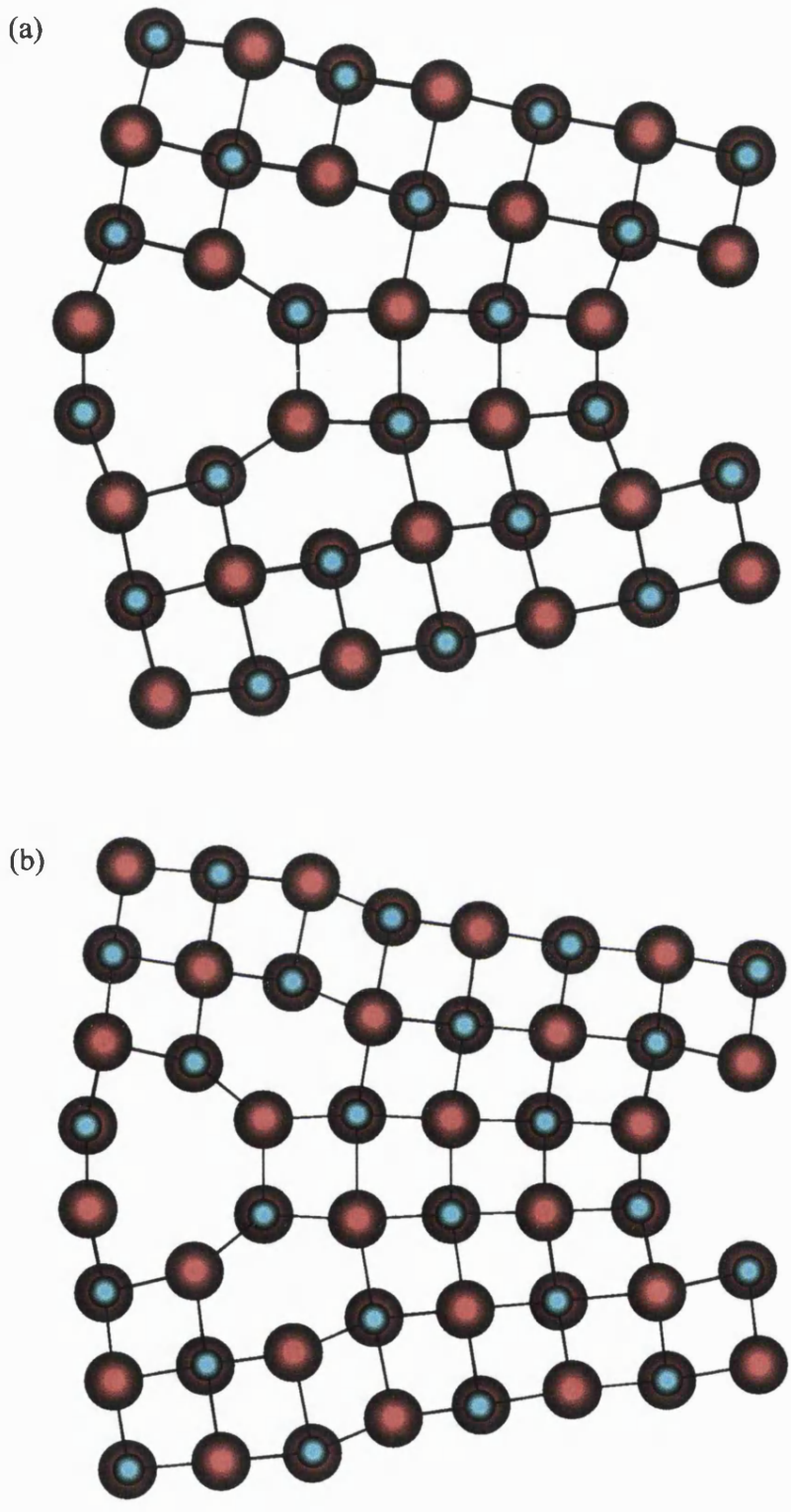

Figure 5.8. The minimised structure of the a) {510} and

b) {610} symmetric tilt grain boundaries at 30 GPa and 600 K.

5.2.5 MolecOular Dynamics Simulation of Structural Transition

We examined the thermal stability of the metastable structures predicted by performing lattice dynamics and molecular dynamics calculations on both the {410} and {510} symmetric tilt grain boundaries within the isothermal-isobaric (NPT) ensemble. The boundaries were calculated for 10 ps scaling and 10 ps data collection and the average structures at this pressure were identical to those calculated using lattice dynamics. The formation enthalpy for the {410} boundary from MD was 1.79 Jm^{-2} compared to the Lattice Dynamics value of 1.73 Jm^{-2} for the Gibbs free energy of formation at 0 GPa and 300 K whilst the {510} boundary using MD gave 1.83 Jm^{-2} compared to 1.78 Jm^{-2} from LD.

The pressure was then increased to 40 GPa at the same temperature. Both boundaries compressed to form the high pressure structures calculated from lattice dynamics (see figures 5.6a and 5.8a). The {410} boundary had a formation enthalpy of 4.59 Jm^{-2} compared to the Gibbs free energy of 4.85 Jm^{-2} whilst the {510} had an enthalpy of 3.04 Jm^{-2} compared to 2.76 Jm^{-2} for the free energy.

Upon releasing the pressure back to 0 GPa at 300 K it was found that both structures immediately reverted back to their original low pressure structures, unlike the lattice dynamic calculations. This suggests that although there was an activation barrier for this transition, which lattice dynamics was unable to overcome, it was small with respect to kT.

5.2.6 Examination of imaginary phonon modes

Zone centre phonon calculations have found that the {110} boundary was dynamically unstable at 0 GPa and the {210} unstable at 17 GPa. Further simulations

were required on the {310} and {410} boundaries at pressures above 40 GPa to determine whether these boundaries would also become unstable as a result of pressure. Earlier calculations demonstrated that temperature had little effect upon the structure or energies of the boundaries therefore only one temperature, 600 K, was chosen. Above 40 GPa the free energies of both boundaries continued to increase as the pressure increased however the rate of this increase gradually reduced. Both boundaries showed a softening of an optical mode in the [001] direction from phonon dispersion plots as shown in figure 5.9a for the {310} boundary. Animation of this imaginary mode showed that the boundaries sheared about an [001] axis as shown for the {310} boundary in figure 5.9b.

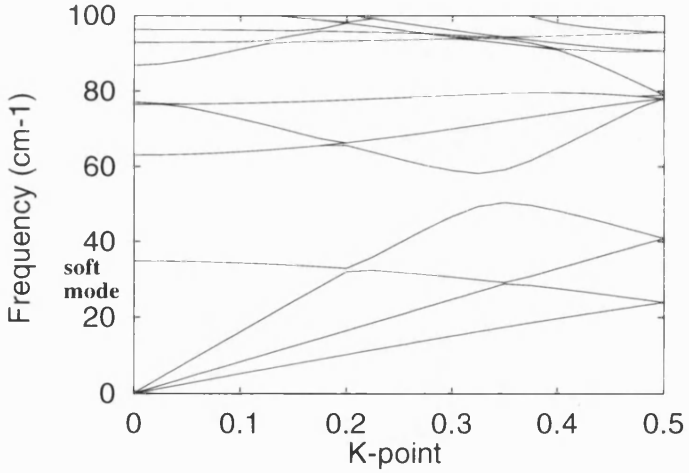

Figure 5.9a. Phonon dispersion curve for the {310} tilt grain boundary showing the softening phonon mode in the [001] direction.

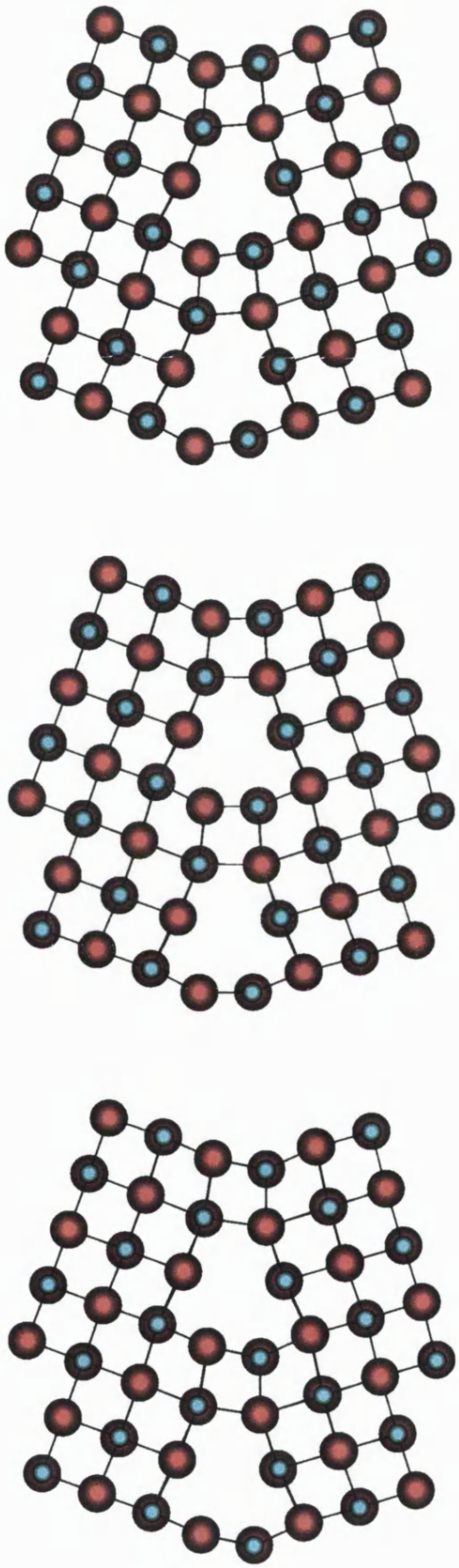

Figure 5.9b. Vibration of the imaginary mode in the {310} symmetric tilt grain boundary of MgO.

This mode became imaginary in the {310} boundary at approximately 48 GPa whilst for the {410} boundary this occured at approximately 64 GPa. The distribution in the Brillouin zone of the soft optical mode suggested the presence of a shear similar to those found for the {110} and {210} boundaries. Thus increasing the index of the boundary (and therefore increasing density of crosslinking interactions per unit area) increased the pressure required to shear the boundary. Note that with the static simulations presented in chapter 4 the crosslink density decreased with increasing index up to the {410} for the (h10) boundaries however the structural transitions described in section 5.2.2 to 5.2.4 result in a greater density of crosslinks than for the low pressure boundaries.

MD has proven itself to be a good complementary technique for studying structural transitions as a function of pressure on grain boundaries. Therefore MD simulations were performed on the {210}, {310} and {410} symmetric tilt grain boundaries at the pressures where the imaginary modes were calculated to occur from the lattice dynamics; i.e. 17, 48 and 64 GPa respectively. In each case the boundary sheared as a result of the pressure and formed a structure which was very similar to the {310} asymmetric boundary presented in chapter 4. This structure was previously suggested for NiO, isostructural with MgO, by Harding et al. (1989). The calculations presented in chapter 4 suggested that at 0 GPa the asymmetric boundary was less stable than the symmetric boundary, although the MD simulations presented here suggest that at higher pressures the asymmetric boundary may be the more stable of the two. This may also help explain why this asymmetric structure is accessible to experiment (Merkle 1987a) because the preparation conditions on the boundary may be sufficiently harsh to set up stresses that help form this boundary prior to quenching.

5.3 Effect of Pressure on Asymmetric Grain Boundaries

The {210}, {310} and {410} asymmetric boundaries were modelled at a range of pressures (up to 100GPa) at 600 K. The formation free energies (table 5.2), lattice energies and PV terms are plotted for each of the grain boundaries in figure 5.10. In each case the free energy increased with increasing pressure however the rate of change of energy was lower than that found for the symmetric tilt boundaries. This was primarily due to the formation PV term which for symmetric boundaries increased at a greater rate due to the larger dilation upon formation of the boundary. As the pressure increased above 40 GPa the rate of change of the PV term decreased as the compressesion of the structure counterbalanced the increasing pressure. The difference in the rate of change of free energy results in the asymmetric boundaries becoming more stable than the symmetric boundaries at high pressures. Comparison with the free energies of the symmetric boundaries showed that this occured at approximately 10 to 20 GPa.

In each of the three asymmetric boundaries studied there is a discontinuity in the lattice energy and PV term which affects the free energies at very high pressures. Examination of the zone centre phonon frequencies for each boundary revealed that as the pressure increased towards the point at which the discontinuity occurred one phonon frequency decreased; for the {210} the frequency became imaginary at 70 GPa, the data for this pressure has been included in fig 5.10a for completeness. After the discontinuity the phonon frequency increased again. As figure 5.10 clearly shows the PV term for each boundary decreases sharply and becomes negative at approximately 100 GPa for each boundary. Examination of the 100 GPa structures revealed that another shear had occured leading to a very compact boundary which

produced negative formation dilations. As figure 5.11a shows for the {310} boundary at 100 GPa the boundary contains 7 coordinate magnesium and oxygen ions. This is a result of the shear which generated a structure similar to a spiral dislocation at the boundary as shown in figure 5.11b with a triangular spiral of bonds running up through the centre of the boundary. Similar structures were predicted for the other boundaries modelled.

Pressure (GPa)	{210}		{310}		{410}	
	Sym	Asym	Sym	Asym	Sym	Asym
0	1.53	-	1.71	2.08	1.78	2.25
10	2.50	2.53	2.79	2.66	2.76	2.75
20	3.35	2.93	3.52	3.10	3.43	3.21
40	-	3.55	4.20	3.78	4.03	3.90
50	-	3.80	4.81	4.06	4.59	4.17
60	-	4.04	5.84	4.32	5.55	4.42
80	-	3.92	-	4.74	-	4.80
100	-	3.93	-	4.54	-	4.91

Table 5.2. Formation Gibbs free energies as a function of pressure for symmetric and asymmetric tilt grain boundaries of MgO.

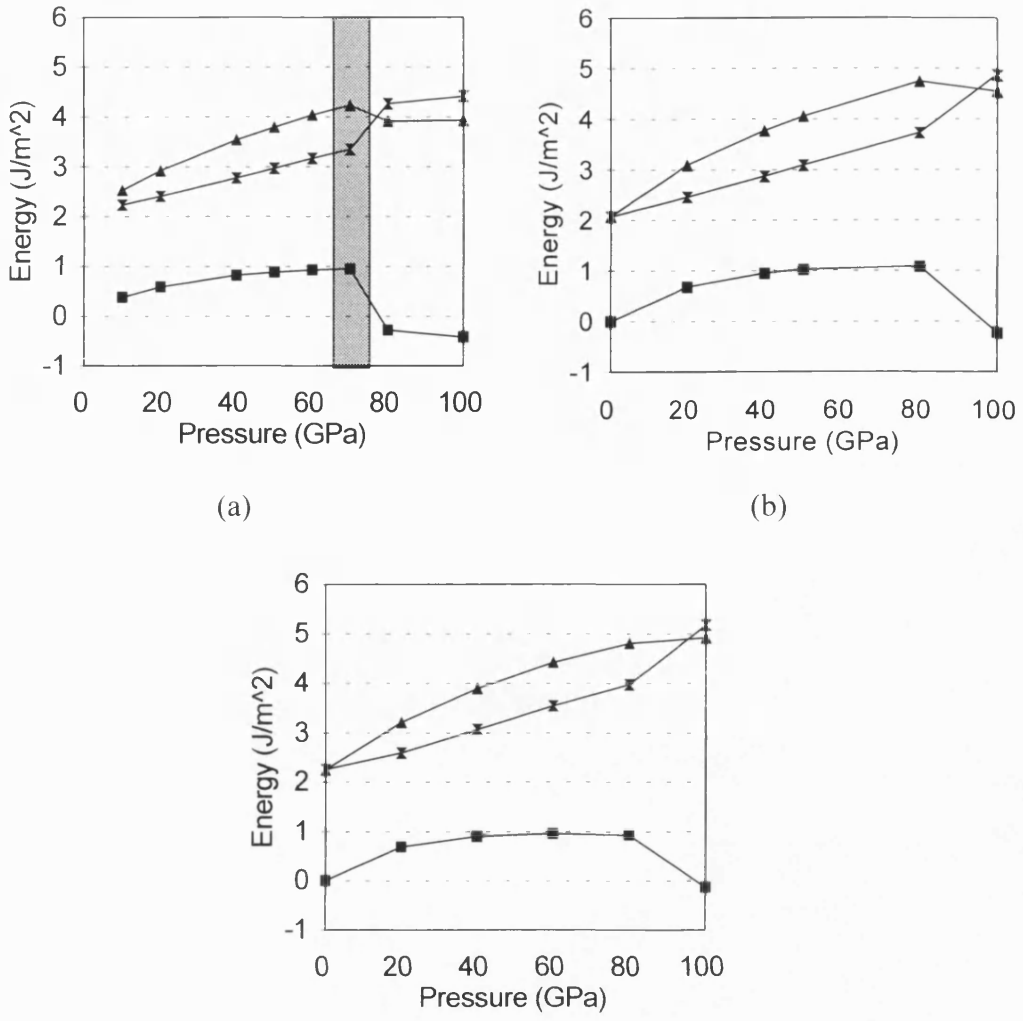

Figure 5.10. The energies of formation for a) the (210), b) the {310}, and c) the {410} asymmetric tilt boundaries as a function of pressure at 600 K. Squares represent PV, hourglasses the static lattice energy and triangles the Gibbs Free energy. Shaded regions show where imaginary frequencies were calculated.

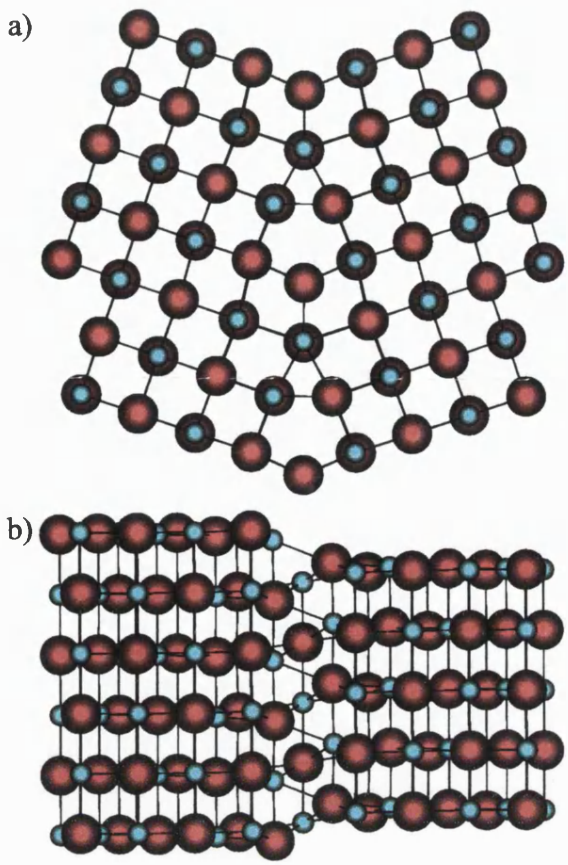

Figure 5.11. The minimised {310} asymmetric tilt grain boundary at 100 GPa and 600 K looking in the a) [001] and b) [010] directions.

The reversibility of the phase transitions was modelled using lattice dynamics by reducing the pressure in stages back to 0 GPa. The Gibbs free energy, PV term and lattice energy were plotted as a function of pressure and are given in figure 5.12. All data is given, however shaded regions on the graph are pressures where imaginary frequencies were found.

For both the {210} and {310} boundaries the structural transition was found to remain irreversible until pressures below the pressure at which the transition originally occured. Thus the high pressure form of the {210} boundary which was formed at approximately 80 GPa remained stable until the pressure was reduced to

approximately 50 GPa. The formation energies at pressures below 50 GPa were identical to the energies of the boundary at the same pressures before the transition illustrating that it had reverted to its original structure. Similarly, the high pressure form of the {310} boundary remained stable until the pressure was below 80 GPa. However, the structure formed was not dynamically stable and imaginary phonon frequencies were calculated for these boundaries suggesting that the phase transition was not completely reversed upon release of pressure. Instead it formed a structure midway between the initial and high pressure structures. The {410} boundary was found to be fully reversible upon release of pressure with the structure reverting back at the same pressure at which it originally underwent a transition. However, the structure was unable to return to its initial 0 GPa symmetric structure and thus an imaginary phonon frequency was calculated for this pressure.

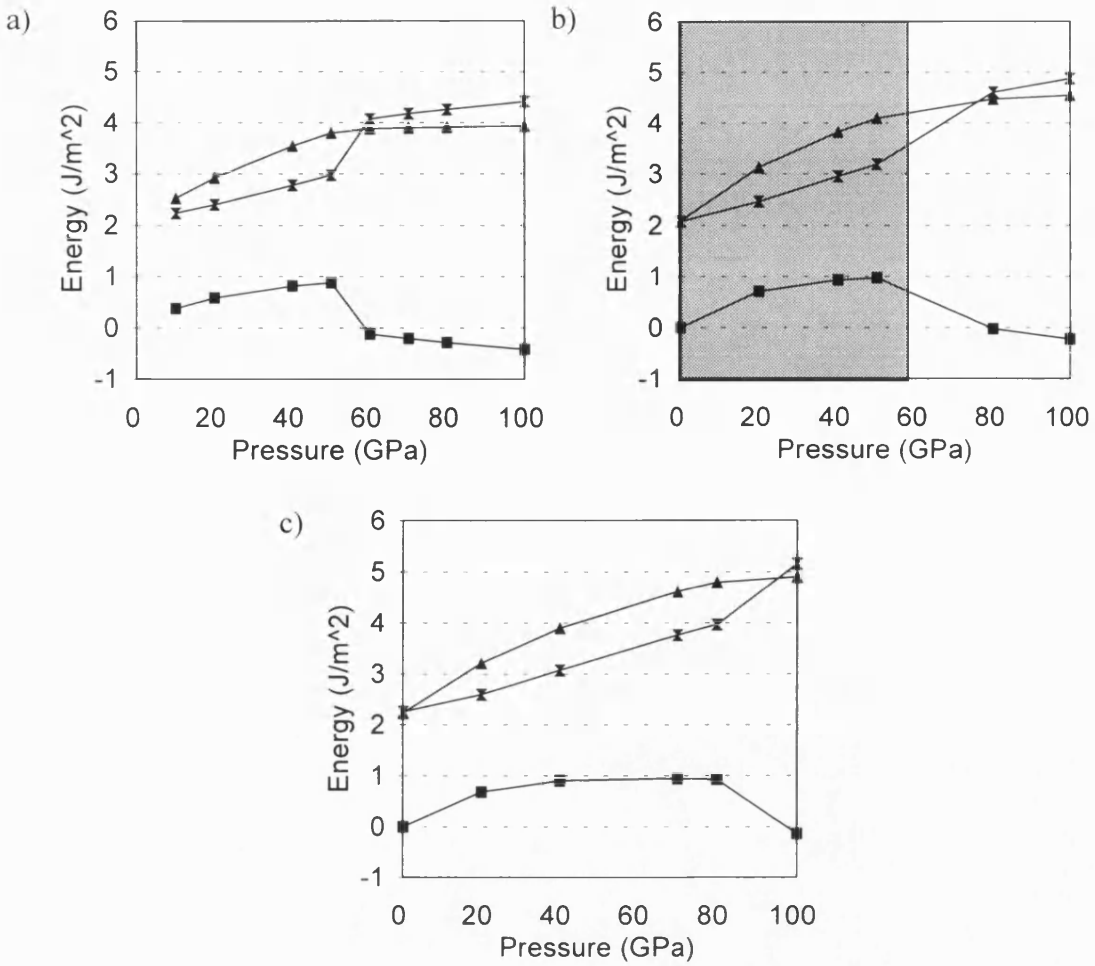

Figure 5.12. The energies of formation for a) the (210), b) the {310}, and c) the {410} asymmetric tilt boundaries as a function of pressure at 600 K.

5.4 Summary of phase transitions in grain boundaries

Each of the three boundaries ({210}, {310} and {410}) follows a similar trend with respect to structural changes due to increasing pressure. At 0 GPa the symmetric boundaries are the most stable however as the pressure increases to approximately 20 GPa the asymmetric boundaries become the most thermodynamically stable. Molecular dynamics has shown that for the {310} and {410} boundaries pressures in excess of 20 GPa are required to cause the structural transformation to the asymmetric

structure although at approximately 20 GPa in each case the channels at the boundary undergo collapse to form a denser structure. The asymmetric structures undergo a shear at approximately 80 GPa to form a denser structure which contains highly coordinated magnesium and oxygen ions and which resemble a spiral dislocation. Figure 5.13 plots the formation Gibbs free energy as a function of pressure and shows the most stable structure in each case.

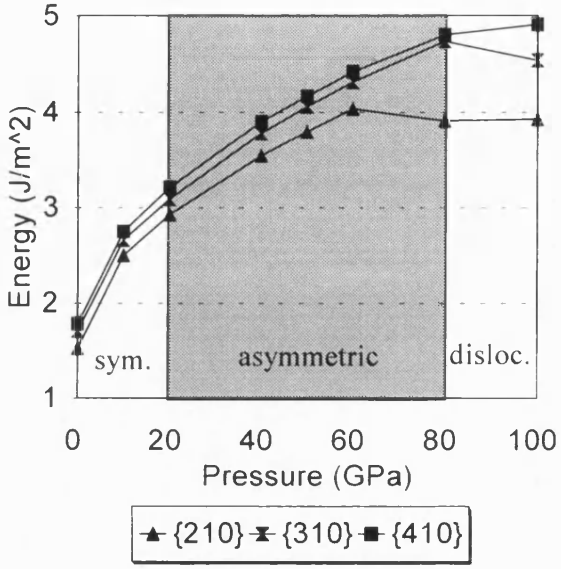

Figure 5.13. Formation Gibbs free energy as a function of pressure for MgO tilt grain boundaries indicating three structural types, symmetric, asymmetric and spiral dislocation.

5.5 Effect of pressure on Mantle properties

The grain boundaries calculated may have a significant effect compared to bulk on properties of the mantle such as seismic velocities and heat capacities. In addition the presence of discontinuities in the boundary structure as a function of pressure (and thus depth within the Earth's mantle) for both symmetric and asymmetric tilt grain boundaries should further effect these properties. To test this the

seismic velocities, heat capacities and phonon dispersion curves were plotted as a function of pressure at 600 K.

Figure 5.14 shows the velocity of a primary seismic wave, V_p, increased with increasing pressure for both bulk and each of the grain boundries with a discontinuity in the value of V_p for the {310} boundary at the pressure where the boundary collapsed. The variation of V_p with pressure was much smoother for the {410} grain boundary which may have been a result of the gradual collapse predicted for this boundary. As expected V_p was smaller for the boundaries than for the bulk due to the lower densities of the boundaries.

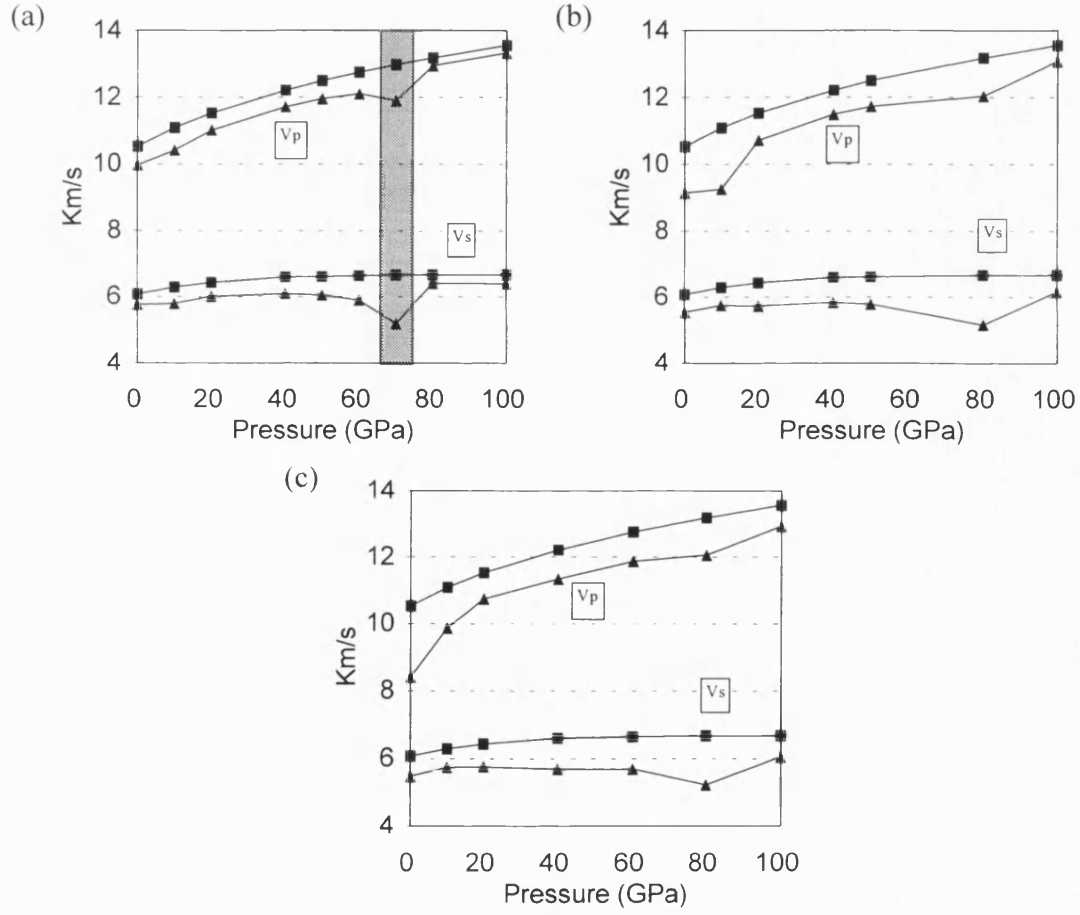

Figure 5.14. Seismic wave velocities for (squares) bulk and (triangles) the a) {210}, b) {310} and c) {410} tilt grain boundaries.

Shaded regions indicate areas where imaginary frequencies were calculated.

The boundaries had a discontinuity in V_p at approximately 70-80 GPa as shown in figure 5.14 which coincided with the structural transition to the compact structure containing seven coordinate magnesium and oxygen ions. The data point for the {210} boundary at 70 GPa is given despite the fact that it was imaginary to illustrate the trend. The more compact structure of the high pressure structures resulted in smaller formation dilations and therefore the V_p's were also closer to the bulk value than at lower pressures where the symmetric boundaries were more stable.

For all the boundaries V_s increased with increasing pressure before reaching a maxima and decreasing again. The decrease in V_s was attributed to the softening of the optical phonon mode which, as previously discussed in section 5.2.4, resulted in the structure shearing. Further evidence for this was found from the asymmetric boundaries where V_s decreased as the phonon frequency of the softening mode decreased until the pressure at which the structural transition occured was reached. At this point V_s began to increase again as the phonon frequency of the soft mode increased.

The heat capacities of the boundaries (as shown in figure 5.15 for the {310} and {410}) were lower than the bulk heat capacities at equivalent pressures which was probably a result of the lower phonon frequencies found at grain boundaries. This can be emphasised by summing the difference between the bulk and boundary density of states and plotting the running total against the frequency. Frequencies with a positive total are more abundant in the boundary whilst those with a negative total are more common in the bulk cell. As shown in figure 5.16 each of the boundaries had a greater number of low frequency vibrations and less high frequency vibrations than the bulk

and is probably the result of the increased space for vibration at the boundary caused by the formation of the channels which reduces the frequency of the vibrations.

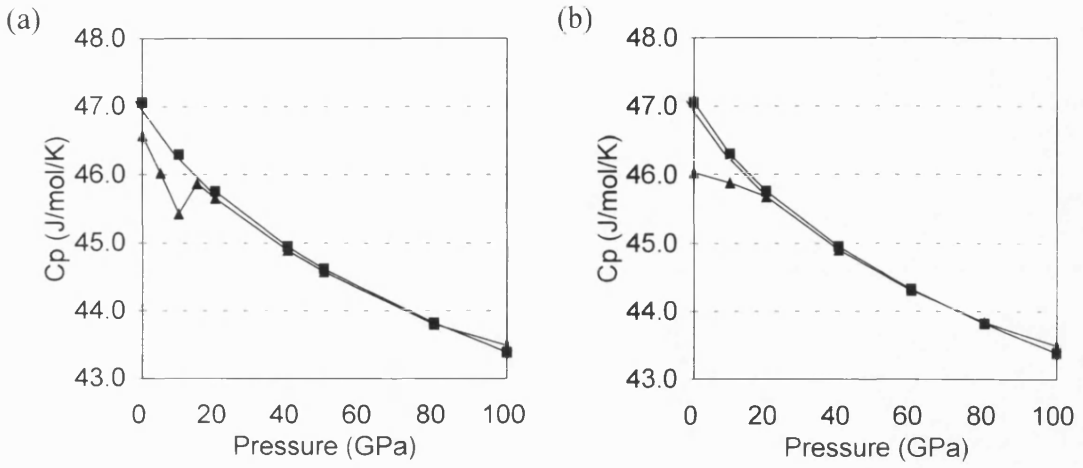

Figure 5.15. Heat Capacities for (squares) bulk and (triangles) the a) {310} and b) {410} tilt grain boundaries.

A similar pattern was found when the phonon frequencies in the asymmetric boundaries were considered. As figure 5.16 shows for the {310} and {410} asymmetric boundaries there was a greater number of low frequency phonon vibrations in the boundary compared to the bulk and a lower number of high frequency vibrations. As pressure was increased the phonon vibration content was shifted towards higher frequencies which was due to the frequencies in the boundary shifting towards bulk values as the boundaries increased in density faster than the bulk.

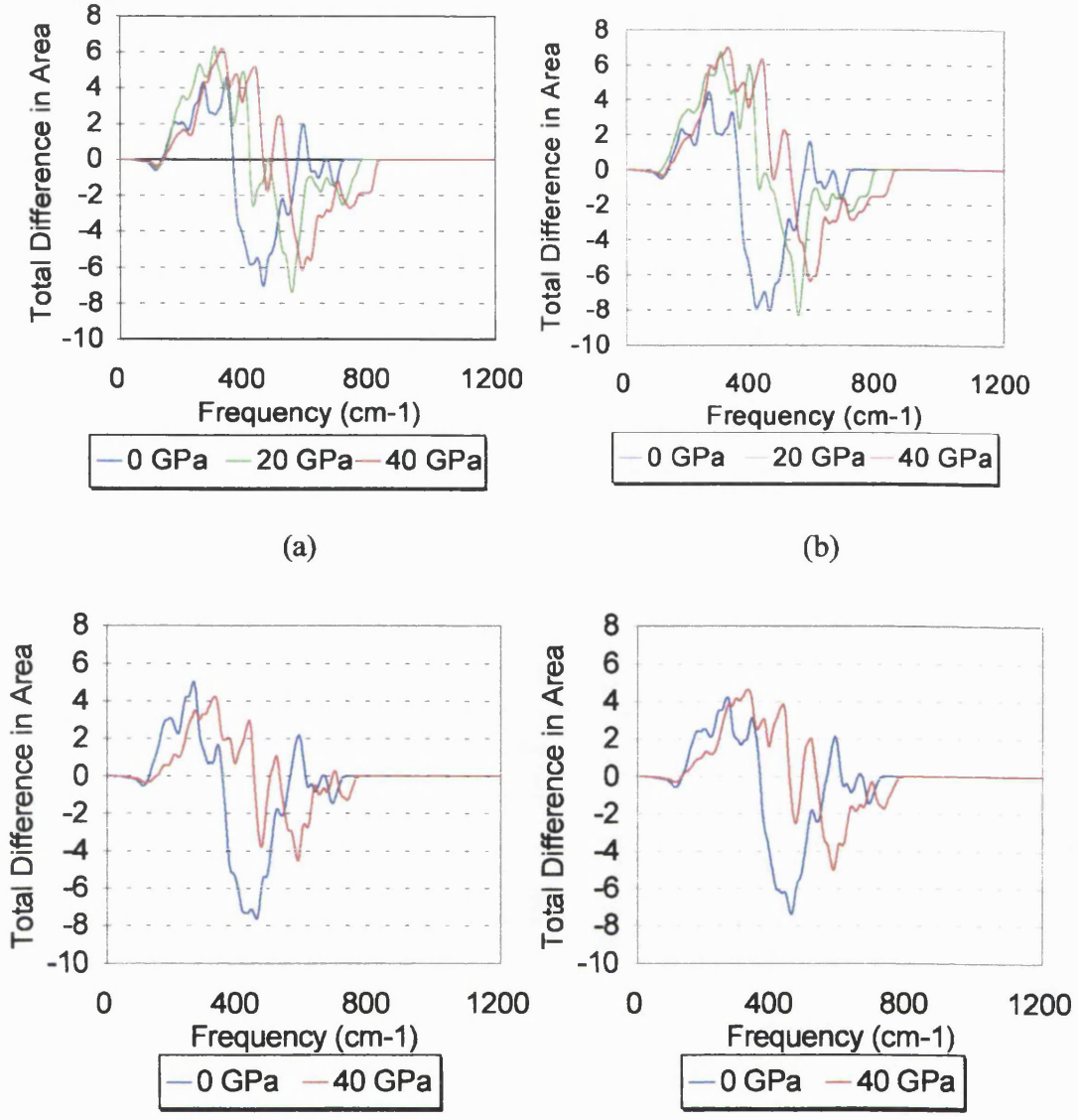

Figure 5.16. Plots of difference in phonon frequencies between bulk and boundary as a function of pressure for the a) {310} symmetric, b) {410} symmetric, c) {310} asymmetric and d) {410} asymmetric tilt grain boundaries.

5.6 Molecular Dynamics Modelling of Bulk and Boundary Melting

There is little variation of boundary properties at temperatures well below the melting point as has been shown earlier in this chapter. However previous work on surfaces of NiO (Oliver et al. 1995) demonstrated that premelting of the surface may

occur which leads to a lower melting point for the surface. To see if this also applied to grain boundaries a series of Molecular Dynamics (MD) calculations were carried out on both bulk and the {410} boundary of MgO.

Previous bulk simulations (Ferneyhough et al. 1994, Vocadlo and Price 1996) suggested that the melting point is very sensitive to the potential used. Therefore two sets of potential parameters were chosen for these simulations both of which were derived by Lewis and Catlow (1985) (LC 8 and LC 14), the difference between them was the result of a different method being used to derive the parameters describing the magnesium oxygen interaction, see table 5.3. The potentials were modified to be the rigid ion model by removing the shell model parameters because of the constraint on the size of the simulation cells required. The LC8 potential was used in order to determine what effect, if any, that increasing the size of the simulation cell would have upon the calculated melting point of bulk MgO and compared to the LC14 potential at a single size. The melting point can be determined by calculating the mean volume of the simulation cell over the time of the simulation cell. Melting is judged to have occured when there is a sudden increase in the volume caused by the ions moving away from their equilibrium lattice positions. A second method of measuring this is to consider the Mean Square Deviations (MSDs) as a function of time. At temperatures well below the melting point the gradient would remain zero because the ions would be vibrating about their equilibrium positions. As the temperature increases to the melting point the ions move further and thus the MSDs will increase linearly as a function of time (see chapter 3 for a more detailed explanation).

Interaction	A (eV)	ρ (Å)	C (eV Å^6)
O^{2-}- O^{2-}	22764.3	0.149	27.88
Mg^{2+}- O^{2-} LC8	821.6	0.3242	-
Mg^{2+}- O^{2-} LC14	1428.5	0.2945	-

Table 5.3. Short range potential parameters for the LC8 and LC14 potentials of Lewis and Catlow.

Four sizes of simulation cell were chosen, a 4x4x4, 5x5x5, 6x6x6 and 7x7x7 cell which contained 512, 1000, 1728 and 2744 ions respectively using the LC8 potential, whilst for the LC14 potential a single size of 4x4x4 was chosen. Figure 5.17 shows a plot of the molar volume against temperature for each of these calculations. From the graph it was clear that the cell size had very little effect upon either the molar volume or melting temperature however the two potentials did give different values for the melting point of bulk MgO with a calculated average melting point of 3950 K for the LC8 potential and 4750 K for the LC14 potential. These were both much higher than the experimental value of 3125 K possibly due to the derivation of the potentials which were both fitted to experimental data at temperatures well below the melting point. Since the intention of this work was to model the grain boundaries of mantle minerals including boundaries between different materials the LC14 potential was chosen for further investigation since it is used in the THB1 potential which has been shown to accurately model a number of magnesium silicates (Price and Parker 1987a, 1987b, Parker and Price 1989).

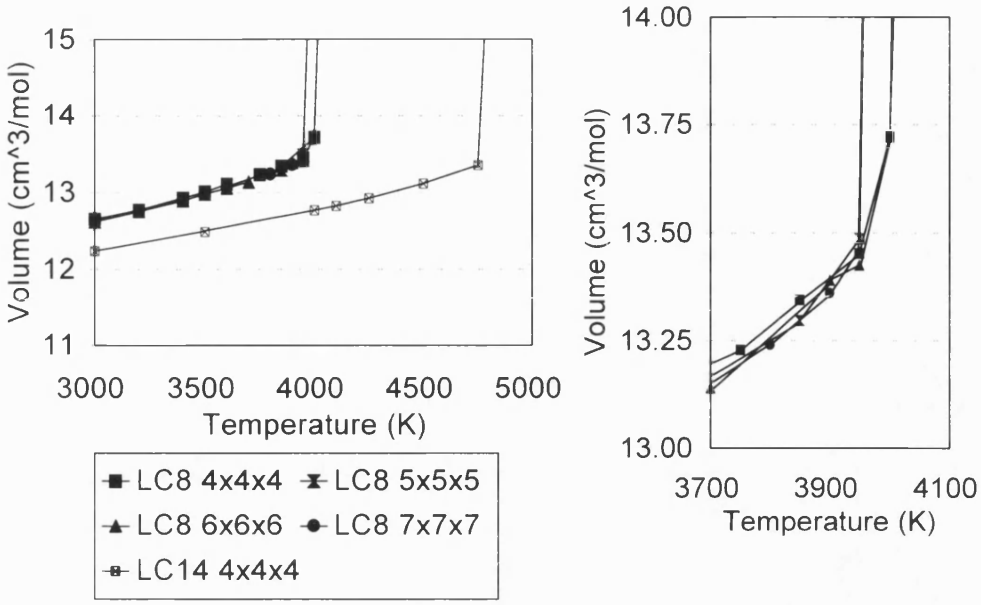

Figure 5.17. Plots of molar volume as a function of temperature for bulk comparing LC 8 and LC 14 potentials showing expanded detail.

MD simulations of the {410} symmetrical tilt grain boundary were performed 4x4x4 unit cell and 7x7x7 unit cell sized cells at a series of temperatures to determine the melting point. The molar volume was plotted as a function of temperature and as shown in figure 5.18 was seen to increase suddenly at approximately 4100 K and 3600 K for 960 species and 3008 species cells respectively indicating that melting had occured. Examination of the MSDs and structures showed that for the 960 ion cell at 3950 K the ions were vibrating about their equilibrium positions keeping an ordered structure. As the temperature increased to 4100 K all of the MSDs increased as a function of time which indicated that the cell had melted. Beginning at 4050 K there was a breakdown of order in the region of the grain boundary which increased with increasing temperature until the whole cell had melted by 4100 K (figure 5.19). A similar effect has been observed in simulations of surfaces of NiO (Oliver et al. 1995)

and grain boundaries of $KCaF_3$-perovskite (Watson 1994) which seem to be areas where the melting process is initialised before the disorder spreads to the rest of the crystal as the temperature increases. For the boundaries this may be a result of the extra freedom of the ions at the grain boundary which are able to diffuse into the channel forming the boundary.

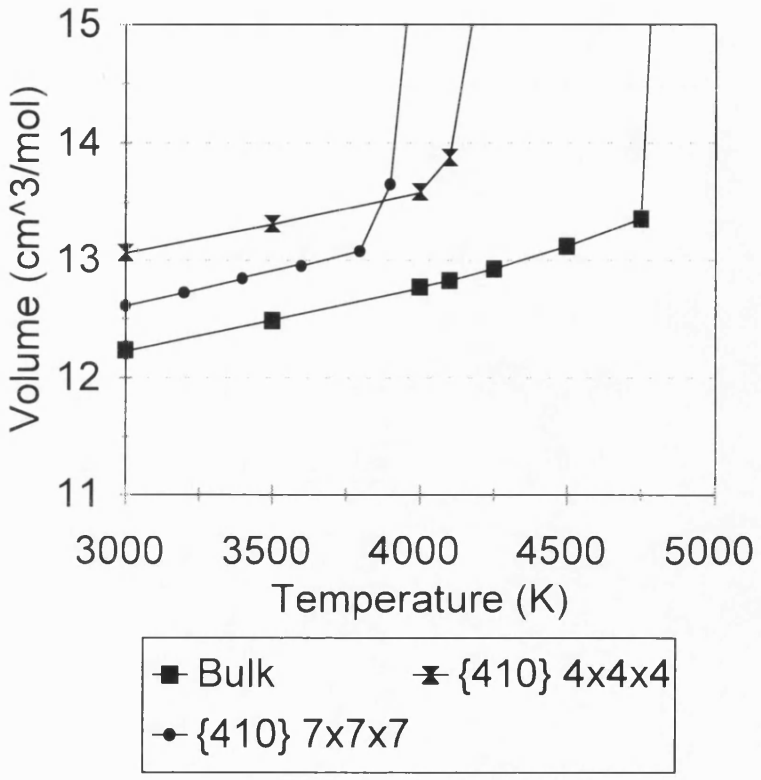

Figure 5.18. Plot of molar volume as a function of temperature for LC14 potential comparing bulk and the {410} tilt grain boundary.

In summary, there was little variation in the melting temperature as a function of cell size, however the presence of the grain boundary caused a lowering of the melting point which may be due to the extra freedom of ions at the boundary.

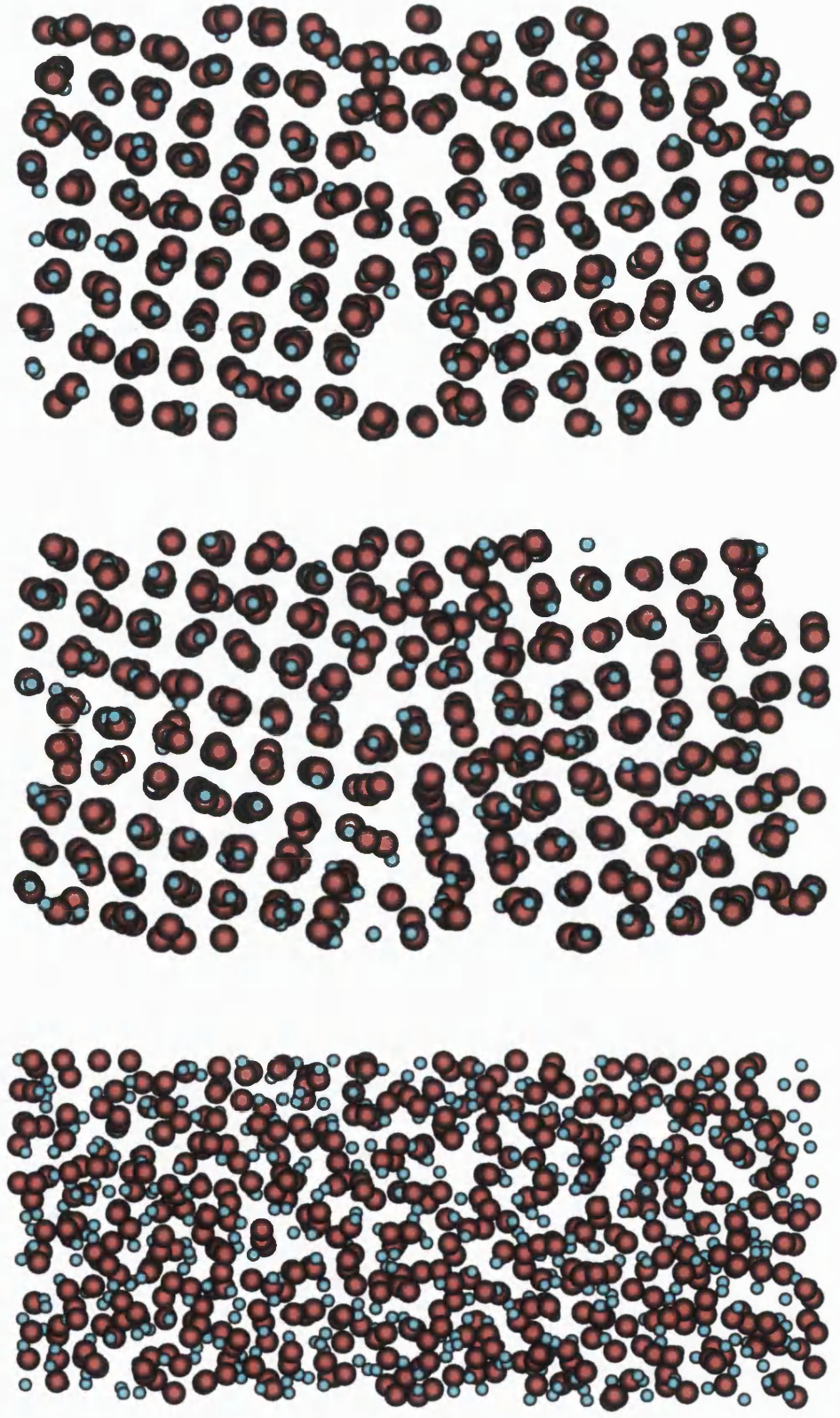

Figure 5.19. Average structure of the {410} boundary at a) 4000 K,

b) 4050 K and c) 4100 K.

5.7 Effect of Pressure on Twist Grain Boundaries

The effect of pressure and temperature upon the structure and energies of twist grain boundaries has also been calculated. Of the four boundaries previously chosen for static simulation (see chapter 4) only three, the 22.62°, 28.07° and 36.87° boundaries were chosen for lattice dynamics studies since the 16.25° boundary required too many ions for convergence of the free energy. The previous studies showed further that the effect of temperature is small therefore we considered only two temperatures, 300 and 1000 K, for each boundary. Once again it was found that temperature had little effect upon the structure and energies of the boundaries due to the small vibrational entropy and energy and zero point energy.

Lattice dynamics calculations were performed at pressures up to 40 GPa. As predicted for the tilt boundaries pressure proved to have a greater effect than temperature. Figure 5.20 shows that for each of the boundaries there was an increase in the formation free energy with increasing pressure, primarily due to the increase in the PV term. The rate of this increase was not as great as that found for the symmetric tilt grain boundaries but was more like the rate for the asymmetric boundaries which is reasonable when one considers the structures of the different types of boundaries. The twist boundaries are very compact with no large channels such as those found in symmetric tilt grain boundaries, thus the dilation upon formation is small which results in a smaller PV term compared to that for symmetric tilt grain boundaries.

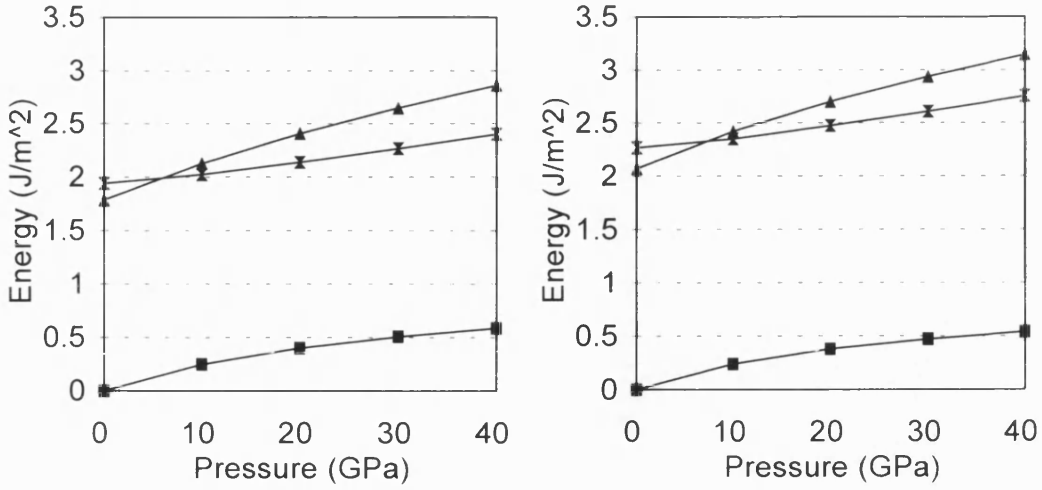

(a)

(b)

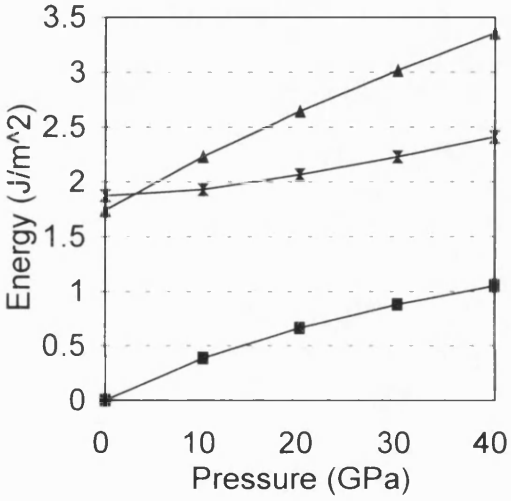

(c)

Figure 5.20. The energies of formation for a) the 22.62°, b) the 28.07°, and c) the 36.87° twist boundaries as a function of pressure at 1000 K. Squares represent PV, hourglasses the static lattice energy and triangles the Gibbs Free energy.

This increased density was also evident in the effect on seismic velocities due to the grain boundaries. A plot of V_p and V_s as a function of pressure showed that the three twist boundaries studied had very similar velocities to each other and that these velocities were close to that of bulk for both V_p and V_s (figure 5.21a). There were no

discontinuities in the rate of change of velocity with pressure which was to be expected since there was no significant structural change.

The heat capacities for the boundaries were also very similar to that of bulk. A plot of Cp as a function of pressure at 1000 K showed that the boundaries all had very similar heat capacities which decreased as a function of pressure (figure 5.21b), however they were very slightly lower than the bulk values. Examination of the phonon frequency content of the boundary compared to the bulk as a function of pressure using the difference plots explained in section 5.4 showed that the boundaries had a more of the low frequency vibrations compared to bulk but a lesser number of the high frequency phonon vibrations. The frequency content of the boundary shifted to higher frequencies as the applied pressure upon the cell was increased which was similar to the trend found for the tilt grain boundaries.

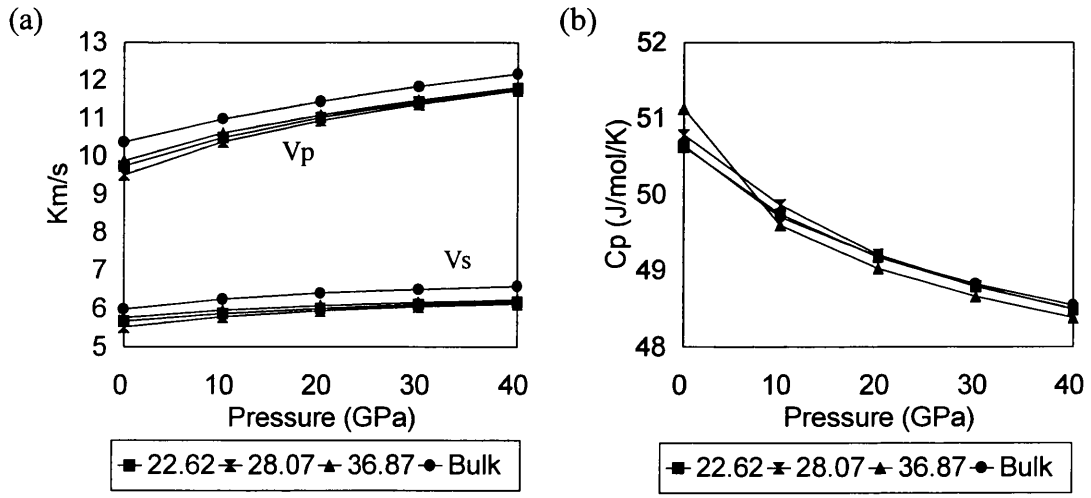

Figure 5.21. The a) Seismic wave velocities and b) heat capacities of the twist boundaries of MgO

5.8 Conclusions

This chapter has presented the results of computer simulations to determine the effect of pressure and temperature upon the structure and energies of grain boundaries in MgO. For all of the grain boundaries modelled it was calculated that temperatures well below the melting point had little effect upon the properties of the grain boundaries. This was primarily due to the small formation vibrational entropy and vibrational energy of the boundaries. The only significant effect of temperature was on the melting point depression from the bulk value, but even here this was only by about 8%.

Conversely pressure had a significant effect upon the structure of the tilt grain boundaries and a lesser effect upon the structure of the twist grain boundaries modelled. The symmetric tilt grain boundaries first underwent a compression and collapse of the channels forming the boundary before shearing as the pressure increased to form an asymmetric boundary. As the applied pressure was increased still further a phonon mode softened again before a further shear generated a highly dense structure which contained 7 coordinate ions at the boundary due to the presence of a spiral dislocation-like structure. The symmetric tilt boundaries had lower energies than the twists at 0 GPa but as the pressure was increased the twist boundaries became the most stable.

Relaxation of these structural phase transitions in both Lattice and Molecular Dynamics revealed that these processes were reversible. The tilt transformation did require an energy barrier to be overcome but the high pressure asymmetric transformation did not.

6 Grain Boundaries of Stishovite and Perovskite

6.1 Introduction

The previous two chapters have considered MgO, a simple cubic structure. In this chapter we expand the scope of this work to include the high pressure form of SiO_2, stishovite, and $MgSiO_3$ perovskite, two other minerals which are thought to be a major component of the Earth's mantle (Anderson 1989, Lee and Gonze 1994). The aim of this work is to establish the viability of these methods to modelling grain boundaries in complex silicate materials, to identify the difficulties and to investigate the effect of high pressures on this structure and stability. For each mineral a series of boundaries are first modelled using static energy minimisation and then the effect of pressure and temperature is calculated for each boundary using lattice dynamical techniques.

6.2 Stishovite

Stishovite is a polymorph of silica (SiO_2) which has been synthesised experimentally at pressures greater than 10 GPa and is believed to be the stable form of free silica found within the Earth's mantle (Finger and Hazen 1991). Stishovite is tetragonal and has the rutile (TiO_2) structure (fig 6.1) consisting of edge linked chains of distorted SiO_6 octahedra that extend parallel to the c axis and are corner linked to four adjacent chains. The six co-ordinate silicon has four short and two long silicon oxygen bonds and is unusual for an oxide because the oxygen is three co-ordinate rather than four or six as commonly found in ionic oxides or two as found in some silica frameworks.

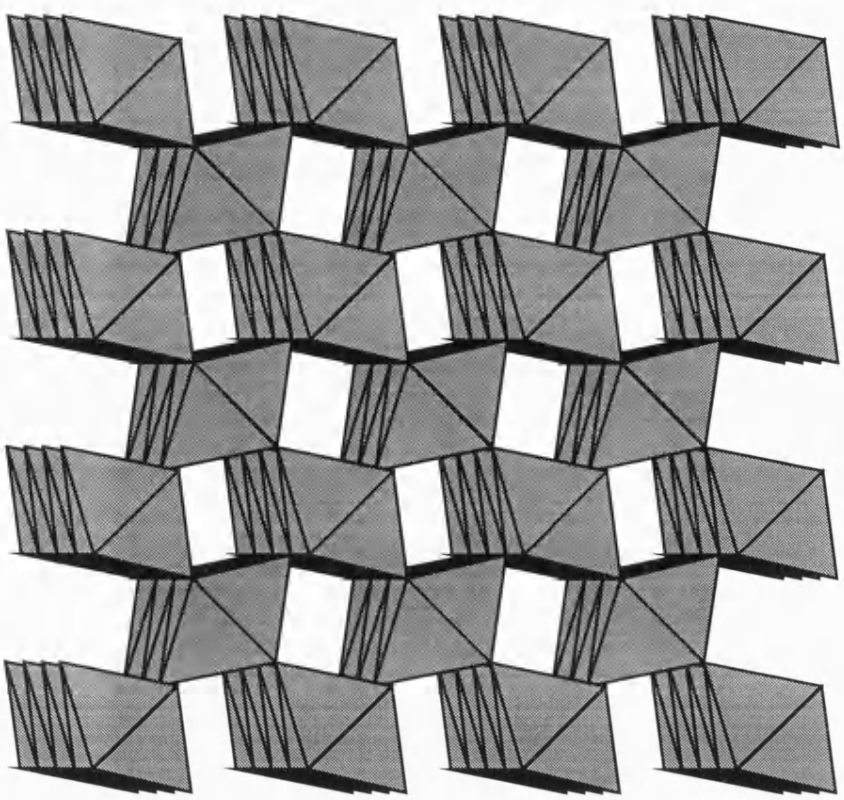

Figure 6.1. Rutile structure of stishovite showing edge linked SiO_6 octahedra.

6.3 Potential Models for Stishovite

Several sets of potential parameters are available to study stishovite of which two were chosen to help assess the sensitivity of the results to the details of the parameters. These potentials were those derived by Sanders et al. (1984) and by van Beest et al. (1990). The Sanders potential was empirically derived for α-quartz using experimental data including the elastic constants, static dielectric constants and high frequency dielectric constants and was tested by calculating phonon densities of state, high pressure structure and structures of other polymorphs of silica (containing four co-ordinate silicon). In each case it showed good agreement with available experiment

(Sanders et al. 1984). The model uses formal charges, includes the shell model to simulate the polarisability of the oxygen ions and has a three body bending term to confer the directionality of the partially covalent bonding within the SiO_4^{4-} tetrahedra (see table 6.1).

The van Beest potential, in contrast, is a simple two body rigid ion model that ignores polarisability. It was partially derived from *ab initio* cluster calculations on H_4SiO_4 to obtain the nearest neighbour parameters and then modified by empirically fitting to experimental data for α-quartz including elastic constants and unit cell dimensions in order to obtain the correct long range interactions. Unlike the Sanders model the van Beest potential uses partial charges and the empirical fitting produces large C/r^6 terms (table 6.2) to compensate. This potential has previously been tested on a number of silica polymorphs including stishovite and in each case showed good agreement with experimental data (van Beest et al. 1990). It has also been shown to give good reproduction of the structure of α-quartz as a function of pressure (up to 20 GPa) (Watson 1994, de Boer et al. 1996) illustrating its ability to model changes in bond length.

An important assumption of this work is that the potential models derived for silicon in four fold co-ordination are applicable to a system in which the silicon atom is octahedrally co-ordinated. We first tested this assumption using both potentials within the computer code PARAPOCS (Parker and Price 1989) to minimise the bulk structural parameters which were then compared to experimental data.

a)

Species	Charge (e)	Mass (g mol^{-1})
Si	4.0	28.0855
O (core)	0.86902	15.9994
O (shell)	-2.86902	0.00

b)

Interaction	Force Constant	Reference
O_{core} - O_{shell}	74.92 eV $Å^{-2}$	Catlow 1977
O_{shell} -Si - O_{shell}	2.09724 eV rad^{-2}	-

c)

Interaction	A (eV)	ρ (Å)	C (eV $Å^6$)	Reference
O - O	22764.000	0.150	27.88	Catlow 1977
Si - O	1283.907	0.32053	10.66158	-

Table 6.1. Potential parameters based on the three body shell model potential of Sanders et al. 1984 showing a) charges and masses, b) shell model and three body constants, c) short range Buckingham parameters.

a)

Species	Charge (e)	Mass (g mol^{-1})
Si	2.4	28.0855
O	-1.2	15.9994

b)

Interaction	A (eV)	ρ (Å)	C (eV $Å^6$)
O - O	1388.7730	0.3623188	175.0000
Si - O	18003.7572	0.2052048	133.5381

Table 6.2. Potential parameters based on the two body potential of van Beest et al. 1990 showing a) charges and masses and b) short range Buckingham parameters.

6.3.1 Structure

The lattice vectors and unit cell volumes were calculated for both potentials at 0 GPa first neglecting temperature and then at 300 K. Comparison with experimental data obtained at room pressure and temperature using single crystal and powder x-ray diffraction (table 6.3) shows that the van Beest potential gives better agreement with the experimental data. The lattice vectors were within 1% and the cell volumes were within 2% of the experimental results. In contrast the difference between the Sanders potential and experiment is larger, of the order of 3 - 5 % different.

Property	Single Crystal Data		Powder Diffraction		Potential			
					Sanders		van Beest	
	i	ii	iii	iv	0 K	300 K	0 K	300 K
a=b	4.177	4.177	4.179	4.180	4.015	4.023	4.145	4.159
c	2.6651	2.6655	2.6649	2.666	2.787	2.788	2.660	2.665
V	46.499	46.506	46.541	46.581	44.93	45.13	45.70	46.11
c/a	0.638	0.638	0.638	0.638	0.694	0.693	0.642	0.641

Table 6.3. Experimental and calculated lattice properties of stishovite. Experimental data given for i) Sinclair and Ringwood (1978), ii) Hill et al. (1983), iii) Chao et al. (1962), iv) Liu et al. (1974).

The stishovite structure has two sets of silicon to oxygen bond lengths with two longer than the remaining four due to the distortion of the edge and corner sharing octehedra. The bond lengths and smallest oxygen-silicon-oxygen angle have been measured for the Sanders and van Beest potentials at 300 K and compared to experimentally determined values obtained from single crystal studies (table 6.4). An important point to note is that the Sanders potential incorrectly gives four long and two short silicon-oxygen bonds as compared to the experimentally two long and four short. This may be a result of the Sanders potential underestimating the oxygen-oxygen repulsion and the oxygen-silicon-oxygen bond angle. This problem has previously been noted by Watson (1994) and de Boer et al. (1996) for calculations upon α-quartz. The van Beest potential shows a better agreement with experimental data than the Sanders potential especially when considering the oxygen-silicon-oxygen bond angle.

	Si-O (4) (Å)	Si-O (2) (Å)	mean Si-O (Å)	O-Si-O (°)
Sanders	1.78	1.73	1.77	77.02
Van Beest	1.76	1.80	1.77	81.33
Single Crystal Data				
i	1.76	1.81	1.77	81.34
ii	1.76	1.81	1.77	81.34

Table 6.4 Calculated and experimental bond lengths of stishovite.

Experimental data of i) Sinclair and Ringwood (1978), ii) Hill et al. (1983).

6.3.2 Elastic Properties

The Voigt bulk modulus for stishovite was calculated from the elastic constants and compared to the values obtained experimentally (table 6.5). The Voigt bulk modulus is given by:

$$K_V = \frac{1}{9} \sum_{nm}^{3,3} \underline{\underline{C}}_{nm} \qquad 6.1$$

where $\underline{\underline{C}}$ is the elastic constant matrix.

Both potentials showed good agreement with the experimentally determined Voigt bulk modulus for the shockwave data although the single crystal value was lower. The elastic constants are not as well modelled but the values shown are good given the uncertainties in the pressure and temperature of the experiment.

Technique	K_V (GPa)	C_{11}	C_{33}	C_{44}	C_{66}	C_{12}	C_{13}
Sanders	432.0	474	885	156	396	307	361
Van Beest	417.0	628	935	269	262	236	272
Single crystal	324.0	453	776	252	302	211	203
Shockwave	435.0	Not Available					

Table 6.5 Voigt bulk moduli and elastic constants (GPa) for stishovite

Experimental data : Single crystal - Weidner et al. (1982)

Shockwave - Mcqueen et al. (1963)

6.3.3 Summary of potentials testing

In summary, the van Beest potential models the structural properties of stishovite with the greatest accuracy. However the van Beest potential does not contain electronic polarisability which can be important in surface and defect calculations (Catlow and Mackrodt 1982). Thus in the following sections most of the calculations have been carried out using both the Sanders and van Beest potentials to provide a comparison.

6.4 Surface Energies and Morphologies of Stishovite

The surface structure and energies of stishovite were calculated using the computer code METADISE (see chapter 3). Surfaces were considered up to and including a Miller index of two giving a total of 12 unique planes (because of the tetragonal symmetry). However for each of these planes a number of cuts were often

possible leading to 23 possible surfaces. Higher index surfaces were not considered since this would result in too many to investigate thoroughly.

A test for convergence of the surface energy with increasing region I size was carried out for each potential and a region I size of ten repeat units (i.e. 60 species) was found to be adequate for both. An example of convergence with region size for the {102} surface using the van Beest potential is given in fig 6.2.

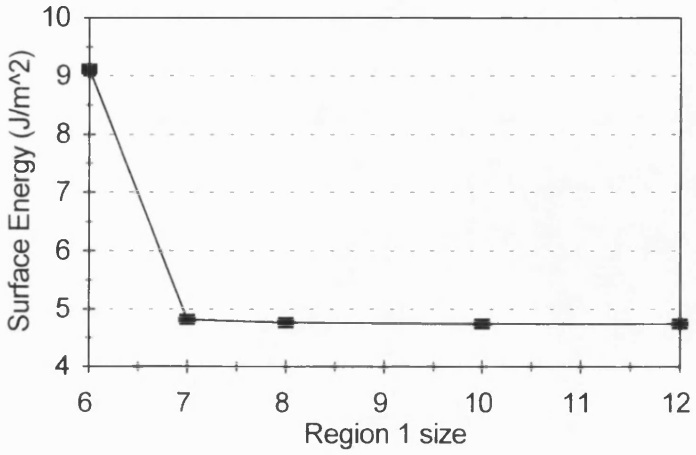

Figure 6.2. Convergence of surface energy with region size in METADISE for the van Beest potential.

The resulting surface energies for both potentials are given in table 6.6 with the lowest energies given where multiple cuts were possible. This gives 12 surfaces of which a selection of the more stable calculated using the van Beest potential are shown in figure 6.3 with the surfaces at the top of each block. The unrelaxed surface energies for both potentials were comparable however the relaxed energies calculated using the van Beest potential were significantly higher than those calculated using the Sanders potential although the reason for this is not known. For both potentials the

{100} and {110} surfaces were low in energy and therefore important for the equilibrium morphology. In addition, for the Sanders potential, the {221} surface had a very low energy of 1.08 Jm^{-2} compared to the other surfaces. Examination of the relaxed structures showed that the low energy surfaces had almost fully co-ordinated silicon ions at the surface as table 6.6 shows. Relaxation of the {001} surface resulted in the four co-ordinate silicon being pulled in towards the bulk. The {011}, {110} and {201} surfaces had almost no distortion from the bulk structure thus relaxed to a low energy surface which appears in the morphology predicted using the van Beest potential.

Index	No. cuts	Surface Energies (Jm^{-2})				Surface Ion Co-ordination		Face found in equilibrium morphology
		Sanders		van Beest				
		Unrel.	Rel.	Unrel.	Rel.	O	Si	
{001}	2	13.33	2.23	13.71	4.48	2	4	Sanders, vB
{100}	2	10.62	1.56	9.83	3.22	2	5	van Beest
{101}	2	8.38	1.50	9.57	3.85	2	5	Sanders, vB
{110}	1	9.89	1.54	8.99	3.11	2	5	van Beest
{111}	2	21.70	2.72	17.54	4.11	2	4	-
{102}	2	45.33	5.26	47.60	4.74	2	3	-
{112}	2	29.86	5.26	21.45	6.60	2	3	-
{201}	2	14.22	1.59	12.72	3.85	2	4	van Beest
{210}	2	39.65	1.41	25.43	5.21	2	4	-
{211}	2	13.10	3.15	12.24	3.91	2	4	-
{212}	2	23.48	2.30	17.36	4.46	2	2	-
{221}	2	22.46	1.08	16.75	3.56	2	4	Sanders, vB

Table 6.6 Surface Energies and properties for stishovite using the van Beest and Sanders potentials.

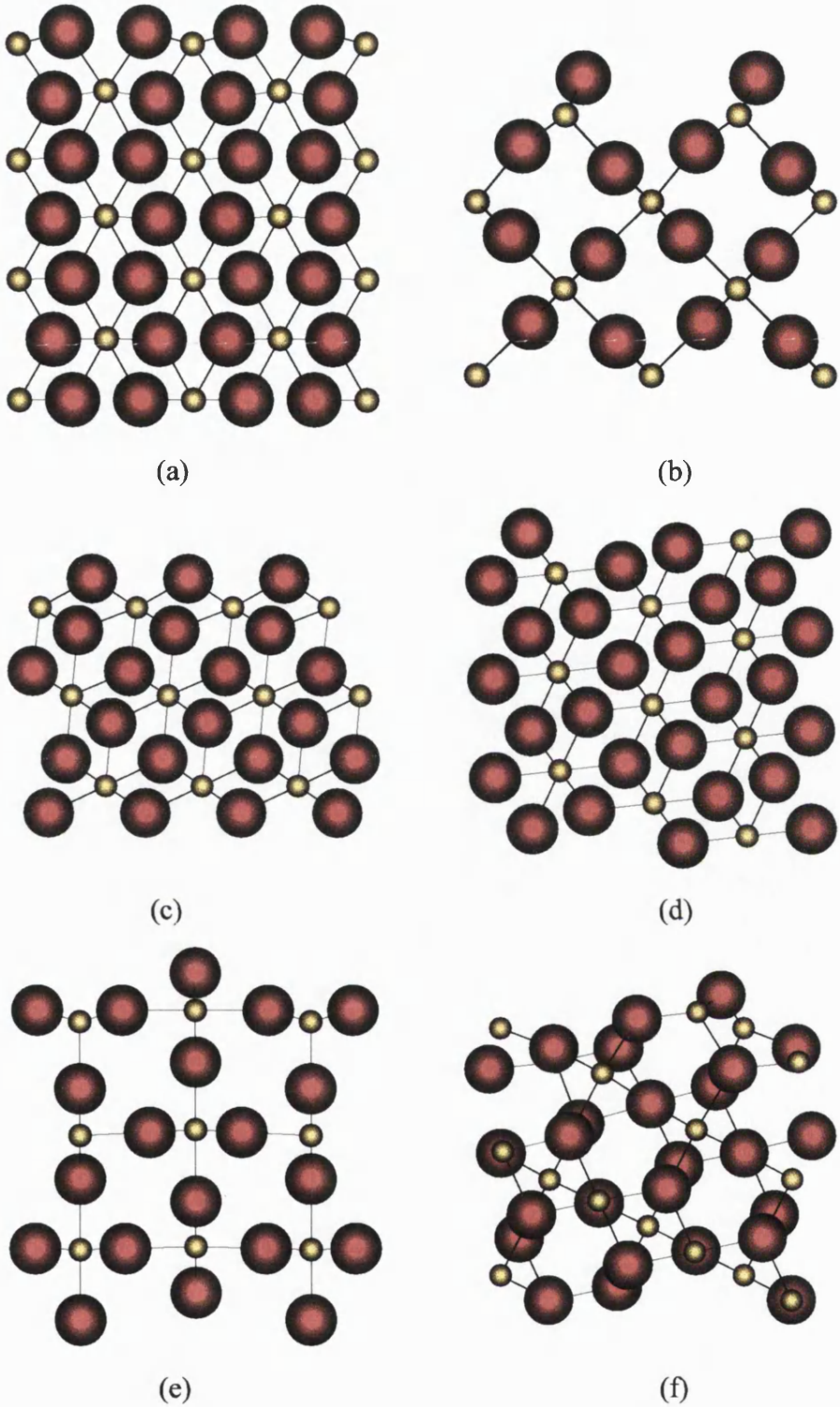

Figure 6.3. Relaxed surfaces of stishovite showing a) {001}, b) {100}, c) {101}, d) {201}, e) {110}, f) {221}. Surfaces are at the top of each block. Silicons are yellow, oxygens are red.

The resulting morphologies for stishovite can be displayed using the program GEM (Generation of Equilibrium Morphologies, Parker et al. 1992). Figure 6.4 compares the calculated morphologies with that of rutile (TiO_2 in the same structure (Kostov 1968)) as no complete experimentally derived morphology is available for stishovite, although Weidner et al. (1982) and Hill et al. (1983) synthesised single crystals of stishovite for x-ray diffraction and observed that they formed rectangular {110} prisms terminated with pyramidal {111} faces. The two calculated morphologies differ in that the {221} surface completely dominates the morphology in the Sanders potential due to its very low energy making it completely different to the experimental morphology of rutile which consists mainly of the {110}, {010} and {011} surfaces. The van Beest morphology shows better agreement to that of TiO_2 with large {110} and {010} components although the {221} surface is more pronounced than in the rutile case and there are no {111} surfaces present.

One of the difficulties when considering equilibrium morphologies is that the importance of a given surface may be determined by kinetic control. Although this is dependent on many properties work by Hartman and Bennema (1980) has suggested that the rate of growth of a surface can be related to the attachment energy. This attachment energy is essentially the energy given out when a slab of material binds onto the surface. As such it assumes bulk termination of the surface and thus does not take into account surface relaxation. Another energy which can be calculated is the surface excess which is the difference in energy between bulk and surface ions expressed per ion.

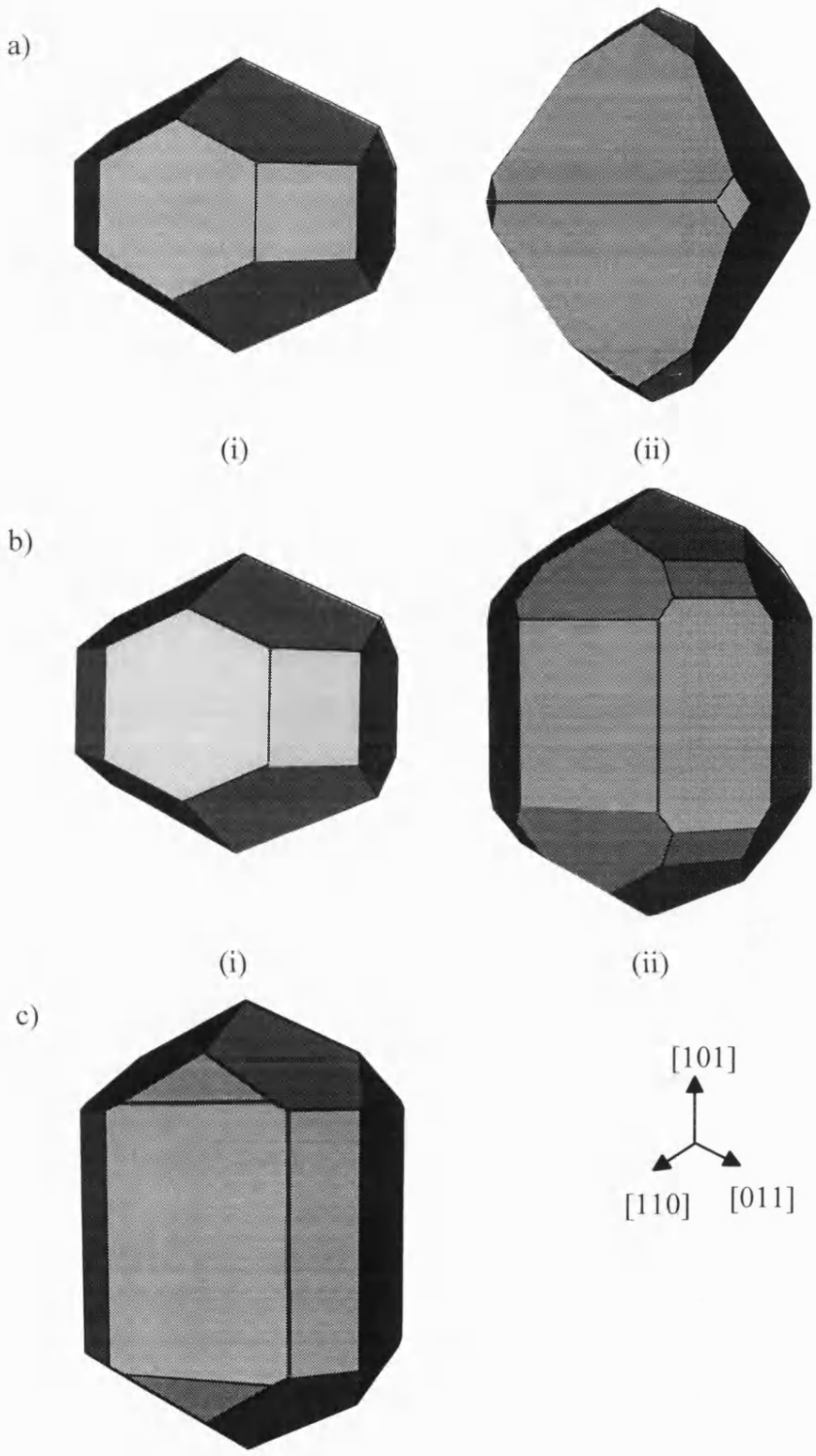

Figure 6.4 Calculated equilibrium morphologies i) before and ii) after relaxation from a) Sanders potential and b) van Beest potential.

c) Experimental morphology of TiO_2-rutile (Kostov 1968).

Table 6.7 shows the surface excess and attachment energies for stishovite. These gave kinetic morphologies of stishovite (fig 6.5) in which the {011} and {110} faces dominated. The fast growing faces, such as the {102} and {112}, would grow out quickly until they disappeared. The kinetic and surface excess morphologies for the van Beest potential are identical to each other and to the Sanders kinetic morphology whilst they are different to the Sanders equilibrium morphology. This suggests that the Sanders potential is incorrectly modelling the {221} surface leading to an equilibrium morphology which contains almost no other faces.

Index	Surface Excess (eV per uncoordinated Si on surface)				Attachment Energy (eV)	
	Sanders		van Beest		Sanders	van Beest
	unrelax.	relaxed	unrelax.	relaxed		
{001}	26.82	8.98	14.70	9.62	1.51	0.74
{100}	14.83	4.37	6.77	4.44	0.84	0.74
{101}	10.27	3.60	6.10	4.91	1.27	0.61
{102}	96.57	22.4	30.40	10.60	10.05	3.03
{201}	24.48	5.40	11.20	6.80	2.76	2.22
{110}	9.77	3.05	4.40	3.00	1.07	0.44
{111}	61.20	15.36	25.60	11.92	3.30	1.27
{112}	66.93	23.60	25.20	6.00	7.08	2.52
{121}	48.69	23.46	22.80	14.80	2.75	1.14
{122}	119.63	23.51	46.00	23.6	6.45	2.29
{210}	61.94	4.40	19.60	8.00	6.50	1.96
{221}	49.80	4.82	18.60	8.00	2.69	1.86

Table 6.7. Surface Excess and attachment energies for stishovite.

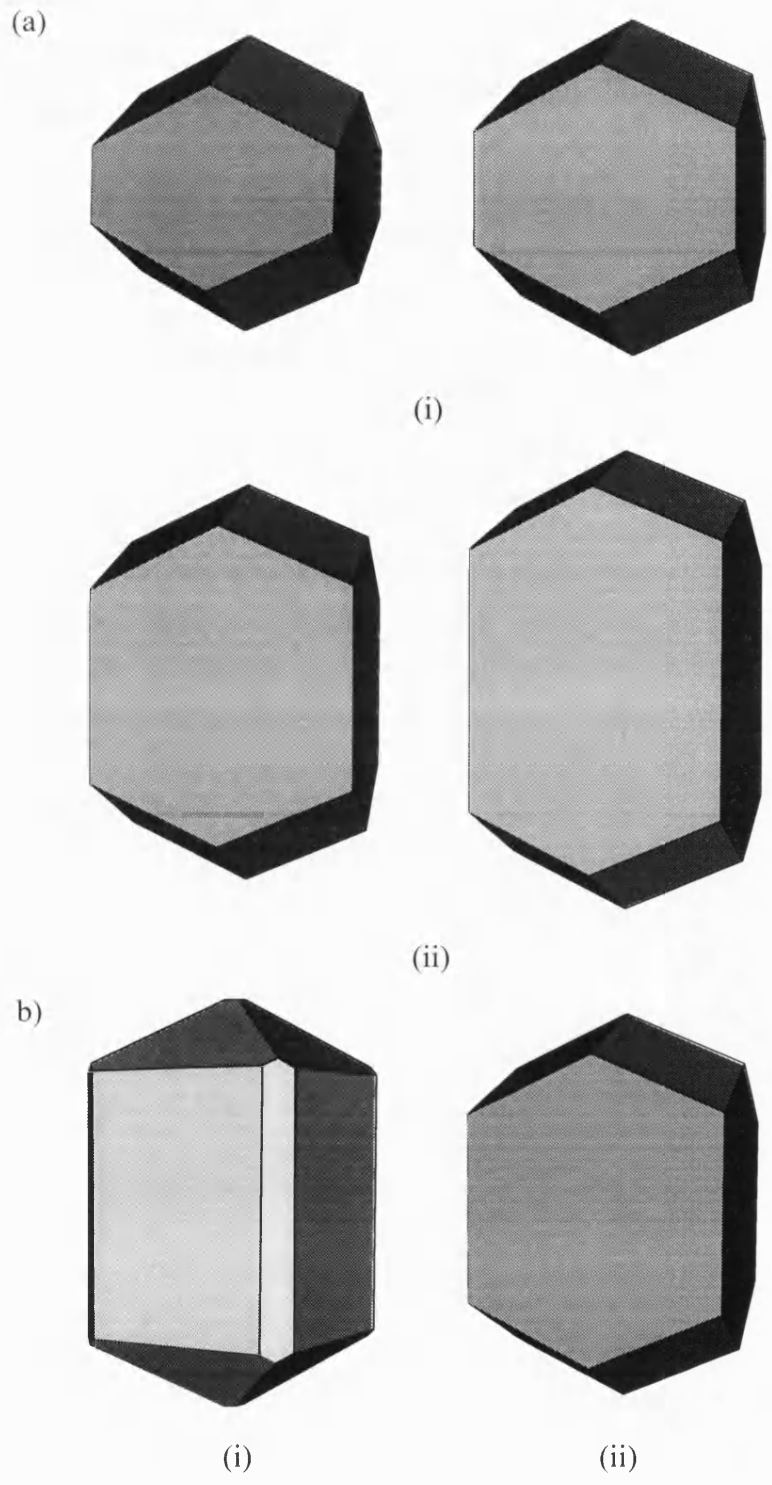

Figure 6.5 Morphologies derived from a) surface excess i) unrelaxed and relaxed Sanders, ii) unrelaxed and relaxed van Beest and b) attachment energies i) Sanders, ii) van Beest.

Directions are the same as for fig 6.4.

6.5 Grain Boundaries

A variety of low angle grain boundaries were selected for examination including the tilt (201), (210) and (301) boundaries and the mirror (101) and (301) boundaries which are a special type of tilt boundary where the two blocks are mirror images of each other. The (301) and (101) boundaries have previously been studied computationally and experimentally for TiO_2-rutile (Lee et al. 1993) and thus a comparison of the relative structures and stabilities can be made.

6.5.1 Static calculations

Starting points for minimisation for each of the grain boundaries were chosen using the DELTAMOVE program (see section 4.4.2) to generate a contour map as a function of YZ displacement. An example of one of these contour maps is given for the {201} boundary in figure 6.6. The contour plot shows that there are two low energy starting points for the minimisation which both generated identical boundaries upon minimisation.

The boundaries were minimised using the code METADISE and the static lattice properties were calculated for the van Beest potential. Initially the {201} and {210} boundaries were also modelled using the Sanders potential to allow comparison between the potentials. The resulting formation and adhesion energies (i.e. the energy to form the boundary from bulk material and the energy to separate the boundary into two surfaces respectively) are given in table 6.8.

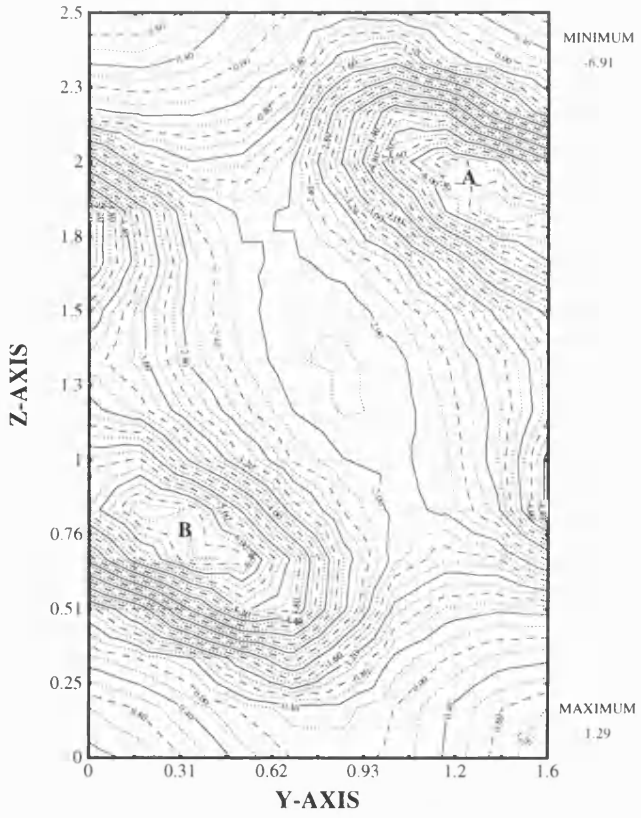

Figure 6.6. Contour plot for the {201} tilt grain boundary.

Boundary t=tilt m=mirror	Energies (Jm^{-2})			
	Sanders		van Beest	
	Formation	Adhesion	Formation	Adhesion
{201}t	1.80	2.78	3.30	4.40
{210}t	2.11	1.40	6.18	4.24
{301}t	-	-	4.82	2.74
{301}m	-	-	0.63	14.60
{101}m	-	-	0.51	7.24

Table 6.8. Calculated static formation and adhesion lattice energies for stishovite grain boundaries.

The structures of these boundaries using the van Beest potential are given in figure 6.7. From table 6.8 it is clear that the mirror boundaries are much more stable than their tilt counterparts.

Both potentials gave similar boundaries; the relaxed structure of the {201} boundary (figure 6.7a) contained pairs of silicon oxygen bonds linking the two grains across the boundary. The lengths of these cross links bonds were 1.62Å and 1.73Å respectively. The energies calculated using the van Beest potential were higher than the Sanders values which is similar to the trend calculated for the surface energies. The formation energy was also relatively high compared to the mirror grain boundaries as might be expected since the two grains were linked by very few bonds. This was reflected in the adhesion energy which was much lower than that of the mirror boundaries.

The minimised {210} grain boundary (figure 6.7b) also contained silicon oxygen cross links which were 1.70Å and 1.64Å in length. Again the Sanders potential gave a lower set of energies compared to the van Beest potential. The formation energy was higher than for the (201) boundary suggesting that the (201) tilt grain boundary would be formed preferentially to the (210) boundary. Since the van Beest and Sanders potentials gave similar trends for the {201} and {210} boundaries it was decided to continue using only the van Beest potentials for the static work since this potential had shown the best results during testing (see section 6.3).

The minimised {301} tilt boundary consisted of two cross links which were 1.80Å and 1.78Å in length. The grain boundary formation energy was higher than for the {201} suggesting this boundary would not be preferred.

The mirror boundaries contained symmetry of the silicon and oxygen ions as shown in figure 6.7c, d where the boundaries are indicated by the black lines. Comparison of the two {301} boundaries and the {101} boundary with the work of Lee et al. (1993) on rutile shows good agreement. They calculated the structure and energies of these three boundaries using the MIDAS program (Harding 1988) and then compared these to HREM images. They found that the {301} mirror boundary was more stable than the tilt boundary and that the {101} boundary was more stable than the {301} mirror as did we. The calculated and experimental structures showed good agreement with the structures calculated in this work.

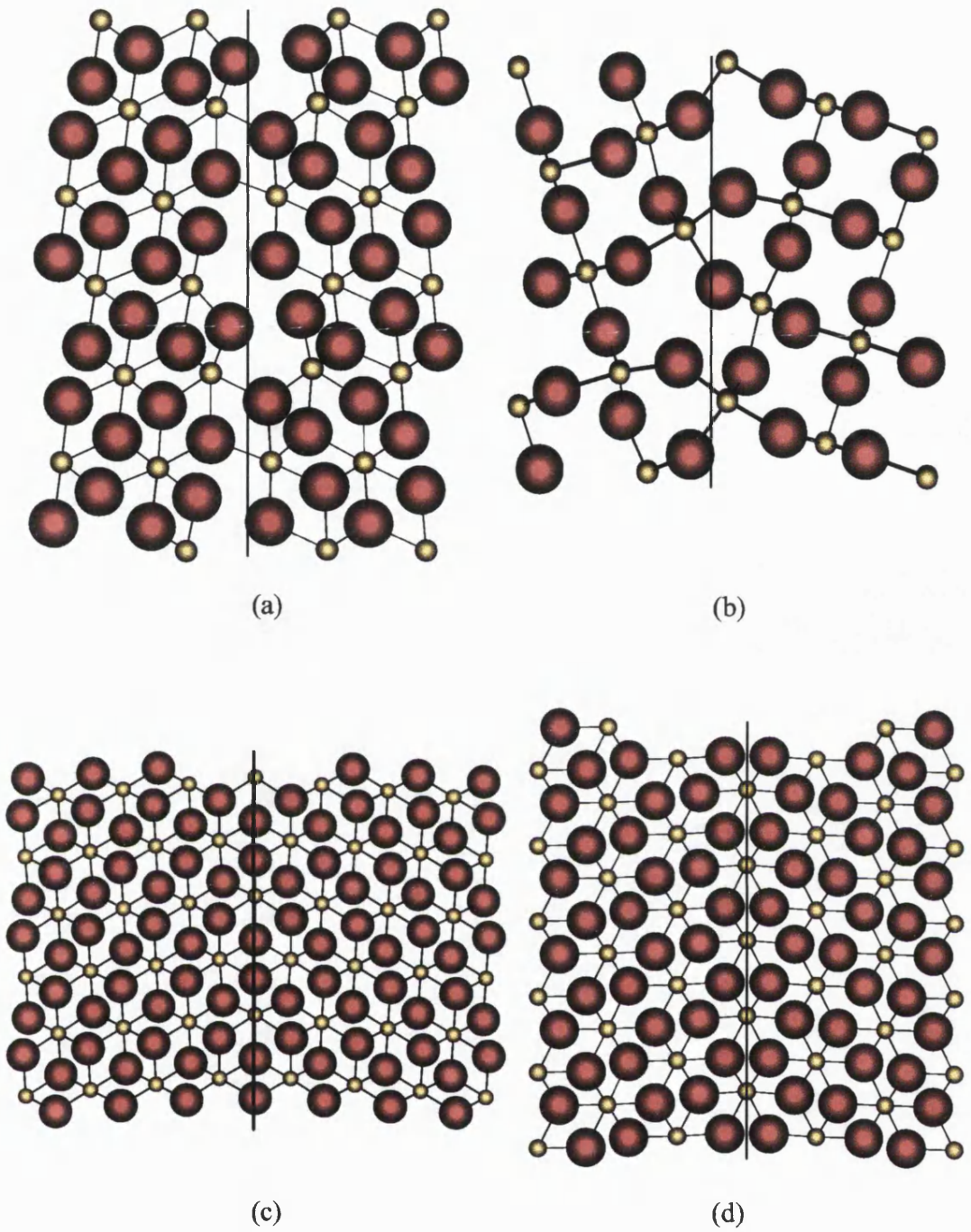

Figure 6.7. Relaxed structures of the a) {201}, b) {210}, c) {101} mirror and d) {301} mirror grain boundaries of stishovite. The black lines illustrate the position of the boundary in each case.

6.5.2 The Effect of Temperature and Pressure

The {201} tilt and the {101} and {301} mirror boundaries were chosen for calculating the effect of temperature and pressure on the structures and energies of these boundaries. Initially the {201} boundary was modelled using both potentials up to 1200 K and the van Beest potential up to 100 GPa and the Sanders up to 40 GPa. Above this pressure (at 45 GPa for bulk and 90 GPa for the boundary cell) the calculation using the Sanders potential broke down due to an imaginary phonon frequency in the [001] direction (figure 6.8). As discussed in chapter 5 this suggests a phase change in the material.

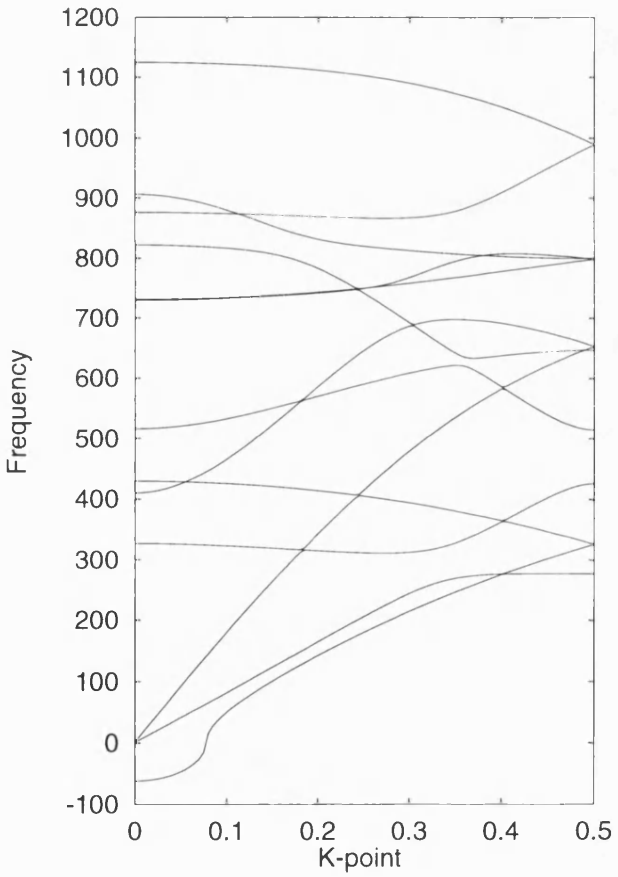

Figure 6.8 Phonon dispersion curve for stishovite along the [001] at 45 GPa showing the imaginary frequency.

Animation of the imaginary mode appeared to show the structure deforming to that of the $CaCl_2$ structure before the calculation broke down (Fig 6.9). This phase change has been seen experimentally (Tsuchida and Yagi 1989) by heating a sample of stishovite at pressures in excess of 108 GPa and greater and has been shown to be reversible. Attempts to minimise a $CaCl_2$ structure using the van Beest and Sanders potentials have both failed as the structure reverts to distorted structure midway between stishovite and $CaCl_2$.

For both potentials there was almost no structural or energy change with variation of temperature. Similarly to the MgO examples this was attributed to the low entropy of formation. Thus, for brevity, the following results are quoted at 600 K.

The {201} boundary showed a discontinuity in the plots of formation lattice energy at approximately 25 GPa (figure 6.10a). This was most noticeable for the Sanders potential which is due to the channel structure of the boundary collapsing slightly as a result of the applied pressure.

Above 25 GPa the Sanders potential gives a decreasing PV term, a result of the faster decrease in formation volume with pressure than is found for the van Beest potential. The van Beest shows a steady increase in all three energies up to 100 GPa. The faster collapse of the boundary for the Sanders potential may be a result of the underestimation of the repulsive O-O term as discussed in section 6.3.2.

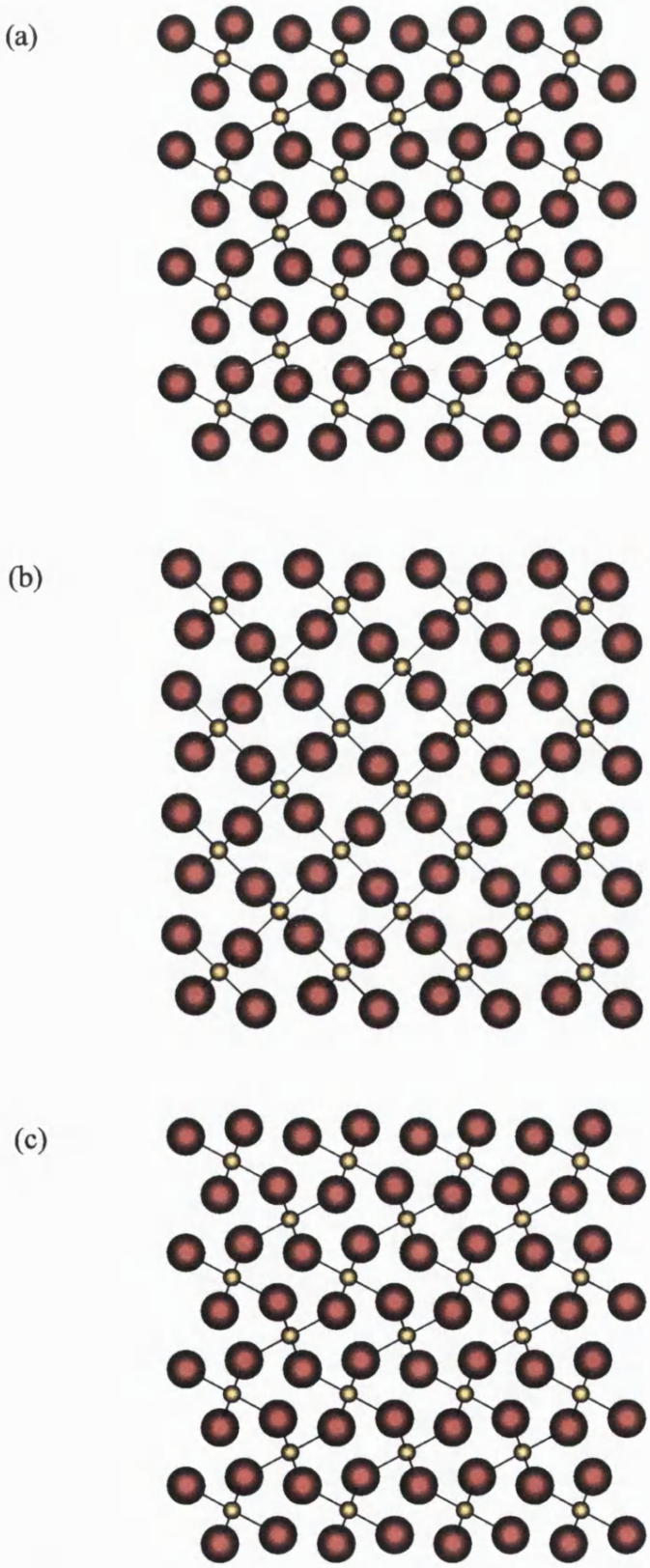

Figure 6.9. Vibration of the imaginary mode in bulk stishovite showing the transition from a) $CaCl_2$ to b) rutile to c) $CaCl_2$ structures.

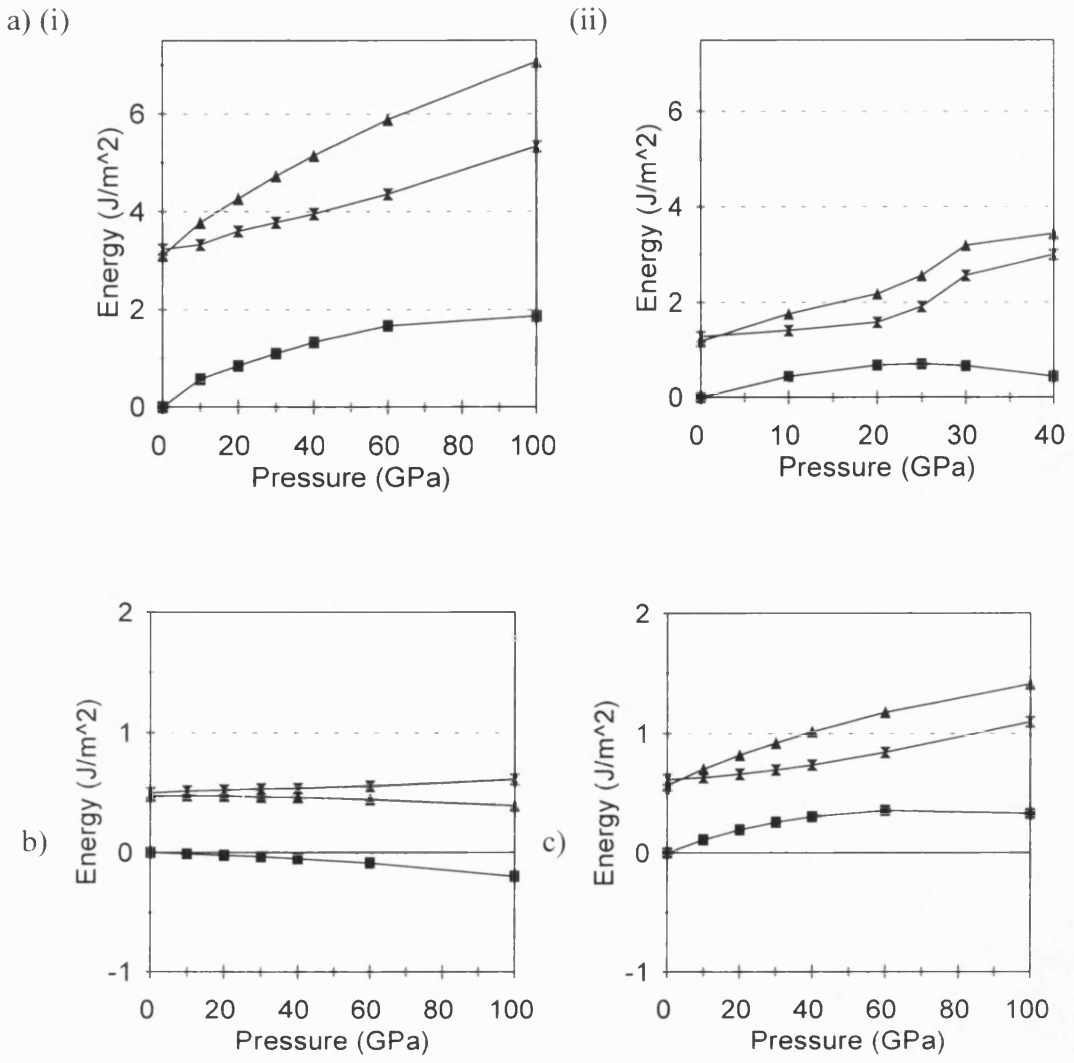

Figure 6.10. Formation energies for the a) {201} using the i) van Beest and ii) Sanders potentials, b) {101} and c) {301} tilt grain boundaries of stishovite using the van Beest potential. Squares represent PV, hourglasses lattice energy and triangles the Gibbs free energy.

The {101} mirror boundary showed almost no structural or energy changes as a function of temperature or pressure. As figure 6.10b shows the formation energies remained either constant or slowly decreased which was due to the boundary having such a bulk like structure. At higher pressures the volume of the boundary unit cell

was actually lower than that of bulk resulting in a negative PV term and thus a slight decrease in free energy. The {301} boundary showed slightly more effect with increasing pressure (figure 6.10c) although compared to the {201} boundary this change was small.

6.5.3 Effect of pressure on Mantle properties

The seismic wave velocities and heat capacities of the {201} tilt and {101} and {301} mirror boundaries were calculated and the resulting plots as a function of pressure are given in figure 6.11 compared to those of bulk. The seismic wave velocities were similar to those of bulk for the {101} and {301} boundaries due to their dense structure whereas the {201} velocities were lower due to the presence of the channel at the boundary, however there was a small discontinuity at approximately 20 GPa due to the channel collapsing slightly causing an increase in density.

The heat capacities were also similar to bulk for all the boundaries although again there was a slight discontinuity for the {201} boundary. Plots of the difference between bulk and boundary phonon densities of states revealed that the {201} boundary contained more of the lower frequencies, similar to that calculated for MgO, whilst the {101} and {301} boundaries there was no noticable difference. Examples of these plots are shown in figure 6.12 for the {201} and {101} boundaries.

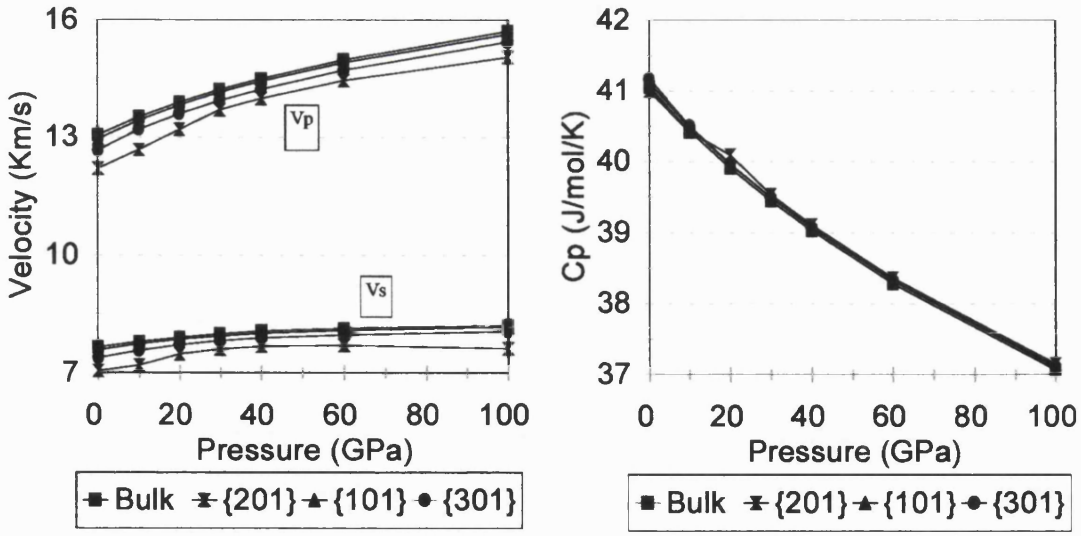

(a) (b)

Figure 6.11. Plot of a) seismic velocities and b) heat capacity

for stishovite grain boundaries as a function of pressure at 600 K.

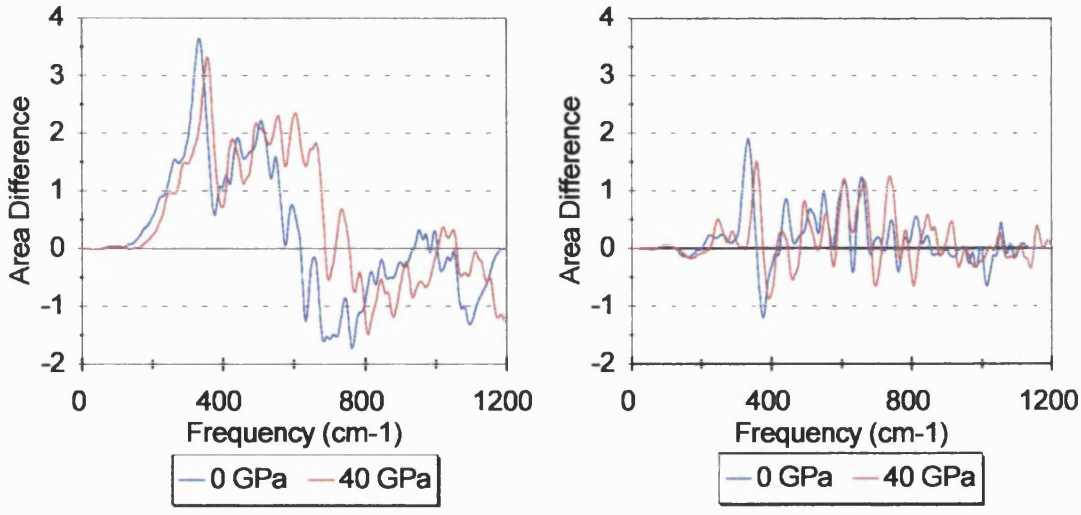

(a) (b)

Figure 6.12. Difference plots for phonon densities of states for the a) {201} and b)

{101} tilt grain boundaries of stishovite at 600 K.

6.6 Summary of Stishovite Calculations

Calculations to determine the morphology of stishovite demonstrated that the van Beest potential gave the best agreement with the experimental data available. This potential was used to calculate a number of grain boundaries of stishovite as a function of pressure and temperature. It was found that the tilt grain boundaries showed the largest variation of formation energy with pressure due to the open structure of the boundary unlike the mirror boundaries which were bulk-like. For both types of boundaries temperature had little effect upon both the structure and energies. Calculations of the mantle properties for each boundary showed that the mirror boundaries closely matched the properties of bulk.

6.7 Perovskite Grain Boundaries

$MgSiO_3$ Perovskite is commonly found within the Earth's lower mantle and is the end product of the phase transition between olivine, spinel and perovskite. The structure is orthorhombic with SiO_6 octahedra edge linked.

The empirical potential model of Matsui (1994) was used for perovskite. This potential was developed to be transferable within the $CaO\text{-}MgO\text{-}Al_2O_3\text{-}SiO_2$ (CMAS) system and uses a rigid ion model that describes the short range forces using a Buckingham potential (see table 6.9). Partial charges are used to represent the ions. The potential has previously been shown to reproduce structural data for $MgSiO_3$ which compares well with experimental values (Matsui 1994).

Three grain boundaries have been observed experimentally for perovskite which correspond to the {110} tilt, {112} tilt and a 90° twist about an axis

perpendicular to the (110) plane (White et al. 1985, Wang et al. 1990, Hu et al. 1992). However, we have only studied the tilt grain boundaries in this work.

(a)

Species	Charge (e)	Mass (g mol^{-1})
Si core	1.89	28.09
O core	-0.945	15.99
Mg core	0.945	24.305

(b)

Interaction	A (eV)	ρ (Å)	C (eV $Å^6$)
Mg - Mg	17648326.55	0.08	8.74
Mg - Si	367655325.24	0.063	14.84
Mg - O	32582.36	0.178	27.28
Si - Si	79937060336.29	0.046	25.19
Si - O	50197.87	0.161	46.29
O - O	6462.69	0.276	85.09

Table 6.9 . Potential parameters based on the rigid ion model potential of Matsui (1994). a) charges and masses, b) short range Buckingham parameters

6.7.1 The {110} tilt grain boundary

The stacking arrangement of perovskite results in several different possible cuts of the {110} plane however, we considered only grain boundaries composed of identical cuts. For each of these a DELTAMOVE plot was generated in order to find

the lowest energy starting point for grain boundary formation. Minimisation of the lowest energy configuration produced the structure shown in figure 6.13. The structure was very similar to bulk with the same coordination numbers. However, at the boundary the structure resembled a stacking fault with a layer of cubic perovskite between the opposite orthorhombic distortions on either side of the boundary. The static lattice formation energy for this structure was calculated to be 0.73 Jm^{-2}.

Free energy minimisation was performed on the boundary to determine the effect of pressures and temperature. For completeness pressures between 0 and 100 GPa and temperatures up to 1200 K were modelled, however, the quasi harmonic approximation began to break down for perovskite at temperatures above 1000 K for 0 GPa conditions causing the program to fail and thus no energies were calculated at 0 GPa for either the 1000 K or 1200 K structures. This was not a serious problem because the structure and energies of the boundary showed little variation due to temperature and results at 600 K will again be quoted. As has been the case for most of the grain boundaries studied in this work increasing pressure from 0 GPa to 100 GPa again had a great effect as the formation PV increased linearly and at a faster rate than the formation lattice energy (see figure 6.14) causing a linear increase in free energy from 0.57 Jm^{-2} to 2.37 Jm^{-2} (table 6.10). As expected the change in free energy was lower than had been seen for the MgO and stishovite boundaries which contained channels and more in keeping with that found for the bulk like boundaries of stishovite. There was no significant structural change up to 100 GPa which was probably due to the compact, almost bulk like, nature of the boundary.

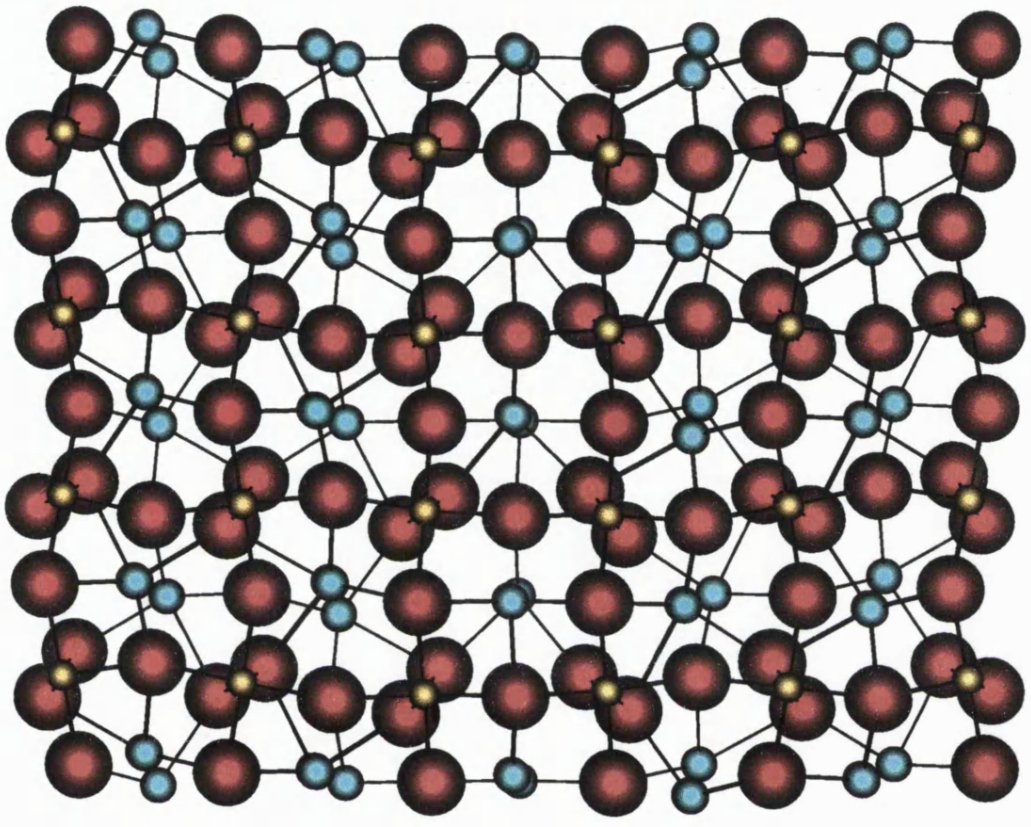

Figure 6.13. Relaxed structure of the {110} tilt grain boundary of perovskite.

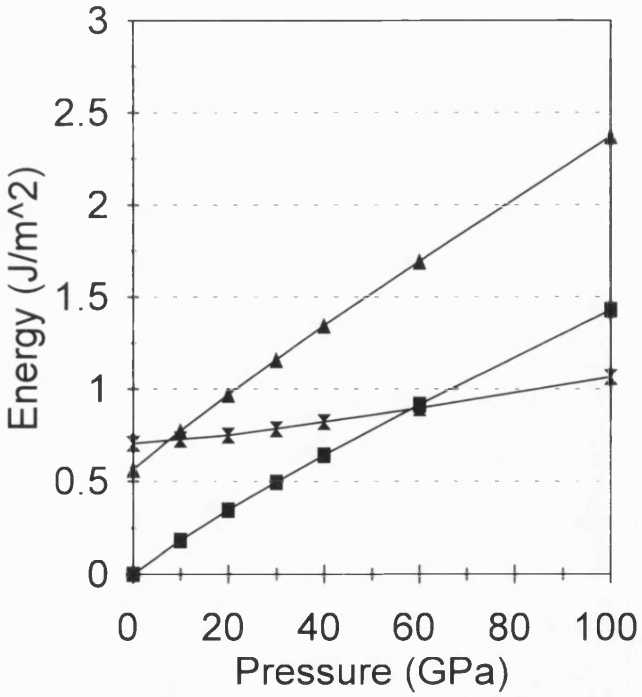

Figure 6.14. Formation energies of the {110} boundary of $MgSiO_3$ perovskite as a function of pressure. Squares represent the PV term, hourglasses the lattice energy and triangles the free energy.

Pressure (GPa)	Formation Free Energy (Jm^{-2})
0	0.57
10	0.77
20	0.97
30	1.16
40	1.34
60	1.69
100	2.37

Table 6.10. Formation free energies for the {110} tilt grain boundary of perovskite.

6.7.2 The {112} tilt grain boundary

Similarly to the {110} boundary several different cuts were possible for the {112} plane which produced several different grain boundaries. The structures of three of these are given in figure 6.15. Structure A was the least stable with a formation static lattice energy of 4.84 Jm^{-2}, structure B had an energy of 1.66 Jm^{-2} whilst structure C was the most stable with an energy of 0.55 Jm^{-2}. Structure C was bulk like with a slight variation in the stacking angle to either side of the boundary. In structure B the boundary was more noticeable with the presence of channels which limit the number of bonds across the boundary, hence the higher formation energy. This trend continued for the A structure which had larger channels and thus fewer cross links.

Free energy minimisation of structure C at pressures up to 100 GPa and temperatures up to 1200 K again showed that pressure had a greater effect than temperature. At 600 K there was a linear increase in formation free energy from 0.44 Jm^{-2} at 0 GPa to 1.65 Jm^{-2} at 100 GPa (figure 6.16 and table 6.11) whilst the structure did not undergo any significant structural change beyond a reduction in volume.

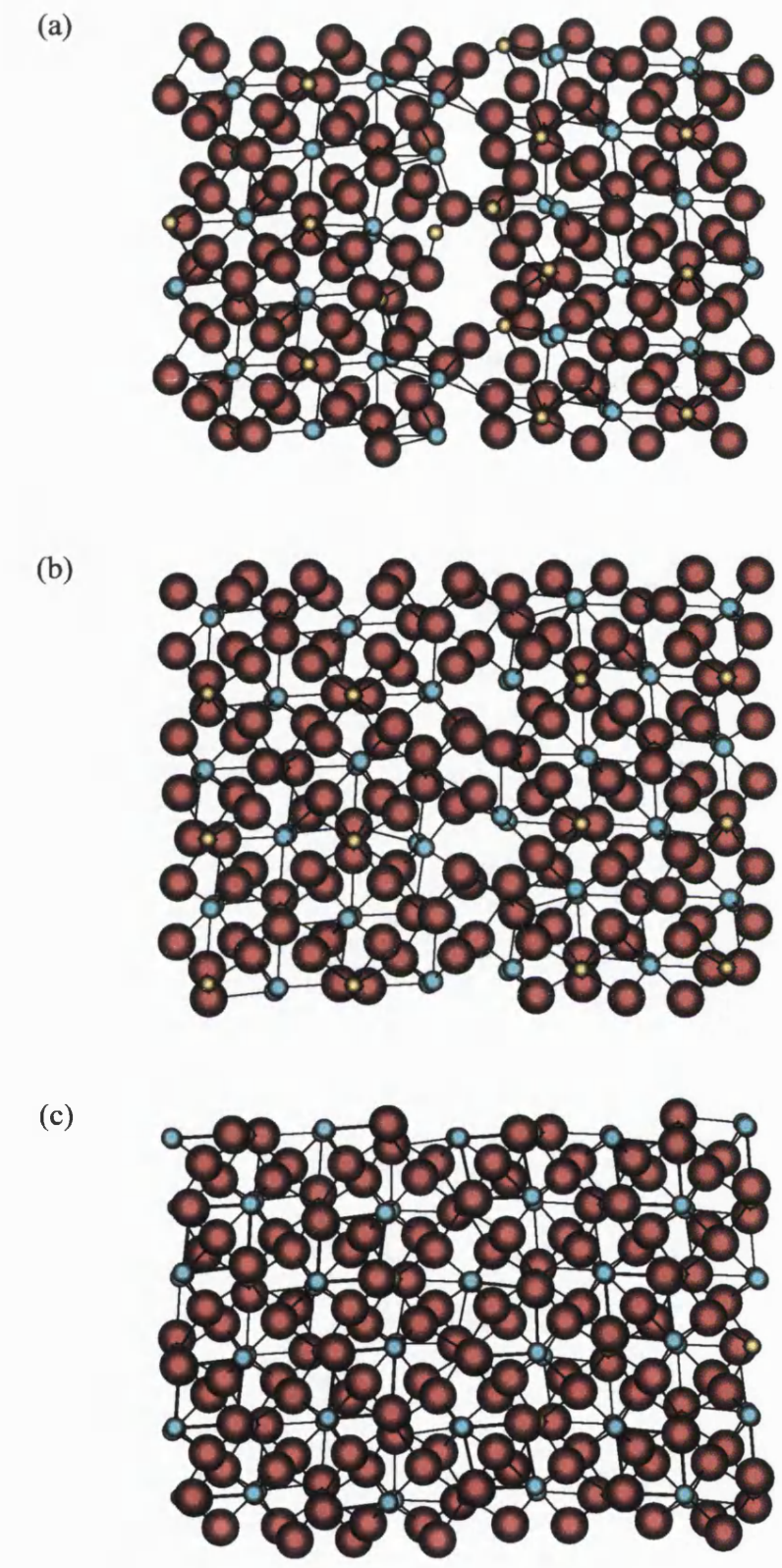

Figure 6.15. Possible structures of the {112} tilt grain boundary of $MgSiO_3$ perovskite at 0 GPa and 600 K.

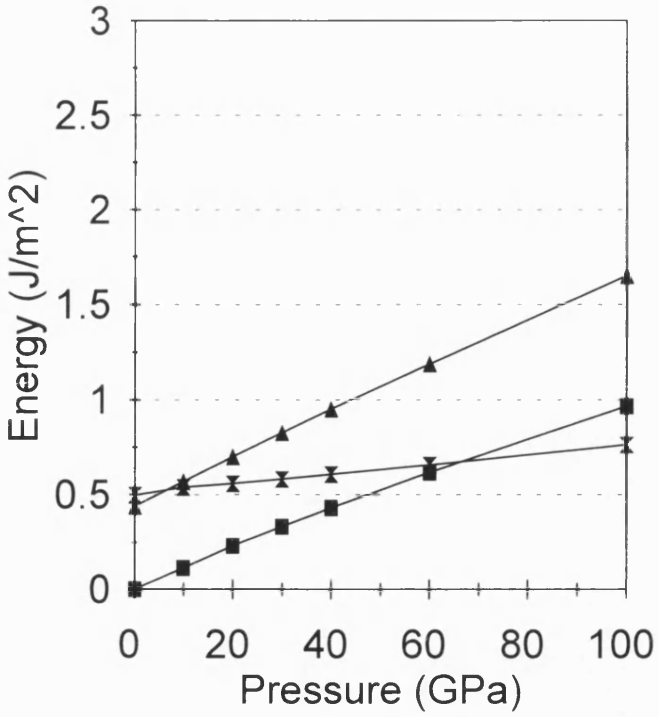

Figure 6.16. Formation energies of the {112} boundary of $MgSiO_3$ perovskite as a function of pressure. Squares represent the PV term, hourglasses lattice energy and triangles free energy.

Pressure (GPa)	Formation Free Energy (Jm^{-2})
0	0.44
10	0.57
20	0.70
30	0.83
40	0.95
60	1.19
100	1.65

Table 6.11. Formation free energies for the {112} tilt grain boundary of perovskite.

6.7.3 Effect of pressure on mantle properties

The seismic wave velocities and heat capacities were calculated as a function of pressure at 600 K for each of the boundaries and compared to the bulk values. The seismic wave velocities for both boundaries were comparable to each other and lower than the bulk values as shown in figure 6.17 indicating that the boundary was a region of lower density than the bulk despite their compact structure.

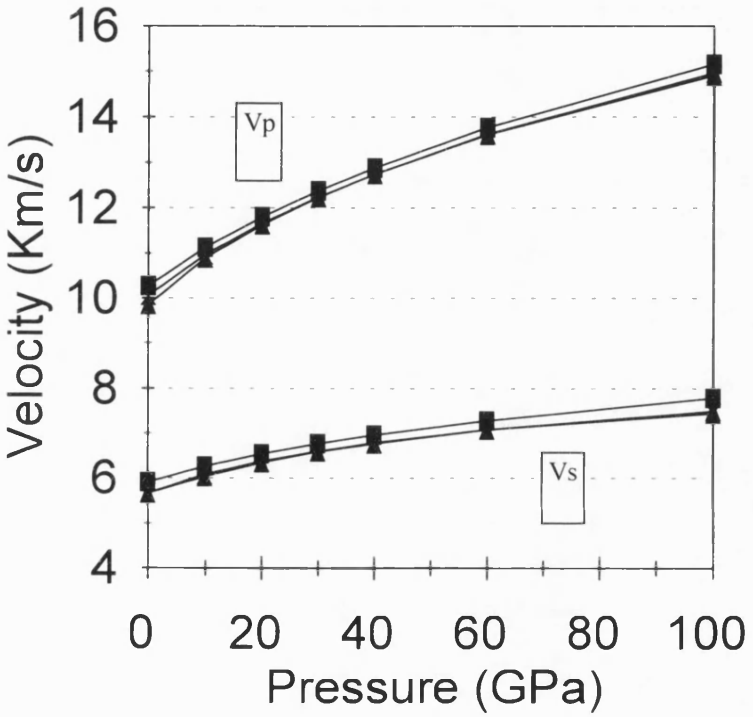

Figure 6.17. Calculated V_p and V_s as a function of pressure at 600 K for the {110} and {112} tilt grain boundaries of perovskite compared to bulk.
Squares represent bulk, hourglasses the {110} and triangles the {112} boundaries.

In the case of the heat capacities (figure 6.18) the values calculated for the boundaries were very similar to those calculated for bulk. As explained previously (see section 5.5) the heat capacity depends upon the phonon frequencies. Examination

of the phonon density of states indicated that there were a greater number of lower frequency vibrations in the boundary but less than had been calculated for the channel structures of stishovite (section 6.5.3) and MgO (section 5.5).

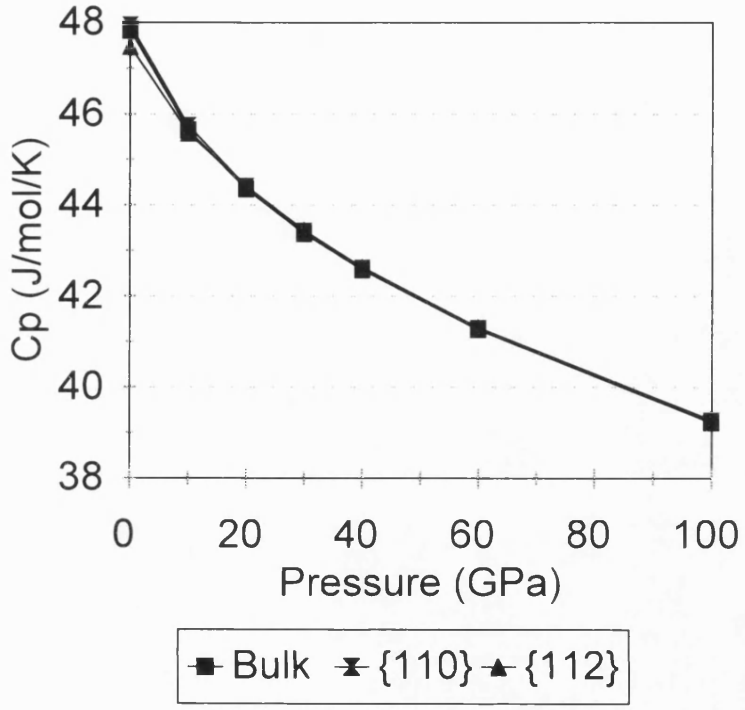

Figure 6.18. Calculated heat capacities as a function of pressure.

6.7.4 Summary

Calculations have been performed on two grain boundaries of perovskite, the {110} and {112}, using the Matsui potential. The boundaries were very compact although the {110} boundary did contain a distortion from orthorhombic to cubic. For both boundaries there was an increase in formation energy with increasing pressure whilst temperature had little effect. Mantle properties were almost identical to those calculated for bulk.

6.8 Conclusions

The structure and energies for a number of surfaces of stishovite and grain boundaries of stishovite and perovskite have been calculated. Crystal morphologies of stishovite have been elucidated from the calculated relaxed surface energies. The van Beest potential gave a morphology which was in reasonable agreement with the experimental data, however there were problems with the Sanders potential. It was unable to correctly model the structural properties of stishovite, which may have been a result of the underestimation in the O-O nearest neighbour repulsion. This is in part due to the fact that the potential was derived for quartz and not tested on stishovite. The kinetic morphologies calculated from the surface excess showed better agreement with each other and with experiment, although the attachment energy morphologies still differed with the Sanders potential giving a different morphology to that of the van Beest.

Several grain boundaries have been calculated for stishovite as a function of pressure and temperature and, for the (101) and (301) grain boundaries, showed good agreement with the previous study carried out on TiO_2-rutile (Lee et al. 1993) at low pressure. A direct comparison with experimental work on stishovite itself is not possible due to the lack of experimental work carried out on this material. A key reason for this is the problems involved with reproducing the very high pressures of the lower mantle under experimental conditions. Temperature was not found to have a large effect upon the structure and energies of the boundaries in contrast to that of pressure. The tilt grain boundaries showed a large increase in the formation free energy with increasing pressure due to the open structure at the boundary whereas the mirror boundaries, which were almost bulk like in structure, showed little effect.

Mantle properties such as the heat capacity were found to be similar to the bulk whilst the seismic wave velocities decreased in the order {101}>{301}>{201}, i.e. as the density of the boundary decreased.

The perovskite boundaries considered were also very compact with the {112} boundary bulk like and the {110} boundary containing a distortion from orthorhombic to cubic within the boundary. There were no significant structural changes as a function of pressure beyond a decrease in volume with increasing pressure. Again the heat capacities were very similar to the bulk and the seismic wave velocities of the two boundaries were almost identical and both were slightly lower than the bulk.

In summary we have again shown that temperature has little effect upon the grain boundary structure whereas pressure has a much larger effect. This is due primarily to the PV term in the free energy since in all cases the change of PV term with pressure was greater than the change of lattice energy. This suggests that grain boundaries which are not bulk like will become destabilised as a function of depth in the Earth.

The generation of boundaries using the methods described in the previous chapters can lead to several possibilities for further work. Firstly the simulation of boundaries between materials of different composition, for example between MgO and SiO_2. Secondly, the structures generated can be used to determine the pathways and energies for diffusion at grain boundaries. An approach for calculating the diffusion will be covered in the following chapter.

7 Vacancy Migration at Boundaries in MgO and stishovite

7.1 Introduction

In this chapter are presented the results of calculations to investigate the effect of pressure upon the self diffusion pathways and activation energies at tilt grain boundaries in MgO and stishovite. The rate and pathway of diffusion along grain boundaries are important for understanding the rheology of polycrystalline phases as this gives information on the mechanism by which the grains slide. As such they are vital in understanding processes such as creep (Poirier 1985) which is believed to be a mechanism for convection within the mantle (Anderson 1989). However, the variation of the mantle's viscosity as a function of depth is poorly constrained, with little information regarding the creep behaviour of lower mantle materials (primarily $(Mg,Fe)SiO_3$ perovskite, (Mg,Fe)O and SiO_2, stishovite) at mantle conditions. Such an understanding is required if the dynamics of the mantle are to be understood.

Experiments to measure the rheological behaviour of minerals under mantle conditions are at present difficult due to the high temperatures and pressures required. Simulations have been performed to study defect formation in bulk MgO (Mills et al. 1991) which indicated that the defect formation volume is important and highly dependent on pressure. More recently Vocadlo et al. (1995) calculated the activation energies for self diffusion in MgO as a function of temperature and found that the energies decreased with increasing temperature whilst the migration volume increased.

Although these studies have all considered bulk MgO, real materials are polycrystalline and hence contain grain boundaries. There is considerable evidence to

suggest that grain boundaries are regions of high diffusivity in ionic crystals. Atkinson and Taylor (1981) measured the grain boundary diffusion coefficient in polycrystalline NiO, a compound isostructural with MgO, and found the activation energy to be significantly lower than for bulk diffusion in single crystal NiO (Atkinson and Hughes 1981). Duffy and Tasker (1986) used computer simulation to calculate the activation energy for cation vacancy hopping in the {310}/[001] symmetric tilt grain boundary of NiO and also found that the activation energy was lower than the bulk value.

7.2 Methods

7.2.1 Defect Calculation

Two different methods are available for the calculation of defect energies, notably the Mott-Littleton approach (Mott and Littleton 1938) employed in programs such as CASCADE (Leslie 1982) and CHAOS (Duffy and Tasker 1983c) and the super cell approach (Harding 1990), used in this work, in which the defect is placed within a cell using periodic boundary conditions. Although Coulombic interactions between defects and their images are removed in PARAPOCS and a correction is made for the defect's charge, short range interactions are still important and thus the cell must be made large enough to reduce these interactions as much as possible. In the case of Molecular Dynamics the Coulombic interactions between defects are not removed which can lead to a small error in the energy proportional to the inverse of the defect-defect separation (r^{-2}), therefore large cells are used to minimise this error. The defect energy is calculated by comparing the energy of a defective cell with a similar non-defective cell.

7.2.2 Calculation of Diffusion Pathways

Previous simulations of ionic diffusion along grain boundaries have used static lattice techniques in which the moving ion is systematically fixed at a series of positions whilst the rest of the cell is allowed to relax around it (Duffy and Tasker 1986). However, the difficulty in locating the saddle points and the number of possible pathways that must be considered proved to be time consuming. In this work we have used a new MD method for locating diffusion pathways and calculating activation energies for vacancy migration.

The difficulty in using traditional Molecular Dynamics for modelling diffusion is that when the activation energies is much greater than the thermal energy available diffusion will not take place over the timescale of the simulation and hence the pathway and activation energy can not be identified except at very high temperatures or by using extremely long runs as exemplified by Meyer et al. (1996). We chose a different route, not least because we also wanted to calculate the diffusion processes for the slowest moving species, upon which the creep of crystals is based. We have, therefore modified a MD code to directly calculate diffusion pathways and activation energies. This was achieved by setting up the simulation cell such that there was one vacancy per cell and applying a small force to an adjacent ion in the direction of the vacancy. The force was added such that the net force on the moving ion always contained a small component in the direction of the vacancy thus moving it toward the vacancy but also allowing perpendicular movement. A counter force equal but in the opposite direction was spread over the remaining ions thus ensuring no translational momentum was added to the cell.

In addition, the volume was kept constant at the volume obtained from the MD simulation described in chapter 5 under NPT conditions and the velocities of the ions were scaled each step to ensure that no net kinetic energy was added to the system from the applied forces. Thus we were simply allowing the crystal to relax as the ion moved from one site to another such that the pathway perpendicular to a line joining the starting and finishing positions was not constrained.

7.3 MgO

We have considered cation and anion vacancy formation and migration in the {410}/[001] symmetric tilt grain boundary of MgO as a function of pressure. The {410} grain boundary of MgO was chosen for several reasons. Firstly MgO is an important ceramic and mineral (believed to be a significant component of the lower mantle). Secondly, it is a simple face centred cubic crystal which makes it ideal as a model system. Thirdly, previous calculations have been carried out for bulk MgO which can be utilised for determining the validity of our approach. Finally, as described in chapter 5 the {410} grain boundary had been modelled as a function of pressure using LD and MD which had shown an interesting structural transition under high pressure (see chapter 5). This allowed us to identify reasonable starting configurations for the MD simulations.

The forces between the ions were evaluated at each time step using interatomic potentials of which two, those of Sangster and Stoneham (SS) (1981) and Lewis and Catlow (LC14) (1985), were chosen initially to provide some verification of the results i.e. those properties that are insensitive to the potential parameters are considered more reliable. These potentials differ in the values of the parameters in the

analytical expressions used to describe the short range interactions. The potential parameters have been described in chapter 4.

Normally these potentials incorporate a shell model (Dick and Overhauser 1958) to simulate the electronic polarisability of the ions. The size of the cell that would be needed combined with the very short time step required meant that a rigid ion model was needed if all possible pathways were to be considered

7.3.1 Vacancy Formation at the Interface

The first step was to calculate the formation energies and thus identify the most stable sites and for both magnesium and oxygen vacancies. After applying a simple mass action treatment we could evaluate the relative concentrations of the vacancies in the grain boundary compared to the bulk.

The simulations required simulation cells of 960 atoms to minimise defect - defect interactions between cells. Several sites were available for defect formation at the boundary as shown for the 0 GPa structure in figure 7.1 where L and R are used to distinguish similar sites to the left and right of the boundary. It should be noted that positions A and A' on the figure legend are equivalent sites.

Table 7.1 shows the partial Schottky energies for these sites at 0 and 40 GPa from MD of the 300 K structures at constant volume and static lattice calculations using both the rigid ion and shell models for the SS and LC14 potentials. The Schottky energy is defined as the energy required to create (in the case of MgO) a pair of vacancies and place the ions at the bulk edge, forming new crystal. Since we were interested in single vacancies we have defined partial Schottky energies as the energy to remove a single ion with the bulk energy term defined as the energy of the same ion

within the bulk structure. Although the partial Schottky energies are not measurable experimentally they are useful as a comparison of relative site stabilities. The results in table 7.1 show that the two different models (LC14 and SS) gave similar results, in each case the rigid ion potentials gave slightly higher energies than the corresponding shell potentials for each vacancy position and that the MD and static lattice calculations are in accord.

At 0 GPa the positions marked A and D in figure 7.1 had the lowest partial Schottky energies for both cation and anion vacancies with approximately equal energies. In addition, these energies were lower than those for bulk, for example, the partial Schottky energy for magnesium vacancies is 3.53 eV at site A and 3.69 eV at site D compared to a bulk value of 4.16 eV using the LC14 rigid ion potential. On increasing the pressure to 40 GPa the order of stability of the site energies remains the same although the sites A and D are relatively more stable than the other sites in the boundary or bulk, i.e. the magnesium vacancy is 2.49 eV more stable in site A than in the bulk at 40 GPa compared to 0.63 eV at 0 GPa. The reason for the site energies being identical at 40 GPa was that when the vacancy was placed at either position D or A' then the ion at the other site hopped into an interstitial position between the two sites giving rise to identical structures (figure 7.2). Site B also had lower Schottky energies at 40 GPa than at 0 GPa whilst sites C and E became slightly less stable as the pressure increased.

The good agreement between the rigid ion and shell model potentials suggests that it is a reasonable approximation to use the rigid ion model for these simulations. Additionally, since the LC14 and SS potentials gave reasonably good agreement with each other we have continued with only one potential for evaluating the activation

energies, the LC14 potential. We chose this potential because it is the most compatible with silicate potentials such as THB1 (Parker and Price 1989) and would therefore allow direct comparison if future work considers heteroepitaxial interfaces, i.e. for diffusion between grains of different composition.

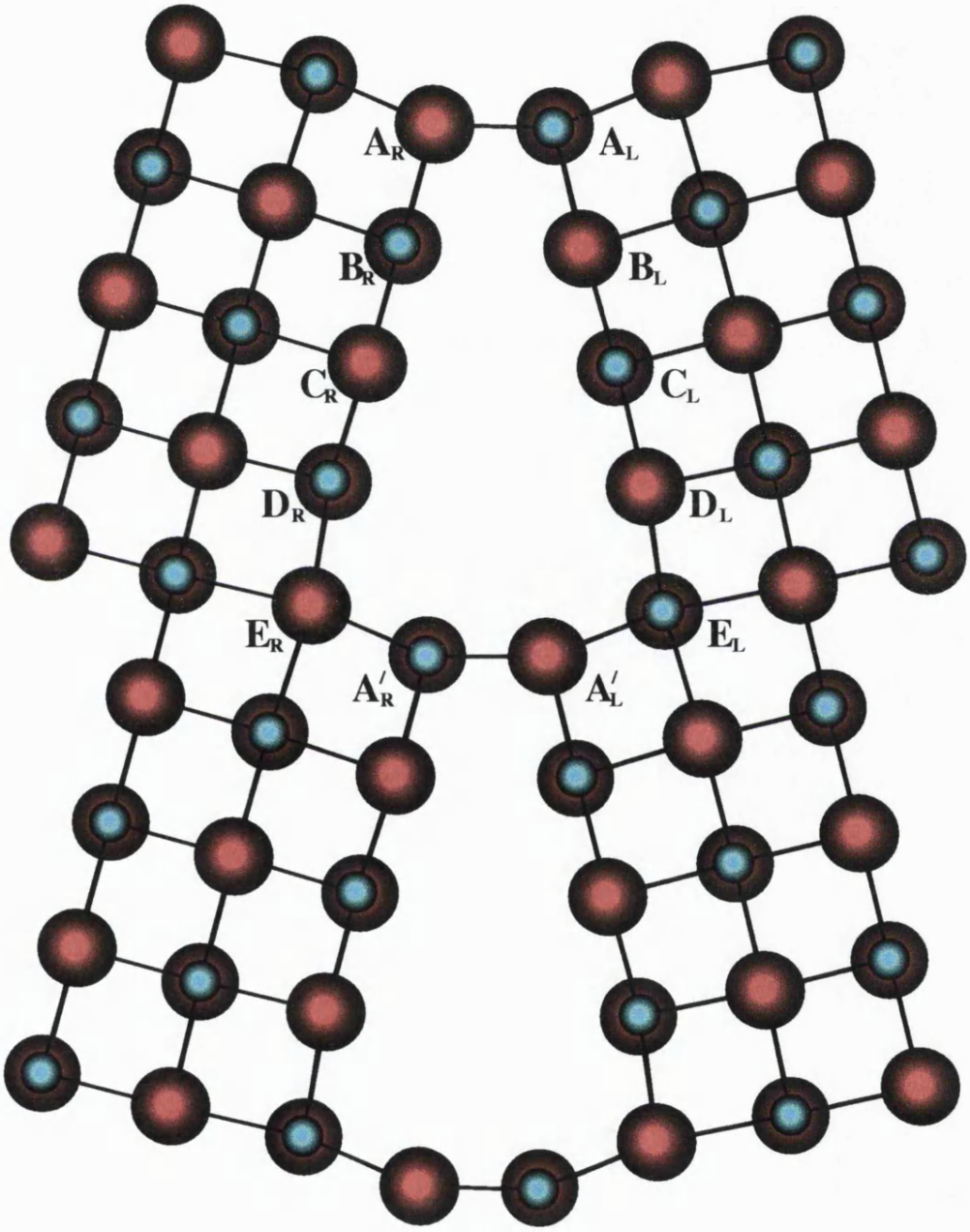

Figure 7.1. Sites for vacancy formation in the {410} tilt grain boundary of MgO.

Vacancy Site (type)	Potential Model				
	MD LC14	LC14 (ri)	LC14 (sh)	SS (ri)	SS (sh)
A (Mg)	3.32	3.53	3.26	3.30	3.09
B (Mg)	3.81	4.11	3.73	3.90	3.60
C (Mg)	3.92	4.21	3.84	3.97	3.68
D (Mg)	3.31	3.69	3.24	3.41	3.07
E (Mg)	4.61	4.99	4.40	4.84	4.40
Bulk (Mg)	3.63	4.16	3.55	3.92	3.47
A (O)	3.77	3.97	3.75	3.63	3.44
B (O)	4.21	4.44	4.35	4.15	4.02
C (O)	4.35	4.59	4.37	4.27	4.07
D (O)	3.71	4.05	3.96	3.68	3.59
E (O)	4.99	5.34	5.10	5.11	4.92
Bulk (O)	4.08	4.62	4.27	4.24	3.99

Table 7.1a. Cation and anion partial Schottky energies (in eV) for the {410} tilt grain boundary of MgO calculated using static lattice energy minimisation with the rigid ion (ri) and shell (sh) model versions of the Lewis-Catlow (LC14) and Sangster-Stoneham (SS) potentials and using molecular dynamics (MD) with the rigid ion Lewis-Catlow potential at 0 GPa.

Vacancy Site (type)	Potential Model				
	MD	LC14 (ri)	LC14 (sh)	SS (ri)	SS (sh)
A (Mg)	2.12	2.43	2.03	2.01	1.71
B (Mg)	3.56	3.67	2.98	3.32	2.78
C (Mg)	4.62	4.73	4.18	4.58	4.18
D (Mg)	2.07	2.43	2.03	2.01	1.71
E (Mg)	5.07	5.32	4.32	5.05	4.28
Bulk (Mg)	4.42	4.92	4.09	4.67	5.22
A (O)	2.83	3.08	2.63	2.49	2.12
B (O)	4.06	4.16	3.95	3.69	3.52
C (O)	5.16	5.23	4.88	4.96	4.68
D (O)	2.78	3.08	2.63	2.49	2.12
E (O)	5.58	5.80	5.48	5.41	5.16
Bulk (O)	4.94	5.47	4.99	5.06	5.87

Table 7.1b. Cation and anion partial Schottky energies (in eV) for the {410} tilt grain boundary of MgO calculated using static lattice energy minimisation with the rigid ion (ri) and shell (sh) model versions of the Lewis-Catlow (LC14) and Sangster-Stoneham (SS) potentials and using molecular dynamics (MD) with the rigid ion Lewis-Catlow potential at 40 GPa.

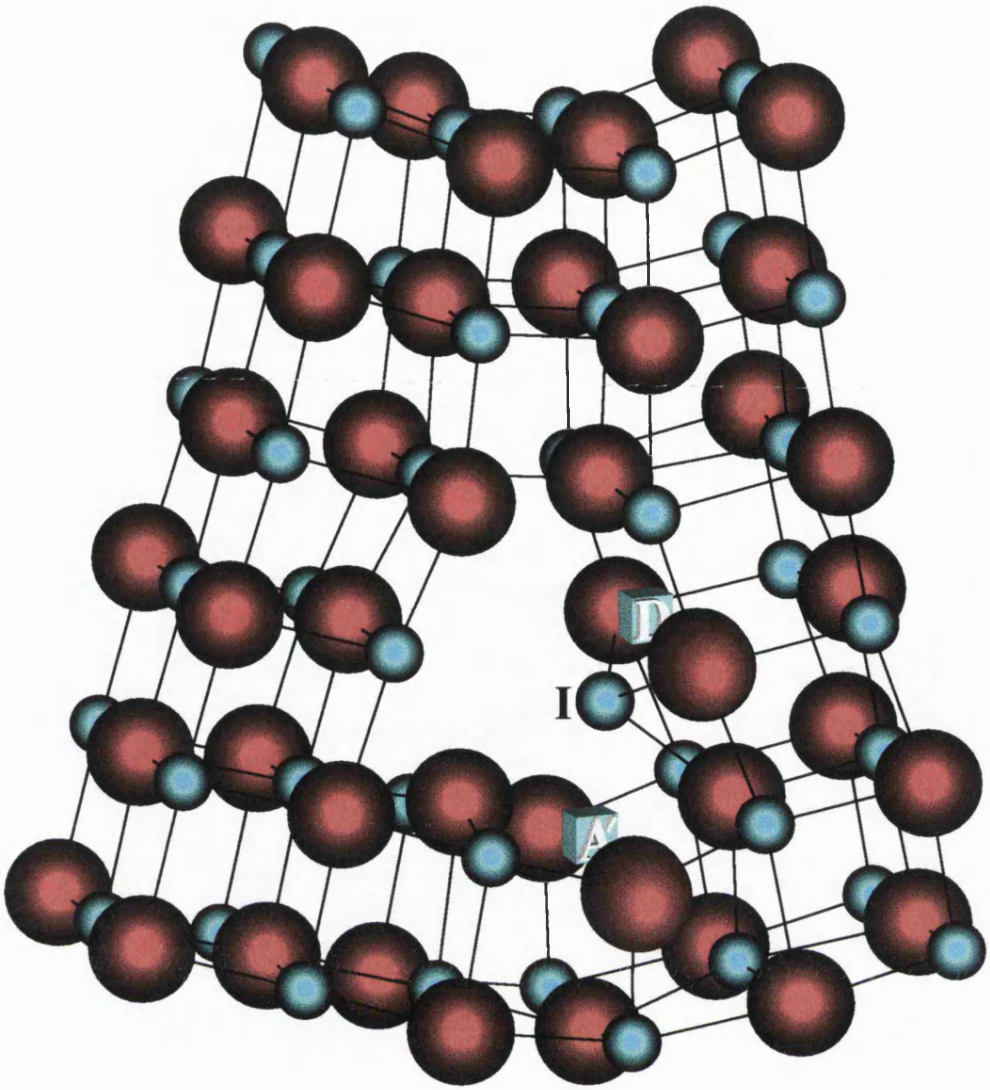

Figure 7.2. Structure of the {410} boundary at 40 GPa with vacancies at sites D and A' and an interstitial (I) between these sites.

7.3.2 Relative vacancy concentrations at the boundary

The low partial Schottky energies found for the majority of the sites at the boundary compared to the bulk suggest that vacancy concentrations will be greater at the boundary than in bulk MgO. As the relative diffusivity in the bulk and at the boundary depend on the relative concentration of mobile species we need a

quantitative estimate of the relative defect concentrations. In addition, as we are considering charged species, the calculation of the relative defect concentrations should also include a treatment of the space charge and hence we follow the work of Duffy and Tasker (1984) for the determination of space-charge effects.

For a bulk crystal with N sites available for vacancy formation, the fraction of bulk sites occupied by vacancies (n_0) to total sites (N), assuming that all the vacancies are thermally generated, is given by:

$$\frac{n_0}{N} = \exp\left[-\left(\frac{F^{Mg} + F^{O}}{2kT}\right)\right] \qquad 7.1$$

where F^{Mg} and F^{O} are the bulk partial Schottky energies. The fraction of sites (n_b) occupied at a grain boundary with N_b available low energy sites in the boundary plane is given by:

$$\frac{n_b}{N_b} = \left(\frac{n_0}{N}\right)\exp\left(-\left[\frac{F_I^{Mg} + F_I^{O}}{2kT}\right]\right)(1+\delta) \qquad 7.2$$

where $F_I^{Mg} = F_B^{Mg} - F^{Mg}$ and $F_I^{O} = F_B^{O} - F^{O}$ (F_B^{Mg} and F_B^{O} are the boundary partial Schottky energies), and δ is given by:

$$\delta = \frac{\left(2\kappa^{-1}\left(\frac{N}{N_b}\right)\exp\left[\frac{F_I^{Mg}+F_I^{O}}{2kT}\right]\sinh\left[\frac{F_I^{Mg}-F_I^{O}}{4kT}\right]\right)}{\left(1+\kappa^{-1}\left(\frac{N}{N_b}\right)\exp\left[\frac{F_I^{Mg}+F_I^{O}}{2kT}\right]\cosh\left[\frac{F_I^{Mg}-F_I^{O}}{4kT}\right]\right)} \qquad 7.3$$

where κ^{-1} is the screening length given by:

$$\kappa^{-1} = \left(\frac{\varepsilon_0 \varepsilon kT}{2e^2 n_0}\right)^{\frac{1}{2}} \qquad 7.4$$

For the purposes of this treatment we considered only the lowest energy A site in the {410} boundary. For our simulation cell at 1500 K and 0 GPa we found N to be $5.4\text{x}10^{28}$ m^{-3} and N_b is $2.7\text{x}10^{18}$ m^{-2} and thus the ratio of the fraction of boundary sites to bulk sites occupied was calculated as 11.4. In contrast, at 40 GPa and 1500 K the ratio was calculated to be $4.3\text{x}10^{7}$. These ratios demonstrate that at low pressures the relative defect concentration will cause an enhancement in diffusivity and the effect is greatly amplified at higher pressures. These factors may be further modified by the difference in the relative activation energies for migration which is discussed in the following sections and by the presence of impurites such as calcium and iron which are commonly found in the mantle.

Furthermore, the results suggest that there will be equal concentrations of cation and anion vacancies. Therefore we considered bound magnesium oxygen vacancy pairs at the grain boundary which may affect the migration properties of the vacancies.

Using the equations given previously the relative concentration of bound pairs at the boundary relative to isolated vacanciès in the bulk was calculated, and clearly as bound pairs are charge neutral the value of δ given in equation 7.3 is zero. The Schottky energies for a bound pair at the A site in the boundary were calculated as 4.26 eV at 0 GPa and 0.19 eV at 40 GPa. This resulted in boundary to bulk defect concentration ratios of $6.30\text{x}10^{5}$ at 0 GPa and $2.57\text{x}10^{15}$ at 40 GPa, much higher than those calculated for isolated vacancies at the boundary.

In summary, there will be an enhancement of vacancies at the boundary but the low Schottky energies suggest that there will be higher concentrations of magnesium and oxygen vacancies which will be largely bound together.

7.3.3 Diffusion Path for Isolated Vacancies in the Bulk

Previous calculations on diffusion properties have used static lattice calculations in which the moving ion is held fixed at the point estimated to be the saddle point of the migration whilst the rest of the cell is allowed to relax around it. Using this method Mackrodt and Stewart (1979) calculated activation energies for vacancy migration of 2.16 eV for magnesium and 2.38 eV for oxygen in bulk MgO. More recent calculations using the SS potential (Sangster and Stoneham 1981) by Vocadlo et al. (1995) predicted activation energies of 1.99 eV for magnesium and 2.00 eV for oxygen. Experimental activation energies for magnesium vacancy migration are available which include values of 2.28 eV (Sempolinski and Kingery 1980) and 1.57-3.46 eV (Freer 1980). In addition NMR relaxation times have been used to estimate activation energies at 800 °C. This gives rise to 2.00 eV and 1.56 eV for oxygen and magnesium respectively (Fiske et al. 1994).

In order to test the viability of our approach we initially calculated diffusion pathways and activation energies for cation and anion vacancy migration in bulk MgO. The rest of the crystal was kept at 10 K, using constant energy scaling, to allow the ions to relax around the moving ion. A plot of the lattice energy of the cell with respect to the distance travelled by the moving magnesium vacancy at 0 GPa is shown in figure 7.3. This gave an activation energy of 1.94 +/- 0.1 eV for magnesium diffusion and 2.12 +/- 0.1 eV for oxygen. These energies are approximate since the

saddle point energy was estimated from the thermal average of the MD energies such as those shown in figure 7.3a. These energies compared favourably with the experimental and calculated data. Examination of the pathway taken by the migrating vacancy showed that it followed a linear route between the two sites diagonally across the face of an MgO cube (figure 7.3b) which agreed with the low temperature data calculated by Vocadlo et al. (1995). At 40 GPa the moving vacancy followed an identical route with an increase in activation energy for magnesium and oxygen vacancy migration to 2.68 +/- 0.1 eV and 2.58 +/- 0.1 eV respectively. We now apply this approach to modelling diffusion at the grain boundary.

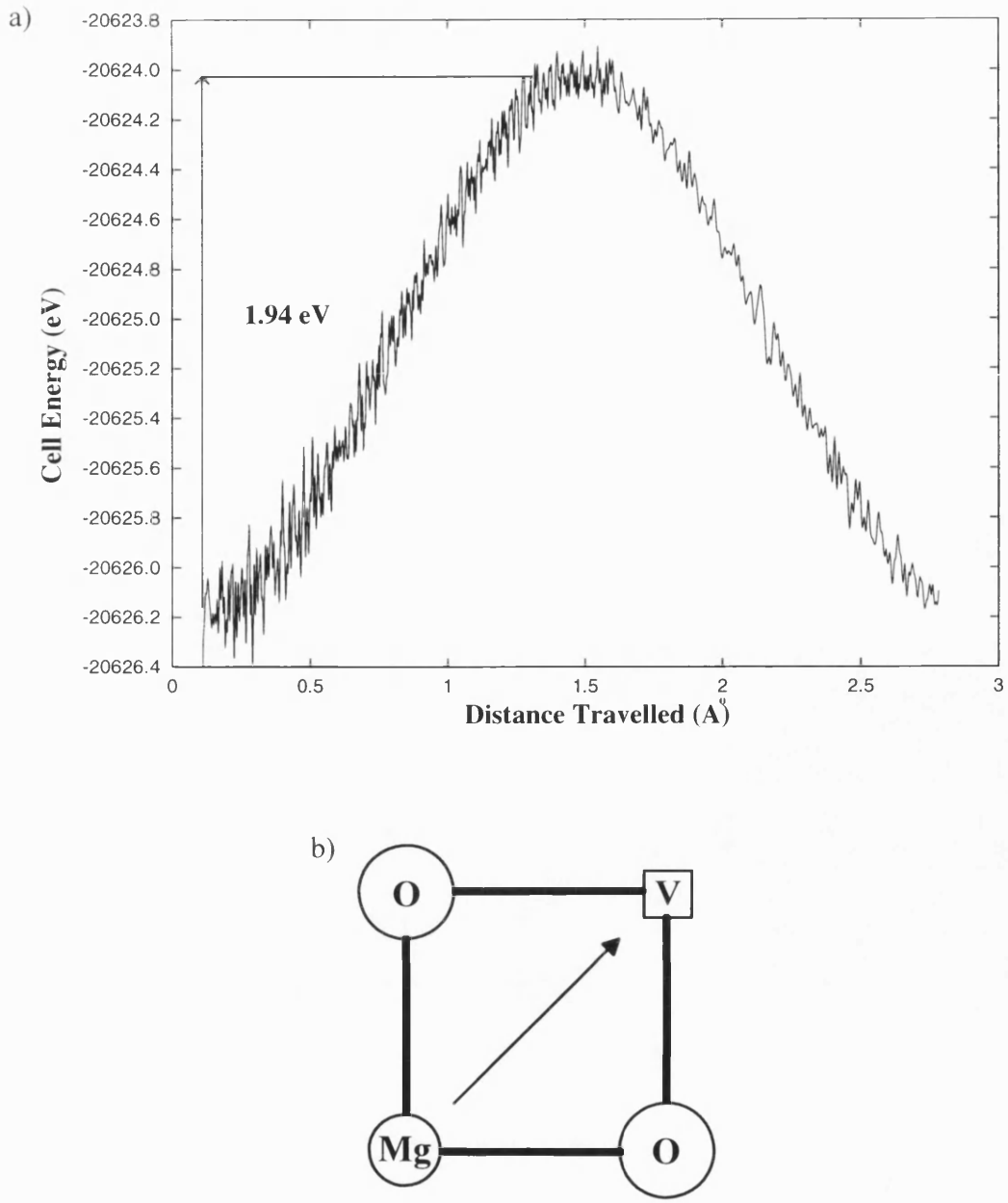

Figure 7.3. a) Energy profile and b) schematic representation of the diffusion pathway for diffusion of a magnesium ion in bulk MgO at 0 GPa.

7.3.4 Diffusion Path for Isolated Vacancies at a Grain Boundary at 0 GPa

Diffusion in the 0 GPa structure was modelled first by introducing an isolated vacancy at the boundary and pushing an ion of the same type as the vacancy from a neighbouring site towards it. There are a number of possible diffusion pathways for

the {410}/[001] boundary which can be simplified by considering the grain boundary to be made up of a series of dislocation pipes (see section 1.4). We report the two lowest energy mechanisms for diffusion along the boundary. These are for diffusion, (1) between the dislocation pipes, defined as diffusion along the same side of the boundary without travelling to the opposite face. For example, between sites B_R and C_R (figure 7.1), and (2) down the dislocation pipes, defined as diffusion from one side of the grain boundary to the opposite face, for example between sites B_R and C_L (figure 7.1).

Figure 7.4a shows the direction of travel and associated activation energies for magnesium vacancy hopping in the {410} boundary whilst figure 7.4b shows the energies for oxygen vacancies. The energies are very similar in both cases with less than a 0.14 eV variation between corresponding activation energies. Thus for brevity, unless otherwise stated, only the energies and trends for magnesium vacancies are described in the following sections.

7.3.5 Diffusion Between the Dislocation Pipes at 0 GPa

Diffusion via mechanism 1 (along the boundary) resulted in activation energies which in most cases were lower than those calculated for the bulk. The exception was for vacancy migration to the least stable vacancy site E from sites D and A'. Generally it was found that the activation energy for migration was lower when moving to a more stable site than to a less stable site. The lowest activation energies for mechanism 1 were found for migration to the D site with energies of 0.78 +/- 0.1 eV and 0.98 +/- 0.1 eV for migration from C and E respectively. Conversely migration away from this site required energies of 1.39 +/- 0.1 eV and 2.29 +/- 0.1 eV

respectively, significantly greater, indicating that a vacancy would not only be attracted but also bound to this site. Thus the overall activation energy for migration between pipes is 2.29 eV, which is slightly greater than the bulk value of 1.94 eV.

Animation of the ions in the simulation allowed us to investigate the diffusion pathway along the grain boundary (figure 7.5). It showed that the moving ion did not take the direct route between two sites but rather a curved trajectory which allowed it to travel into the channel at the grain boundary, for example during diffusion between the C and D sites the moving ion was displaced by approximately 0.1 Å into the grain boundary. The non-linear trajectory occurred for all of the diffusion routes modelled, a result similar to that found by Duffy and Tasker (1986) for cation vacancy migration in the {310} tilt grain boundary of NiO and illustrates the difficulty static simulations have in locating saddle points. A plot of the lattice energy of the cell with respect to the distance travelled by the moving magnesium vacancy for diffusion between sites C and D at 0 GPa is shown in figure 7.6 illustrating the smooth progression of the ion and the calculation of the activation energies for the forward and reverse processes.

(a)

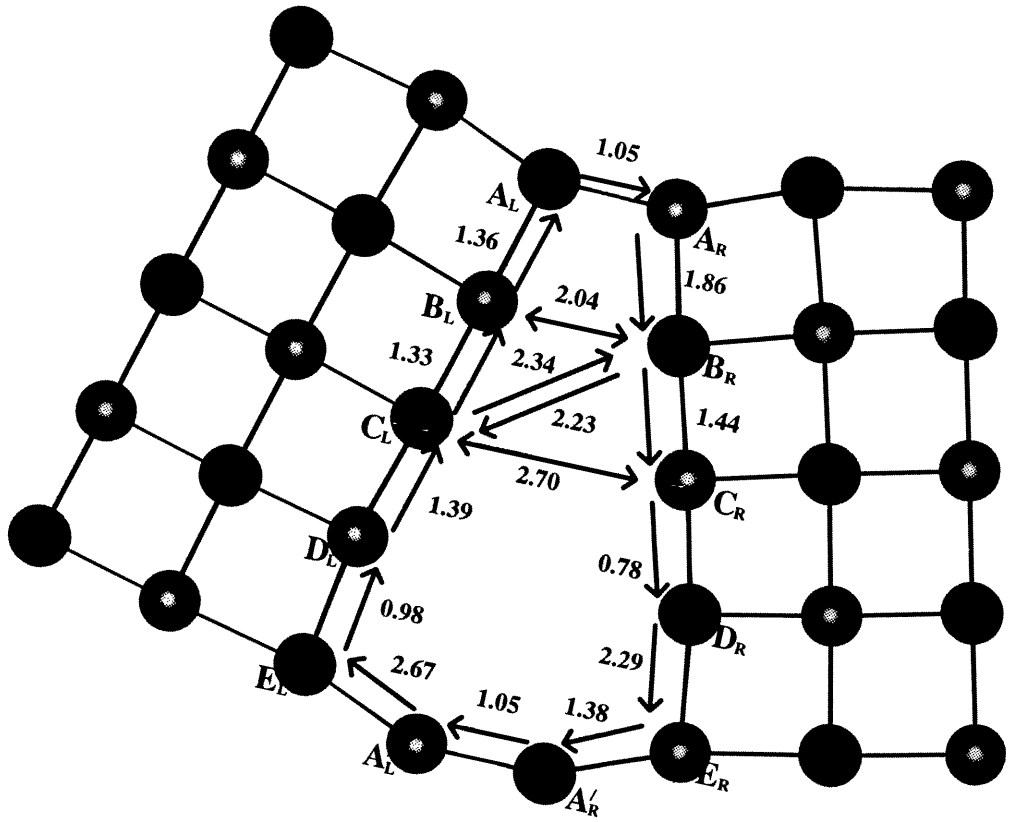

(b)

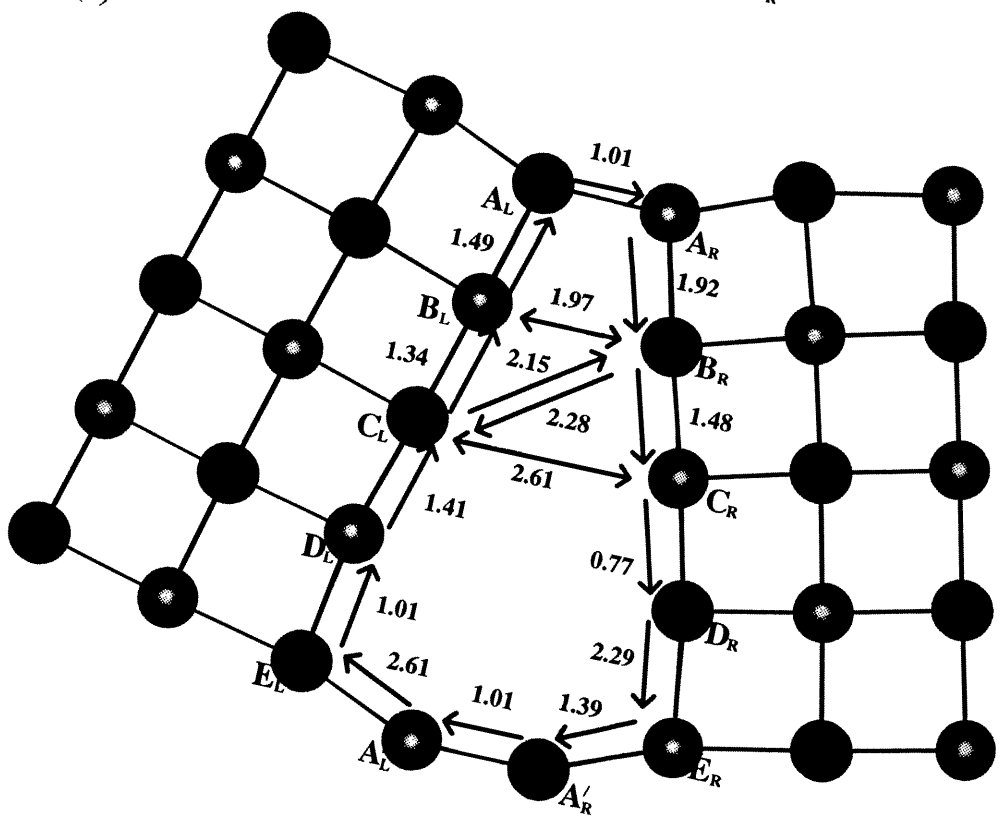

Figure 7.4. The activation energies for a) magnesium and b) oxygen vacancy migration at the grain boundary at 0 GPa.

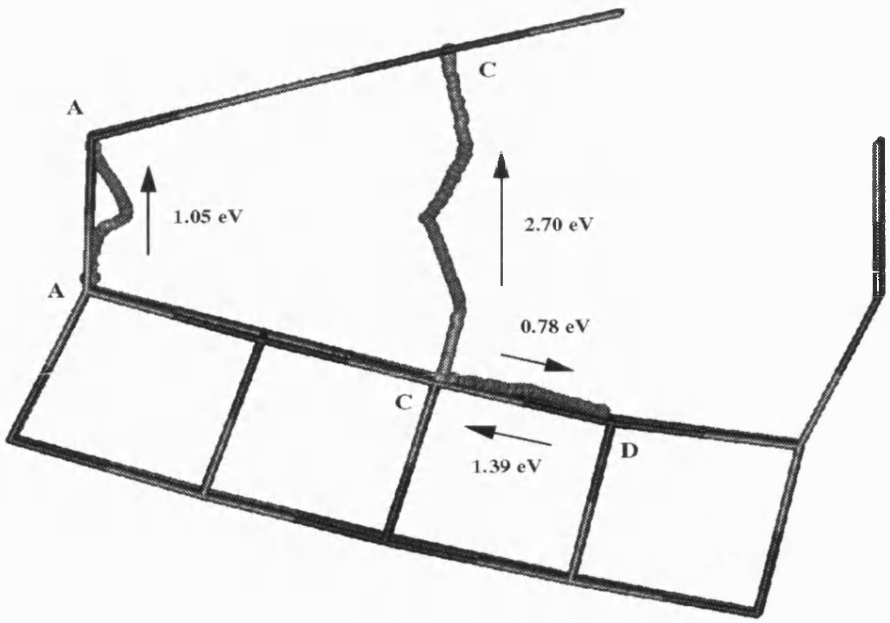

Figure 7.5. Diffusion pathway for magnesium diffusion between various sites in the {410} tilt grain boundary of MgO at 0 GPa.

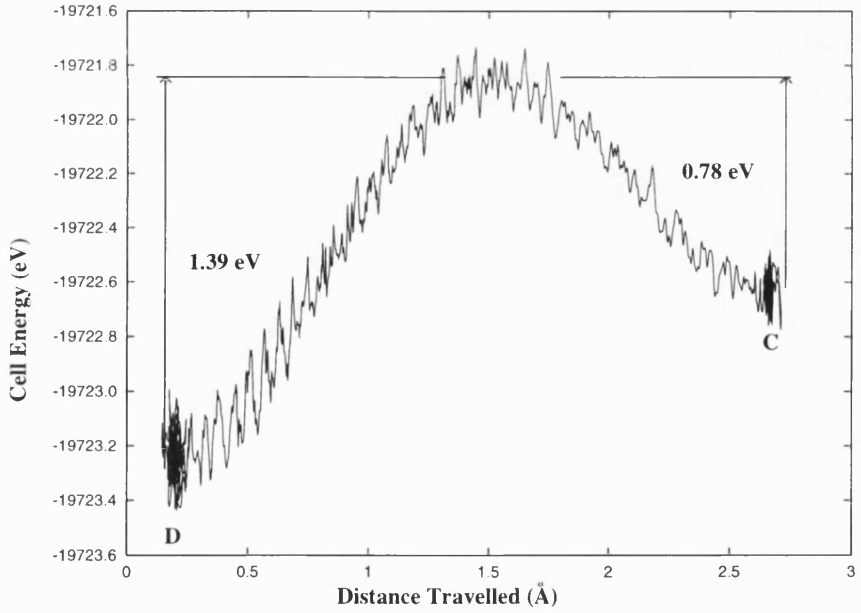

Figure 7.6. Energy profile for diffusion of a magnesium vacancy between positions C and D in the {410} tilt grain boundary of MgO at 0 GPa.

7.3.6 Diffusion Down the Dislocation Pipes at 0 GPa

The most favourable route for diffusion down the dislocation pipes involved vacancy hopping between A_L and A_R which required an activation energy of 1.05 +/- 0.1 eV. This mechanism became more unfavourable for sites further along the boundary where the distance to be crossed was larger resulting in activation energies of 2.00 +/- 0.1 eV and 2.70 +/- 0.1 eV. Diffusion pathways showed that a curved route was followed for migration from A_L to A_R (figure 7.5), similar to that seen for diffusion between the dislocation cores. Diffusion from sites C_L to C_R showed a more complicated non-linear route as the moving ion was influenced by its neighbours (figure 7.5).

In summary the diffusion process is anisotropic with diffusion down the dislocation pipes in the [001] direction, with an activation energy of 1.05 +/- 0.1 eV, preferred to diffusion between the pipes, with an activation energy of 2.29 +/- 0.1 eV. This agrees with the experimental work of Stubican and Osenbach (1984), who studied chromium diffusion in oxide boundaries including MgO, and of Turnbull and Hoffman (1954) who looked at silver bicrystals. In addition, the activation energies were much lower than in the bulk at 0 GPa which agrees with the relationship found in experimental studies of diffusion in polycrystalline NiO by Atkinson and Taylor (1981) who measured an activation energy of 1.78 eV compared to the value of 2.5 eV measured for bulk diffusion in single crystal NiO (Atkinson and Hughes 1981).

7.3.7 Diffusion Path for Isolated Vacancies at the Grain Boundary at 40 GPa

The diffusion pathways and activation energies were then considered for the 40 GPa structure. The activation energies and directions of travel are given in figure 7.7a for magnesium and figure 7.7b for oxygen.

7.3.8 Diffusion Between the Dislocation Pipes at 40 GPa

Diffusion pathways between dislocation pipes were altered as a result of the enclosed structure; although the moving ion still exhibited a curved trajectory the pathway took the ion slightly into the bulk and away from the boundary for diffusion between sites A, B, C and D (figure 7.8). A vacancy initially at the D position was stabilised by the movement of the ion at A' to a point between the two sites as explained in section 7.3.1. As an ion moved towards position D this magnesium moved back to its original position at site A'. Between C and D the moving ion was displaced approximately 0.3 Å perpendicularly to the main direction of travel into the bulk (figure 7.8). Finally, diffusion followed similar pathways to those calculated at 0 GPa between the remaining sites (i.e. D, E and A'). One reason for the different diffusion pathways at high pressure was the increased space between the boundary layer and the first 'bulk' layer (figure 7.8) due to the C sites on either side of the boundary drawing together whilst the bulk remained relatively stationary.

The relative change in the activation energies as a result of high pressure mirrored the change in the formation energies such as a decrease in activation energy from 1.15 eV to 0.23 eV for migration of a magnesium vacancy to the more stable A site from the less stable E site. However, the overall activation energy for diffusion between dislocation cores was 3.82 eV compared to 2.29 eV at 0 GPa.

(a)

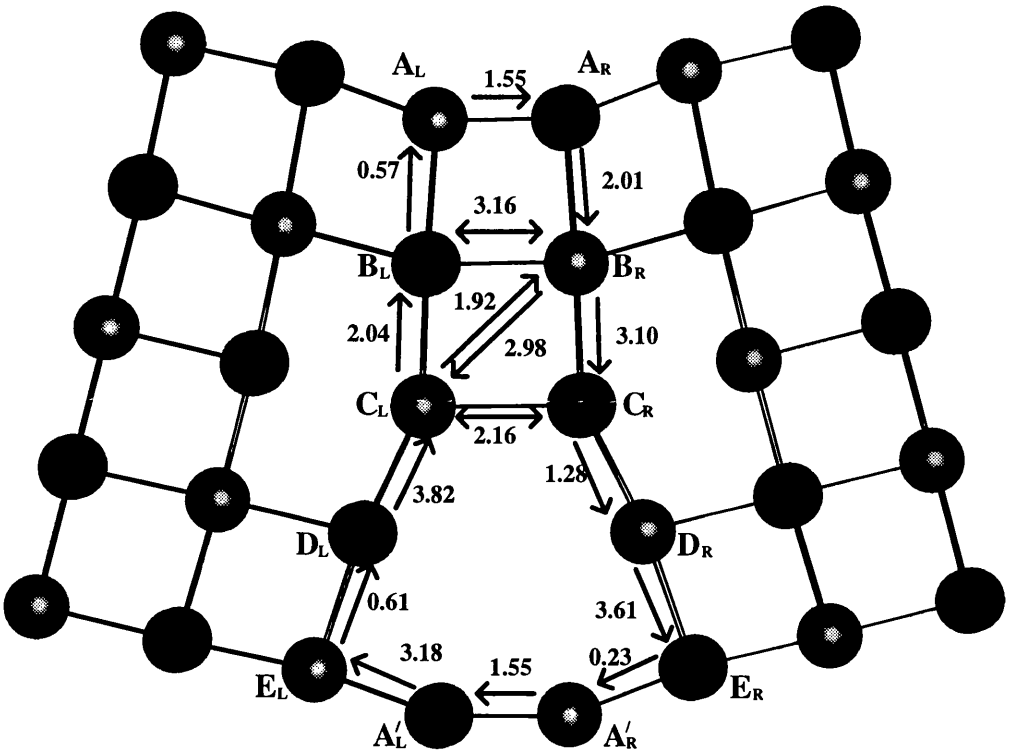

(b)

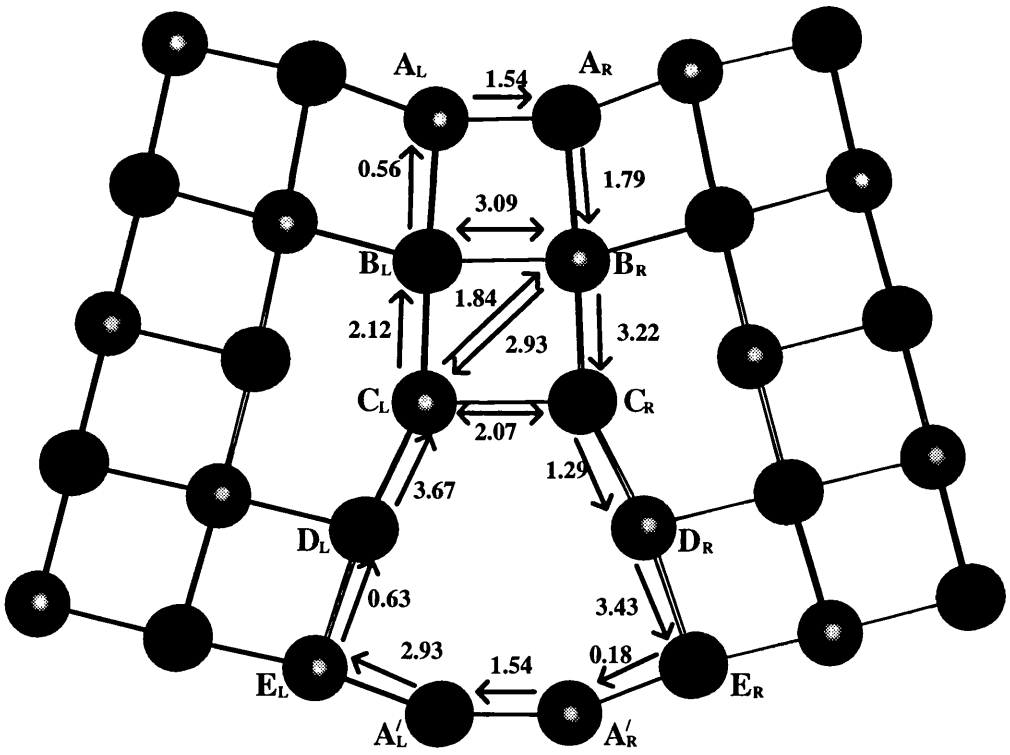

Figure 7.7. The activation energies for a) magnesium and b) oxygen vacancy migration at the grain boundary at 40 GPa.

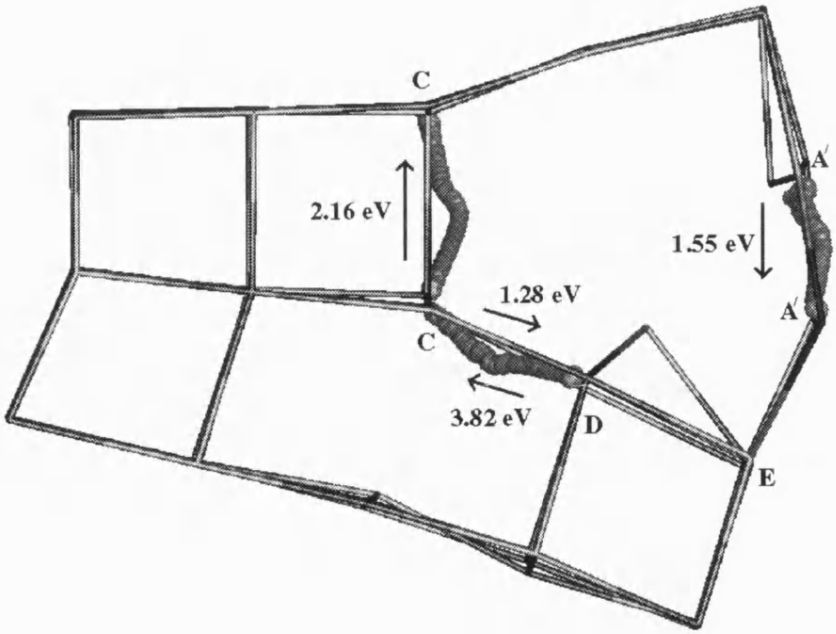

Figure 7.8. Diffusion pathway for magnesium diffusion between various sites in the {410} tilt grain boundary of MgO at 40 GPa.

7.3.9 Diffusion Down the Dislocation Pipes at 40 GPa

Diffusion down the dislocation pipes was greatly altered by the change in grain boundary structure at high pressure. The route A'_L to A'_R was still the preferred route with an activation energy of 1.55 +/- 0.1 eV. However, animation of the diffusion pathway showed that the movement of the ion into the grain boundary was not as pronounced as at 0 GPa (figure 7.8). Relaxation of the grain boundary accounted for much of the change in activation energies, e.g. for B_L to B_R the reduction in free space for the ion to move resulted in an increase in activation energy of 1.12 eV whereas between C_L to C_R the activation energy was lowered because the ion was able to move into the open channel of the grain boundary as shown in figure 7.8.

The most interesting point concerned diffusion at the boundary between sites B and C which can proceed either between (R - R, L - L) or down (L - R, R - L) the

dislocation cores. Diffusion away from the C position was preferred to diffusion towards this site, however the activation energies for diffusion down the pipes were lower than those for diffusion between the pipes by 0.12 eV in contrast to the 0 GPa case of 2.34 +/- 0.1 eV for diffusion down the pipes and 1.33 +/- 0.1 eV for diffusion between the pipes. This may be due to the route taken by the ion crossing the boundary. As noted earlier, an ion travelling between the pipes from site B_L to C_L followed a curved trajectory which takes it slightly into the bulk. In contrast an ion travelling down the pipes from site B_L to C_R followed a linear route. This ion travelled a shorter distance and this could contribute to the lower energy of activation.

In summary, in a similar manner to the 0 GPa case the most favoured route for diffusion was down the dislocation pipes between the A_L and A_R sites with an activation energy at 40 GPa of 1.55 +/- 0.1 eV for magnesium and 1.54 +/- 0.1 eV for oxygen. Once again these were much lower than the high pressure bulk values of 2.68 +/- 0.1 eV and 2.58 +/- 0.1 eV respectively. In contrast to the 0 GPa case it is unlikely that a vacancy migrating betweeen the pipes would become bound at site D since it was found that this is equivalent to site A and thus diffusion would then proceed down the dislocation pipes.

7.3.10 The Mobility of Bound Defects

The calculations presented suggest enhanced diffusion rates are obtained at the grain boundary as a result of the lower activation energies and increased free vacancy concentrations which agrees with the MD study in the {310}/[001] NiO tilt grain boundary (Meyer et al. 1996). However, the binding energies of the vacancy pairs are high and depending on the preparation conditions the defect concentration might be

sufficient that the rate determining step for a vacancy migrating along the boundary may be the activation energy of separating a bound pair. Which of the two limits, either diffusion of unbound or bound vacancies, that is observed will depend upon the experimental conditions.

The binding energy for a vacancy pair at 0 GPa was calculated from the partial Schottky energies (table 7.1a) giving a value of 2.83 eV. Calculations of the diffusion pathway for migration of this bound pair showed that the vacancies were able to separate. The activation energy at 0 GPa for vacancy migration from A_L to A_R was calculated starting with a bound pair and separating the vacancies to the second and third nearest neighbour positions. As figure 7.9 shows, the highest activation energy of 1.87 +/- 0.1 eV was obtained for separation to the third nearest neighbour position. This is higher than the single vacancy activation energy of 1.05 +/- 0.1 eV and closer to the bulk value of 1.94 +/- 0.1 eV. We must note that the binding energies calculated will not be precise due to the size restriction of the cell, i.e. as a vacancy moves from one site to another away from the vacancy it moves closer to the image of the vacancy in the adjacent cell. For this reason the activation energy for migration to the fourth nearest neighbour site was not calculated since the cation vacancy would be equidistant between two anion vacancies. Despite this problem the calculated binding energies do give a general indication of the effect of increased defect concentration upon the activation energies.

In comparison, at 40 GPa the binding energy was calculated as 4.83 eV suggesting that the vacancies would prefer to remain bound. Indeed, the simulations showed that when the ion moved towards its corresponding vacancy the neighbouring ion moved with it resulting in the vacancies remaining bound. The activation energy

for this move was calculated as 2.49 +/- 0.1 eV compared to 2.68 +/- 0.1 eV for bulk magnesium single vacancy migration. Thus it appears that concerted migration of a vacancy pair is preferred to separating the vacancies.

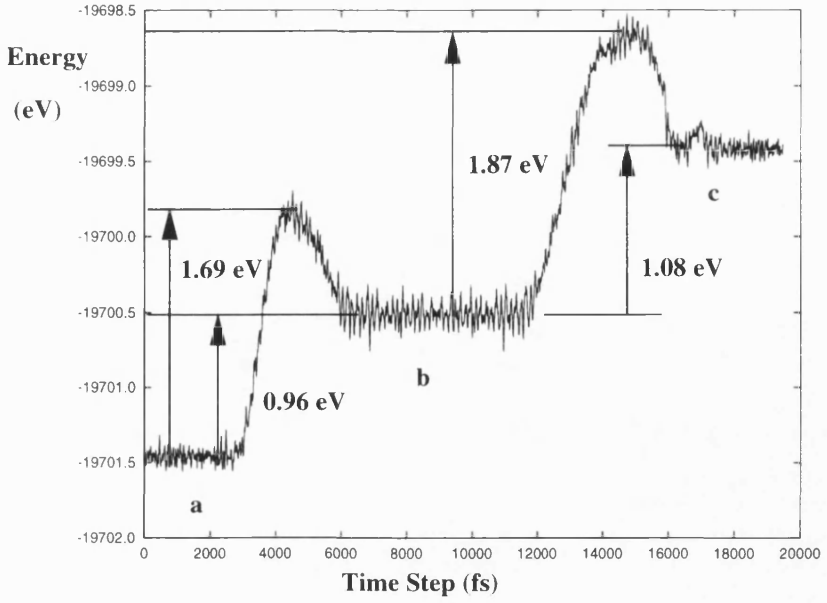

Figure 7.9. Energy profile for diffusion of a magnesium vacancy between positions A_R and A_L at 0 GPa showing the change in binding energy between a) nearest neighbour, b) second nearest neighbour and c) third nearest neighbour positions.

In summary, the results suggest that the enhanced diffusion found experimentally is a result of the increased defect concentration at the boundary since the activation energies for migration of bound vacancies are similar to the bulk energies.

7.4 Stishovite

The modified MD method was next used to study vacancy formation and diffusion in bulk and in the {201} tilt grain boundary of stishovite at 10 and 40 GPa.

Although no experimental results are available for stishovite this boundary was chosen since the channel structure would provide more freedom of motion for diffusing ions compared to the bulk and the mirror boundaries modelled in chapter 6. A pressure of 10 GPa was chosen since this is the pressure at which stishovite has been observed to form experimentally (Ross et al. 1990). As discussed in chapter 6 at higher pressures the two sides of the boundary draw slightly closer together which allows us to calculate the effect of this structural change upon the diffusion. For these calculations the rigid ion potential of van Beest (van Beest et al. 1990) was used.

7.4.1 Vacancy formation

The vacancy formation energies were calculated for both oxygen and silicon in the bulk and at the grain boundary using lattice dynamics. We considered only an anhydrous phase which allowed us to study simple single vacancies and ignore the more complicated vacancies such as the hydrogarnet defect which forms in silica (Cordier et al. 1994, Wright et al. 1995). The partial Schottky energies for each of the vacancy sites shown in figure 7.10 and for bulk sites are given in table 7.2. Due to time constraints only a selection of the silicon sites, namely those which were close together with clearer routes for diffusion, were chosen for study. An important result was that the formation energies for oxygen vacancies are negative suggesting that oxygen vacancies would spontaneously form. This illustrates the problems with using partial Schottky energies. The negative values may be a result of the potential using partial charges to define the silicons and oxygens but, since the calculation of diffusion enhancement due to defect concentrations requires the relative difference in energies between the boundary and bulk sites, these energies can still be used. A full

Schottky defect requires the removal of two oxygens and a silicon resulting in a positive energy due to the high energy required for silicon removal.

At 10 GPa the calculated defect energies at sites along the boundary were much lower than within the bulk crystal. For both bulk and the grain boundary the partial Schottky energies for silicon vacancies were much greater than that of oxygen which was primarily due to the magnitude of the charge in the vacancy formed. In hydrogarnet defects this is balanced by the presence of protons bonded to the oxygens (Wright et al. 1995). The most stable site for silicon vacancy formation of those studied was the H and I positions with a partial Schottky energy of 15.44 eV which both produced identical structures as a result of the ion at the filled site moving to a position midway between the two (similar to the process calculated for positions A and D in the {410} boundary of MgO at 40 GPa in section 7.3.1). The most stable site for oxygen vacancy formation was the C site with a partial Schottky energy of -3.63 eV. The vacancy at the C site caused almost no distortion of the surrounding lattice unlike the case for the least stable position (A and F) which generated a midway structure between the two similar to that calculated for the H-I silicon sites.

At 40 GPa the I site became the most stable site for silicon vacancies with little distortion. A vacancy at the H site still caused the generation of a structure with an ion midway between sites H and I. The defect energies increased compared to the 10 GPa energies with the I site having a partial Schottky energy of 17.08 eV (table 7.2). Conversely the oxygen defect formation energies decreased with the increase of pressure with the C site remaining the most stable. The site was so stable compared to the D site that removing an ion from the D site caused the ion at C to move into the D site, thus moving the vacancy back to C.

Using the equations of Duffy and Tasker (1984) given in section 7.3.2 the relative concentrations of vacancies in the boundary compared to the bulk were calculated. At 10 GPa, considering only the C and H-I sites, N was 8.962×10^{28} m^{-3} and N_b was 5.73×10^{18} m^{-2}. At 1500 K this resulted in a ratio of the fraction of boundary to bulk sites occupied of 2.28×10^{29} which was primarily due to the large difference in energy between boundary and bulk sites. This ratio increased to 1.94×10^{36} at 40 GPa and 1500 K as the boundary site became more stable relative to the bulk. These values are much larger than those calculated for vacancies in MgO and reflect the large difference in defect energy of sites at the boundary compared to sites at the bulk.

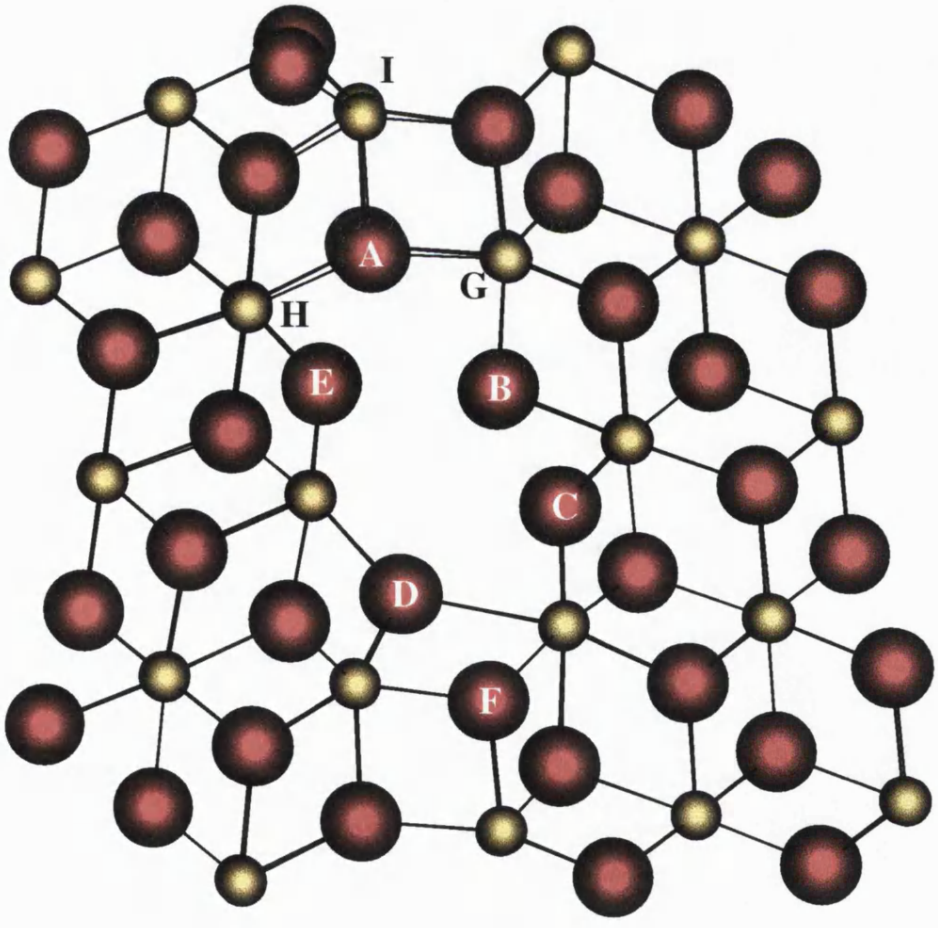

Figure 7.10. Structure of the {201} tilt grain bounary of stishovite at 10 GPa indicating the sites selected for vacancy formation.

Vacancy Site (type)	Pressure (GPa)	
	10 GPa	40 GPa
A (O)	-2.01	-3.76
B (O)	-2.84	-3.21
C (O)	-3.63	-5.03
D (O)	-2.02	-5.03
E (O)	-2.40	-3.45
F (O)	-2.01	-3.76
G (Si)	17.36	18.82
H (Si)	15.44	28.05
I (Si)	15.44	17.08
Bulk O	-0.28	-0.45
Bulk Si	20.39	22.32

Table 7.2. Cation and anion partial Schottky energies in eV for the {201} tilt grain boundary of stishovite calculated using static lattice energy minimisation at 10 and 40 GPa.

7.4.2 Diffusion of isolated Vacancies in Bulk Stishovite

Diffusion of oxygen and silicon vacancies in bulk stishovite was considered for the routes shown in figure 7.11. For oxygen at 10 GPa the moving ion travelled directly between the starting and finishing points with no lateral movement calculated. The ions surrounding the vacancy were displaced slightly from their perfect lattice positions but relaxed back when the vacancy was filled. The activation energy for this

migration of the vacancy was calculated at 0.55 +/- 0.2 eV. Diffusion of the silicon was a much higher energy process. The silicon ion travelled via a curved pathway which took it around the pair of oxygen ions between it and the vacancy and as a result the migration required an activation energy of 2.32 +/- 0.2 eV.

Increasing the pressure to 40 GPa increased the activation energy in each case. The oxygen diffusion still followed a linear pathway however the activation energy doubled to 1.11 +/- 0.2 eV. Silicon diffusion also followed the same pathway as the low pressure case with a slight increase in the activation energy to 2.85 +/- 0.2 eV.

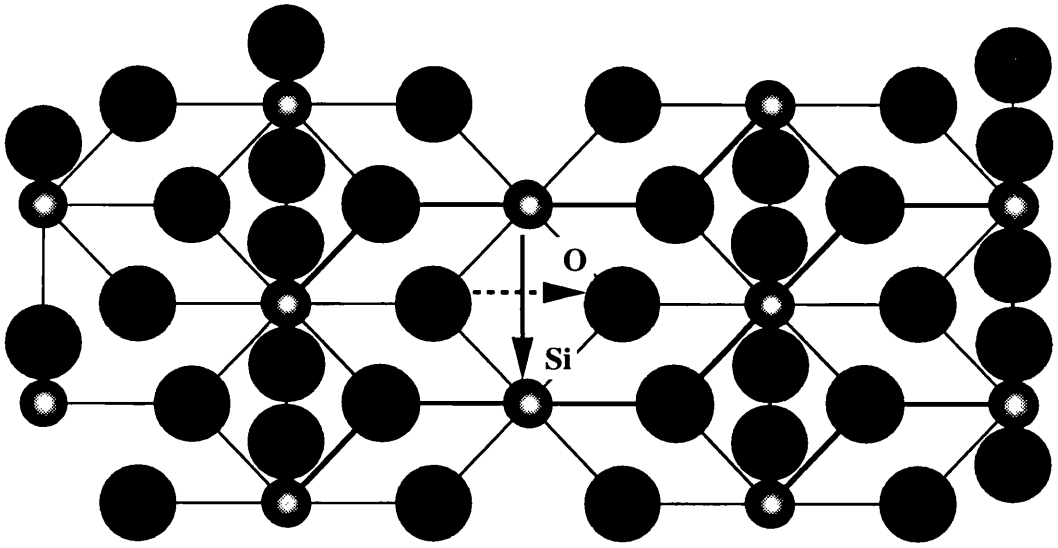

Figure 7.11. Direction for migration of vacancies in bulk stishovite.

Dashed line indicates oxygen path and solid line indicates silicon path.

7.4.3 Diffusion of Isolated Vacancies at the Boundary at 10 GPa

Diffusion of vacancies at the {201} grain boundary of stishovite is not as simplistic as for MgO due to the relaxation of the structure around the vacancies which causes neighbouring ions to move away from their starting positions. In many cases any diffusion caused a long range changed in order which affected the

neighbouring channels of the grain boundary. To prevent this from affecting the boundaries in the mirrored cells the unit cell was large enough to incorporate three channels and thus required 1260 species.

Considering first the migration of oxygen vacancies migration of the vacancy away from the B site (figure 7.10) required a larger activation energy than migration to this site. Migration from B to A resulted in a secondary migration of the vacancy to D-F in the neighbouring channel, ensuring that the vacancy did not remain at the least stable site, with the overall process requiring an activation energy of 1.76 +/- 0.2 eV. A similar effect was calculated for migration of the vacancy from the D-F site to the A-F site; the ion at E moved to mid A-F to create a vacancy at E, the more stable site. Migration away from the C site was very unfavourable with activation energies of 2.62 +/- 0.2 eV for migration to B and 4.00 +/- 0.2 eV for migration to D. Examination of the diffusion pathways showed that the moving ion tended to follow a slightly curved route between the start and finish positions causing it to travel into the channel of the grain boundary.

Migration of silicon vacancies was modelled for only two routes, between H and I and between I to G, since these routes appeared to be the most open and thus would be expected to be more favourable. Of these routes migration of the vacancy from I to G was the least favoured with an activation energy of 4.79 +/- 0.2 eV. Migration between H and I required an activation energy of only 0.30 +/- 0.2 eV although the return route required an activation energy of 3.36 +/- 0.2 eV. The migration pathway of the moving ion was found to have a curved trajectory which took the moving silicon around the pair of oxygen ions blocking its path.

Thus the most favoured route for oxygen diffusion at 10 GPa was between B and A with the resultant rearrangement to place the vacancy at a stabilised D-F position (figure 7.12) which required a maximum activation energy of 1.76 +/- 0.2 eV, larger than the bulk value. Silicon diffusion was most facile between H and I with an activation energy of 1.93 +/- 0.2 eV, slightly higher than for oxygen. The larger energy for silicon vacancy migration may be a result of the smaller space that the moving silicon ion had for diffusion compared to oxygen which was able to move into the channel forming the boundary. The silicon activation energy was slightly lower than the bulk value of 2.32 +/- 0.2 eV.

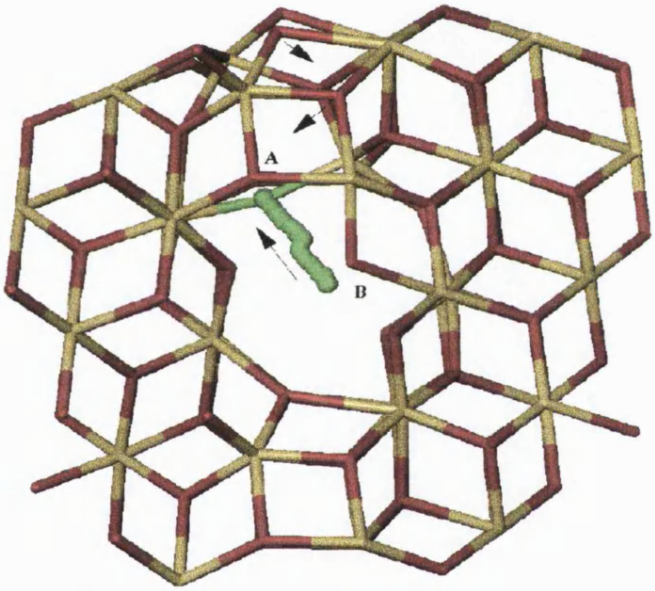

Figure 7.12. Diffusion pathway for silicon diffusion between the B and A sites in the {210} tilt grain boundary of stishovite at 10 GPa.

7.4.4 Diffusion of Isolated Vacancies at the Boundary at 40 GPa

As a result of the increase in pressure causing the two sides of the boundary to draw closer together the B site became more unstable relative to the other sites and consequently at 40 GPa migration of the vacancy to this site was unfavourable

compared to diffusion away from the site. The same alteration in structure produced the same effect at site E causing diffusion to other sites to become slightly more favourable. For example migration of the vacancy from E to A required an activation energy of only 0.26 +/- 0.2 eV whilst migration from A to E required an activation energy of 1.14 +/- 0.2 eV. C was the preferred site and this was reflected in the reduced energies of activation for diffusion of the vacancy to C compared to diffusion away. For example diffusion to the unstable B site required an activation energy of 4.37 +/- 0.2 eV whilst the return route required 1.80 +/- 0.2 eV to overcome the energy barrier. Diffusion of the vacancy to D was not possible since as soon as the force was removed from the ion moving it to C it immediately returned to the mid D-F position leaving the vacancy at C.

Due to the more restricted environment of silicon vacancies at 40 GPa migration became slightly less favourable than for the 10 GPa case with activation energies for diffusion between H and I of 0.41 +/- 0.2 eV compared to 0.30 +/- 0.2 eV at 10 GPa. The reverse direction required an activation energy of 2.78 +/- 0.2 eV compared to 1.93 +/- 0.2 eV at 10 GPa.

Thus the most facile migration of the oxygen vacancy at 40 GPa was between sites A and E with an activation energy of 1.14 +/- 0.2 eV, whilst for silicon the reduced space for diffusion resulted in an activation energy between sites H and I of 2.78 +/- 0.2 eV, both similar to bulk. This suggests that enhanced diffusion would be a result of defect concentration only and that this effect would be greater at high pressure.

7.5 Conclusions

The effect of pressure upon the defect partial Schottky energies and vacancy migration pathways has been calculated for MgO and stishovite. In both cases it was found that thermally generated vacancy concentrations were higher at the boundary than within the bulk. This relative concentration increased as the pressure was increased due to the vacancy sites in the boundary becoming even more stable relative to the bulk. In the case of the {410} tilt grain boundary of MgO the lowest energy site had a similar geometry to the lowest energy site found by Duffy and Tasker (1986) in the {310} tilt grain boundary of NiO. At high pressure a vacancy at this site caused the formation of a structure in which a neighbouring ion moved to a position midway between the two sites allowing a short circuit for diffusion.

We have demonstrated that the ability of relaxation via modified molecular dynamics is a useful tool for predicting the pathways when the activation energies are too high to be accessed using traditional MD within an ensemble. Diffusion for isolated magnesium and oxygen vacancy hopping down dislocation pipes forming the grain boundary was found to have a lower activation energy than that for bulk diffusion which agreed with experimental observations of NiO (Atkinson and Hughes 1981, Atkinson and Taylor 1981). This may be a result of the lower density of the grain boundary compared to the bulk which allows the diffusing ion to follow a curved trajectory into the boundary. In the case of stishovite the activation energies were often equal to or greater than the bulk values.

The low boundary vacancy energies suggest that there will be high vacancy concentrations at the boundary and that they will be bound. Pressure increases the concentration and likelihood of bound vacancies. Calculations considering MgO

showed that the activation energy of the bound defects is close to the bulk value and hence enhanced defect concentration due to the low vacancy formation energies gives rise to high diffusion coefficients for boundary migration. This result, albeit a different material, has been observed by Wuensch and Tuller (1994) where the activation energy for Ni^{2+} diffusion at grain boundaries of ZnO was similar to that of the bulk and the increased diffusivity was attributed to the enhanced carrier concentration at the boundary. Furthermore, if the orientation of the dislocation pipes in MgO was such that the migrating species had to move between them then the observed grain boundary activation energy would appear higher than that of the bulk.

Since this method facilitates determining the location of saddle points future work should investigate the use of LD to calculate the hopping frequency which would allow the direct calculation of the diffusion coefficient. Additionally the modified MD method should be used to investigate bound vacancies in stishovite.

8 Simulation of Grain Growth

8.1 Introduction

A real rock matrix system consists of many grains with different orientations. The sizes of the grains increase via a process of grain growth as a function of time after annealing. Since the sum total of the individual grain areas remains constant this process must occur at the expense of other grains, usually the smaller ones, which are eliminated. Two types of grain growth have been defined, normal and abnormal. In normal grain growth the grains exhibit a uniform increase in size whilst for abnormal growth some grains grow more rapidly than others. Some work has been done on this latter type of grain growth (Srolovitz et al. 1985, Brandt et al. 1996) however in this work only normal grain growth has been considered.

In this chapter we intend to extend the scope of the simulation methods to model grain growth in two dimensions. Furthermore, we will extend the scale of the calculations by considering grains on the mesoscopic scale. One of the central aims of this work is to utilise the energies calculated via atomistic simulation in chapter 4 to provide a material specific treatment of grain growth and migration.

8.2 Previous Studies of Grain Growth

It is commonly accepted that the driving force for normal grain growth is the reduction of the grain boundary interfacial energy (Atkinson 1988). Burke and Turnbull (1952) determined that the growth kinetics followed a parabolic relationship given by

$$R(t) = kt^n \qquad 8.1$$

where R is the average grain radius, k is a constant, t is the time and n is the grain growth exponent. Experiments have determined n to vary from the classical value of 0.5 (Rios 1992) to an average of 0.4 (Liu 1993, Dresen et al. 1996, Gill and Cocks 1996, Vogel and Klimanek 1996).

Several approaches have been used to model grain growth using a Monte Carlo technique (Mulheran 1992, 1994, Zhu and Smith 1992), however in this work we have applied the method of Sorolovitz et al. (Anderson et al. 1983, 1984, Grest et al. 1985 and Srolovitz et al. 1984a, 1984b, 1985) wherein the microstructure is mapped onto a discreet lattice and the growth was simulated via a Potts model. This is similar to the traditional Ising model except that instead of two orientations the spins can have any number. Srolovitz's method was extended by Mulheran and Harding (1991) to simulate a three dimensional system which allowed them to calculate the grain volume size distribution and growth rates for two and three dimensional systems. Using a statistical model they obtained grain growth exponents within 20% of the values found using the Pott's model. Fradkov et al. (1994) used experiment and simulation to show that the grains retained their shape as they altered size.

Liu et al. (1989) simulated fcc crystal growth using a model which treated the interaction energy of atoms within the bulk of grains differently from the energy of those near the surface. Using this technique they calculated the growth rate for a series of surfaces and found that the driving force increased with surface roughness.

Huse (1991) used a Gaussian model (which avoids energy degeneracy of configurations at low temperatures) to examine the change in average grain size with

time on a cubic lattice and looked at the relationship between grain size and the grain wall density. By plotting size against time he found that for a large enough sample size the grain size and inverse grain wall density became independent of the sample size.

The Potts model also works well when considering adsorption onto a surface. For example, Metiu et al. (1992) modelled the growth of aluminium-gallium-arsenide (AlGaAs) during vapour deposition. They also considered the deposition of silicon onto the Si(100)2×1 surface. This has also been simulated by Rockett (1994) who found that the atoms formed islands of long dimer strings.

Most grain growth models consider the growth to be isotropic. Work has been carried out to add some degree of anisotropy to monte carlo calculations. For example Nagai et al. (1994) considered orientation effects by assigning a number of energies to the orientations and found that this produced a broadening of the grain size distribution. Kunaver and Kolar (1993) divided the grains into isotropic matrix grains and anisotropic grains which experienced different energies in different directions. They obtained elongated grains whose size depended upon the energy ratio and the ratio of isotropic to anisotropic grains. Ito and Fuller (1993) varied the shapes of seeds placed into the matrix for anisotropic growth and found that the aspect ratio distribution was controllable but that the size or grain edge number was not.

8.3 Relationship between Interfacial Energy and Orientation

As we have briefly shown in chapter 4, there exists a relationship between the grain boundary formation energy and the misorientation angle between two grains. Since the microstructure would be dependent upon the boundary formation energies it

is to be expected that there is a relationship between the angle of misorientation and the microstructure. Characterisation of microstructures has shown that such a relationship does exist (Alarco et al. 1995, Singh and Sangal 1997). In this section we discuss this relationship further and describe an experimental method by which the energies can be measured.

8.3.1 Measurement of Relative Grain Boundary Energy

The relative grain boundary energies can be measured using an experimental technique known as thermal grooving or thermal etching. Within a material most grain boundaries meet in sets of three at a triple point. When a material is heated, grooves form at the points where a boundary meets the surface (shown schematically in figure 8.1).

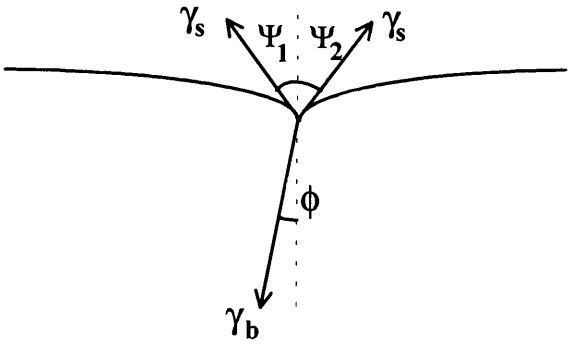

Figure 8.1. Schematic representation of the intersection between a grain boundary and the surface where γ_s is the surface energy, γ_b is the boundary energy, ϕ is the angle between the boundary and its equilibrium position and $\Psi_1 + \Psi_2$ is the angle between tangents to the surface, known as the dihedral angle.

It is generally accepted that these grooves are caused by an adjustment to equilibrium of the grain boundary and surface free energies (Chalmers et al. 1948). This equilibrium is between the interfacial tensions, $\gamma_i \hat{t}_i$, which are tangents to each interface and the torsional forces, $(\delta\gamma/\delta\alpha)_i n_i$, which rotate each of the interfaces around the line of intersection to bring them into a minimum energy position where $\hat{t}_i$ is a unit vector normal to the line of intersection of the interfaces and n_i is the product of $\hat{t}_i$ and a unit vector along the line of intersection.

This can be described using the Herring formula (Herring 1951)

$$\sum_{i=1}^{3}\left[\gamma_i \hat{t}_i + \left(\frac{\partial\gamma}{\partial\alpha}\right)_i n_i\right] = 0 \qquad 8.2$$

Generally the torque term has been ignored (Hodgson and Mykura 1973) and thus the boundary energy can be calculated as

$$\gamma_b = \gamma_{s1}\cos(\Psi_1) + \gamma_{s2}\cos(\Psi_2) - \left(\frac{\partial\gamma_{s1}}{\partial\Psi_1}\right)\sin(\Psi_1) - \left(\frac{\partial\gamma_2}{\partial\Psi_2}\right)\sin(\Psi_2) \qquad 8.3$$

If the surface tension anisotropy can be neglected and a symmetrical tilt grain boundary normal to the surface is considered (i.e.. $\Psi_1 + \Psi_2 = \Psi/2$) this leads to

$$\gamma_b = 2\gamma_s\cos\left(\frac{\Psi}{2}\right) \qquad 8.4$$

which allows the relative energy of the boundary to the surface, γ_b/γ_s, to be calculated by measuring the dihedral angle. We have calculated the relative energies for a series of [001] and [011] symmetric tilt grain boundaries of MgO with varying

misorientation angle θ. Experiments have previously been carried out on NiO (isostructural with MgO) which will provide a comparison. This will be described in the following sections.

8.3.2 Symmetric [001] tilt grain boundaries

Using the data calculated in chapter 4 the ratio of boundary to surface energies were calculated for the (h10) indexes. These are presented in table 8.1 with the experimental data collected by Dhalenne et al. (1979) for boundaries in NiO. It should be noted that it is difficult to compare the calculated ratios with the experimental ones since the surfaces observed experimentally are not defined. Thus table 8.1 contains two calculated ratios, one using the corresponding surface for each index and one which uses the average surface energy of the points chosen which gives 1.69 Jm^{-2}.

It can be seen that there is a good match in the shape of the curve between the experimental values and the values calculated using the average surface energy. The other calculated values continue to increase as the misorientation angle decreases unlike the experimental data. This seems to be a result of the surface energies dropping faster than the grain boundary energies. The large shift in the ratio between the experimental and calculated values may be a result of the differences in the composition of the material, e.g. the surfaces of NiO may be oxidised.

Index	θ (°)	γb (Jm^{-2})	γs (Jm^{-2})	γb/γs		
				calculated γs	γs=1.69 Jm^{-2}	Expt.
110	90.0	1.10	2.90	0.38	0.65	-
210	53.1	1.60	2.00	0.80	0.94	-
310	36.9	1.77	1.72	1.03	1.05	0.67
410	28.1	1.82	1.57	1.16	1.08	0.64
510	22.6	1.80	1.49	1.21	1.07	0.58
610	18.9	1.75	1.43	1.22	1.04	0.52
710	16.3	1.73	1.39	1.24	1.03	0.47
810	14.3	1.70	1.36	1.25	1.01	0.39
910	12.7	1.69	1.31	1.29	1.00	0.32
16 1 0	7.15	1.35	1.26	1.07	0.82	0.16
100	0	0	1.16	-	-	0

Table 8.1. Calculated and experimental boundary to surface energy ratios for [001] tilt grain boundaries.

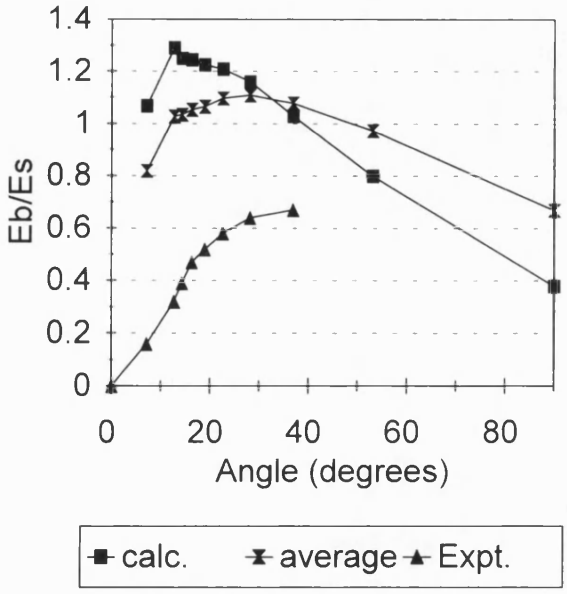

Figure 8.2. Plot of boundary to surface energy ratios for [001] tilt grain boundaries using calculated and averaged γ_s and comparing with experimental data.

8.3.3 Symmetric [011] tilt grain boundaries

A series of [011] symmetric tilt grain boundaries and surfaces have been simulated as shown in figure 8.3. The surface energies and grain boundary formation energies are given in table 8.2. Again there is ambiguity about which surface is observed experimentally so two calculations were performed to determine the relative energies. Calculation 1 used the corresponding surface index whilst calculation 2 used an average surface energy of 3.26 Jm^{-2}. Experimental data is taken from Dhalenne et al. (1982).

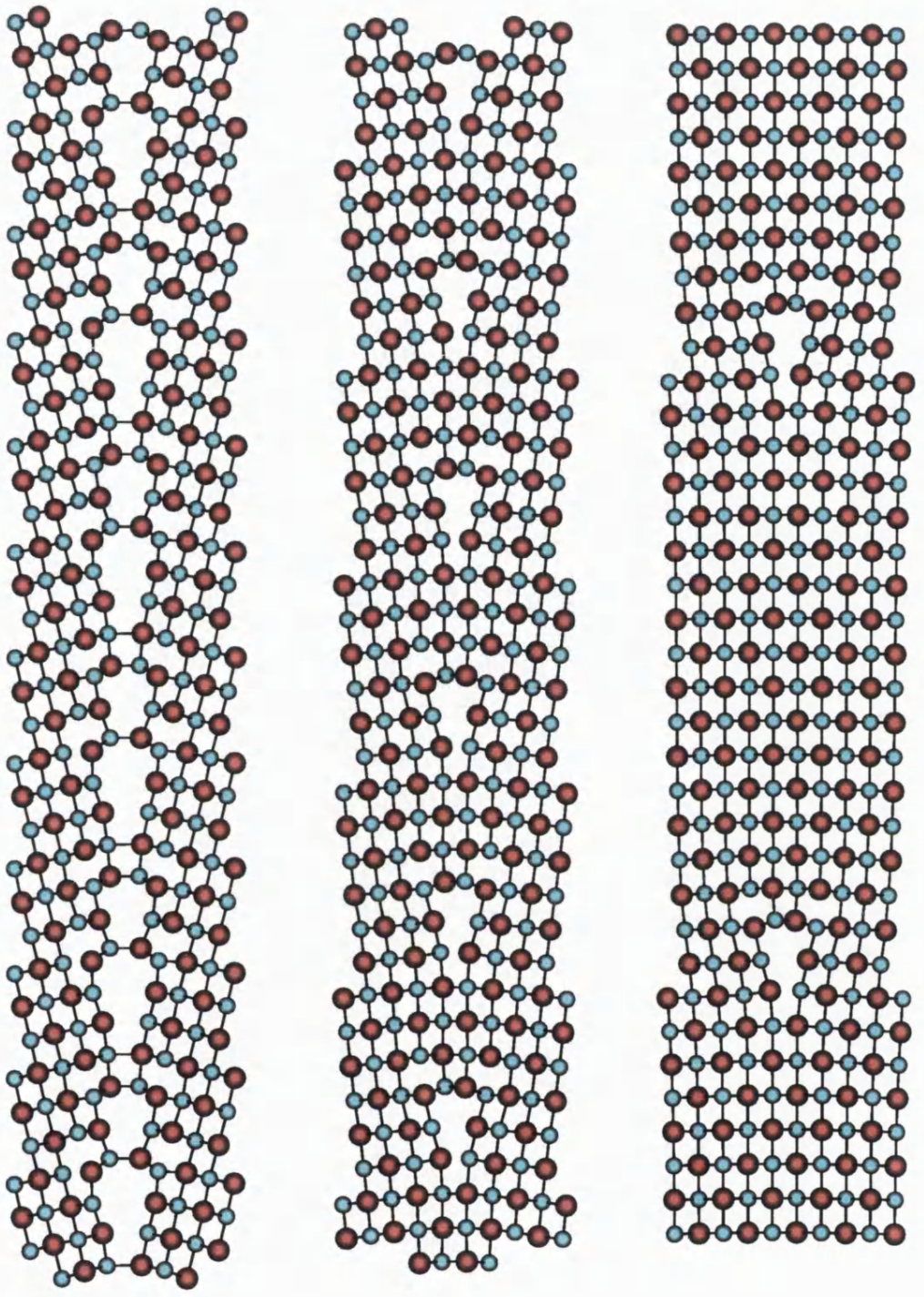

Figure 8.3. The relaxed structures of the a) $\{1\bar{3}3\}$, b) $\{1\bar{6}6\}$, and c) $\{1\overline{18}18\}$ tilt grain boundaries of MgO showing the increasing distance between dislocation cores.

The results show that for most indexes there is a good match between the experiment and the shape of both of the calculated plots (figure 8.4). However, a problem arises for a misorientation angle of 47.7°. The experiment and the calculation using the average surface energy show an increase in the ratio at this point resulting in a minima or 'cusp' at 39°, however the calculation via method 1 shows that the ratio continues to decrease. A similar problem was observed by Duffy and Tasker (1983b) who determined that a cusp which was observed experimentally at 130° did not occur in their calculations. As stated above, the experimental data ignores the torque term of the Herring formula, however previous calculations (Tasker and Duffy 1983b) have indicated that the torque term is comparable to the boundary energy for oxides and as such, cannot be ignored.

Index	θ (°)	γb (Jm^{-2})	γs (Jm^{-2})	γb/γs		
				calculated γs	γs=3.26 Jm^{-2}	Expt.
(1 -18 18)	4.50	1.14	3.10	0.37	0.34	0.22
(1 -8 8)	10.10	1.87	3.23	0.58	0.57	0.58
(1 -6 6)	13.44	2.11	3.25	0.65	0.64	0.65
(1 -4 4)	20.05	2.49	3.28	0.76	0.75	0.76
(1 -3 3)	26.53	3.52	3.25	1.09	1.06	0.87
(3 -7 7)	33.72	3.27	3.30	0.99	0.99	0.81
(1 -2 2)	38.94	2.49	3.38	0.74	0.75	0.71
(5 -8 8)	47.69	2.68	3.71	0.72	0.81	0.87

Table 8.2. Calculated and experimental boundary to surface energy ratios for [011] tilt grain boundaries.

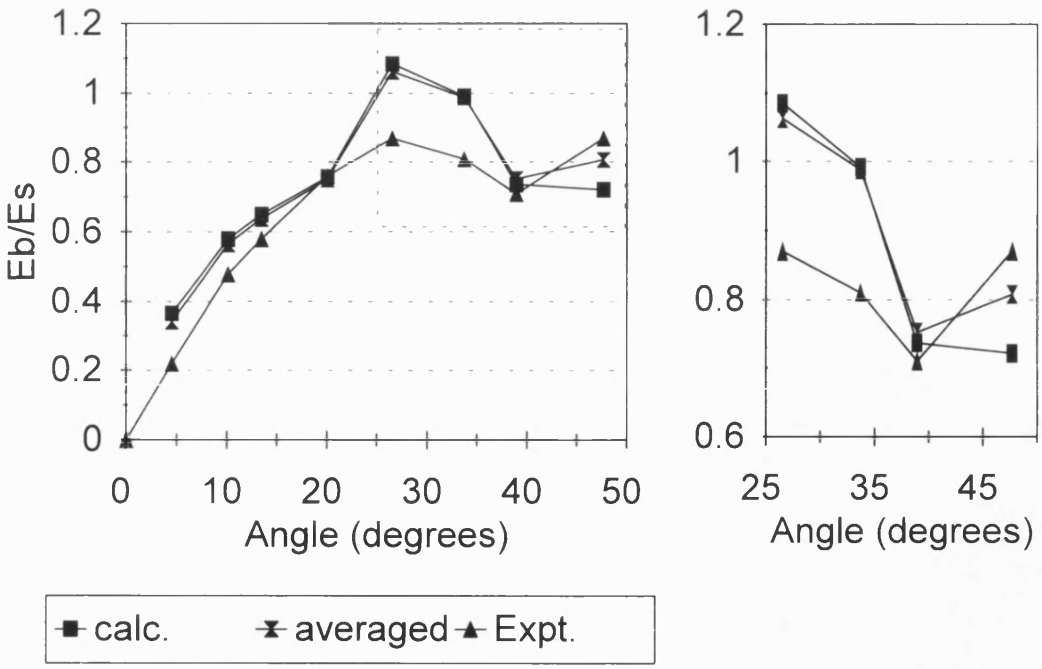

Figure 8.4. Plot of boundary to surface energy ratios for [011] tilt grain boundaries using calculated and averaged γ_s and comparing with experimental data. The 25° to 50° section is expanded to show detail.

8.3.4 Inclusion of the Torque Term

The boundary energy calculated including the torque term is given by

$$\gamma_b = 2\gamma_s \cos\left(\frac{\Psi}{2}\right) + 2\sin\left(\frac{\Psi}{2}\right) \cdot \left(\frac{\partial \gamma_s}{\partial \Psi}\right) \qquad 8.5$$

Since the experiments assumed that the torque term was not required they calculated γ_b as shown in equation 8.4. To test if the torque term had any effect we calculated the value of Ψ using an iterative scheme. Our trial value of Ψ for each index was obtained from equation 8.4 using our calculated values of γ_b and γ_s. $(d\gamma_s/d\Psi)$ was then obtained for consecutive pairs of indexes and used to obtain a new value of Ψ using equation

8.5. This was iterated until the input Ψ was identical to the output Ψ. Table 8.3 gives the values of Ψ calculated from our γ_b and γ_s values by the experimental method without torque and with the torque term .

The results show that there is almost no effect of including the torque term on the dihedral angles. This suggests that it is quite reasonable to ignore this term during experimental calculations.

Index	Angle (°)	Ψ (°)	
		No Torque	Torque
(1 -18 18)	4.50	158.92	158.92
(1 -8 8)	10.10	146.30	146.29
(1 -6 6)	13.44	142.07	142.07
(1 -4 4)	20.05	135.45	135.44
(1 -3 3)	26.53	114.29	114.29
(3 -7 7)	33.72	120.52	120.53
(1 -2 2)	38.94	136.76	136.76
(5 -8 8)	47.69	137.72	138.05

Table 8.3. Effect of Torque term on calculated dihedral angle.

8.4 The Monte Carlo Model

The relationship between dihedral angle and microstructure suggested above should make it possible to devise a model for grain growth which is anisotropic. By determining the angle at which two grains meet and knowing the relevant surface

energies of the grains it should be possible to assign an interaction energy between the two particles using equation 8.3. To simulate grain growth in two dimensions I have written a program called SMOGG (Statistical Model Of Grain Growth) which uses the Monte Carlo (MC) method. A two dimensional system has been chosen since it requires a smaller number of lattice sites than for three dimensions and allows easier visualisation of the domain configuration topology. This gives a good starting point for testing the program with the aim of eventually modelling a three dimensional system. In the following sections the results of initial testing of the program will be presented.

The rock matrix is simulated by mapping the microstructure onto a two dimensional lattice of size m×m. For this work m was chosen to be 200 which ensured a large number of points, 40000, for the lattice. Grain growth is modelled using the following approach. Each point in the lattice is randomly assigned a value from 1 to Q which represents the orientation of the individual grains within the matrix. Burke (1949) assumed that the surface tension of the grain boundaries provided the driving force for the growth by reducing the free energy stored in the system and hence the total grain boundary area. To calculate the total free energy for the system each point on the grid is considered in turn. If a nearest neighbour is of identical orientation the interaction energy is considered to be zero. If the neighbour is of a different orientation an interaction energy, G, is added to the sum of the energy for the whole system. Formation of clusters of grid points with like orientations will thus be favourable since this will reduce the total free energy.

The Monte Carlo routine is performed as follows, first a point on the grid is randomly selected and is then assigned a new, randomly determined, orientation as a

trial step. By comparing the original total free energy of the system to the new, trial, free energy the probability, P, of acceptance of this trial move can be determined as

$$P = 1;\ \Delta G \leq 0 \qquad 8.6$$

$$P = \exp\left(\frac{-\Delta G}{k_B T}\right);\ \Delta G > 0 \qquad 8.7$$

where ΔG is the change in free energy caused by the change in orientation, k_B is the Boltzman constant and T is the temperature. If the condition of equation 8.6 is satisfied the trial is accepted, if not then a random number between zero and one is then generated and compared with the probability, P (equation 8.7). If this number is smaller then the trial move is accepted and the configuration is added to the statistics. Another trial step is then generated and this process is repeated a large number of times. The system is initialised by performing a number of monte carlo steps at high temperature, ensuring that every trial is accepted, and thus a random array of orientations is produced. The duration of the data collection run is measured in terms of the number of MC steps per lattice site in the grid (i.e. the number of complete sweeps of the grid).

A number of factors can be varied in the above approach and in the following sections each of these will be tested to determine their effect on the simulation. These factors include the shape of the grid and thus the number of nearest neighbours, the number of orientations available, and the temperature. Initially, the tests were performed with the assumption that the interaction energy between nearest neighbours was either zero or one J/K depending on whether they were of the same orientation or

not. No account was taken of the content of each grain or which crystal surfaces, and thus what energy, each orientation represented.

8.5 Variation of Morphology with Q

The first stage of testing the program considered the effect that varying the number of possible orientations, Q, had upon the morphology of the growing grains. Four values of Q were chosen for study, 3, 6, 12 and 64 to match those chosen by Anderson et al. (1984). In each case the grid was initialised for 50000 MCS/Site before data collection occurred. During the data collection run the average energy of the system was calculated.

The resulting grain morphologies are shown in figure 8.5 for each value of Q. Solid lines represent the boundaries between regions of unlike orientation. The times used were similar to those used by Anderson et al. to yield comparable grain sizes. The average free energies of the systems and the acceptance ratio is given in table 8.4. The results obtained have been compared to work carried out by Anderson et al. (1983, 1984) on similar triangular two dimensional grids.

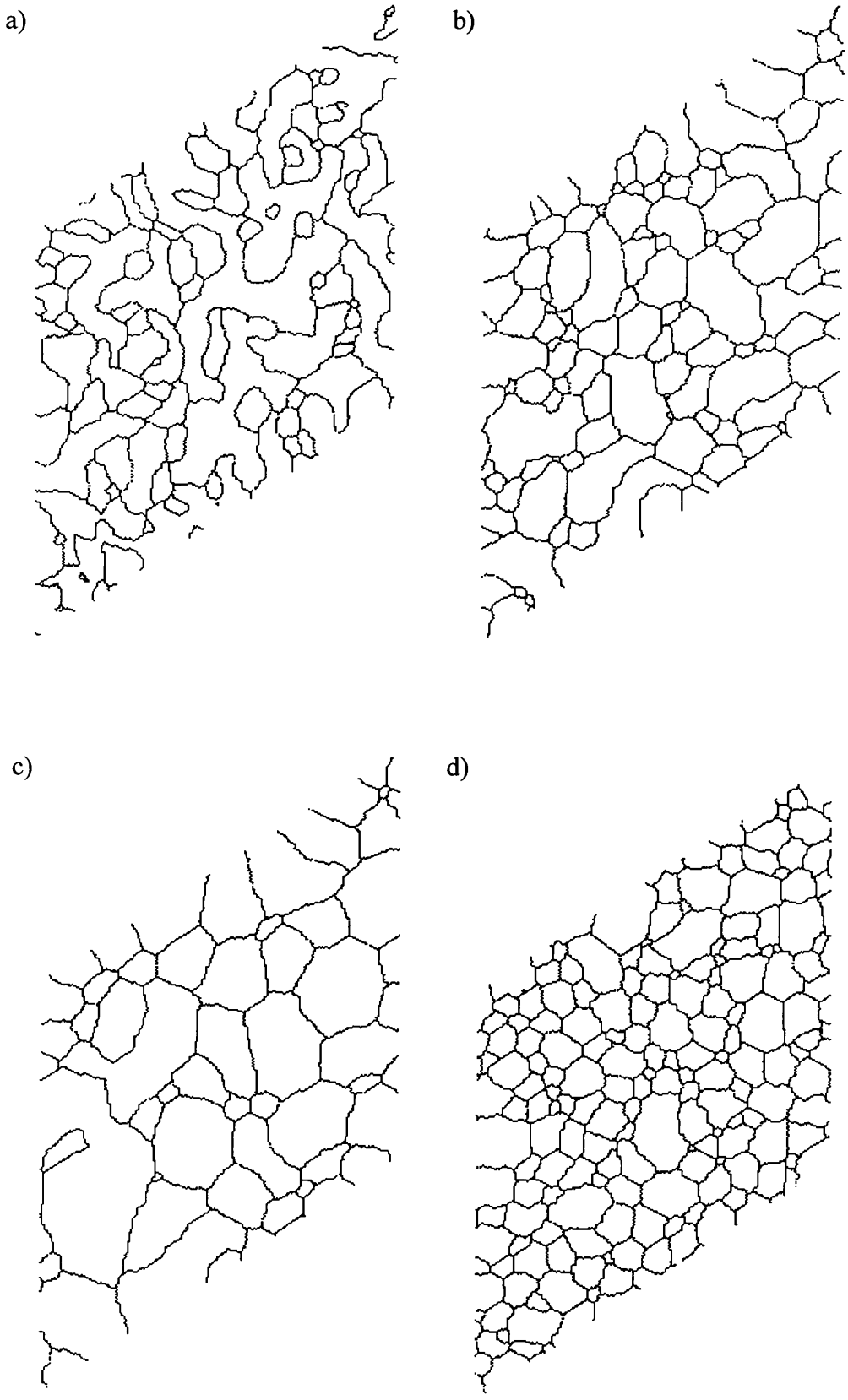

Figure 8.5. Domain configurations for Q values of a) 3, b) 6, c) 12 and d) 64.

Q	NoMC/site	Average Energy (J)	Acceptance ratio
3	100	14601.8	0.575
6	625	6386 .7	0.219
12	1500	4068.8	0.211
64	10000	1049.3	0.019

Table 8.4 Effect on matrix properties for increasing Q.

The acceptance ratio is the ratio of acceptance to rejection of all the data gathered during the MC step trial moves. As the MC stage continues this value will approach a steady value as the grid approaches equilibrium. For Q=3 over half of all trial moves are accepted. This ratio decreases as the value of Q increases. This can be explained by considering the number of orientations that can be randomly assigned as a trial move in each case. For small values of Q (i.e. approaching the Ising value Q=2) there is a large probability that the trial orientation will be favourable with several neighbours causing the move to be accepted. As Q increases this probability will decrease leading to a decrease in the ratio.

As figure 8.5 shows low values of Q lead to configurations consisting of very irregular and asymmetric grains. For higher values of Q the grains are more compact and tend towards a regular morphology which reflects the underlying lattice to some extent. The average energy of the system decreases with increasing Q as the formation of these compact grains causes a decrease in the total length of grain boundary in the system.

The difference in the domain configurations for differing values of Q can be explained by considering the possible modes of growth at the two limits. Figure 8.6 and 8.7 show the development of domain configurations for Q=4 and Q=64 respectively. As fig 8.6 shows, in the low Q limit large discontinuous changes occur in the area of individual grains when two grains of like orientation are brought together due to an intervening grain disappearing. The chance of this occurring is given by: (Anderson et al. 1983)

$$P = 1 - \left(1 - \frac{1}{Q}\right)^{Z} \qquad 8.8$$

For large Q this reduces to Z/Q, where Z is the number of second nearest neighbour grains. Thus coalescence events are forbidden at this limit and this can be seen in figure 8.7 for the Q=64 case by the rarity of coalesced grains. This trend in domain configuration with Q shows good agreement with the work of Anderson et al. (1983, 1984) and is supported by the good comparison with observed cross-sections of pure, annealed metals and ceramics (fig 8.8). A value for Q of 40 was chosen for further work as this had been shown to be beyond the limit where the grain growth exponential became independent of Q.

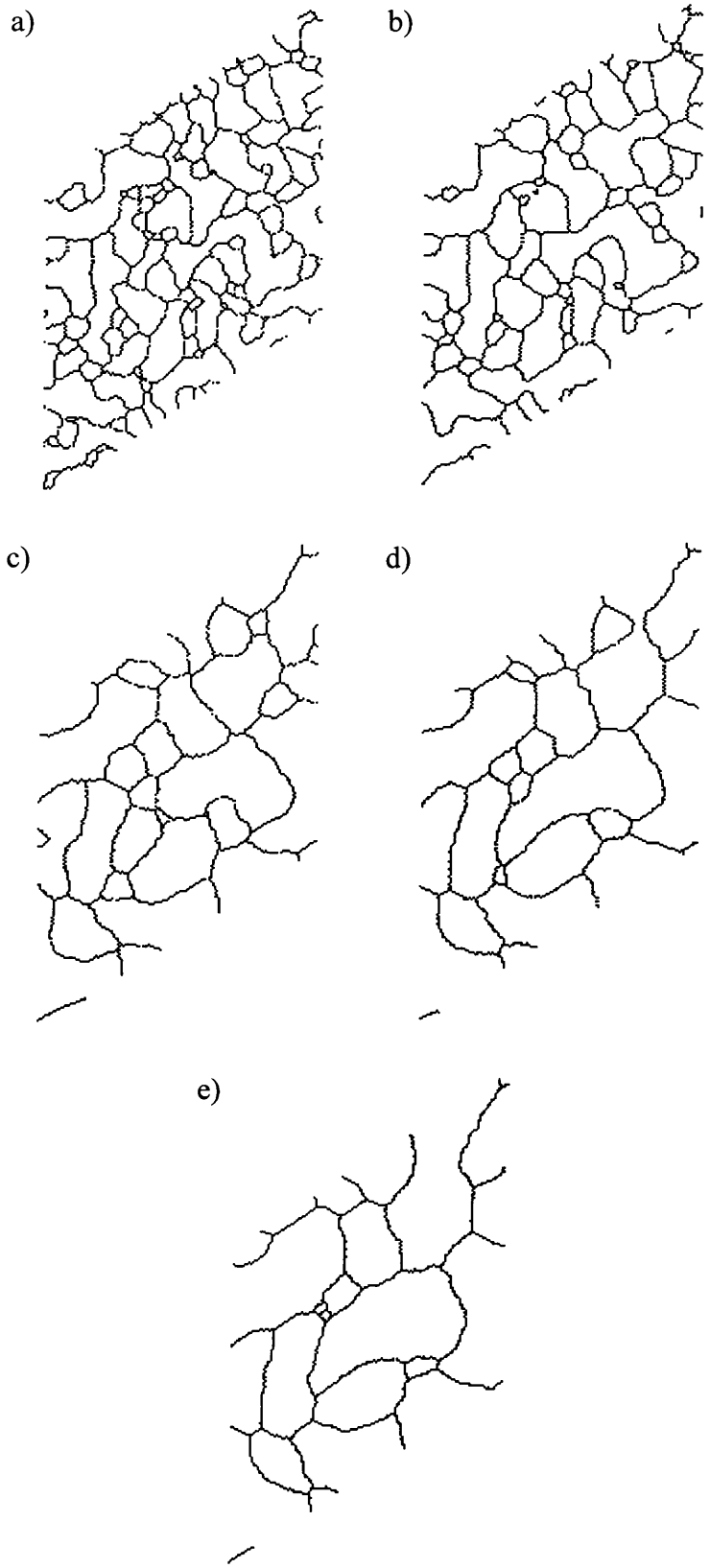

Figure 8.6. Development of grain morphology with time for Q=4 at

a) 250, b) 500, c) 1000, d) 1500 and e) 2000 MCS/Site.

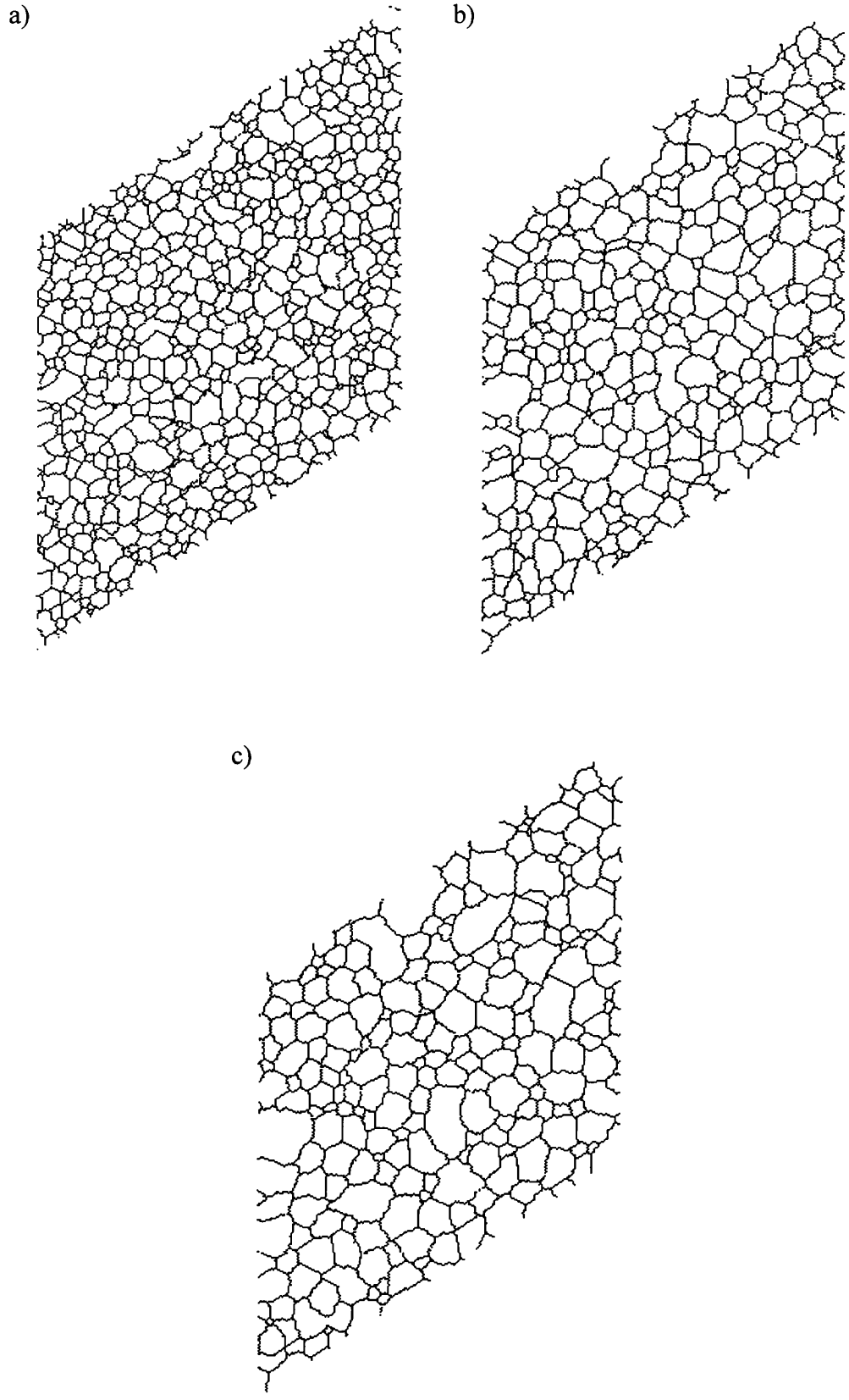

Figure 8.7. Development of grain morphology with time for Q=64 at

a) 2500, b) 5000, c) 7500 MCS/Site.

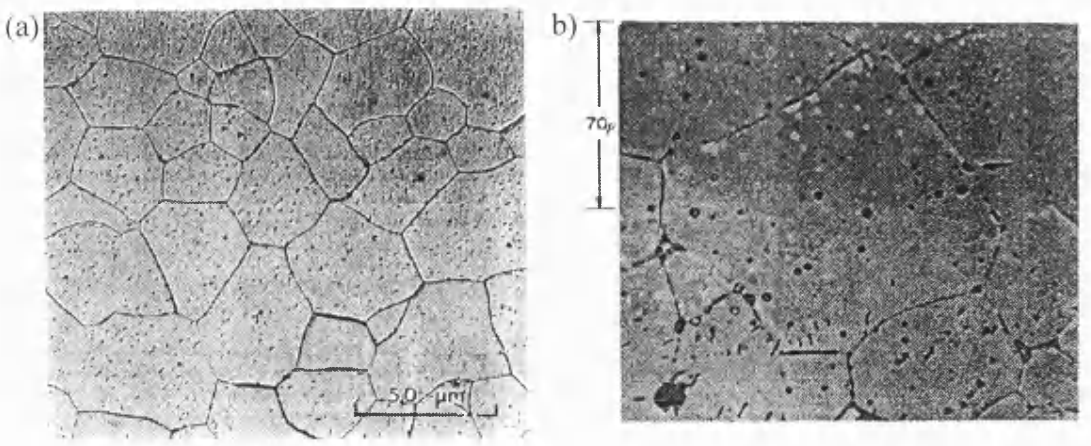

Figure 8.8 Cross-sections through a) polycrystalline iron (Anderson et al. 1983)

b) MgO (Leipold 1966)

8.6 Introduction of grain content

In the initial testing stages no account was taken of what each lattice site represented. Since the aim of this work was to produce a program which could calculate grain growth for a simple cubic system such as MgO each grain was considered to be representing a cube of a given volume containing a number of ions determined from the volume of the block and the density of the material the block represented. Since the program was only considering 2-D ordering of these blocks this lead to two arrangements depending upon whether the underlying lattice was a square or hexagonal lattice. This is shown schematically in figure 8.9.

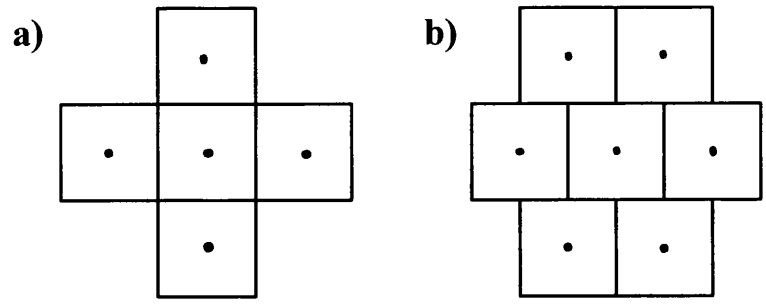

Figure 8.9. Schematic illustrating the arrangement of blocks for a) a square lattice and b) a hexagonal lattice.

Increasing the volume of the cube increased the number of ions in each block and thus the value of nkT in equation 8.6 was scaled to account for this.

8.7 Variation of Grain Growth with Temperature

The temperature of the system is important because the probability of acceptance of a higher energy trial move is dependent upon it. At a high temperatures all moves will be accepted leading to a very disordered system. This is known as the melting or disordering temperature, T_m. In order to ensure that the grid is composed of random orientations at the start of the data collecting, the system is initialised by carrying out a large number of MC steps at temperatures approaching or in excess of T_m.

To test which of the two grids would provide the most realistic model of grain growth calculations of the grain growth exponent were performed with the system quenched at a series of temperatures for the data collection run. The data was collected for 10000 MCS. Figure 8.10 shows the results of these calculations for both the square and hexagonal grids for blocks with each face having an area of 16 Å.

For the hexagonal grid between 0 and 1000K the grain growth exponent remained constant at 0.45. As the temperature increased above 1000 K there was a steady decrease of n until it reached 0 at 3000 K where the temperature was high enough to ensure that the majority all trial moves were accepted (see table 8.5). Conversely for the square grid n was very low at 0 K. As the temperature increased the grain growth exponent also increased until it reached a maxima at 1000 K. As the temperature increased further n decreased until it reached 0 at 2000 K.

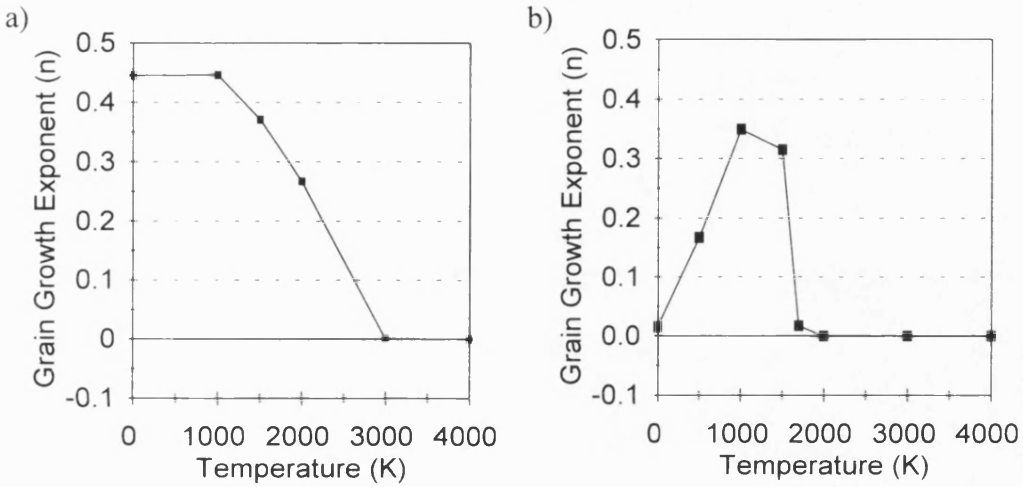

Figure 8.10. Plots of grain growth exponent versus temperature for a) an hexagonal lattice and b) a square lattice.

The calculations on the hexagonal grid suggest that there will be a rapid growth in grain size when the temperature is very low due to the large grain growth exponent at this temperature. This is unreasonable since there would not be enough energy in the system to allow the grains to re-orientate at low temperature. This problem may be a result of the increased number of nearest neighbours compared to

the square grid which allows more freedom for grain growth. The square grid provides a better model although grain growth occurs across a narrower range of temperatures than for the hexagonal grid. For this reason the square grid was chosen for further development of the program.

Grid Type	Percentage acceptance of moves						
	0 K	500 K	1000 K	1500 K	2000 K	3000 K	4000 K
Hex	2.755	-	2.848	3.452	6.385	73.660	83.590
Square	2.680	2.709	3.388	11.753	67.382	75.473	88.839

Table 8.5. Percentage acceptance of trial moves for hexagonal and square grids as a function of temperature.

8.8 Variation of Grain Growth with contact Area

The previous calculations considered the contact area between grains to have a surface area of only 16 $Å^2$. Calculations were performed upon the square lattice to determine the effect that altering the area would have upon the grain growth as a function of temperature. Sizes of 8 and 32 Å were chosen for comparison. The results are plotted in figure 8.11 and show that there is little change in the temperature at which maximum growth occurs. Increasing the area does however decrease the value of T_m, the temperature at which all trial moves are accepted, and as a result produces a narrower temperature range over which grain growth can occur. For the remaining calculations an area of 16 Å was chosen since this had provided the highest growth exponent.

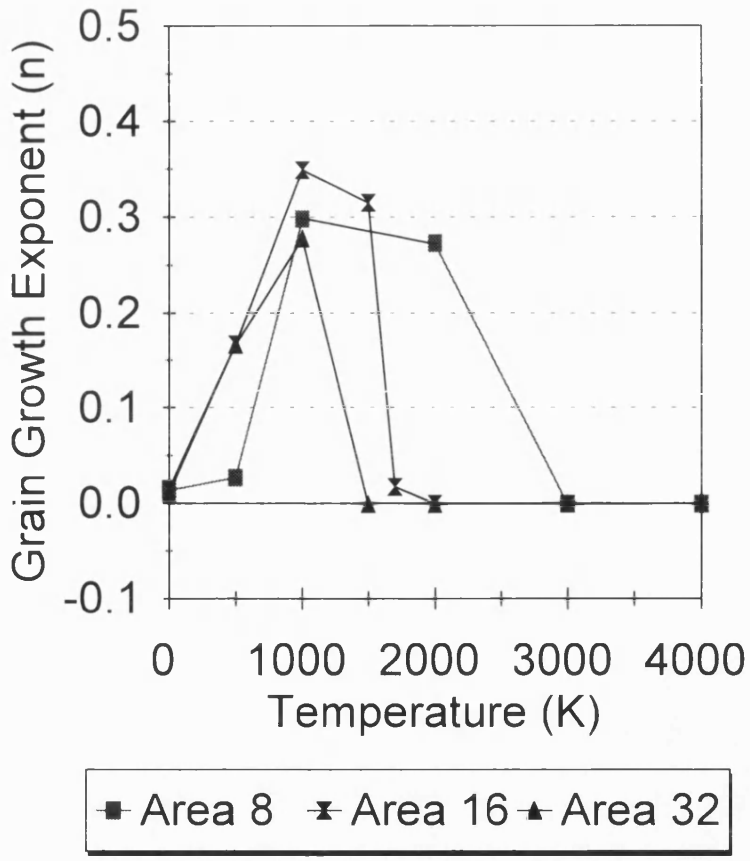

Figure 8.11. The effect of grain area on the rate of grain growth as a function of temperature.

8.9 Introduction of surface energies

The final stage of the program development was to use real energies to determine which grain orientations would grow preferentially in an attempt to model a 'real' rock matrix. Boundaries which were found to be favourable from this study could then be atomistically simulated and properties such as diffusion along the boundary could be examined.

To this end each orientation was assigned to represent a unique set of (hk0) surfaces. Since MgO was being modelled this simplified matters since each of the four sides in the box represented equivalent surfaces. For example, figure 8.12 shows the

case where one side represents the (310) surface and the others represent three equivalent surfaces. Using the computer code METADISE a series of surface energies were calculated as shown in table 8.6.

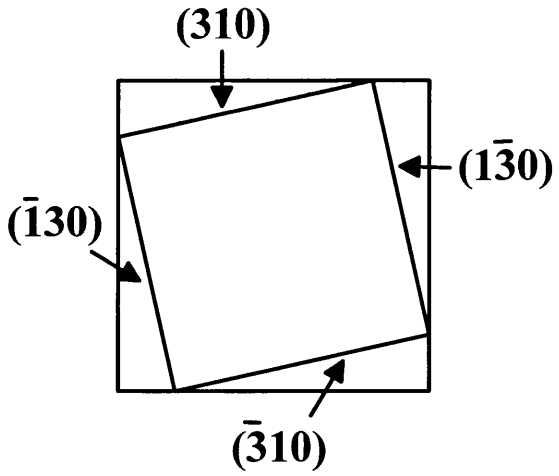

Figure 8.12. Schematic illustrating the surfaces assigned to the four sides of the box.

As an initial test the surface energies were included into the calculation in the following manner. As usual, if neighbouring points were of identical orientation then the energy between them was assumed to be zero. However, if the two sites were of differing orientation then the assumption was made that the interaction energy was the average of the two surface energies.

Calculations were performed for a series of lengths, however in each case it was discovered that the system quickly reverted to only one orientation, that representing the (100) surface. This was a result of the very low energy of this surface relative to the other orientations and shows that the kinetics of transformation from one orientation must be considered.

Q	Index	γ_s (Jm^{-2})	Q	Index	γ_s (Jm^{-2})
1	(100)	1.16	21	(740)	2.24
2	(110)	2.90	22	(750)	2.46
3	(210)	2.06	23	(760)	2.66
4	(310)	1.72	24	(830)	1.88
5	(410)	1.62	25	(850)	2.33
6	(510)	1.49	26	(870)	2.68
7	(610)	1.45	27	(920)	1.57
8	(710)	1.39	28	(940)	2.01
9	(810)	1.36	29	(950)	2.21
10	(910)	1.32	30	(970)	2.56
11	(10,1,0)	1.30	31	(980)	2.70
12	(11,1,0)	1.28	32	(10,3,0)	1.73
13	(320)	2.39	33	(10,7,0)	2.44
14	(430)	2.52	34	(10,9,0)	2.72
15	(520)	1.93	35	(11,2,0)	1.48
16	(530)	2.29	36	(11,3,0)	1.67
17	(540)	2.59	37	(11,4,0)	1.86
18	(650)	2.63	38	(11,5,0)	2.03
19	(720)	1.70	39	(11,6,0)	2.19
20	(730)	1.98	40	(11,7,0)	2.35

Table 8.6. Surface index and energies assigned to each orientation (Q).

One method of introducing some artificial constraint into the system was to ensure that during the stage of the program where the orientation was altered it was

only possible to choose an orientation either one higher or one lower than the current orientation, e.g. orientation 2 could become only either orientation 1 or 3. This was tested however the program still produced a grid composed entirely of orientation 1. Due to time constraints on the project it was not possible to continue further testing.

8.10 Conclusions

Calculations have been performed on [001] and [011] tilt grain boundaries in order to demonstrate a relationship between the ratio of boundary to surface energy and the dihedral angle. The shape of the curves for the calculated relationship and the available experimental data were in good agreement. A computer program has been written with the intention of using this relationship to model microstructure and initial testing has been conducted. The tests conducted on the program without realistic surface energies have shown good agreement with both the work carried out by Anderson and experimentally observed cross sections of metals and ceramics. It was found that a value for Q of at least 40 produced satisfactory microstructures for grain growth. Using a cubic grid it was shown that grain growth would not occur at very low temperatures due to there being not enough energy to allow reorientation. Grain growth also did not occur at temperatures approaching T_m, the melting temperature, since every trial move was accepted. The hexagonal grid produced unrealistic results which suggested that grain growth would occur at 0 K.

Inclusion of real surface energies produced grids composed of only one orientation. This was due to the very low energy of this orientation relative to the others and may also be a result of the lack of suitable definition of the variation in grain growth with grain size or in the energies. Further work could add in the use of

equation 8.3 to determine grain interaction energies in an attempt to produce more realistic microstructures which agree with the experimentally observed patterns.

One major addition to the program which was not possible due to time constraints is the conversion from a 2D to a 3D model. In the case of the cubic grid this could be easily accomplished by the addition of two nearest neighbours to give a total of six.

The relationship between dihedral angle and microstructure is an important one in mineralogy when considering magma melts. At disconnected pockets it is difficult for the melt to leave the polycrystalline material. However, Breeré (1975) showed that at low dihedral angles (typically <60°) a stable interconnecting framework was formed which allowed the passage of the melt. It is thought that the silicate melt in the Earth should form such an interconnecting network (McKenzie 1985), provided that there is a long enough time period for this to occur (approximately 10^3-10^4 years). Given our grain boundary energies we have calculated that we would require a decrease in the surface energy of approximately 1.5 Jm^{-2} in order to produce a dihedral angle of less than 60°. Recent simulation (Oliver et al. 1995, de Leeuw et al. 1995, Watson et al. 1996) has shown that facetting of the {110} surface of cubic oxides lowers the surface energy (e.g the {110} surface of MgO reduces 3.02 Jm^{-2} to 1.87 Jm^{-2} on facetting). Further work could consider the effect of facetting on the [011] surfaces which are essentially stepped {110}. Thus using this model it should be possible to determine routes for the passage of melts in a polycrystalline structure.

9 Thesis Conclusions

This thesis has demonstrated the use of atomistic simulation as a useful tool for predicting the effect of pressure and temperature on the structure and properties of the mantle forming minerals MgO, SiO_2-stishovite and $MgSiO_3$-perovskite. Static calculations were able to generate simple tilt and twist boundaries for MgO and tilt grain boundaries for stishovite and perovskite which generally agreed with experimental data of the structure and relative energies where available.

For MgO tilt grain boundaries the simulations calculated the presence of cusps in the ratio of the grain boundary formation energy to surface energy where the energy reached a maxima or minima. For example, the [001] symmetric tilt grain boundaries had a maxima at a misorientation angle of 28.1°, whilst the [011] tilts had a maxima at a misorientation of 26.5° and a minima at 38.9°. The slope of the variation in energy with misorientation angle was in agreement with thermal grooving experiments which measure the dihedral angle of the boundary.

In all cases, inclusion of increasing temperatures well below the melting point had little effect on the structure or properties of the grain boundaries studied beyond thermal expansion. Molecular Dynamics calculations showed that the melting of the MgO tilt grain boundaries occurred at a lower temperature than for the bulk which may have been a result of the extra freedom of the ions to move into the channels of the boundary.

Pressure had a more significant effect than temperature. For grain boundaries with an open, channel structure, increasing the pressure initially caused the sides of the channel to collapse inwards, increasing the density of the boundary. At greater

pressures the boundary sheared, resulting in the formation of asymmetric boundaries which at low pressure had been less stable than the symmetrical tilt grain boundaries. At still greater pressures the boundary sheared again to produce highly dense boundaries containing structures similar to spiral dislocations. These transitions were generally reversible upon the release of pressure although some transitions did require that an energy barrier be overcome. HRTEM studies of the analogous NiO tilt grain boundaries have shown differences between the observed and calculated structures. The presence of these structural transitions would suggest that the differences observed between experimental and calculated grain boundary structures may be a result of the harsh conditions of preparation of the samples which may lead to the generation of metastable grain boundaries, similar to the asymmetric boundaries, not found using atomistic simulation.

The grain boundary energy for most of the boundaries studied increased with increasing pressure which was primarily due to the PV term increasing. The only exceptions were the {101} and {301} mirror boundaries of stishovite where there was almost no increase in free energy suggesting that these boundaries would be the most stable type at high pressure.

Supercell calculations on MgO and stishovite have shown that grain boundaries are regions of high defect concentration due to the segregation of defects from the bulk to the boundary. Increasing the pressure causes the defect stability to increase in most sites leading to higher concentrations.

Diffusion in MgO grain boundaries was preferred down the dislocation pipes which formed the grain boundary rather than between them. For single vacancies the activation energy was lower than that of the bulk. However, the high defect

concentration calculated suggested that the vacancies would remain largely bound at the grain boundary. The calculated activation energy for bound vacancies was comparable to the bulk which suggests that the experimentally observed enhancement to diffusion is a result of the increased vacancy concentrations at the boundary agreeing with the experiments of Wuensch and Tuller (1994). The calculations showing high defect concentrations at the boundary suggest that the diffusion is concentration and not activation energy controlled. Additionally, although the activation energy for diffusion down the dislocation cores is comparable to bulk, diffusion between the channels requires a higher activation energy. Thus if the orientation of the dislocation pipes in polycrystalline MgO was such that the migrating species had to move between them then the observed grain boundary activation energy would appear higher than that of the bulk.

Chapter 8 considered grain growth. A simplistic two dimensional model which did not consider real surface energies showed good agreement with previous models. Temperature was shown to be important to the grain growth process since growth did not occur if either the temperature were too low or of it approached the melting temperature. The hexagonal grid models used in previous models did not follow this trend as they suggested that growth would be able to occur at zero Kelvin. Inclusion of surface energies into the simulation caused the model to break down with a single orientation dominating the microstructure.

Future work in this area could consider several features. Firstly, the modelling statically and dynamically of more complicated boundaries such as combinations of tilts and twists or boundaries between differing materials such as MgO and stishovite. Secondly, the diffusion studies can be extended to consider the effect of impurities

which are commonly found within the mantle such as calcium, manganese and iron. The differing sizes of these ions may have a significant effect upon the diffusion pathways and energies. Thirdly, extending the grain growth model to three dimensions and finding a way to modify the model such that it correctly models the variation in grain growth with area. One possible method of using experimental energies is to assign each orientation a misorientation angle. By using the equations to calculate the dihedral angle from the relevant misorientation angle it should be possible to generate growth microstructures based on experimental energies.

References

Ahrens, T.J. (1987) in *Methods of Experimental Physics*, Ed. Sammis, C.G. and Henyey, T.L., Academic, NY, **24A**, 185.

Akaogi, M.; Yusa, H.; Shiraishi, K. and Suzuki, T. (1995) *Journal of Geophysical Research-Solid Earth* **100**, 22337.

Alarco, J.A.; Olsson, E.; Ivanov, Z.G., Winkler, D.; Stepantsov, E.A.; Lebedev, O.I.; Vasiliev, A.L.; Tzalenchuk, A.Y. and Kiselev, N.A. (1995) *Physica C* **247**, 263.

Allan, N.L.; Mackrodt, W.C. and Leslie, M. (1987) *Adv. Ceram.* **23**, 257.

Allen, M.P. and Tildesley, D.J. (1989) *Computer Simulation of Liquids*, Oxford University Press, UK.

Anderson, D.L. (1989) *Theory of the Earth*, Blackwell Scientific Publications, UK.

Anderson, M.P.; Srolovitz, D.J.; Grest, G.S.; Sahni, P.S. and Safran, S.A. (1983) *Physical Review* **B28**, 2705.

Anderson, M.P.; Srolovitz, D.J.; Grest, G.S. and Sahni, P.S. (1984) *Acta Metallurgica et Materialia* **32**, 783.

Ashby, M.F.; Spaepen, F. and Williams, S. (1978) *Acta Metallurgica* **26**, 1647.

Atkinson, A. and Hughes, A. E. (1981) *Phil. Mag.* **A43**, 1071.

Atkinson, A. and Taylor, R. I. (1981) *Phil. Mag.* **A43**, 979.

Atkinson, H.V. (1988) *Acta Metallurgica* **36**, 469.

Balluffi, R.W. and Bristowe, P.D. (1984) *Surface Science* **144**, 28.

Balmer, M.L.; Huang, Q.; WongNg, W.; Roth, R.S. and Satoro, A. (1997) *Journal of Solid State Chemistry* **130**, 97.

Bell, P.M.; Mao, H.K. and Goettel, K. (1984) *Science* **226**, 542.

Belonoshko, A.B. and Dubrovinski, L.S. (1995) *Geochimica et Cosmochimica Acta* **59**, 1883.

Belonoshko, A.B. and Dubrovinski, L.S. (1996) *Phys. Earth and Planetary Interiors* **98**, 47.

Bollmann, W. (1970) *Crystal Defects and Interfaces*, Springer, New York.

Born, M. and Huang, K. (1954) *Dynamical theory of Cryst. Lattices*, Oxford University Press

Bourgeois, S.; Jomard, F. and Perdereau, M. (1992) *Surface Science* **279**, 349.

Bragg, W.L. (1940) *Proc. Phys. Soc.* **52**, 54.

Brandt, R.; Abbruzzese, G. and Lucke, K. (1996) *Materials Science Forum* **204**, 295.

Brown, G.C. and Mussett, A.E. (1981) *The Inaccessible Earth*, Allen and Unwin, London.

Burgers, J.M. (1939) *Proc. K. Ned. Akad. Wet. Ser. B* **42**, 293.

Burke, J.E. (1949) *Trans. Am. inst. Min. Engrs.* **180**, 73.

Burke, J.E. and Turnbull, D. (1952) *Prog. Metal Phys.* **3**, 220.

Catlow, C.R.A. (1989) *J. Chem. Soc. Far. Trans. II* **85**, 335.

Catlow, C.R.A. and Heyes, M.R. (1972) *Journal of Physics* **5**, L237.

Catlow, C.R.A. and Mackrodt, W.C. (1982) *Computer Simulation of Solids*, Springer Verlag, Berlin.

Catlow, C.R.A.; Faux, I.D. and Norgett, M.J. (1976) *J. Physics C: Solid State Physics* **5**, 415.

Catlow, C.R.A.; Thomas, J.M.; Parker, S.C. and Jefferson, D.A. (1982) *Nature* **295**, 658.

Catlow, C.R.A.; Bell, R.G.; Gale, J.D. and Lewis, D.W. (1995) *Studies in Surface Science and Catalysis* **97**, 87.

Catlow, C.R.A.; Ackermann, L.; Bell, R.G.; Gay, D.H.; Holt, S.; Lewis, D.W.; Hygren, M.A.; Sastre, G.; Sayle, D.C. and Sinclair, P.E. (1997) *Journal of Molecular Catalysis A-Chemical* **115**, 431.

Catti, M. (1981) *Physics and Chemistry of Minerals* **7**, 20.

Catti, M.; Ferraris, G.; Hull, S. and Pavese, A. (1994) *European J. Mineralogy* **6**, 171.

Causa, M.; Dovesi, C.; Pisani, C. and Roetti, C. (1986a) *Acta Crystallographica* **B42**, 247.

Causa, M.; Dovesi, C.; Pisani, C. and Roetti, C. (1986b) *Surface Science* **175**, 551.

Chalmers, B.; King, R. and Shuttleworth, R. (1948) *Proc. Royal Soc. A* **193**, 465.

Chao, E.C.T.; Fahey, J.J.; Littler, J. and Milton, D.J. (1962) *J. Geophysical Research* **67**, 419.

Chen, H.C.; Liu, Z.Y.; Chuang, Y.C. and Xu, L.K. (1993) *Thin Solid Films* **232**, 161.

Chen, F-R.; Chu, C-C.; Wang, J-Y. and Chang, L. (1995) *Phil. Mag.* **A72**, 529.

Cochran, J.W. (1973) *The Dynamics of Atoms in Crystals*, Edward Arnold, London.

Cochran, W. (1977) *Crit. Rev. Solid State Science* **2**, 1.

Colburn, E.A. (1992) *Surface Science Reports* **15**, 281.

Cordier, P.; Weil, J.A.; Howarth, D.F. and Doukhan, J.C. (1994) *European Journal of Mineralogy* **6**, 17.

Counterman, C.; Chen, L-Q. and Kalonji, G. (1988) *Journal de Physique* **49**, C5-139.

Dahmen, U.; Hetherington, C.J.D.; O'Keefe, M.A.; Westmacott, K.H.; Mills, M.J.; Daws, M.S. and Vitek, V. (1990) *Phil. Mag. Lett.* **62**, 327.

Dahman, U.; Paciornik, S.; Solorzano, I.G. and Vandersande, J.B. (1994) *Interface Science* **2**, 125.

Davidson, W.C. (1959) *AEX Report ANL-5990.*

Davies , M.J. (1992) *PhD Thesis*, University of Bath.

Davies, M.J.; Parker, S.C. and Watson, G.W. (1994) *J. Materials Chemistry* **4**, 813.

de Boer, K.; Jansen, A.P.J.; van Santen, R.A. and Parker, S.C. (1996) *Phys. Rev. B-Condensed Matter* **54**, 826.

de Leeuw, N.H.; Watson, G.W. and Parker, S.C. (1995) *J. Phys. Chem.* **99**, 17219.

Dhalenne, G.; Revcolevschi, A. and Gervais, A. (1979) *Phys. Stat. Sol.* **56**, 267.

Dhalenne, G.; Déchamps, M. and Revcolevschi, A. (1982) *Communications of the American Ceramic Society* **65**, C11.

Dick B.G. and Overhauser A.W. 1958. *Physics Review* **112**, 90.

Dove, M.T. (1989) *American Mineralogist* **74**, 774.

Dresen, G.; Wang, Z. and Bai, Q. (1996) *Tectonophysics* **258**, 251.

Duffy, D.M. (1986) *Journal of Physics C: Solid State Physics* **19**, 4393.

Duffy, D.M. and Tasker, P.W. (1983a) *Phil. Mag.* **A47**, 817.

Duffy, D.M. and Tasker, P.W. (1983b) *Phil. Mag.* **A48**, 155.

Duffy, D.M. and Tasker, P.W. (1983c) *Harwell Report, AERE-R11059*, Harwell, UK.

Duffy, D.M. and Tasker, P.W. (1984) *Phil. Mag.* **A50**, 143

Duffy, D.M. and Tasker, P.W. (1986) *Phil. Mag.* **A54**, 759.

Duffy, D.M.; Harding, J.H. and Stoneham, A.M. (1992) *Acta Metall. Mater.* **40**, A11.

Duffy, D.M.; Harding, J.H. and Stoneham, A.M. (1993) *Phil. Mag.* **A67**, 865.

Duffy, D.M.; Harding, J.H. and Stoneham, A.M. (1995) *Acta Metall. Mater.* **43**, 1559.

Duffy, T.S. and Anderson, D.L. (1989) *J. Geophysical Research-Solid Earth* **94**, 1895.

Ewald, P.P. (1921) *Ann. Physik* (Leipzig) **64**, 253.

Faux, I.D. (1971) *J. Physics C: Solid State Physics* **4**, L211.

Ferneyhough, R.; Fincham, D.; Price, G.D. and Gillan, M.J. (1994) *Modelling and Simulation in Materials Science and Engineering* **2**, 1101.

Fifield, R. (1988) *New Scientist* **117**, A1.

Fillipini, G.; Gramaccioli, C.M.; Simonetta, M. and Suffritti, G.B. (1976) *Acta Crystallographica* **A31**, 259.

Finger, L.W. and Hazen, R.M. (1991) *Acta Crystallographica* **B47**, 561.

Fiske, P. S.; Stebbins, J. F. and Farnan, I. (1994) *Physics and Chemistry of Minerals*, **20**, 587.

Fletcher, R. and Powell, M.J.D. (1963) *Computer Journal* **6**, 16.

Fletcher, R. and Reeves, C.M. (1964) *Computer Journal* **7**, 149.

Fowler, P.W. and Tole, P. (1988) *Surface Science* **197**, 457.

Fradkov, V.E.; Glicksman, M.E.; Palmer, M. and Rajan, K. (1994) *Acta Metallurgica et Materialia* **42**, 2719.

Freer, R. (1980) *Journal of Material Science*, **15**, 803.

Gale, J.D.; Catlow, C.R.A. and Mackrodt, W.C. (1992) *Modell. Simul. Mater. Sci. Eng.* **1**, 73.

Gao, Y.; Shewmon, P. and Dregia, S.A. (1988) *Scripta Metallurgica* **22**, 1521.

Gear, C.W. (1966) *The numerical integration of ordinary differential equations of various orders*, Report ANL 7126, Argonne Laboratory.

Gear, C.W. (1971) *Numerial Initial value problems in ordinary differential equations*, Prentice-Hall, Englewood Cliffs, NJ.

Gill, S.P.A. and Cocks, A.C.F. (1996) *Acta Materialia* **44**, 4777.

Gilman, J.J. (1960) *Journal of Applied Physics* **31**, 2208.

Godwal, B.K.; Meade, C.; Jeanloz, R.; Garcia, A.; Liu A.Y. and Cohen, M.L. (1990) *Science* **248**, 462.

Goodhew, P.J. (1980) in *Grain Boundary Structure and Kinetics Amer. Soc. for Metals*, Metals Park, Ohio.

Gordon, R.G. and Kim, Y.S. (1972) *J. Chem. Physics* **56**, 3122.

Greenwood, N.N. and Earnshaw, A. (1984) *Chemistry of the Elements,* Pergamon Press, 3.

Grest, G.S.; Srolovitz, D.J. and Anderson, M.P. (1985) *Acta Metall.* **33**, 509.

Hagege, S.; Carter, C.B.; Cosandey, F. and Sass, S.L. (1982) *Phil. Mag.* **A45**, 723.

Harding, J.H. (1988) *U.K.A.E.A. Report, AERE-R-14300*, United Kingdom Atomic Energy Authority, Harwell, UK.

Harding, J.H. (1990) *Rep. Prog. Phys.* **53**, 1403.

Harding, J.H.; Parker, S.C. and Tasker, P.W. (1989) in *Non-Stoichiometric Compounds, Surfaces, Grain Boundaries and Structural Defects*, Ed. Nowotny, J. and Weppner, W., UKAEA, Harwell.

Harris, D.J.; Watson, G.W. and Parker, S.C. (1996) *Phil. Mag.* **A74**, 407.

Harris, D.J.; Watson, G.W. and Parker, S.C. (1997) *Phys. Rev. B-Condensed Matter* **56**, 11477.

Harrison, N.M. and Leslie, M. (1992) *Molecular Simulation* **9**, 171.

Hart, R.S.; Anderson, D.L. and Kanamori, H. (1977) *J. Geophysical Research* **82**, 1647.

Herring, C. (1951) in *Physics of Powdered Metallurgy*, Ed. Kingston, W.E., Mcgraw-Hill, NY.

Hill, R.J.; Newton, M.D. and Gibbs, G.V. (1983) *J. Solid State Chemistry* **47**, 185.

Höche, T.; Kenway, P.R.; Kleebe, H-J. and Rühle, M. (1994) *J. Am. Ceram. Soc.* **77**, 339.

Hodgson, B.K. and Mykura, H. (1973) *J. Materials Science* **8**, 565.

Hoover, W.G. (1985) *Physical Review* **A31**, 1695.

Hu, M.; Wenk, H-R. and Sinitsyna, D. (1992) *American Mineralogist* **77**, 359.

Huse, D.A. (1991) *Phys. Rev. B-Condensed Matter* **43**, 8673.

Ito, O. and Fuller, E.R. (1993) *Acta Metallurgica et Materialia* **41**, 191.

Jackson, R.A. and Price, G.D. (1992) *Molecular Simulation* **9**, 175.

Jayaraman, A. (1983) *Review of Modern Physics* **55**, 65.

Jeanloz, R. and Heinz, D.L. (1984) *Journal de Physique* **45**, 83.

Johnsson, P.A.; Eggleston, C.M. and Hochella, M.F. (1991) *American Minerologist* **76**, 1442.

Kapusta, B. and Guillope, M. (1988) *Phil. Mag.* **A58**, 809.

Kapusta, B. and Guillope, M. (1993) *Physics of the Earth and Planetary Interiors* **75**, 205.

Karato, S. (1981) *Physics of the Earth and Planetary Interiors* **24**, 1.

Katkov, V.F.; Ivon, A.I. and Chernenko, I.M. (1996) *Inorganic Materials* **32**, 342.

Kenway, P.R. (1994) *J. Am. Ceram. Soc.* **77**, 349.

Kerr, R.A. (1991) *Science* **254**, 1295.

Kingery, W.D. (1954) *J. Am. Ceram. Society* **37**, 42.

Kittel, C. (1963) *Introduction to Solid State Chemistry*, John Wiley and Sons Inc., NY.

Kostov, I. (1968) *Mineralogy*, Oliver and Boyd, London.

Kubicki, J.D. and Lasaga, A.C. (1992) *American Journal of Science* **292**, 153.

Kunaver, U. and Kolar, D. (1993) *Acta Metallurgica et Materialia* **41**, 2255.

Landolt, H.H. and Borstien, R. (1979) *Numerical Data and Functional Relationships in Science and Technology New Series*, Ed. Hellwege, K.H., Group III Crystal and Solid State Physics, **11**, Springer-Verlag.

Lee, C. and Gonze, X. (1994) *Physical Review Letters* **72**, 1686.

Lee, W-Y.; Bristowe, P.D.; Gao, Y. and Merkle, K.L. (1993) *Phil. Mag. Letters* **68**, 309.

Leipold, M.H. (1966) *J. Am. Ceram. Soc.* **49**, 498.

Leslie, M. (1982) *SERC Daresbury Report, DL/SCI/TM31T*, SERC Daresbury Laboratory, UK.

Lewis, G.V. and Catlow, C.R.A. (1985) *J. Physics C: Solid State Physics* **18**, 1149.

Liu, D.M. (1993) *Journal of Materials Science* **28**, 6353.

Liu, J.; Jin, J. and Ming, N. (1989) *Solid State Comm.* **70**, 763.

Liu, L.; Bassett, W.A. and Takahashi, T. (1974) *J. Geophysical Research* **79**, 1160.

Mackrodt, W.C. (1986) in *Ceramic Microstructures '86*, Ed. Pask, J.A. and Evans, A.G. Plenum Press, NY & London.

Mackrodt, W.C. (1992) *Phil. Trans. R. Soc. Lond. A* **341**, 301.

Mackrodt, W. C. and Stewart, R. F. (1979) *J. Physics C: Solid State Physics*, **12**, 431.

Manassidis, I. and Gillan, M.J. (1994) *J. Am. Ceram. Soc.* **77**, 335.

Mason, B. (1966) *Principles of Geochemistry*, John Wiley and Sons Inc., NY.

Matsui, M. (1994) *Mineralogical Magazine* **58A**, 571.

Matsui, M. and Price, G.D. (1992) *Physics and Chemistry of Minerals* **18**, 365.

Mckenzie, D. (1983) *Scientific American* **249**, 51.

McKenzie, D. (1985) *Earth and Planetary Science Letters* **74**, 81.

McQueen, R.G; Fritz, J.N. and Marsh, S.P. (1963) *J. Geophysical Research* **68**, 2319.

Melcholsky, J.J.; Freiman, S.W. and Rice, R.W. (1976) *J. Materials Science* **11**, 1310.

Merkle, K.L. (1994) *Journal of the Physics and Chemistry of Solids* **55**, 991.

Merkle, K.L. and Smith, D.J. (1987a) *Physical Review Letters* **59**, 2887.

Merkle, K.L. and Smith, D.J. (1987b) *Ultramicroscopy* **22**, 57.

Metiu, H.; Lu, Y. and Zhang, Z. (1992) *Science* **255**, 1088.

Metropolis, N.; Rosenbluth, A.W.; Rosenbluth, M.N.; Teller, A.H. and Teller, E. (1953) *J. Chem. Phys.* **21**, 1087

Meyer, M.; Karakasidis, T. and Waldburger, C. (1996) *Materials Science Forum* **207-209**, 525 .

Mills, D. R.; Parker, S. C. and Wall, A. (1991) *Phil. Mag.* A, **64**, 1133.

Mitchell, P.J. and Fincham, D. (1993) *Journal of Physics: Condensed Matter* **5**, 1031.

Mott, N.F. and Littleton, M.J. (1938) *Trans. Faraday Soc.* **34**, 485.

Mulheran, P.A. (1992) *Acta Metallurgica et Materialia* **40**, 1827.

Mulheran, P.A. (1994) *Acta Metallurgica et Materialia* **42**, 3589.

Mulheran, P. and Harding, J.H. (1991) *Acta Metallurgica et Materialia* **39**, 2251.

Mykura, H.; Bansal, P.S. and Lewis, M.H. (1980) *Phil. Mag.* **A42**, 225.

Nagai, T.; Fuchizaki, K. and Kawasaki, K. (1994) *Physica* A **204**, 450.

Navrotsky, A. (1987) *Progress in Solid State Chemistry* **17**, 53.

Nikolopoulos, P. (1985) *J. Mat. Science* **20**, 3993.

Norgett, M.J. and Fletcher, R. (1970) *J. Physics C: Solid State Physics*, **3**, 163

Nosé, S. (1984) *J. Chem. Phys.* **81**, 511.

Nosé, S. (1990) *J. Phys.: Condensed matter* **2**, SA115.

Oliver, P.M.; Watson, G.W. and Parker, S.C. (1995) *Phys. Rev. B-Condensed Matter* **52**, 5323.

Parikh, N.M. (1958) *J. Am. Ceram. Soc.* **41**, 18.

Parinello, M. and Rahman, A. (1981) *Journal of Applied Physics* **52**, 7182.

Parker, S.C. (1983a) *PhD Thesis*, University of London.

Parker, S.C. (1983b) *Solid State Ionics* **8**, 179.

Parker, S.C. and Price, G.D. (1989) *Advances in Solid State Chemistry* **1**, 295.

Parker, S.C.; Davies, M.J.; Oliver, P.M.; Kelsey, E.T. and Watson, G.W. (1992) Program GEM (Generation of Equilibrium Morphologies).

Parry, D.E. (1975) *Surface Science* **49**, 433.

Parry, D.E. (1976) *Surface Science* **54**, 195.

Patel, A.; Price, G.D. and Mendelsohn, M.J. (1991) *Physics and Chemistry of Minerals* **17**, 690.

Patel, A.; Price, G.D.; Matsui, M.; Brodholt, J.P. and Howarth, R.J. (1996) *Physics of the Earth and Planetary Interiors* **98**, 55.

Pavese, A.; Artiloi, G. and Prencipe, M. (1995) *American Mineralogist* **80**, 457.

Pawley, A.; McMillan, P.F. and Holloway, J.R. (1993) *Science* **261**, 1024.

Peckham, G. (1967) *Proc. Phys. Soc.* **90** 657.

Poirier, J-P. (1985) *Creep of Crystals*, Cambridge University Press, UK.

Poirier, J-P. (1991) *Introduction to the Physics of the Earth's Interior*, Cambridge University Press, UK.

Pond, R.C.; Smith, D.A. and Vitek, V. (1978) *Scripta Metallurgica* **12**, 699.

Price, G.D. and Parker, S.C. (1984) *Physics and Chemistry of Minerals* **10**, 209.

Price G.D.; Parker S.C. and Leslie M. (1987a) *Mineralogical Magazine* **51**, 157.

Price, G.D.; Parker, S.C. and Leslie, M. (1987b) *Physics and Chemistry of Minerals* **15**, 181.

Purton, J.; Parker, S.C. and Bullett, D.W. (1997) *Journal of Physics-Condensed Matter* **9**, 5709.

Read, W.T. and Shockley, W. (1950) *Physical Review* **78**, 275.

Rice, R.W.; Freiman, S.W. and Becher, P.F. (1981) *J. Am. Ceram. Soc.* **64**, 345.

Rios, P.R. (1992) *Acta Metallurgica et Materialia* **40**, 873.

Rockett, A. (1994) *Surface Science* **312**, 201.

Ross, N.L.; Shu, J-F.; Hazen, R.M. and Gasparik, T. (1990) *American Mineralogist* **75**, 739.

Sanders, M.J.; Leslie, M. and Catlow C.R.A. (1984) *J. Chem. Soc., Chem. Comms.* 1271.

Sangster, M.J.L. and Stoneham, A.M. (1981) *Phil. Mag.* **B43**, 597.

Sayle, D.C.; Parker, S.C. and Harding, J.H. (1994) *Molecular Simulation* **12**, 127.

Sayle, D.C.; Sayle, T.X.T.; Parker, S.C.; Harding, J.H. and Catlow, C.R.A.. (1995) *Surface Science* **334**, 170.

Sayle, D.C.; Gay, D.H.; Rohl, A.L.; Catlow, C.R.A.; Harding, J.H.; Perrin, M.A. and Nortier, P. (1996) *J. Materials Chemistry* **6**, 653.

Sayle, T.X.T.; Catlow, C.R.A.; Sayle, D.C.; Parker, S.C. and Harding, J.H. (1993) *Phil. Mag.* **A68**, 565.

Sempolinski, D. R. and Kingery, W. D. (1980) *J. Am. Ceram. Soc.*, **63**, 664.

Sinclair, W. and Ringwood, A.E. (1978) *Nature* **272**, 714.

Singh, K.K. and Sangal, S. (1997) *Materials Science Forum* **243**, 149.

Srolovitz, D.J.; Anderson, M.P.; Sahni, P.S. and Grest, G.S. (1984a) *Acta Metall.* **32**, 793.

Srolovitz, D.J.; Anderson, M.P.; Grest, G.S. and Sahni, P.S. (1984b) *Acta Metall.* **32**, 1429.

Srolovitz, D.J.; Grest, G.S. and Anderson, M.P. (1985) *Acta Metall.* **33**, 2233.

Stubican, V. S. and Osenbach, J. W. (1984) *Solid State Ionics*, **12**, 375.

Sutton, A.P. and Vitek, V. (1982) *Acta Metallurgica* **30**, 2011.

Sutton, A.P. and Vitek, V. (1983a) *Phil. Trans. R. Soc. A* **309**, 1.

Sutton, A.P. and Vitek, V. (1983b) *Phil. Trans. R. Soc. A* **309**, 37.

Swainson, I.P. and Dove, M.T. (1995) *Journal of Physics: Condensed Matter* **7**, 1771.

Tasker, P.W. (1990) *Journal of the Chemical Society-Faraday Transactions* **86**, 1311.

Tasker, P.W.; Colbourn, E.A. and Mackrodt, W.C. (1985) *J. Amer. Ceram. Soc.* **68**, 74.

Tasker, P.W. and Stoneham, A.M. (1987) *Journal de Chimie Physique et de Physico-Chemie Biologique* **84**, 149.

Theunissen, G.S.A.M.; Winnubst, J.A. and Burggraaf, A.J. (1992) *J. Mat. Science* **27**, 5057.

Titiloye, J.O.; Parker, S.C.; Stone, F.S. and Catlow, C.R.A. (1991) *J. Phys. Chem.* **95**, 4038.

Tsuchida,Y. and Yagi,T. (1989) *Nature* **340**, 217.

Turnbull, D. and Hoffman, R. E. (1954) *Acta Metallurgica*, **2**, 419.

van Beest, B.W.H.; Kramer, G.J. and van Santen, R.A. (1990) *Phys. Rev. Letters* **64**, 1955.

Vocadlo, L. and Price, G.D. (1996) *Physics and Chemistry of Minerals* **23**, 42.

Vocadlo, L.; Wall, A.; Parker, S.C. and Price, G.D. (1995) *Physics of the Earth and Planetary Interiors* **88**, 193.

Vogel, S. and Klimanek, P. (1996) *Materials Science Forum* **204**, 449.

Vogt, T. and Schmahl, W.W. (1993) *Europhysics Letters* **24**, 281.

Wall, A. and Price, G.D. (1989) *Physics of the Earth and Planetary Interiors* **58**, 192.

Wall, A.; Parker, S.C. and Watson, G.W. (1993) *Physics and Chemistry of Minerals* **20**, 69.

Wang, L.Q.; Baer, D.R.; Engelhard, M.H. and Schultz, A.H. (1995) *Surface Science* **344**, 237.

Wang, Y.; Guyot, F.; Yeganeh-Haeri, A. and Liebermann, R.C. (1990) *Science* **248**, 468.

Watson, G.W. (1994) *PhD Thesis*, University of Bath.

Watson, G.W. (1996) *Private Communication.*

Watson, G.W. and Parker, S.C. (1994) *Phil. Mag. Letters* **71**, 59.

Watson, G.W.; Parker, S.C. and Wall, A. (1992) *Journal of Physics: Condensed Matter* **4**, 2097.

Watson, G.W.; Wall, A. and Parker, S.C. (1995) *Physics of the Earth and Planetary Interiors* **89**, 137.

Watson, G.W.; Kelsey, E.T.; de Leeuw, N.H.; Harris, D.J. and Parker, S.C. (1996) *Journal of the Chemical Society-Faraday Transactions* **92**, 433.

Watson, G.W., Wall, A., and Parker, S.C. (1997) *In preparation.*

Webb, S.L. and Jackson, I. (1993) *European Journal of Mineralogy* **5**, 1111.

Weidner, D.J. (1986) *Advances in Physical Geophysics* **6**, 251.

Weidner, D.J., Bass, J.D., Ringwood, A.E. and Sinclair, W. (1982) *J. Geophysical Research* **87**, 4740.

Westwood, A.R.C. and Hitch, T.T. (1963) *Journal of Applied Physics* **34**, 3085.

White, T.J., Segall, R.L., Barry, J.C. and Hutchinson, J.L. (1985) *Acta Cryst.* **B41**, 93.

Winkler, B. and Dove, M.T. (1992) *Physics and Chemistry of Minerals* **18**, 407.

Winkler, B.; Dove, M.T. and Leslie, M. (1991) *American Mineralogist* **76**, 313.

Wright, K. and Catlow, C.R.A. (1994) *Physics and Chemistry of Minerals* **20**, 500.

Wright, K.; Freer, R. and Catlow, C.R.A. (1995) *American Mineralogist* **80**, 1020.

Wuensch, B. J. and Tuller, H. L. (1994) *J. Phys. Chem. Solids*, **55**, 975.

Wyckoff, R.W.G. (1963) *Crystal Structures* **1**, Wiley, NY.

Xu, C. and Goodman, D.W. (1997) *Chemical Physics Letters* **265**, 341.

Xu, C.; Oh, W.S.; Guo, Q. and Goodman, D.W. (1996) *Journal of Vacuum Science and Technology A-Vacuum surfaces and Films* **14**, 1395.

Xu, J.A.; Mao, H.K. and Bell, P.M. (1986) *Science* **232**, 1401.

Zha, C.S.; Duffy, T.S.; Downs, R.T.; Mao, H.K. and Hemley, R.J. (1996) *Journal of Geophysical Research-Solid Earth* **101**, 17535.

Zhu, P. and Smith, R.W. (1992) *Acta Metallurgica et Materialia* **40**, 683.